PhD Thesis

2017

An *in vivo* investigation of choroidal vasculature in age-related macular degeneration

Louise Terry

Under the supervision of Dr Ashley Wood, Prof Tom Margrain, and Prof Rachel North

Acknowledgements

I would like to extend my sincere thanks to many people who have made this work possible. Firstly, to my supervisors Ashley Wood, Tom Margrain, and Rachel North, for their academic support and advice throughout this project. To my advisor John Wild for encouraging me to pursue a career in academia, and to Sue Hobbs for postgraduate support over the last few years. I am also grateful to the members of the Macular Research Group for their help overcoming the numerous obstacles encountered.

Acknowledgments go also to my collaborators on this work; Nick White and James Fergusson at Vision Science Bioimaging Labs, for their help with imaging and technical queries; Xianghua Xie, Jingjing Deng, and Dafydd Ravenscroft at Swansea University for their invaluable data analysis; and to Mr Al-Bermani at University Hospital of Wales, and the staff at Cardiff University Optometrists, for supporting participant recruitment.

A special thanks to my friends and colleagues for their feedback and support, and for keeping me (relatively) sane. Particular thanks go to Lindsay, Shindy, Flors, James, Nikita, Melissa, and Neema. And to my parents, for teaching me that the sky's the limit.

Finally, but by no means least, to my long-suffering husband Tom – I honestly couldn't have done this without you.

Summary

Age-related macular degeneration (AMD) is the leading cause of visual impairment in the developed world. Whilst the pathogenesis is complex and not fully understood, changes to the choroidal vasculature in AMD have been demonstrated using histology. Advances in imaging technology, particularly long-wavelength optical coherence tomography (OCT), allow *in vivo* visualisation and investigation of this structure. The aim of this work is to determine whether changes to the choroidal vasculature are detectable in AMD using *in vivo* imaging. This was achieved through the evaluation of parameters for quantifying the structure, and the application of a machine learning approach to automated disease severity classification, based on choroidal appearance.

Participants with early AMD (n=25), neovascular AMD (nAMD; n=25), and healthy controls (n=25) underwent imaging with a non-commercial long-wavelength (λ_c=1040 nm) OCT device. Subfoveal choroidal thickness, choroidal area, and luminal area were significantly lower in the nAMD group than the healthy and early AMD groups, whilst vessel ratio was significantly greater ($P<0.05$ in all cases). There was no significant difference in visible vessel diameter, choroidal vascularity index, luminal area ratio, or luminal perimeter ratio between the groups. No significant differences were found between the healthy and early AMD groups for any of the eight vascular parameters assessed.

Classification of the disease groups based on choroidal OCT images was demonstrated using machine learning techniques. Textural features within the images were extracted using Gabor filters, and K-nearest neighbour, support vector machine, and random forest classifiers were assessed for this classification task. Textural changes were most pronounced in late-stage disease, although attribution to pathology or pharmacological intervention (anti-VEGF treatment) was not possible. Changes were also discernible in the early AMD group, suggesting sensitivity of this approach to detecting vascular involvement in early disease.

In conclusion, structural changes to the choroidal vasculature in AMD are detectable *in vivo* using OCT imaging, demonstrated with both manual and automated analysis techniques. Whilst changes were most prominent in late-stage disease, subtle structural changes in early AMD were identified with texture analysis, warranting further investigation to improve our understanding of choroidal involvement in the pathogenesis of early AMD.

Table of Figures

List of Tables

Abbreviations

AEL	Axial eye length
AMD	Age-related macular degeneration
ANOVA	Analysis of variance
ANSI	American National Standards Institute
AREDS	Age-related eye disease study
AUC	Area under the curve
BP	Blood pressure
CA	Choroidal area
CNN	Convolutional neural network
CNV	Choroidal neovascularisation
CSC	Central serous chorioretinopathy
CSME	Clinically significant macular edema
CoR	Coefficient of repeatability
CVI	Choroidal vascularity index
DME	Diabetic macular edema
DR	Diabetic retinopathy
EDI	Enhanced depth imaging
ETDRS	Early treatment of diabetic retinopathy study
FD-OCT	Frequency domain optical coherence tomography
GA	Geographic atrophy
ICC	Intra-class correlation coefficient
ICNIRP	International Commission on Non-Ionizing Radiation Protection
IOL	Intraocular lens
IOP	Intraocular pressure
KNN	K-nearest neighbour
LA	Luminal area
LAR	Luminal area ratio
LOCS	Lens opacities classification system
LogMAR	Log minimum angle of resolution
LOOCV	Leave-one-out cross-validation

LPR	Luminal perimeter ratio
nAMD	Neovascular age-related macular degeneration
NICE	National Institute for Health and Care Excellence
OCT	Optical coherence tomography
OCTA	Optical coherence tomography angiography
ONH	Optic nerve head
PCV	Polypoidal choroidal vasculopathy
PDT	Photodynamic therapy
PED	Pigment epithelial detachment
PEDF	Pigment epithelium derived factor
RFS	Random forest
ROC	Receiver operating characteristic
ROI	Region of interest
ROS	Reactive oxygen species
RPD	Reticular pseudodrusen
RPE	Retinal pigment epithelium
SD	Standard deviation
SD-OCT	Spectral domain optical coherence tomography
SFCT	Subfoveal choroidal thickness
SE	Standard error
SLD	Superluminescent diode
SNR	Signal-to-noise ratio
SS-OCT	Swept source optical coherence tomography
SVM	Support vector machine
TD-OCT	Time-domain optical coherence tomography
VA	Visual acuity
VEGF	Vascular endothelial growth factor
VKH	Vogt-Koyanagi-Harada
VR	Vessel ratio
VVD	Visible vessel diameter

Table of Contents

1 Introduction

1.1 Outline

This thesis describes a series of studies designed to detect structural changes in the choroidal vasculature of patients with age-related macular degeneration (AMD), using *in vivo* imaging. AMD is the leading cause of visual impairment in the developed world, and has been estimated to affect 8.7% of people aged 45-85 (Wong et al. 2014). It is generally experienced as visual distortion and a progressive loss of central vision, causing difficulties with simple daily tasks such as reading, face recognition, and ability to drive. This often results in loss of independence, and feelings of isolation, with up to 45% of people with AMD showing clinical signs of depression (Dawson et al. 2014). With increasing life expectancy, the prevalence of AMD is predicted to rise, reaching 196 million people worldwide in 2020, and 288 million by 2040 (Wong et al. 2014). Treatment is currently only available for the wet sub-type of AMD (accounting for ~10% of cases), in the form of intravitreal anti-VEGF injections. The vision loss associated with dry AMD is irreversible, and is typically managed by provision of visual aids through low vision services. This lack of early intervention, coupled with the relatively high cost of pharmacological therapy (~£550-£815 per injection; British Medical Association 2017), imposes a considerable economic burden on healthcare services.

Although the underlying pathogenesis of AMD is not yet fully understood, it is known that changes to the choroidal blood supply contributes to the retinal degeneration seen in AMD (Zarbin 2004). Traditionally, histological techniques have been used to identify these changes *ex vivo*, but advances in imaging technology increasingly allows *in vivo* visualisation of this structure. In particular, optical coherence tomography (OCT) imaging now provides a means for fast, non-invasive imaging of the posterior eye, and is becoming increasingly prevalent in both primary and secondary care. Although this technology is primarily used for retinal imaging, it has recently been optimised for choroidal imaging (Ferrara et al. 2016). A number of parameters for quantifying the choroidal structure have been described, including choroidal thickness, and vessel diameter. However, these parameters are

not yet used in clinical assessment. Development and optimisation of such parameters may provide novel methods of early diagnosis or monitoring of AMD.

Machine learning is a contemporary and increasingly popular approach to complex image analysis problems, including medical image analysis and computer aided diagnosis (Wernick et al. 2010; Alpaydin 2014; de Bruijne 2016). There are two main aspects to this approach; feature extraction, and prediction. For instance, structural or textural features may be extracted from an OCT image, and algorithms are trained to make predictions from these features, such as disease classification. To date, this approach has not been applied to automated disease classification of AMD severity, using choroidal OCT images. Accurate classification of disease status using this method would support the hypothesis that the choroid has a significant role in AMD pathogenesis, and that these structural changes are detectable using OCT imaging. It would also confirm that machine learning is a feasible approach for assessing structural change to the choroid in AMD.

This thesis initially reviews the current literature regarding physiological and pathological variations in the choroid, the current understanding of AMD pathogenesis (particularly choroidal involvement), application of OCT to choroidal imaging, and image analysis techniques. The following chapters describe the development of protocols for image acquisition, processing, and analysis. Previously described methods for quantifying the choroid are evaluated and assessed for repeatability, as well as the application of machine learning techniques to the classification of AMD from choroidal OCT images. The results from this automated approach are discussed in relation to potential clinical application of choroidal investigation in AMD, and other pathologies involving the choroid.

The principle aim of the work described in this thesis is to determine whether structural changes to the choroidal vasculature in AMD are detectable using *in vivo* OCT imaging.

To achieve this, three supplementary aims are as follows:

1) To optimise protocols for image acquisition and processing for enhanced visualisation of the choroidal vasculature.
2) To evaluate parameters describing the choroidal vasculature, including assessment of inter-session repeatability.

3) To explore the feasibility of applying machine learning techniques to automated classification of AMD by disease severity, based on choroidal appearance.

1.2 The healthy eye

Before considering the pathology, it is important to have an understanding of the basic structural and functional properties of the tissue or structure in question. This section provides an overview of the principle structures implicated in the pathophysiology of AMD (anterior to posterior); the retina, retinal pigment epithelium (RPE), Bruch's membrane, and the choroid. The typical physiological ageing changes for each structure have also been outlined.

1.2.1 Retina

When viewed histologically, the retina can be divided into a number of distinct layers, as seen in Figure 1.1. These layers are representative of the highly organised cellular structure of the retina, with each comprising a number of specific cell types. The ultimate purpose of the retina is the absorption of light and the

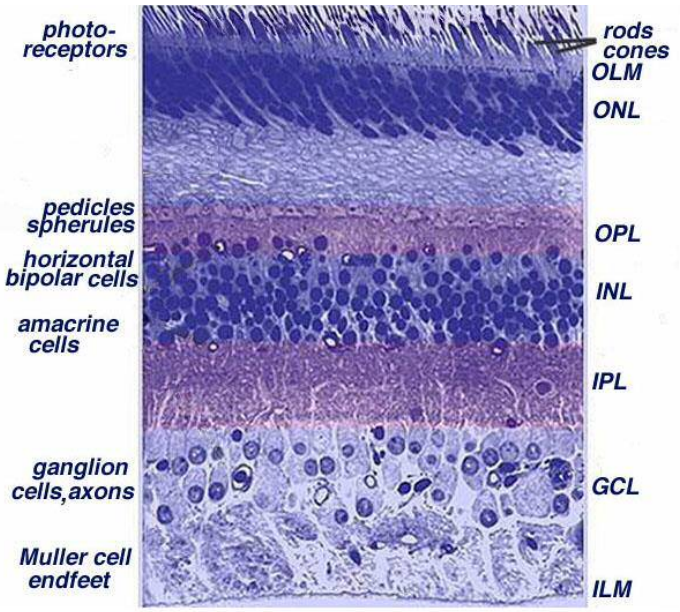

Figure 1.1 Light microscope image of a vertical section through the human retina, showing the distinct layers, and the types of retinal cell. The vitreous is adjacent to the ILM, and the RPE neighbours the photoreceptors. OLM = outer limiting membrane; ONL = outer nuclear layer; OPL = outer plexiform layer; INL = inner nuclear layer; IPL = inner plexiform layer; GCL = ganglion cell layer; ILM = inner limiting membrane. Image from Kolb (2014).

conversion, through a process known as phototransduction, into a neural signal for transmission to the brain (via the optic nerve). In AMD, it is primarily the outer retina containing the light-sensitive photoreceptors that is affected, with other structures becoming increasingly disrupted with disease progression.

1.2.2 Macula

The macula is the region of the retina centred on the fovea, and is responsible for high acuity vision. Anatomically, the macula is defined as the region of retina in which the ganglion cell layer is more than one cell in thickness. This has an approximate diameter of 5.5 mm (Hogan et al. 1971). For simplicity, clinical grading systems generally define the macula as a circle of 6 mm diameter, centred on the foveal pit (Bird et al. 1995; AREDS 2001a; Figure 1.2). This corresponds to approximately the central 20° of visual field. The macula is surrounded by the vascular arcades branching from the optic nerve head, but the central 500 μm of the fovea is avascular, to allow for uninterrupted high acuity vision (Hendrickson 2005). A higher concentration of pigment in the macula gives it a darker appearance in retinal images than the surrounding retina (Snodderly et al. 1984a).

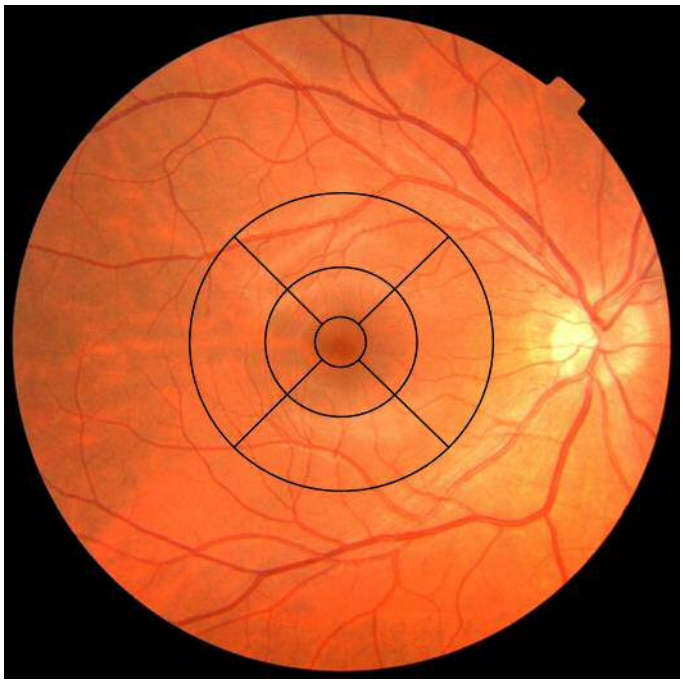

Figure 1.2 Retinal photograph of a healthy right eye. The vascular arcades can be seen encircling the macula, which appears more pigmented than the rest of the retina. The overlaid grid is 6 mm in diameter, demonstrating the total size of the macular region by standard clinical definition (Bird et al. 1995; AREDS 2001a). Image acquired by L. Terry during conduct of this study.

There are two types of photoreceptor in the human retina; rods and cones (Figure 1.3). Rods provide monochromatic vision optimised for scotopic conditions. Cones are responsible for colour vision and high acuity vision, and hence are of high density at the macula. Both types of photoreceptor have an inner and outer segment. The outer segment contains a stack of membranous discs embedded with photopigments, which are formed at the base of the outer segment, and then migrate along its length before being shed at the apex and phagocytosed by the RPE (Strauss 2005). The inner segment contains a high number of mitochondria and other sub-cellular components required for energy production and maintenance of the cell.

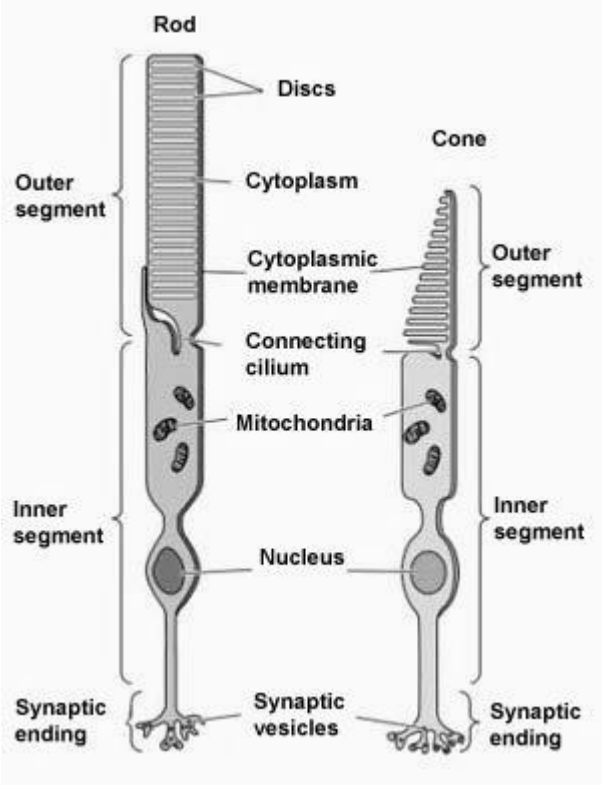

Figure 1.3 Schematic of the two types of photoreceptor, showing the inner and outer segments. The outer segments are surrounded by apical processes from the RPE (not shown). Image adapted from Dubuc (2014).

Photoreceptors require large amounts of energy to function, particularly in the dark when the rod cells are most active. In daylight, rod responses are suppressed, reducing total energy consumption by >75% (Okawa et al. 2008). Oxygen is required for this energy production process, hence the high oxygen demand of the outer retina, particularly under scotopic conditions (Lamb and Pugh 2004). As the fovea is avascular, it receives this oxygen solely from the choroidal supply (through Bruch's membrane and the RPE), clearly demonstrating the importance of choroidal circulation in maintaining high acuity vision.

1.2.3 Retinal pigment epithelium

The RPE is a monolayer of pigmented hexagonal-shaped cells with a regular arrangement, located between Bruch's membrane and the outer neural retina (photoreceptors). At the apical surface, long microvilli extend to surround the rod and cone cells, increasing the area of contact between the photoreceptors and the RPE. The cells of the RPE are bound together by tight junctions, forming part of the blood-retina barrier (Campbell and Humphries 2012).

The RPE has numerous functions (as summarised in Figure 1.4), including the transportation of water, nutrients and ions from the choroid to the outer retina and sub-retinal space. The protein RPE65 found in RPE cells is required for the isomerisation of all-trans-retinal to 11-cis-retinal; an essential component of the visual cycle (Redmond et al. 1998). Furthermore, the highly pigmented RPE absorbs stray light not absorbed by photoreceptors, protecting the retina from photo-oxidative damage (Strauss 2005).

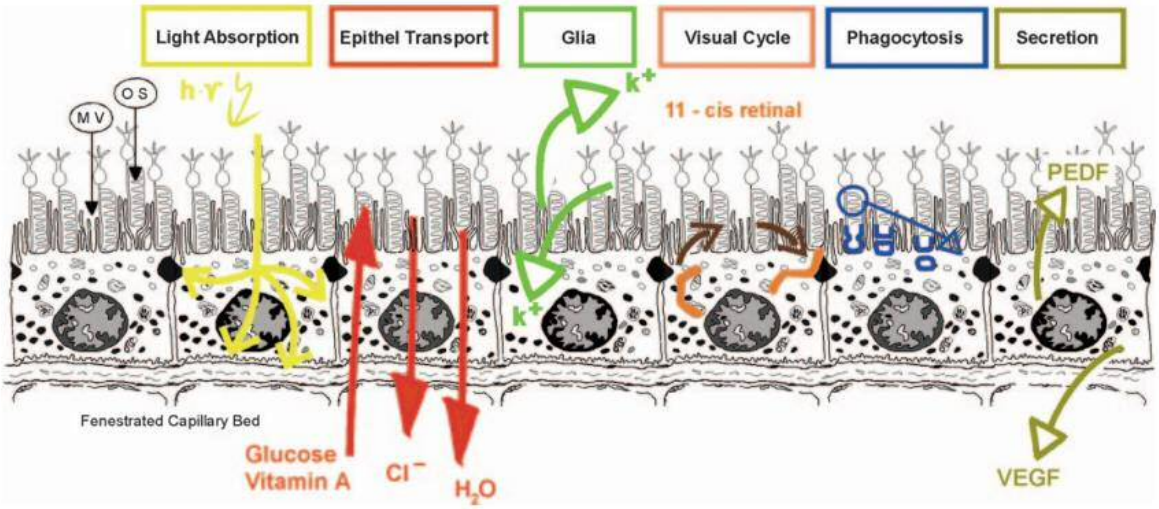

Figure 1.4 A schematic summary of the functions of the RPE. Abbreviations include: OS = outer segments; MV = microvilli; PEDF = pigment epithelium derived factor; VEGF = vascular endothelial growth factor; Epithel = epithelial. Image from Strauss (2005).

The RPE is also responsible for the phagocytosis of shed photoreceptor outer segments. However, the structure is susceptible to oxidative damage since these outer segment membranes have a high polyunsaturated fatty acid content, and are easily oxidised if not disposed of (Beatty et al. 2000). Incomplete digestion of these membranes is thought to result in a build-up of the pigment lipofuscin, which itself leaves the RPE prone to further oxidative damage (Margrain et al. 2004). The RPE is protected from this damage by light absorbing pigments including melanin, and

antioxidant enzymes such as catalase (Simó et al. 2010). Furthermore, the adjacent photoreceptors contain antioxidant carotenoids including lutein and zeaxanthin, believed to help minimise oxidative damage (Beatty et al. 2000; Strauss 2005).

In addition, the RPE maintains the retina and adjacent structures by producing growth and other factors, including vascular endothelial growth factor (VEGF) and pigment epithelium derived factor (PEDF). These factors have pro- and anti-angiogenic properties respectively, and are essential for maintaining choroidal health and structure. However, these factors also have a pivotal role in the development of neovascular membranes in wet AMD (Bhutto et al. 2005; Section 1.4.3).

1.2.4 Bruch's membrane

Bruch's membrane is a thin (2-4 μm), acellular layer of extracellular matrix located between the RPE and the choroidal vessels. The membrane acts as a barrier, allowing metabolites and waste products to pass from the choroid to the outer retina and *vice versa*. It is structurally comparable to the renal glomerulus, providing a basis for commonality between aspects of retinal and kidney disease (Kim et al. 1997; Weiner et al. 2011).

1.2.4.1 Ageing changes

With age, Bruch's membrane becomes thicker for a number of reasons, including increased deposition of oxidised metabolic waste and cross-linking of collagen fibres (Ramrattan et al. 1994; Booij et al. 2010). Lipids and advanced glycation end-products, along with basal laminar and linear deposits have all been found to accumulate with age, and alter the permeability of the membrane (Guymer et al. 1998; Yamada et al. 2006; Booij et al. 2010). An increase in collagen cross-linking has also been identified, as well as a reduced membrane permeability in aged eyes (Karwatowski et al. 1995; Guymer et al. 1998). Finally, a reduction in the integrity and flexibility of the elastic layer of Bruch's membrane has been shown in early age-related disease (Loffler and Lee 1986; Chong et al. 2005). These ageing changes to Bruch's membrane are thought to act as a barrier to the exchange of metabolites between the choroid and the RPE and outer retina (Guymer et al. 1998).

1.2.5 Choroid

The choroid is a highly vascularised structure located between the RPE and sclera, and forms the uveal tract, along with the iris and ciliary body. It is comprised of three layers – the choriocapillaris; a dense capillary bed adjacent to Bruch's membrane; and the Sattler and Haller layers, comprising medium and large blood vessels respectively, with the latter being adjacent to the sclera (Figure 1.5). The choriocapillaris is fed by (and drains into) these larger vessels. The choroid is supplied by the short posterior ciliary arteries (deriving from the ophthalmic artery), and drained by the vorticose veins into the ophthalmic veins (Snell and Lemp 1998).

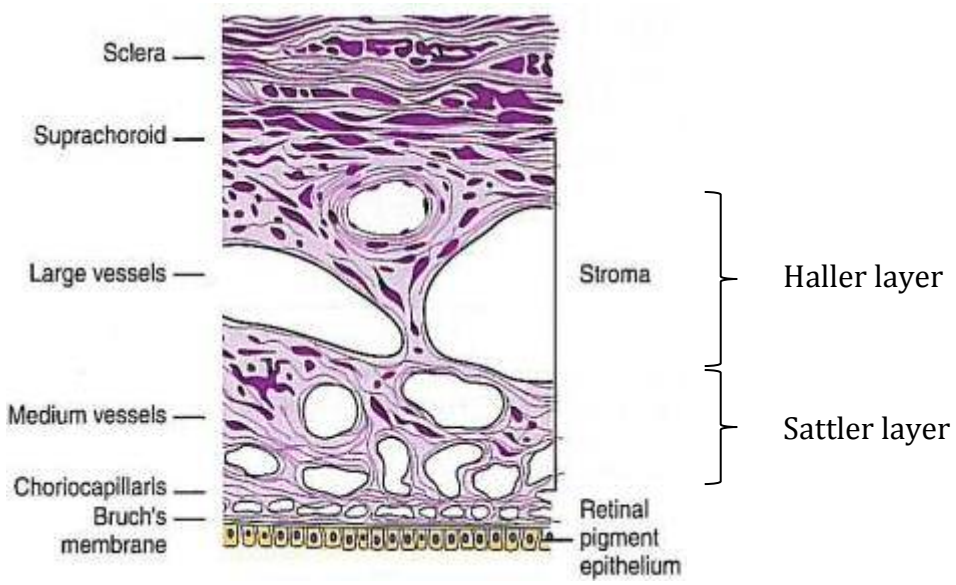

Figure 1.5 Schematic of the choroid and its surrounding structures, showing the distribution of the large and medium vessels as well as the choriocapillaris (not to scale). Image adapted from Remington (2005).

Advances in imaging technology (particularly OCT imaging, see Section 1.6.1) have facilitated investigation of the choroid *in vivo*. The healthy choroid has a reported mean subfoveal thickness ranging from 196 μm to 354 μm (Margolis and Spaide 2009; Ikuno et al. 2010; Rahman et al. 2011; Ding et al. 2011; Lee et al. 2013c). This demonstrates the large variability in choroidal thickness between individuals. The choroid is thicker temporally than nasally, and superiorly than inferiorly (Ikuno et al. 2010; Tan et al. 2014). Variations in choroidal thickness due to several factors are discussed in more detail in Section 1.3.

The choriocapillaris is comprised of small capillaries, typically ranging from ~7-10 μm in diameter, measured with histology (Ramrattan et al. 1994; Spraul et al.

1996). Reported mean diameter of the large choroidal vessels with *in vivo* OCT imaging ranges from 122.5 μm to 159.8 μm in young, healthy eyes (Yang et al. 2013; Bittencourt et al. 2014; Park and Oh 2014).

Primarily, the vasculature of the choroid supplies metabolites to the outer retina and removes waste products from the retina; the capillaries are fenestrated to allow these molecules to pass through the vessel walls. Photoreceptors are highly metabolically active, and approximately 90% of the oxygen delivered to the photoreceptors is supplied by the choroidal circulation (Ahmed et al. 1993). In the macula, photoreceptors are densely packed to maximise high acuity vision, and there is no retinal vasculature. It has been hypothesised that this physiology makes the macula more susceptible to metabolic deprivation and hence age-related damage than the rest of the retina where a dual blood supply is present (Penfold et al. 2001; Provis et al. 2005).

Another proposed function of the choroid is thermoregulation, facilitated by the very high blood flow, protecting the retina from damage in extreme temperatures (Parver 1991). In low temperatures, the choroid may act as a heat source, warming the retina, and in high temperatures, it may act as a heat sink, directing heat away from the retina. This also applies to the heat generated during exposure of the eye to bright light. However, this theory of thermoregulation provided by the choroid is not universally accepted (Nickla and Wallman 2010). The pigment within the choroid absorbs stray light within the eye not already absorbed by the photoreceptors or RPE, reducing intra-ocular scatter.

It has also been suggested that the choroid plays a role in emmetropization, and has been shown to change in thickness to move the position of the chick retina made functionally myopic or hyperopic using lenses (Irving et al. 1992; Wildsoet and Wallman 1995). Following the removal of the defocussing lenses, the eye compensated in the opposite direction, returning to emmetropia (Wildsoet and Wallman 1995). In humans, optical defocus has been shown to interrupt the natural diurnal rhythm in choroidal thickness (see Section 1.3.6), suggesting the role of defocus (particularly hyperopic) in the development of myopia.

1.2.5.1 Ageing changes

Ageing has been shown to affect the choroid in a number of ways. Advancing age increases capillary spacing, and reduces the number and diameter of vessels (Ramrattan et al. 1994). Doppler flowmetry has been used to identify a reduction in choroidal blood flow and choroidal volume with age (Riva et al. 1994). This disrupted supply of metabolites and removal of waste products may leave the retina susceptible to degenerative ageing changes, including hypoxia and build-up of metabolic waste products (see Section 1.4.3; Chakraborty et al. 2012; Chakraborty et al. 2013).

To conclude, the choroid plays an important role in maintaining the health of the outer retina and RPE. Changes to these structures are therefore likely to have a detrimental effect on retinal integrity, inhibiting retinal function, and resulting in a decrease in visual acuity. Ageing has been shown to alter the composition of both the choroidal vasculature and Bruch's membrane, rendering the outer retina at risk of degenerative changes, particularly at the macula.

1.3 Factors affecting choroidal structure

Several factors have been shown to affect choroidal structure, both physiological and pathological (Table 1.1). It is unsurprising that a number of factors associated with the circulatory system manifest in the choroid, a highly vascular structure. In particular, age, smoking, and hypertension have been associated with an increased risk of both cardiovascular disease and AMD development (Chakravarthy et al. 2010).

This section outlines the literature addressing detectable variations in choroidal structure, including physiological factors, and ocular and systemic pathology. It is important to account for these factors in the study of choroidal structure, so that relevant variables are controlled for in study design and data analysis, where possible. This ensures that any difference detected in the structure can be attributed to the variable being studied, rather than variation resulting from other confounding factors. Whilst choroidal thickness is the most common measure reported in the literature, other parameters that describe choroidal structure are

also discussed. All choroidal measurements discussed in this chapter were obtained from OCT images, unless otherwise stated.

Table 1.1 Factors associated with choroidal thickness and/or structure.

Physiological factors		**Pathological factors**
Non-modifiable	***Modifiable***	
Age	Caffeine intake	Systemic hypertension
Sex	Water intake	Diabetes mellitus
Refractive error	Alcohol intake	Age-related macular degeneration
Axial eye length	Smoking	Central serous chorioretinopathy
	Time of day	Posterior uveitis

1.3.1 Age and sex

Studies have shown a decrease in choroidal thickness with age (Nishida et al. 2012; Wong et al. 2013; Jonas et al. 2014). Regression models have been developed to describe the relationship between these variables. Margolis and Spaide (2009), Ikuno et al. (2010), and Coscas et al. (2012) found choroidal thickness to decrease by 1.56 μm, 1.4 μm, and 1.95 μm per year of age respectively. Agawa et al. (2011) found a significant correlation between choroidal thickness and age in eyes with an axial length >25 mm (myopic eyes only). This is in agreement with Barteselli et al. (2014) who found macular choroidal volume to decrease by 0.32 mm^3 for every decade of life (from a mean total volume of 5.56 mm^3), in high myopes. Given these identified changes, and the demonstrated decrease in choroidal perfusion, age should be controlled for in any study of choroidal structure.

In the Beijing Eye Study (n=3233), a significantly higher choroidal thickness was found in men than women (mean difference 28.5 μm with multivariate analysis; Wei et al. 2013). The mean age in this study was 64.6 years. A study of 93 young, healthy Danish participants found the subfoveal choroid to be 18% thicker in men than women, when adjusted for age and axial eye length (AEL; Li, Larsen and Munch 2011). The authors state that this observation may help explain the sex-linked prevalence of choroid-related conditions such as central serous chorioretinopathy (CSC), AMD, and myopia.

CSC is an idiopathic condition causing a detachment of the retinal layers from the RPE at the macula, resulting in the accumulation of fluid in the sub-retinal space.

The choroid has been found to be substantially thicker in this condition than in healthy subjects, with reported mean thicknesses ranging from 421 μm to 505 μm in the affected eye (Imamura et al. 2009; Pryds and Larsen 2012; Yang et al. 2013). This condition occurs more frequently in men than women, who typically have a thicker choroid (Li et al. 2011; Wei et al. 2013). Conversely, a thinner choroid is generally observed in late-stage AMD (see Section 1.4.5) where the disease prevalence has been reported to be higher in women (Evans 2001; Rudnicka et al. 2012). Furthermore, large population studies have reported a higher prevalence of myopia and higher degrees of myopia in women (Sperduto et al. 1983; Wang et al. 1994; Wong et al. 2000), where the choroid is generally thinner (see Section 1.3.2). However the existence of such a relationship is still debatable, as other studies have not found a significant difference between the sexes, or suggest that women tend slightly towards hyperopia when compared to men (Katz et al. 1997; Shimizu et al. 2003).

Given the evidence for a difference in choroidal thickness between men and women, and with advancing age, any study of choroidal thickness should attempt to control for these factors.

1.3.2 Refractive error and axial eye length

A number of studies have identified a relationship between choroidal thickness and refractive error (Ikuno et al. 2010; Agawa et al. 2011; Coscas et al. 2012; Tan et al. 2014; Barteselli et al. 2014). A study of 124 healthy individuals of Chinese ethnicity, showed the choroid to be thickest among emmetropes, becoming progressively thinner among low, moderate and high myopes (Tan et al. 2014). The same trend was demonstrated for retinal thickness, but this variation was smaller than that of choroidal thickness. However, the study was limited to emmetropes and myopes (refractive error range -10.00D to +0.50D), since only 0.7% of the Chinese population under 30 years of age are hyperopic, making patient recruitment challenging (Wu et al. 2001; Tan et al. 2014). Furthermore, Nishida et al. (2012) found subfoveal choroidal thickness to have a significant inverse correlation with myopic refractive spherical equivalent, as well as with age and logMAR visual acuity in high myopes. The authors suggest choroidal thickness as an important predictor

of visual acuity in high myopia, and that it may have epidemiologic significance with increasing myopia worldwide.

Coscas et al. (2012) found the choroid to be thinner in high myopes (with over -6.00D of myopia), but no significant difference between emmetropes and moderate myopes (under -6.00 D of myopia), whilst Agawa et al. (2011) also found a significant positive correlation between choroidal thickness and magnitude of myopia. In contrast, Ikuno et al. (2010) reported only a borderline positive correlation between these variables, although participants with high myopia (over -6.00 D) were excluded from this study. Jonas et al. (2014) conducted multivariate regression analysis and found choroidal thickness to decrease by 15 μm per dioptre increase in myopia.

These findings are consistent with those of Barteselli et al. (2014), who assessed 98 eyes using a volumetric analysis, due to the nature of the pathological myopia included in the study. Features of pathological myopia, such as lacquer cracks, often result in an uneven thickness across the choroid (Wang et al. 2013); sampling thickness at a single point or points may therefore not be a true representation of overall choroidal thickness. Barteselli and colleagues found a decrease in choroidal volume in highly myopic eyes, particularly those with coexisting myopic traction maculopathy or a history of choroidal neovascularisation. The authors suggest this severe thinning of the choroid in these individuals is likely to lead to insufficient metabolic supply to the macula, and these patients should undergo closer clinical follow-up.

Despite this correlation, the majority of population-based studies have identified no significant association between refractive error and risk of developing AMD (Klein et al. 2004). If anything, increased risk of AMD development has been associated with high degrees of hyperopia rather than myopia (Ikram et al. 2003). It is unclear why this is the case, although there have been several theories presented. Firstly, hyperopic eyes tend to have a higher retinal thickness as well as choroidal thickness. This may lead to a higher demand for metabolites per unit area of retina, increasing the likelihood of a deficit. Secondly, hyperopic eyes tend to have a shorter AEL and therefore a thicker and more compact sclera. This increased stiffness may restrict choroidal flow, thereby restricting exchange of metabolites and increasing risk of hypoxia and oxidative stress (see Section 1.4.3).

Due to the optics of the eye, AEL and refractive error are closely related (myopes often have a longer axial length and *vice versa*; Llorente et al. 2004; Foster et al. 2010). It is therefore unsurprising that a relationship between choroidal thickness and AEL has also been identified (Ikuno et al. 2010; Agawa et al. 2011; Li et al. 2011; Wei et al. 2013; Sanchez-Cano et al. 2014; Barteselli et al. 2014).

Li et al. (2011) used a linear regression model to show that choroidal thickness decreased by 58.2 μm per mm increase in AEL, whilst Sanchez-Cano et al. (2014) found a similar decrease of 43.8 μm per mm. Likewise, Barteselli et al. (2014) demonstrated a decrease in choroidal volume of 0.49 mm^3 per mm increase in AEL in high myopes (from a mean volume of 7.74 mm^3 in emmetropes). Other studies have also documented a significant negative correlation between choroidal thickness and AEL (Ikuno et al. 2010; Agawa et al. 2011; Wei et al. 2013), all in Asian populations.

The possible effect of OCT image magnification should be considered here. Transverse image magnification is known to be different in eyes with different AEL (see Sections 2.3.4 and 3.1). This does not affect axial measurements, such as subfoveal choroidal thickness, but will affect regional thickness or volume measurements. However, the majority of the studies described in this section used axial measurements only, or acquired measurements with a Spectralis OCT (Heidelberg Engineering, Heidelberg, Germany) which makes a compensation for AEL on image scaling, based on corneal curvature and the defocus setting on the instrument (Barteselli et al. 2014). This should therefore minimise this error in these studies.

There is substantial evidence of a relationship between choroidal thickness and refractive error/AEL. Consequently, any study of choroidal structure should control for the potential effect of refractive error and AEL.

1.3.3 Caffeine intake

Several studies have identified a decrease in choroidal thickness following consumption of coffee, or more specifically caffeine (Vural et al. 2014; Zengin et al. 2015; Altinkaynak et al. 2015; Dervişoğulları et al. 2016). The largest of these studies involved 62 healthy individuals in the study group, and 54 healthy controls

(Vural et al. 2014). The study group consumed 100 ml of Turkish coffee (57 mg of caffeine), whilst the control group were given 100 ml water. The study group demonstrated a significant decrease in choroidal thickness from just 5 minutes following caffeine administration; this effect lasted for at least 4 hours but peaked after 2 hours, with a mean decrease in thickness of ~50 μm. No significant variation in choroidal thickness was reported in the control group.

Altinkaynak and colleagues (2015) produced very similar findings, with a mean decrease in choroidal thickness of approximately 66 μm, peaking after 2 hours. However, in this study, administration was via a 200 mg caffeine capsule. Following the same administration method, Zengin et al. (2015) found a mean decrease in thickness of ~26 μm. Although this is a smaller decrease compared to other studies, only two time points were measured; 1 hour and 3 hours after caffeine administration. The maximum difference may have been between these time points, as indicated by the other studies described here.

This is consistent with Okuno et al. (2002), who found that 100 mg of caffeine (approximately the amount found in a single cup of many popular beverages) decreased the microcirculation in both the optic nerve head (ONH) and choroid-retina by 6%. Similarly, Lotfi and Grunwald (1991) reported a 13% decrease in macular blood flow 1 hour after administration of 200 mg of caffeine.

In this context, it is interesting to note that a study in 2014 of over 37,000 people in the USA, aged ≥2 years, found the mean caffeine intake from beverages to be 165 mg per day (Mitchell et al. 2014). This included only self-reported caffeinated beverage consumers, defined as ≥21 'beverage occasions' within a 7 day period. In those aged ≥65 years (the likely age group for an AMD cohort), mean caffeine consumption was 207 mg; of which 159 mg was from coffee, 32 mg from tea, and 16 mg from carbonated soft drinks. Of caffeine consumers aged ≥65 years in the UK, mean daily consumption was ~114 mg; 50 mg from coffee, 39 mg from tea, and 25 mg from energy and soft drinks (Fitt et al. 2013). It therefore seems pertinent to consider recent consumption of these beverages, considering the demonstrated effect of caffeine on choroidal thickness.

These findings strongly suggest that caffeine consumption causes a significant decrease in choroidal thickness; an effect seen as quickly as 5 minutes

following administration, and lasting for at least 4 hours. Given the scale of caffeine consumption in the population, this factor should be controlled for, wherever possible, in studies using choroidal parameters as outcome measures.

1.3.4 Water and alcohol intake

Mansouri et al. (2013) conducted the water drinking test (WDT) on 25 healthy participants to investigate the effect of water consumption on choroidal thickness. This involved drinking 1000 ml of water within a 5 minute period. The authors report an increase in both peripapillary and macular choroidal thickness, by a maximum of 5.7% and 4.3% respectively. Choroidal volume also increased, by 6.4% and 3.9% respectively. This is a relatively small, yet significant, increase in choroidal thickness following water consumption, but choroidal thickness appeared to peak at different points in the study for each individual (ranging from 15 minutes to 120 minutes following the WDT). On a day-to-day basis, the majority of individuals are unlikely to consume a large volume of water over this short time period, hence water drinking is unlikely to have a significant effect on the outcomes of the majority of choroidal studies.

Alcohol consumption has also been shown to cause a short-term increase in choroidal thickness; ~15 μm within a 30 minute period, and returning to baseline within 2 hours (Kang et al. 2016). In the Beijing Eye Study however, there was found to be no significant association between long-term alcohol consumption and subfoveal choroidal thickness (Wei et al. 2013). Since the potential effects of ethanol are small and short-term (<2 hours), it is unlikely that this will have significant implications on clinical or research measurements of choroidal thickness.

1.3.5 Smoking

Sizmaz et al. (2013) measured choroidal thickness in 17 otherwise healthy smokers, and 17 non-smoker controls. No significant difference in choroidal thickness was found between the two groups at baseline, but a statistically significant decrease in mean thickness of around 30 μm was identified following the smoking of a single standard cigarette. This did not return to baseline for at least 3

hours. Ideally this study would be extended to investigate the duration of smoking-induced choroidal thinning, but ethical issues arise from 'heavy' smokers abstaining from smoking for this length of time. Neither smoking duration nor the habitual number of cigarettes smoked per day were found to have a significant correlation with choroidal thickness. During the 3 hour period, there was no fluctuation in thickness in the control group who did not smoke a cigarette. All participants refrained from smoking and drinking caffeinated drinks for a period of 8 hours prior to baseline measurements to control for the effects of these substances. The authors suggest a possible link between the decrease in choroidal thickness and decreased blood flow to the choroid following smoking, which may in part explain the underlying physiology of smoking as a risk factor for AMD (see Section 1.4.2). This being said, increased retinal oxidative stress resulting from smoking is likely a significant contributor to this association (Tan et al. 2007).

In contrast to these findings, Ulaş et al. (2014) recruited 30 'long-term' smokers (≥10 year history; one pack per day minimum for the last 12 months), along with 40 healthy, 'never-smoking' controls. Choroidal thickness was found to increase (by 10-25 μm) in the central, nasal and temporal segments of the fundus, within 5 minutes of smoking. This returned to baseline within 1 hour. Again, there was no significant difference found in baseline choroidal thickness (or retinal thickness) between the study and control groups, which suggests minimal long-term effects of smoking on choroidal thickness. This is in agreement with Kantarci et al. (2016), who also found no difference in choroidal thickness between long-term smokers (≥20 year history) and non-smoking controls.

Choroidal thickness measurements collected by Sizmaz and colleagues (2013) commenced 60 minutes after smoking, by which time choroidal thickness as measured by Ulaş et al. (2014) had returned to baseline. Both study groups underwent the same period of abstinence, but normal blood parameters were used as part of the inclusion criteria for the latter of the studies, which may have affected the results, given the association between long-term smoking and cardiovascular disease.

However, the mean age of participants in these studies was between 29 years and 50 years. In contrast, Sigler et al. (2014) showed the choroid to be thinner in smokers than non-smokers in older eyes (mean age 78 years) with and without

early AMD. These findings may suggest that smoking has a greater effect on choroidal structure in older eyes, resulting in an increased risk of AMD development in this group.

Given that these studies report changes in choroidal thickness following cigarette smoking, albeit over different time periods and in different age groups, it would seem prudent to control for this variable in future study designs investigating the choroid. There is no apparent long-term effect of smoking on choroidal thickness in younger eyes, despite its association with cardiovascular disease and development of late-stage AMD. However, there is evidence that in older eyes, history of smoking may be associated with thinning of the choroid.

1.3.6 Diurnal variation

It is well established that daily rhythms occur in the eye, including fluctuations in intraocular pressure (IOP), corneal thickness, and AEL (Harper et al. 1996; Liu 1998; Stone et al. 2004). However, it wasn't until 2009 that a diurnal change in choroidal thickness of the human eye was proposed. Brown et al. (2009) used partial coherence interferometry to estimate choroidal thickness *in vivo*, at 3-hourly intervals between 7am and 10pm. Choroidal thickness was found to vary over the day, and the authors described it as 'likely a dynamic parameter influenced by oscillations in IOP or the cardiac cycle'.

1.3.6.1 Patterns and peaks

Studies have since investigated this relationship using OCT imaging. There is much debate in the literature as to the pattern of these diurnal changes, and the times at which the maximum and minimum thickness typically occur. Chakraborty et al. (2011) measured choroidal thickness in 30 young adults, over 2 consecutive days. The choroid was found to be thinnest at midday, and increased in thickness progressively through time points at 3pm, 6pm, and 9pm, at which point the study ended. The mean amplitude of change during this time was ~10 μm, a small change when compared to the mean choroidal thickness of 256 ± 49 μm. In the same study, a small diurnal fluctuation of AEL was identified; in near exact anti-phase to the variation in choroidal thickness (a phase gap of 11 hours 56 minutes; Figure 1.6).

Choroidal thickness and IOP also appear to fluctuate in anti-phase, however there has been no definitive relationship identified between these variables (Chakraborty et al. 2011; Lee et al. 2013c).

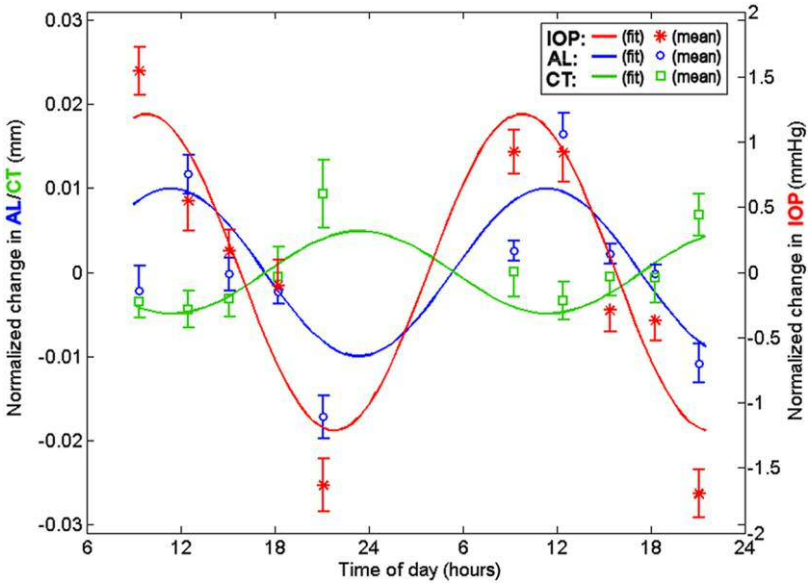

Figure 1.6 Choroidal thickness and AEL were found to be in almost exact anti-phase. IOP showed a similar trend to AEL. IOP = intraocular pressure; AL or AEL = axial eye length; CT = choroidal thickness. Image from Chakraborty et al. (2011).

This diurnal pattern in choroidal thickness is supported by a further study in which choroidal thickness peaked at 9:02pm in 15 young emmetropes (Chakraborty et al. 2013). This was in agreement with Toyokawa et al. (2012), who reported greater subfoveal and nasal choroidal thicknesses in the evening than in the morning. No significant difference was found in the thickness of the temporal choroid. Again, this study found only small mean differences (~10-20 μm), and was limited in size, comprising 12 older Japanese subjects (62.6 ± 14.5 years).

Osmanbasoglu et al. (2013) reported no significant diurnal variation of choroidal thickness during working hours (measurements collected at 9am and 4pm only). However, these time points fall either side of the choroidal thickness minimum identified by Chakraborty and colleagues (2011), which may explain the absence of a significant difference (see Figure 1.6). In younger subjects however, choroidal thickness had a tendency to be higher in the afternoon than in the morning.

Other studies have shown choroidal thickness to peak somewhere between 8am and 9am and then decrease throughout the working day, although the rate of this decrease seems to slow towards 5pm (Tan et al. 2012; Lee et al. 2013c). These

studies found a mean diurnal amplitude of 33.7 μm and 13.4 μm respectively. The more recent of these studies (Lee et al. 2013c) used 100 healthy participants, by far the largest study to date on choroidal diurnal variation. Neither of these studies continued past 5pm, so it was not possible to place the time of minimum choroidal thickness. However, they appear to be around 12 hours out of phase with the findings of Chakraborty et al. (2011) and Toyokawa et al. (2012), despite being of similar study design. A number of smaller studies have shown choroidal thickness to peak in the morning, with times ranging from 6am to 11am (Han et al. 2015; Kinoshita et al. 2016; Zhao et al. 2016). In all cases, the mean amplitude of the variation was <20 μm. Kinoshita and colleagues (2016) attributed the majority of this variation to fluctuation in luminal (vessel) area rather than stromal (surrounding tissue) area.

A diurnal variation pattern was also identified by Usui et al. (2012), who measured choroidal thickness at 3-hourly intervals over a 24 hour period using a long-wavelength OCT (1060 nm). The choroid was found to be thinnest at 6pm and thickest at 3am (mean subfoveal choroidal thickness of 271.9 ± 103.5 μm, and 290.8 ± 110.8 μm respectively). This appears to be out of phase with the aforementioned findings by approximately 6 hours, and the amplitude of change is almost double that found by Chakraborty et al. (2011).

The diurnal pattern of choroidal thickness, and particularly the time of peak thickness, remains disputed in the literature. There is some speculation that this is related to caffeine intake, which was not controlled for in the majority of these studies. The reported decrease in choroidal thickness following caffeine consumption is in the order of 26-66 μm (see Section 1.3.3); larger than the mean diurnal variation amplitude identified by these studies (all <34 μm). No significant diurnal variation was found in the no-caffeine control group of one such study (Vural et al. 2014). Despite the exact pattern and amplitude of these apparent diurnal changes, it seems prudent to control for time of day when assessing the choroid.

1.3.6.2 Retinal thickness

Whilst the retina is not the primary focus of this thesis, it is worth considering any diurnal changes to the structure, given its proximity to the choroid. A number of

studies have found no diurnal variation in retinal thickness in healthy individuals (Larsen et al. 2005; Polito et al. 2006; Jo et al. 2011; Han et al. 2015). Read et al. (2012) found no significant variation in total retinal thickness over a 10 hour period, although a small but significant variation in the thickness of the foveal outer segment layer (7 ± 3 μm) was identified. Jo et al. (2011) found a small variation in retinal thickness with TD-OCT, but attributed this to limited repeatability of the device rather than true tissue variation. Another study found a small but significant decrease in retinal thickness in the nasal and inferior subfields towards the evening, however this fluctuation is again close to the resolution of the OCT device and repeatability (Ashraf and Nowroozzadeh 2014).

In macular oedema, however, diurnal changes have been identified. Kotsidis et al. (2012) measured retinal thickness over a 24-hour period, in 53 diabetic patients with clinically significant macular edema (CSME), 22 diabetic patients without macular pathology, and 36 healthy individuals. Both control groups displayed mean retinal thickness variation throughout the day of 2 μm, which was not significant. The CSME group demonstrated a mean absolute change of 49 μm (a relative change of 17%), with a minimum thickness at 3pm. Visual acuity was poorest at 7am in individuals with CSME, when the retina was thickest. The authors speculate that this variation in macula thickness is likely due to the effect of gravity and hydrostatic pressure on oedema formation, or nocturnal hypotension leading to decreased retinal perfusion overnight.

Retinal thickness does not appear to alter throughout the day in healthy eyes, although diurnal changes have been shown in macular oedema. Therefore, this factor should be considered in clinical assessment of the retina in these patients.

1.3.7 Systemic associations

There are many other factors that have been found to affect choroidal thickness and choroidal blood flow. These include systemic hypertension, hypercholesteremia, obesity, Alzheimer's disease, sleep apnea, exercise, pregnancy, and medications including acetazolamide, sildenafil nitrate, and vasopressin. More detail on the effects of these can be found elsewhere (Riva et al. 1997; Dallinger et al. 1998; Vance et al. 2011; Bogner et al. 2011; Wong et al. 2013; Alwassia et al. 2013;

Takahashi et al. 2013; Bayhan et al. 2014a; Bayhan et al. 2014b; Kara et al. 2014; Yumusak et al. 2016).

Hypertension is the most relevant of these factors to this work, due to its high prevalence in the older population. Masis et al. (2011) undertook a retrospective analysis of 112 patients with systemic arterial hypertension and 15 healthy patients. They found the choroid to be significantly thinner in patients with systemic hypertension than non-hypertensive patients (mean subfoveal choroidal thickness 136.24 ± 46 μm and 173.72 ± 38 μm respectively). However, the control group was relatively small in this study. This is in agreement with the findings of Akay et al. (2015), although this was in young hypertensive adults (mean age 23.8 ± 2.8 years). In contrast to this, Alwassia et al. (2013) investigated the effect of exercise-induced acute hypertension on choroidal thickness in 15 healthy patients with a mean age of 60.6 ± 10.4 years. They found a significant increase in systolic blood pressure following a cardiac exercise stress test, but no change in choroidal thickness. These findings suggest that only pathological, chronic hypertension is associated with a significant change in choroidal thickness.

This highlights the importance of collecting demographic data relating to medical and ocular history when investigating choroidal thickness. Since the choroid is highly vascular tissue, it may be advisable to measure blood pressure at imaging sessions, for consideration when conducting inter-session or inter-group analysis.

1.3.8 Ocular pathologies

A number of studies have investigated structural changes to the choroid at different stages of AMD; these are discussed in detail in Section 1.4.5. Choroidal structural changes have also been identified in other common posterior ocular conditions, including diabetic retinopathy, central serous chorioretinopathy (CSC), and posterior uveitis (Regatieri 2012a; Bittencourt et al. 2014). These identified pathological changes are discussed in the following section.

1.3.8.1 Diabetic retinopathy

The effect of diabetes mellitus on choroidal thickness and choroidal blood flow has been investigated (Nagaoka et al. 2004; Esmaeelpour et al. 2011; Regatieri, Branchini 2012a; Unsal et al. 2014). A reduction in choroidal thickness in type-1 diabetics was demonstrated when compared to non-diabetic controls, with a mean difference of ~90 μm between the healthy and diabetic groups (Esmaeelpour et al. 2012). This was the case in eyes with and without diabetic retinopathy (DR). To investigate the effect of disease severity on choroidal thickness, Esmaeelpour et al. (2011) utilised a non-commercial long-wavelength OCT (1060 nm) to image 42 eyes of type-2 diabetics; divided into 4 groups based on macular involvement; no maculopathy (M0), microaneurysms (M1), exudates (M2) and clinically significant macular oedema (CSME); as well as 16 non-diabetic controls. Mean subfoveal choroidal thickness was found to be 214 ± 55 μm, 208 ± 49 μm, 205 ± 54 μm, 211 ± 76 μm, and 327 ± 74 μm respectively. Subfoveal choroidal thickness was shown to be reduced by ~35% in all diabetic eyes, regardless of disease stage. However, the groups in this study were small (n=12-19 eyes per group) and may not be representative of the variability within each disease state. In the Beijing Eye Study, which had a far larger sample albeit of a different ethnicity, there was no significant association between choroidal thickness and presence of diabetes (Wei et al. 2013).

A number of studies have investigated choroidal thickness in different stages of DR; non-proliferative retinopathy (NPDR) with and without maculopathy (specifically CSME), and proliferative retinopathy (PDR) with a history of panretinal photocoagulation (PRP) treatment (Regatieri et al. 2012a; Unsal et al. 2014). Patients with untreated PDR were excluded. Both studies found the choroid to be significantly thinner in patients with NPDR with CSME, as well as in patients with PDR treated with PDP, when compared to a healthy control group. Neither study identified a statistically significant difference in choroidal thickness between patients with NPDR without CSME and the control group. In other words, both studies identified reduced choroidal thickness in diabetes, but only in eyes with macular oedema or advanced retinopathy treated with PRP.

In contrast to these findings, Kim et al. (2013) found the subfoveal choroid to be significantly thicker in PDR. Eyes were classified by severity into 2 NPDR groups (mild-moderate and severe), and 2 PDR groups (untreated, and treated with PRP).

Eyes that received treatment within the previous 12 months were excluded, to avoid the potential effect of laser-induced choroidal swelling. The group with the highest mean choroidal thickness was the treatment-naïve PDR (363.6 ± 74.9 μm). Eyes with PDR and a history of PRP treatment were found to have far thinner choroids (239.8 ± 57.4 μm). This may explain the difference in findings to the previous studies, which included only treated eyes in the PDR group and found a reduction in thickness. Eyes with CSME were found to have thicker choroids than those without oedema (mean difference ~50 μm). There was no significant difference between the no-DR control group and the two NPDR groups. Some thinning was noted in the no-DR and early NPDR groups when compared to healthy non-diabetic controls (mean difference ~14 μm and ~31 μm respectively), in agreement with the studies described above. The authors speculate that this thinning may be due to vascular constriction or choriocapillaris loss secondary to hypoxia.

Nagaoka et al. (2004) used laser Doppler flowmetry to assess choroidal blood flow in the foveal region of type-2 diabetics. Choroidal blood flow was found to be significantly reduced in all diabetic groups, including those with no DR. The largest reduction in blood flow was seen in NPDR with CSME (58.5% lower than non-diabetic controls). Their findings indicate that choroidal changes may precede DR in a subset of patients. Similar evidence has been reported for AMD, suggesting a link between disrupted blood flow and structural changes (as described in Section 1.4.5).

Cho et al. (2013a) and Takahashi et al. (2008) investigated the effects of PRP treatment on choroidal thickness and choroidal blood flow respectively in patients with severe PDR. Subfoveal choroidal thickness was shown to increase 1 week following PRP, from 318.1 ± 96.5 μm to 349.9 ± 108.3 μm (Cho et al. 2013a). These changes in choroidal thickness did not correlate with changes in macular thickness. The authors comment that changes in choroidal circulation may not be the primary factor causing PRP-induced macular oedema. Choroidal blood flow was found to increase by 46% from baseline to 1 month after PRP treatment (Takahashi et al. 2008). Again, there was no significant correlation between this increase and macular thickness changes. The authors suggest that the increase in choroidal blood flow induced by PRP may be caused by vasodilation of choriocapillaries in the foveal region. Previous or current treatment for severe PDR may therefore skew results of studies on choroidal thickness in diabetics if not controlled for.

1.3.8.2 Central serous chorioretinopathy

As mentioned previously, CSC has been shown to be associated with vascular hyperpermeability and a very thick choroid (Imamura et al. 2009; Pryds and Larsen 2012; Yang et al. 2013; Kuroda et al. 2013). Imamura and colleagues found the mean subfoveal choroidal thickness to be 505 ± 124 μm in 19 patients with CSC, compared to 287 ± 76 μm in healthy individuals. The choroid has also been shown to be thicker bilaterally than in healthy controls, even if subretinal fluid was observed unilaterally (in the region of 324 to 387 μm in the unaffected eye; Pryds and Larsen 2012; Yang et al. 2013). The authors suggest that the increased choroidal thickness may be caused by increased hydrostatic pressure in the choroid. The vessel lumen of the large choroidal vessels has also been demonstrated to be larger in eyes with CSC and (to a lesser extent) fellow unaffected eyes (Yang et al. 2013; Kuroda et al. 2016). Pryds and Larsen (2012) investigated the effects of verteporfin photodynamic therapy (PDT) on the choroid in patients with unilateral CSC. Complete resorption of subretinal fluid was found in all eyes at 1-month follow-up, with choroidal thickness decreasing significantly following treatment in both the treated area and the foveal area. The authors conclude that the process causing choroidal thickening in CSC appears to spread laterally within the choroid, affecting not only the visible pathological area of choroid.

1.3.8.3 Posterior uveitis

Also known as choroiditis, posterior uveitis is associated with an increase in choroidal thickness in the active (inflammatory) stage. This condition is often a manifestation of an underlying systemic inflammatory condition, such as sarcoidosis, Vogt-Koyanagi-Harada (VKH) syndrome, or Behçet's disease. VKH disease in particular has been shown to present with a markedly thick choroid (Maruko et al. 2011; Takahashi et al. 2014), often making it impossible to visualise the posterior boundary of the choroid in OCT images (Nakayama et al. 2012). Maruko and colleagues (2011) found the mean choroidal thickness to be 805 ± 173 μm at presentation, dropping to 341 ± 70 μm following 2 weeks of corticosteroid treatment (n=16 eyes). They suggest this marked thickening of the choroid may be due to inflammatory infiltration and increased exudation, and that OCT could serve to evaluate choroidal involvement in the disease as well as monitoring treatment.

In contrast, chronic uveitis has been associated with a significant reduction in choroidal thickness and vessel diameter (Bittencourt et al. 2014). Takahashi et al. (2014) evaluated the convalescent stage of VKH disease, i.e. patients with no remaining active inflammation. They found the choroid to be thinner in those with severe 'sunset glow' fundus (caused by depigmentation) compared to healthy controls; with a mean subfoveal choroidal thickness of 144 ± 72 μm and 227 ± 58 μm respectively. An inverse correlation between choroidal thickness and disease duration was also demonstrated, possibly caused by latent choroidal inflammation during the convalescent stage of VKH disease, the authors suggest.

Given the relationship between choroidal thickness and several common conditions including diabetes mellitus, CSC, and posterior uveitis, these pathologies should be considered as confounding factors in the design of studies investigating choroidal structure. Patients with a history of these conditions should be excluded from studies of choroidal vasculature in healthy eyes or other specified pathology.

To summarise, many variables have been shown to affect choroidal structure, both physiological and pathological. The choroid becomes thinner with increasing age, axial eye length, and degree of myopia, as well as following the consumption of caffeine. Smoking and diurnal variation have also been shown to affect choroidal thickness, although these effects are not as clear from the literature. Several systemic pathologies have been shown to result in a thinner choroid, including chronic hypertension and diabetes mellitus. Increased choroidal thickness and vessel diameter can result from ocular diseases, including CSC and active posterior uveitis. With so many variables affecting choroidal structure, it is important to consider and control for as many of these as possible in the design of studies investigating the choroid.

1.4 Age-related macular degeneration

AMD is a painless condition affecting the macula, usually bilaterally but asymmetrically, resulting in the loss or distortion of central vision. The condition presents in later life (usually >55 years), and affects the individual's ability to carry out high acuity tasks, such as reading, driving, and face recognition. It does not affect peripheral vision. Whilst treatments exists for the neovascular subtype (discussed

later), there are currently no effective treatments for the atrophic subtype of the disease (although lifestyle advice has been shown to slow progression; Seddon et al. 2006). Consequently, the development of new therapies is a large area of research. A comprehensive understanding of the pathogenesis of AMD is beneficial, to ensure this research is effective. Furthermore, it is imperative that sensitive methods of detecting and monitoring early disease are developed to facilitate early intervention and evaluation of these new therapies.

The following provides an overview of the pathogenesis of AMD, with an emphasis on choroidal involvement, along with an overview of the prevalence, clinical presentation, and current classification and treatment.

1.4.1 Prevalence and incidence

In 2014, a systematic review estimated the global prevalence of AMD (of any stage) to be 8.69% in those aged 45-85 years (Wong et al. 2014). A breakdown of prevalence in different age groups can be seen in Table 1.2. Furthermore, there is expected to be a 3-fold increase globally in the number of people aged 60 and over between 2005 and 2050 (Chamie 2005). This ageing population would result in a continued rise in prevalence of AMD over the coming years. In fact, the projected number of people with AMD in 2020 is 196 million, increasing to 288 million by 2040 (Wong et al. 2014).

Table 1.2 Estimated prevalence figures for a Caucasian population based on a review by Klaver et al. (2004) of 7 epidemiological studies.

Age (years)	Early AMD (%)	Late AMD (%)
65-74	15	1
75-84	25	5
85+	30	13

In the United Kingdom, the prevalence of late-stage AMD has been estimated as 4.8% and 12.2% in those aged over 65 and 80 years respectively (Owen et al. 2012). The condition is responsible for over half of all visual impairment registrations in the UK; more than all other ocular conditions combined (Bunce et al. 2010; Rees et al. 2014).

Vision loss from AMD can be devastating, and is often associated with loss of independence, loss of income, isolation, and depression. It has been reported that almost one third of people with AMD suffer from depression (Brody et al. 2001), even amongst those receiving anti-VEGF treatment (see Section 1.4.4; Casten and Rovner 2013). This is substantially higher than the percentage found in the general population of older adults (~12%; Steffens et al. 2009).

1.4.2 Risk factors

Several risk factors for the development of AMD have been identified, including age, smoking, previous cataract surgery, genetics, race, diet and light exposure (particularly to short-wavelength light). Notably, the primary modifiable risk factor is smoking, which has been shown to produce a 4-fold increased risk of late-stage AMD (Tan et al. 2007). More information about these risk factors can be found in reviews by Evans (2001) and Chakravarthy et al. (2010). The underlying connection of these factors to AMD pathogenesis is briefly explained in Section 1.4.3.

1.4.3 Aetiology and pathogenesis

There are two distinct end points to the condition; atrophic AMD (dry or non-exudative), and neovascular AMD (wet or exudative). The disease is often asymptomatic in the early stages, but sometimes presents with symptoms of mild distortion. From the early stage, the disease may progress to one of two potential late-stages. In the atrophic subtype, a central scotoma typically develops as large areas of the macular atrophy (termed geographic atrophy; GA). In the neovascular subtype (nAMD), new blood vessels grow from beneath the macula, which leak and haemorrhage causing sudden central vision loss. Example retinal photographs and cross-sectional scans of each AMD subtype can be seen in Figure 1.7.

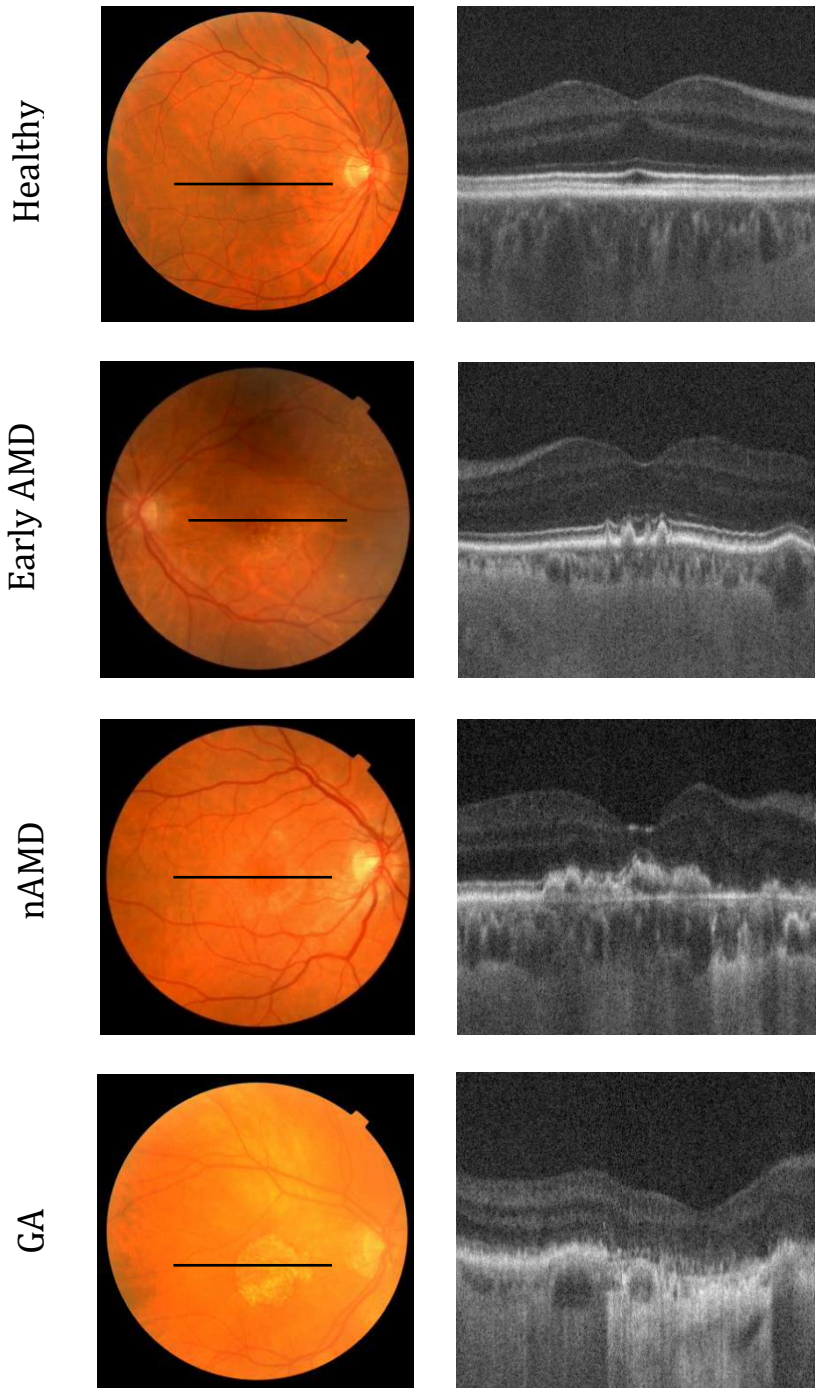

Figure 1.7 Example retinal photographs and macular cross-sectional OCT images of each major AMD subtype. Solid black lines indicate the scan line through the fovea. The following features are visible in each stage: multiple small drusen (early AMD); choroidal neovascular membrane (neovascular AMD; nAMD); atrophy of outer retinal layers, RPE and choroid (geographic atrophy; GA). Images acquired by L. Terry during conduct of this study.

The pathogenesis of AMD is complex and not yet fully understood. To date, the literature has outlined several processes believed to contribute to the development of the condition, to a greater or lesser extent. These include oxidative stress, metabolic insufficiency, chronic inflammation and choroidal vascular changes (Beatty et al. 2000; Zarbin 2004; Ambati and Fowler 2012). AMD is closely linked to age-related changes, hence these changes will be discussed here, with their

believed implications in the development of the condition. The three leading theories for the development of AMD are outlined below; oxidative stress, inflammation, and hypoxia.

1.4.3.1 Oxidative theory

Oxidative stress is a process resulting in cellular damage caused by reactive oxygen species (ROS) and free radicals, and has been implicated in damage to both the RPE and the choriocapillaris in both AMD and ageing (Beatty et al. 2000). This theory is summarised in Figure 1.8. The macula is susceptible to oxidative damage for several reasons. Firstly, there is a high consumption of oxygen by the photoreceptors, which are at highest concentration in the macula. Secondly, the retina is exposed to high light levels, particularly blue light, which has been associated with the development of AMD (Margrain et al. 2004); a finding that explains why excessive exposure to sunlight is a risk factor for the development of the condition (Sui et al. 2013). Thirdly, a high dietary intake of polyunsaturated fatty acids (found in high concentrations in photoreceptor outer segments) has been associated with AMD (Beatty et al. 2000; Seddon et al. 2001; Chong et al. 2009). Smoking is also a contributing factor to oxidative stress, with cigarette smoking having been identified as a major risk factor for the development of late-stage macular degeneration (Klein et al. 1998; Mitchell et al. 2002; Tan et al. 2007).

Mitochondria are the main source of endogenously formed ROS in the photoreceptors and RPE, as a consequence of the mitochondrial respiratory chain. Although these are important for cell signalling, mitochondrial DNA is particularly susceptible to oxidative damage by ROS, which can result in cell death, mutation, and/or overproduction of ROS (Ambati and Fowler 2012). This mitochondrial dysfunction has been demonstrated as a feature of ageing, and is thought to underlie the development of AMD, through excessive oxidative damage and resultant impaired function of the RPE and outer retina (Jarrett and Boulton 2012; Ferrington et al. 2016).

Antioxidants have been shown to protect against oxidative damage in the retina, including vitamins A, C, and E, and enzymes such as catalase (Beatty et al. 2000). The naturally occurring pigments lutein and zeaxanthin are collectively

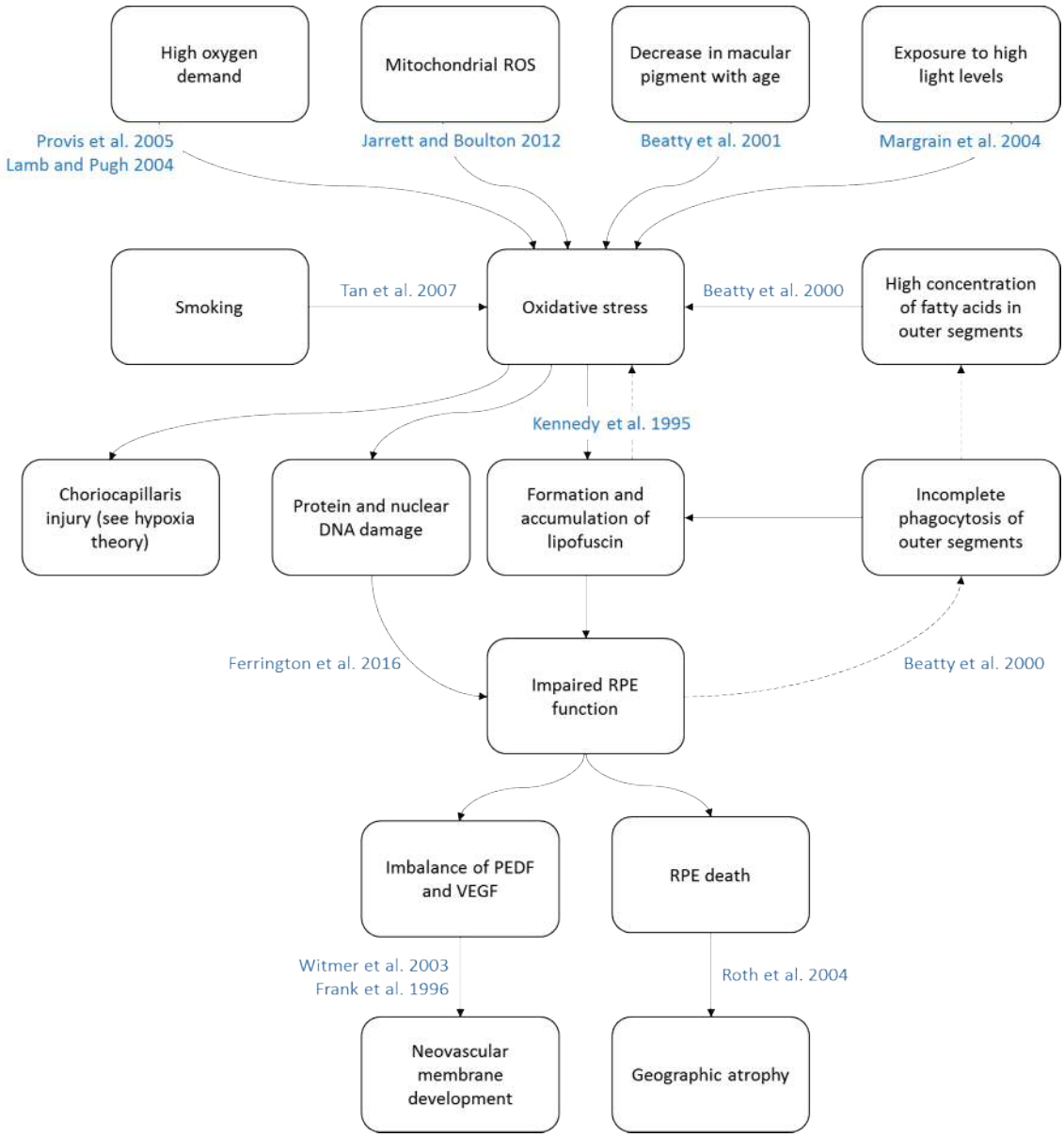

Figure 1.8 Summary of the oxidative theory of AMD development. The arrows depict the theoretical pathways followed in the development of AMD, with supporting evidence (blue) of the principle connections. Feedback loops in RPE dysfunction indicated by dashed arrows.

known as macular pigment. These antioxidant carotenoids are also believed to help protect the retina by filtering out blue light and quenching ROS, and reacting with free radicals (Snodderly 1995). The pigment concentration peaks at the centre of the fovea, where protection is most needed, and diminishes with eccentricity (Snodderly et al. 1984b). A decline in the concentration of macular pigment with age has been demonstrated; it has been suggested that this leaves the macula more susceptible to oxidative damage (Beatty et al. 2001). This is the basis for attempting to increase the concentration of antioxidants at the macula (possibly with high dose supplements of antioxidants combined with zinc, like in the AREDS trial; AREDS 2001b) which could have a potential prophylactic effect on AMD progression (Roth

et al. 2004). It has also been shown that several factors influence the density of macular pigment, including smoking, iris colour and sex; this is consistent with these also being risk factors for AMD (Chakravarthy et al. 2010). It is likely a combination of these contributing factors (decrease in macula pigment, exposure to high light levels, and a high concentration of polyunsaturated fatty acids), coupled with the very high oxygen demand of the outer retina, that results in oxidative stress.

Oxidative stress has been implicated in damage to the choriocapillaris and RPE (Beatty et al. 2000). There is strong evidence to support that lipofuscin is derived, in part, from oxidative damage to photoreceptor outer segments, and incomplete phagocytosis of the outer segments within the RPE (Kennedy et al. 1995; Holz et al. 2001). Lipofuscin itself is thought to drive oxidation through its photo-reactive component A2-E (Beatty et al. 2000; Margrain et al. 2004), further damaging the RPE and impairing phagocytosis of outer segments. This cycle results in an increased concentration of fatty acids from incomplete digestion of outer segments, which are highly vulnerable to oxidation (Beatty et al. 2000). Ultimately, this impairs the RPE, which may cause an imbalance in the production of factors such as VEGF and PEDF. This could lead to the development of a neovascular membrane (Frank et al. 1996; Witmer et al. 2003) or RPE cell death resulting in geographic atrophy (Roth et al. 2004); the two end points of AMD.

1.4.3.2 Inflammation theory

Excessive (chronic) inflammation with involvement of the complement system has also been associated with AMD; it is outlined by Hageman et al. (2001), Johnson et al. (2001), Anderson et al. (2002), and Figure 1.9. This theory stems from RPE dysfunction (discussed in the oxidative theory) causing a breakdown of the blood-retina barrier via the formation of drusen, thickening of Bruch's membrane and disruption of the tight junctions between RPE cells (Cunha-Vaz et al. 2011; Klaassen et al. 2013). This is supported by evidence of inflammatory components found in drusen, including immunoglobin and fragments of complement system proteins C3 and C5 (Johnson et al. 2000). These proteins have been linked to the expression of VEGF, which may contribute to the development of choroidal neovascularisation (Nozaki et al. 2006).

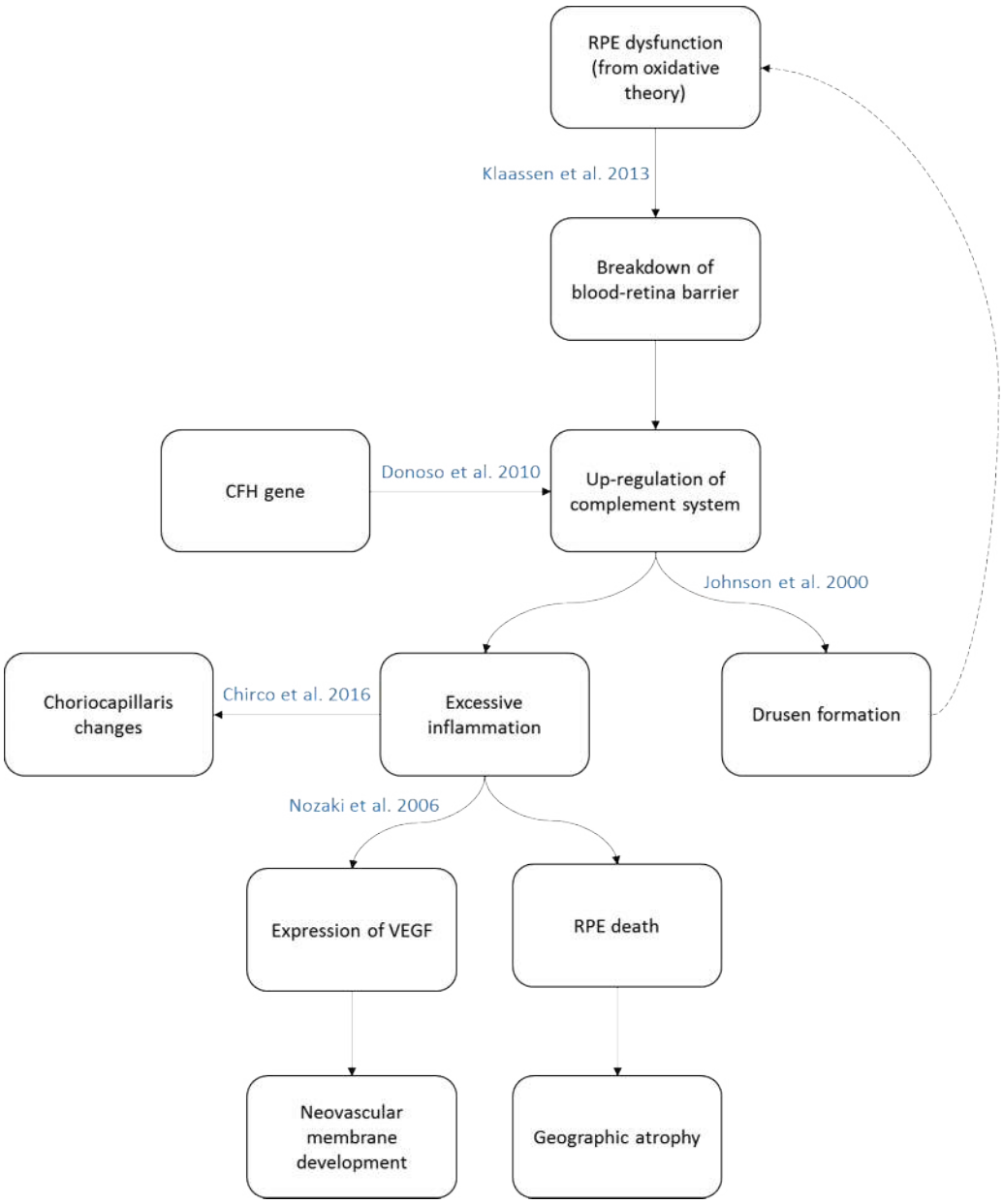

Figure 1.9 Summary of the inflammation theory of AMD development. The arrows depict the theoretical pathways followed in the development of AMD, with supporting evidence (blue) of the main connections. Feedback loop in drusen formation indicated by dashed arrow.

There is also evidence of a genetic predisposition to AMD by the Complement Factor H (CFH) gene, which codes for the CFH protein involved in inhibiting the complement cascade (Donoso et al. 2010). If this gene is faulty, the complement system is not properly regulated, triggering an immune response resulting in excessive inflammation. This in turn has been hypothesised to result in AMD-associated choriocapillaris degeneration (Chirco et al. 2016).

1.4.3.3 Hypoxia theory

The role of hypoxia and metabolic insufficiency at the RPE and outer retina caused by reduced choroidal blood flow and perfusion has been suggested as the primary trigger of AMD (Sarks 1976; Feigl 2007), and an overview can be seen in Figure 1.10. As discussed in Section 1.2.4, age-related changes to Bruch's membrane result in reduced permeability of this membrane, acting as a barrier to metabolic

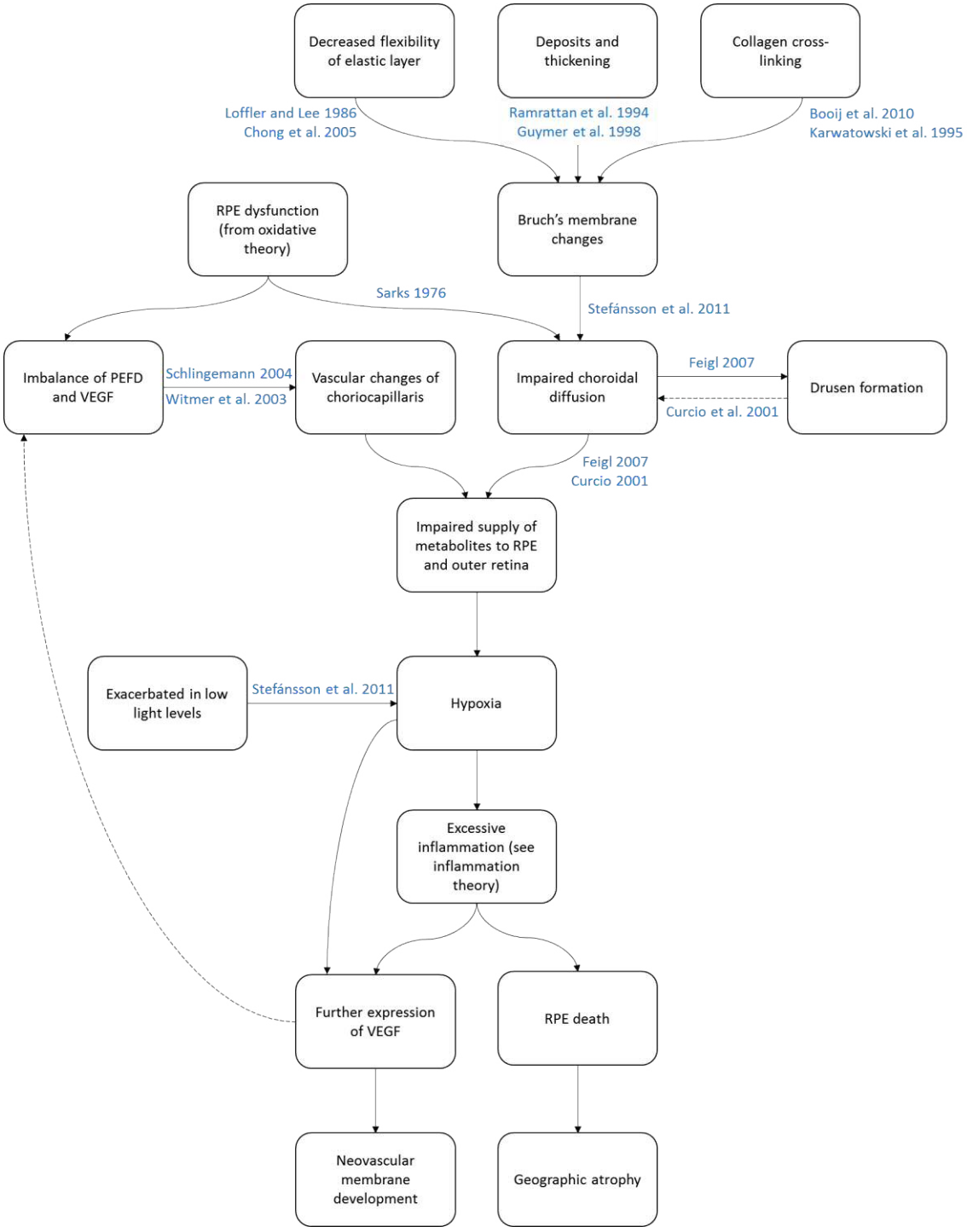

Figure 1.10 Summary of the hypoxia theory of AMD development. The arrows depict the theoretical pathways followed in the development of AMD, with supporting evidence (blue) of the main connections. Feedback loops in VEGF expression and drusen formation indicated by dashed arrows.

exchange between the choriocapillaris, RPE and outer retina (Guymer et al. 1998). This impaired diffusion to and from the choroid promotes the formation of more drusen, further impairing the transport of metabolites through Bruch's membrane (Curcio 2001; Feigl et al. 2007). A review by Stefánsson et al. (2011) proposed that ageing and early AMD changes (including retinal elevation, oedema, drusen and choroidal ischaemia) increase retinal hypoxia due to the reduced oxygen flux from the choroid to the outer retina. This is according to Fick's law of diffusion, and is a result of the increased distance between the choriocapillaris and retina.

These changes are coupled with RPE dysfunction (discussed in the oxidative theory) causing an imbalance of RPE-derived growth factors that leads to vascular changes in the choriocapillaris (Witmer et al. 2003; Schlingemann 2004). The vessels of the choriocapillaris decrease in density and diameter (Sarks 1976; Ramrattan et al. 1994), as well as a general reduction in choroidal thickness in AMD (discussed in more detail in Section 1.4.5). This disruption to the normal blood supply to the outer retina likely leads to further reductions in the supply of metabolites to the macula, which is already susceptible due to its lack of a dual blood supply and the extremely high oxygen demand of the photoreceptors (Provis et al. 2005; Figure 1.11). The combination of these ageing changes results in a hypoxic retina, which is exacerbated in scotopic conditions due to the increased oxygen demand of the photoreceptors (Stefánsson et al. 2011). This chronic ischaemia upregulates VEGF production in the RPE (Feigl 2007; Stefánsson et al. 2011), and possibly also stimulates excessive inflammation (see inflammation theory); ultimately resulting in neovascularisation or RPE atrophy.

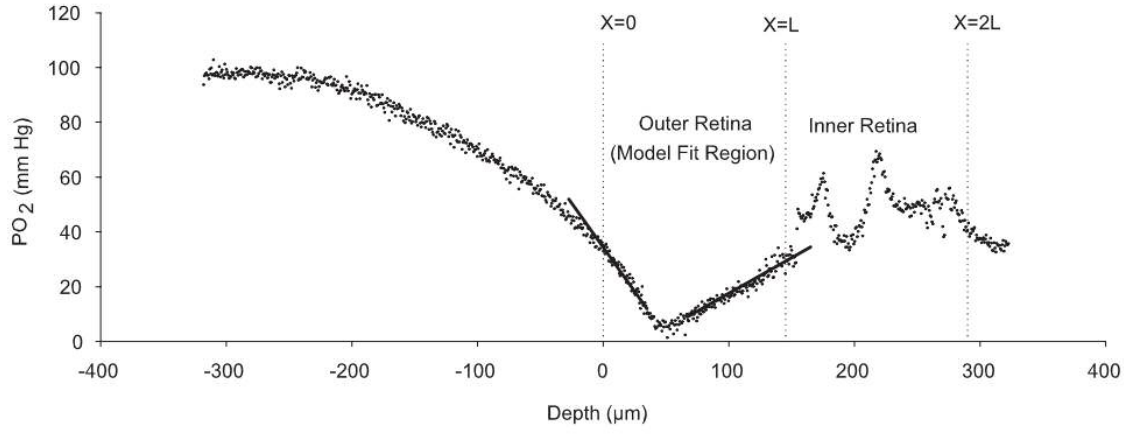

Figure 1.11 Oxygen profile for different depths in the feline retina. In the outer retina, the partial oxygen pressure reaches near zero. X=0 and X=L are the boundaries of the photoreceptor outer segments, and X=2L represents the vitreous-retina border. Figure from Wang and Linsenmeier (2007).

1.4.3.4 Pathogenesis summary

There is significant overlap in these theories (Figure 1.8 to Figure 1.10); it is likely a combination of several of these processes happening simultaneously that results in the development of AMD. Regardless of the specific pathways followed or their relative contributions, the potential end points remain the same; development of a neovascular membrane, or atrophy of the outer retina, RPE and choriocapillaris. It is the expression of VEGF and an imbalance between this and other angiogenesis factors that result in the neovascular end point (Frank et al. 1996; Witmer et al. 2003) and severe loss of central vision.

The 'tipping point' for the progression to nAMD appears to be different for each person, with many individuals with early AMD never reaching this threshold. Consider a single threshold for this exudative change; this limit is raised or lowered with age, genetics, smoking, diet, and other risk factors discussed previously. For example, an individual with a genetic predisposition is more likely to progress to nAMD, despite other risk factors being minimised (e.g. non-smoker, good diet, minimal UV exposure). Conversely, even if all risk factors are met (e.g. a 90 year old heavy smoker with a poor diet), lacking these associated genetic variations may keep the threshold low enough to prevent the progression to nAMD. Although this is theoretical, it provides a potential explanation as to why some individuals progress to late-stage AMD, where others do not.

It is evident that the choroid plays a fundamental role in the pathogenesis of AMD, as it is the sole supply of metabolites to the macula. Although the thickness of the choroid has been shown to decrease in AMD (see Section 1.4.5), the changes to the vessels themselves have been largely assessed using histology, and have not been extensively studied *in vivo* (Sarks 1976; Ramrattan et al. 1994). Having the ability to image the choroidal vascular structure in the living eye using OCT brings new opportunities to study these vessels, in particular how the vascular structure changes throughout the disease process. This provides potential for the development of non-invasive analysis techniques to detect and monitor the condition.

1.4.4 Treatment and prevention

There are currently no effective treatments available for dry AMD, however there are prophylactic measures that can be taken to minimise the risk of progression to nAMD. This involves considering the modifiable risk factors for the condition. For instance, age, sex, and genetics clearly cannot be altered, but patients can be advised to stop smoking and improve their diet by reducing dietary fat and increasing intake of antioxidants (Chakravarthy et al. 2010). There is also some evidence for the benefit to individuals susceptible to AMD of taking antioxidant supplements, although this is disputed (AREDS 2001b; Chong et al. 2007; Evans and Lawrenson 2012). For individuals who suffer from visual loss due to AMD, rehabilitation services are available (e.g. Low Vision Service Wales) to assist the individual in maintaining their quality of life and independence.

Anti-VEGF therapy can be used in the treatment of nAMD, delivered via intravitreal injection. These agents block expression of VEGF produced by the RPE, lessening its angioproliferative effects, and hence preventing the growth of new vessels. Commonly used anti-VEGF drugs include ranibizumab (Lucentis) and bevacizumab (Avastin), which are delivered to the posterior pole via intravitreal injection. These treatments have been shown to be effective in halting the development of neovascular membranes, and improve visual acuity in many cases (Rosenfeld et al. 2009; Martin et al. 2011; Martin et al. 2012). More recently, another anti-VEGF drug (aflibercept; Eylea) was introduced, with efficacy equivalent to ranibizumab (Heier et al. 2012). This has shown potential benefit for cases of nAMD with persistent fluid when treated with ranibizumab and/or bevacizumab (Cho et al. 2013b). The nature and effectivity of these treatments evidences the crucial role of VEGF in the pathogenesis of nAMD. However, this is an invasive therapy, with associated adverse effects, including ocular pain and risk of endophthalmitis and rhegmatogenous retinal detachment (Falavarjani and Nguyen 2013; Sanabria et al. 2013).

1.4.5 Structural changes to the choroid

1.4.5.1 Ex vivo

Although the choroid has been implicated in the pathogenesis of AMD, changes to the vascular structure have predominantly been identified using histology. A decrease in the density of the choriocapillaris with advancing AMD has been identified (Ramrattan et al. 1994; Spraul et al. 1999), as well as a reduction in the diameter of the capillary lumen (Sarks 1976; Ramrattan et al. 1994; McLeod et al. 2009). McLeod and colleagues also reported a decrease in vascular area and loss in capillary fenestration in late-stage AMD (in both the wet and dry subtypes). They concluded that choriocapillaris atrophy occurred secondary to RPE atrophy. However, there is uncertainty over the pathogenesis, since choriocapillaris loss has been identified in eyes without RPE atrophy also (Seddon et al. 2016). Despite this, a significant decrease in vascular area was identified with advancing disease severity, which is consistent with previous findings. The presence of 'ghost' vessels (empty capillaries that were once blood-filled) in early AMD has been used to suggest disease-related capillary loss, rather than a congenitally lower vascular density causing these individuals to be prone to degenerative changes (Whitmore et al. 2015).

Although the majority of histological changes identified in AMD have been at the level of choriocapillaris, these vessels are very small (typically ~7-10 μm), which is nearing the resolution limit of OCT imaging, and therefore cannot be reliably imaged using this technique (see Section 1.5.2). Considering the vessels which can be resolved with OCT imaging, Spraul et al. (1999) identified a reduction in the number of large choroidal vessels in AMD. No significant difference in vessel diameter or choroidal thickness was found between the groups. However, this is based on a single study with limited sample size (51 eyes with AMD, and 40 age-matched controls); this highlights the need for further investigation into structural changes to the choroid in AMD, ideally utilising advances in *in vivo* imaging techniques. The limitations of *ex vivo* measurement using histology are discussed in Section 1.6.2.

1.4.5.2 In vivo

To have a potential clinical application, changes to the choroidal structure must be detectable *in vivo*. A number of studies have identified a reduction in choroidal thickness in patients with AMD, using *in vivo* imaging (Chung et al. 2011;

Sigler and Randolph 2013; Lee et al. 2013b; Esmaeelpour et al. 2014a; Adhi et al. 2014; Lindner et al. 2015; Yiu et al. 2015; Lu et al. 2016). However, it is debated in the literature at which stage in the disease process this thinning occurs.

Considering firstly the early disease stage, Sigler and Randolph (2013) found the choroid to be significantly thinner in early AMD (115 ± 40 μm) when compared to healthy controls (235 ± 49 μm). Conversely, Wood et al. (2011) measured choroidal thickness beneath the fovea, and at 0.5 mm intervals across the central 4 mm of choroid horizontally and vertically (centred on the fovea). No significant difference in choroidal thickness was identified between the early AMD and control groups at any location. However, these were relatively limited in sample size (n= 51 and n=16 healthy eyes, and n=39 and n=16 early AMD eyes, respectively); these studies may therefore have been under-powered to detect small differences in choroidal thickness between groups. Additionally, the potential effects of diurnal variation or caffeine intake were not controlled for in these studies.

Other studies have also found no significant difference in choroidal thickness between early AMD and controls (Kim et al. 2011; Jonas et al. 2014). The more recent of these studies included 204 eyes with AMD, and 228 age-matched control eyes, and found no significant difference in subfoveal choroidal thickness between the control group and the four AMD subgroups (dry AMD, and nAMD sub-divided by predominant feature into; pigment epithelial detachment (PED), retinal oedema, or sub-retinal fibrotic scarring). However, this study did not control for the potential effect of diurnal variation, and all patients in the nAMD group were under bevacizumab therapy at the time of data collection. Medical treatment of nAMD with anti-VEGF has been associated with a reduction in choroidal thickness (Yamazaki et al. 2012), as discussed in Section 1.4.6. Kim et al. (2011) found choroidal thickness in early AMD (186.62 ± 62.02 μm) to be thinner than that of a control group (241.97 ± 102.87 μm), although this difference did not reach statistical significance. No significant difference was found between nAMD (226.46 ± 102.87 μm) and the early AMD or control groups. However, due to the retrospective nature of this study, diurnal variation and caffeine intake were not controlled for, potentially resulting in increased variance and therefore reduced the likelihood of significance.

Ko et al. (2013) reported an inverse correlation between choroidal thickness and drusen area, which was independent of age and sex. They hypothesised that a

thinner choroid leads to a decreased blood flow and decreased waste removal from the outer retina, resulting in drusen formation. This disrupts the RPE, Bruch's membrane and the choriocapillaris, leading to unhealthy or atrophied photoreceptors and a reduction in visual acuity (similar to the hypoxia theory of AMD; see Section 1.4.3.3). This is in line with their finding of a positive correlation between drusen area and logMAR visual acuity (VA). Ko and colleagues go on to suggest drusen load (square root of drusen area) as a useful biomarker in the management of AMD, as well as a potential outcome parameter of clinical trials in dry AMD.

Several studies have found significant thinning in intermediate or late-stage neovascular disease (Lee et al. 2013b; Esmaeelpour et al. 2014a; Yiu et al. 2015; Lu et al. 2016). Esmaeelpour et al. (2014a) acquired long-wavelength OCT images from patients with bilateral intermediate AMD (n=21), intermediate AMD with nAMD fellow eye (n=21), and healthy controls (n=24). The choroid was found to be thinnest in eyes with intermediate AMD (149 ± 60 μm) and a diagnosis of nAMD in the fellow eye (171 ± 78 μm), followed by bilateral intermediate AMD (222 ± 98 μm), and finally healthy eyes (259 ± 95 μm). There was no significant difference in thickness between the two eyes in patients with unilateral nAMD, despite the difference in disease stage. Since disease state of the fellow eye was the only difference between the groups in this study, these findings suggest a symmetry in the pathogenesis of AMD, and may explain why unilateral development of choroidal neovascularisation (CNV) is a major risk factor for progression to nAMD in the fellow eye (Chew et al. 2014). The difference between bilateral intermediate AMD and healthy controls was not statistically significant; this may be limited by the relatively small size of each disease group in this study.

The most marked reduction in choroidal thickness is typically observed in GA, when compared to healthy eyes. Lindner et al. (2015) found a mean difference between groups of ~80 μm, whilst the difference identified by Adhi et al. (2014) was ~110 μm, and this thinning was evident in all vascular layers of the choroid.

Considering variations in the appearance of the disease, advances in imaging technology have revealed a distinct phenotype of drusen, termed reticular pseudodrusen (RPD). These are often visible on colour retinal photographs and OCT, although visualisation may be enhanced using fundus autoflorescence or infrared

imaging (Sohrab et al. 2011). The prevalence of RPD in AMD populations varies greatly, due in part to differences in imaging modalities used, with reported values of 8.4% in early AMD, 22.1% to 36% in nAMD, and 29% to 92.3% in atrophic AMD (Hogg 2014; Wilde et al. 2016). Several studies have compared choroidal thickness in eyes with AMD with and without RPD. Presence of RPD in AMD has been associated with macular choroidal thinning, with mean differences ranging from 40 μm to 155 μm when compared to AMD without RPD (Switzer et al. 2012; Garg et al. 2013; Haas et al. 2014; Zheng et al. 2016). Additionally, eyes with RPD have been shown to have reduced vessel density (Zheng et al. 2016), resulting in a narrow and sparse appearance of choroidal vessels (Ueda-Arakawa et al. 2014) and a lack of detectable choriocapillaris (Sohrab et al. 2012). This may explain why RPD have been strongly linked to development of late-stage AMD (both nAMD and GA; Hogg 2014), due to increased disruption to metabolic supply.

Polypoidal choroidal vasculopathy (PCV) is categorised by some as a subtype of nAMD with a distinct clinical appearance, although others regard it as a neovascular manifestation of several diseases, such as CSC (Koh et al. 2013). It is characterised by multiple detachments of the RPE and neurosensory retina secondary to fluid leakage from networks of abnormal choroidal vessels. This subtype has been shown to have increased choroidal thickness when compared to typical nAMD, with Kim et al. (2011) reporting a mean subfoveal thickness of 319.9 ± 64.0 μm, and 226.5 ± 102.9 μm respectively. Koizumi et al. (2011) reported a similar trend, with mean choroidal thicknesses of 293.4 ± 73.1 μm and 244.6 ± 72.3 μm respectively. This relationship was significant, even when adjusting for age, sex, and refractive error distribution. The authors also reported that those with a subfoveal choroidal thickness of 300 μm or more were 5.6 times more likely to have PCV, and speculated that the development of PCV may be due to altered choroidal circulation similar to that seen in CSC (see Section 1.3.8.2).

Another study involving 87 participants demonstrated a significant thickening of the choroid in eyes with PCV (mean choroidal thickness of 438.3 ± 87.8 μm), in contrast with choroidal thinning in eyes with nAMD and early AMD (mean choroidal thickness of 171.2 ± 38.5 μm, and 177.4 ± 49.7 μm respectively; Chung et al. 2011). The authors suggest that there may be differences in the pathogenic mechanisms of PCV and AMD which explain these findings. Therefore, PCV should

be classified as a separate group to nAMD where possible, particularly when choroidal parameters are used as outcome measures. However, since the estimated prevalence rate of PCV in groups of presumed AMD is 4% to 9.8% in Caucasian populations (Koh et al. 2013), this may not have significant implications. This is more likely to be significant in Asian populations, where the estimated prevalence of PCV in presumed AMD is 23.9% to 54.7%. Furthermore, a number of more recent studies have identified a thicker choroid in PCV than typical AMD, although this did not reach statistical significance (Koizumi et al. 2015; Ting et al. 2016; Wei et al. 2016).

Although choroidal thickness is the most commonly reported parameter, a handful of studies have reported methods of quantifying changes to the choroidal vessels in AMD. From OCT imaging, both choroidal and luminal area have been shown to be significantly lower in nAMD than healthy eyes (Sonoda et al. 2014; Wei et al. 2016). The more recent of these studies also identified a reduction in the ratio of luminal area to choroidal area, suggesting attenuation of vessels in the disease; this ratio was termed choroidal vascularity index (CVI). This is consistent with the decrease in vascular density in AMD noted with histology (Spraul et al. 1999).

Using laser Doppler flowmetry, foveolar choroidal blood flow and blood volume have been shown to be reduced by an average of 37% and 33% respectively in eyes with dry AMD, compared to healthy age-matched controls (Grunwald et al. 1998). There was no difference in blood velocity between groups. Quantification of choroidal blood flow with optical coherence tomography angiography is becoming feasible, with preliminary findings indicating a distribution of blood flow speeds associated with atrophic and neovascular lesions, with lower speeds typically found at the extremities of the lesions (Ploner et al. 2016; Ferrara et al. 2016; see Section 1.5.3.3).

To summarise, the evidence suggests that the choroid changes in AMD, and that such changes are detectable *in vivo*. These changes appear to be associated with disease severity and subtype, and are particularly evident in late-stage disease. Choroidal thickness is the most commonly reported parameter in the current literature, although this measurement is highly variable between individuals. Other methods of quantifying the vasculature to describe these changes are limited (e.g. vessel diameter, see Section 1.7.1). The development and optimisation of

parameters describing the choroidal structure may provide increased sensitivity to the detection of differences between subgroups, including disease severity.

1.4.6 Anti-VEGF therapy and choroidal structure

Anti-VEGF therapy has also been implicated in structural changes to the choroid, and RPE atrophy. This is likely due to the role of VEGF in maintaining healthy choroidal structure (see Section 1.2.3). Rahman et al. (2013) conducted a retrospective case-controlled study, and found no gross difference in subfoveal choroidal thickness between treated and untreated nAMD groups. However, this was cross-sectional in study design, and limited by sample size (n=15 per group). Yamazaki et al. (2012) conducted a longitudinal study comprising 40 patients with unilateral nAMD and fellow eye unaffected by neovascularisation or geographic atrophy. Patients underwent intravitreal injections of ranibizumab (IVRs) monthly for 3 months, then as needed over the following 9 months. Mean subfoveal choroidal thickness was found to decrease following the anti-VEGF therapy, from 244 ± 62 μm at baseline to 226 ± 68 μm at 3 months, which remained almost constant until 12 months when the study ended. This decrease in choroidal thickness was found to be independent of the number of IVRs (mean 5.8 ± 2.9), the subtype of nAMD, or any previous treatments. The authors suggest that IVRs may have a pharmacologic effect on the underlying choroid as well as the neovascular lesion itself, which could explain the decrease in choroidal thickness following treatment.

These findings are in agreement with Ting et al. (2016), who report a mean decrease in subfoveal choroidal thickness of ~10 μm after 3 months of anti-VEGF therapy ($P=0.08$), and ~25 μm after 6 months ($P<0.01$), with no further change until 12 months when the study ended. Bevacizumab was the predominant agent used (77% of injections), and a similar trend in choroidal thickness was identified in treatment of PCV. Again, there was no correlation with number of injections or nAMD subtype, although this should be interpreted with caution, since the number of injections was typically low (3.9 ± 1.3 after 6 months, and 5.6 ± 2.1 after 12 months). There was also no change in the fellow eye during the study period, for either the typical nAMD or PCV group. This suggests that local anti-VEGF therapy has no direct effect on the choroid in the fellow eye, and thus need not be an exclusion criterion for study of the fellow eye in these cases.

Similarly, a significant decrease in macular choroidal thickness (~35 μm) was identified following 3 months of aflibercept therapy (Koizumi et al. 2015). The majority of this change (~22 μm) was found within the first month. The effect of intravitreal injections is important when investigating choroidal changes in nAMD, since patients newly diagnosed with this disease stage typically begin treatment immediately. Choroidal changes caused by the anti-VEGF agent must be distinguished from choroidal changes due to pathology in patients with a history of treatment with anti-VEGF therapy.

1.4.7 Clinical classification of AMD

Classification of disease type and severity is commonly used in the clinical management of several ocular diseases, including AMD, based on underlying pathophysiology. In clinical research, disease classification is often used to group participants according to disease stage for cross-sectional studies, and to allow disease progression monitoring in longitudinal studies. To be useful for these applications, methods of ascertaining a classification should utilise commonly available imaging equipment, and be sensitive to clinical features of each class.

There are a number of established methods of AMD classification (Klein et al. 1991; Bird et al. 1995; AREDS 2001a; Ferris et al. 2005; Danis et al. 2013), one of the earliest being the 'Wisconsin Age-related Maculopathy Grading System' (Klein et al. 1991). This system was devised based on previous methods for grading AMD and DR, and has been independently assessed for performance (Sparrow et al. 1997). Since its development, it has been used over many years for grading purposes in the Beaver Dam Eye Study (Klein et al. 2007), and has spawned a number of new systems, e.g. the International Classification and Grading System (Bird et al. 1995), and the Age Related Eye Disease Study Group Grading System (AREDS 2001a). Both of these methods were devised to enable multicentre grading and classification of AMD for a large-scale epidemiological study and clinical trial respectively. These systems define an age limit (over which retinal features seen are likely attributable to AMD) of 50 and 55 years respectively.

Variations of the AREDS system have since been produced, including the Simplified Severity Scale (Ferris et al. 2005; Ferris et al. 2013), which involves less

demanding grading protocols, and approximates 5-year risk of development of advanced disease. More recently, the AREDS2 system was established for the multicentre AREDS2 clinical trial (Danis et al. 2013). Again, this was based upon the AREDS system, but adopting the modern assumption that the standard optic disc diameter is 1800 μm in size, rather than 1500 μm as assumed by previous systems. This altered the size of the grid overlay used during grading.

The published approaches are all based upon documenting the presence, frequency and location of retinal features associated with AMD, such as drusen and pigmentary abnormalities, from retinal photographs. The features only within a pre-defined macular region are considered, assumed to be a circle of 6000 μm diameter centred on the fovea (with the exception of the AREDS2 system, which is of 7200 μm diameter). This region is subdivided into three annular regions, by two additional circles of 1000 μm and 3000 μm diameter, both centred on the fovea. The outer two annular regions are each further subdivided into 4 equally-sized regions, representing inferior, superior, nasal, and temporal areas (see Figure 1.12). These map sectors were defined by the Early Treatment Diabetic Retinopathy Study Research Group (ETDRS 1991).

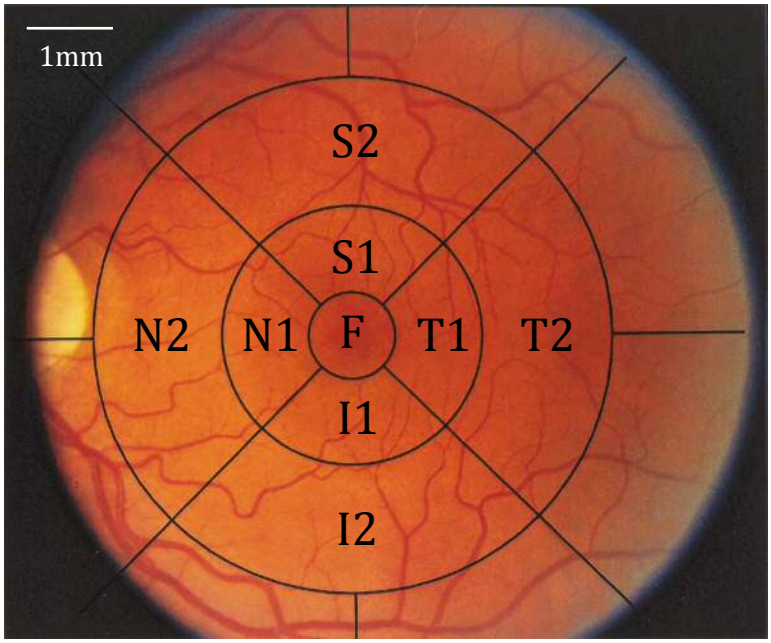

Figure 1.12 Grid overlay for use with AMD classification and grading, with standard sizing used. Notations indicate nasal (N), temporal (T), inferior (I) and superior (S) quadrants in the inner (1) and outer (2) rings, as well as the foveal subfield (F). Image adapted from AREDS (2001b).

These classification systems utilise 30° or 35° stereoscopic retinal photography to gain a degree of insight into depth information e.g. areas of fluid

collection. Other imaging modalities that would enhance clinical signs of AMD have been considered, such as fluorescein angiography, however the benefits of this technique were deemed to not outweigh the invasive nature, and the risk of anaphylaxis and death (AREDS 2001a). Since this time, advances in non-invasive imaging technology now allow a far more detailed appreciation of such information, for example OCT imaging. However, such techniques are yet to be incorporated into AMD disease classification systems. Choroidal features are not included in any classification system, due to the poor visibility of these structures in retinal photography, and the limited understanding of choroidal changes in AMD at the time of development.

The clinical use of stereoscopic retinal photography has largely been replaced by OCT imaging in conjunction with conventional 45° digital retinal photography. Since OCT provides a high resolution view of the retinal layers, some clinical features of AMD such as small drusen may be visible on OCT but not on retinal photography. Following anti-VEGF therapy for nAMD (which was not used at the time of development of these classification systems), intra-retinal and sub-retinal fluid are often reabsorbed. This makes the typical signs of this disease stage difficult or impossible to see with photography in some cases, resulting in misclassification. In light of new imaging equipment and treatment methods, the established classification systems may no longer be appropriate in many cases. An adapted protocol was therefore adopted for the classifications in this thesis (see Section 4.2).

In summary, AMD presents a substantial problem due to its prevalence, debilitating visual symptoms, and lack of cheap and effective treatments (particularly for early and atrophic AMD). Opportunities to develop new therapies are likely to be identified through an improved understanding of the exact pathogenesis of AMD. Retinal signs such as drusen, pigmentary changes, and intra-retinal fluid are currently used to diagnose and monitor AMD. However, presence of the latter sign is indicative of nAMD, by which stage vision is often significantly reduced and intervention is typically required. Considering the suggested role of hypoxia in AMD, the choroid may provide information predictive of change to the overlying retina.

Although the choroid has been implicated in AMD pathogenesis, it is still unclear of the exact mechanisms behind this. Exploiting advances in *in vivo* imaging may help improve our understanding of the role of the choroid in AMD progression, and provide a potential new approach to diagnosing and monitoring the condition. Although subfoveal choroidal thickness is commonly reported in studies of the choroid, this parameter has high variability, and does not describe the vascular structure. Optimisation of existing parameters, and development of new parameters to describe the structure, may provide increased sensitivity to choroidal change throughout the AMD disease process.

1.5 Optical coherence tomography

Optical coherence tomography (OCT) is an optical imaging modality, enabling *in vivo* 3-D visualisation of biological tissue. It is non-invasive, and provides a micron-level resolution view of internal structures, making it ideal for medical diagnostic purposes. Ophthalmic diagnosis is one of the most clinically developed OCT applications, particularly for retinal diseases such as AMD, and OCT imaging is routinely undertaken in hospitals and some high street optometry practices. This section briefly describes the principles and development of OCT technology, and how it has been optimised for imaging the deeper ocular structures pertinent to this work, including the choroid.

1.5.1 Basic principles

The earliest measurements of a one-dimensional axial scan (equivalent to an ultrasound a-scan) were in the 1980s (Fujimoto et al. 1986; Fercher, Mengedoht and Werner 1988), with cross-sectional two-dimensional scans (equivalent to an ultrasound b-scan) being demonstrated in the early 1990s (Huang et al. 1991). The first *in vivo* OCT imaging studies of the human retina followed in 1993 (Fercher er al. 1993; Swanson et al. 1993). Since this time, there has been a tremendous growth in the number of publications and citations in the field; from 19 publications in 1996, to 1081 in 2006, to 4853 in 2016 (number of search results for 'optical coherence tomography' on PubMed.gov for each given year). Commercial OCT instruments are

now commonplace in hospitals, medical imaging centres and high street optometry practices.

OCT is based on the principle of low-coherence optical interferometry. Fundamentally, OCT is analogous to ultrasound, measuring backscattered (reflected) light from within the imaged structure. The sampling depth is determined by the optical equivalent of echo time delay in ultrasound. By obtaining measurements at regular intervals (with increasing depth), OCT is able to produce an axial a-scan. Moving the scanning system laterally allows a series of adjacent a-scans to be obtained, producing a cross-sectional b-scan. Lateral movement in one direction is used to form a two-dimensional b-scan, whilst movement in two directions forms a 3-D c-scan.

The design of OCT is based on a Michelson interferometer, which produces an interference pattern by splitting a beam from a light source into two paths, using a semi-silvered mirror (Figure 1.13A). To produce interference fringes, each path is of a different length or comprised of a different material (with a different refractive index; n). This results in a phase difference, as the light from one path will return to the central mirror before the light from the other path. Once the light returns to the semi-silvered mirror, the two paths are recombined, and directed to a photodetector. The phase difference between the light from each path is evident from the amplitude of the detected signal (resulting from constructive and destructive interference).

The retina is a multi-layered structure, with each layer having different reflective properties. It is therefore possible to assess the reflectivity at different depths in the retina and discern the individual layers, given sufficient resolution. The interferometer within an OCT instrument splits the beam of light in half; the beam that enters the eye, and a reference beam (Figure 1.13B). When the beam passes into the eye, a small portion of the light is reflected by each retinal layer. The reflected beam can be matched to the reference beam by adjusting the position of a reference mirror, until the two optical paths lengths are equal. The position of the reference mirror allows the reference path length to be ascertained, enabling the construction of an image with several predetermined depth points within the retina (a-scan). However, light scattering and absorption within the sample ultimately limit the depth to which useful OCT imaging is possible (Huang et al. 1991).

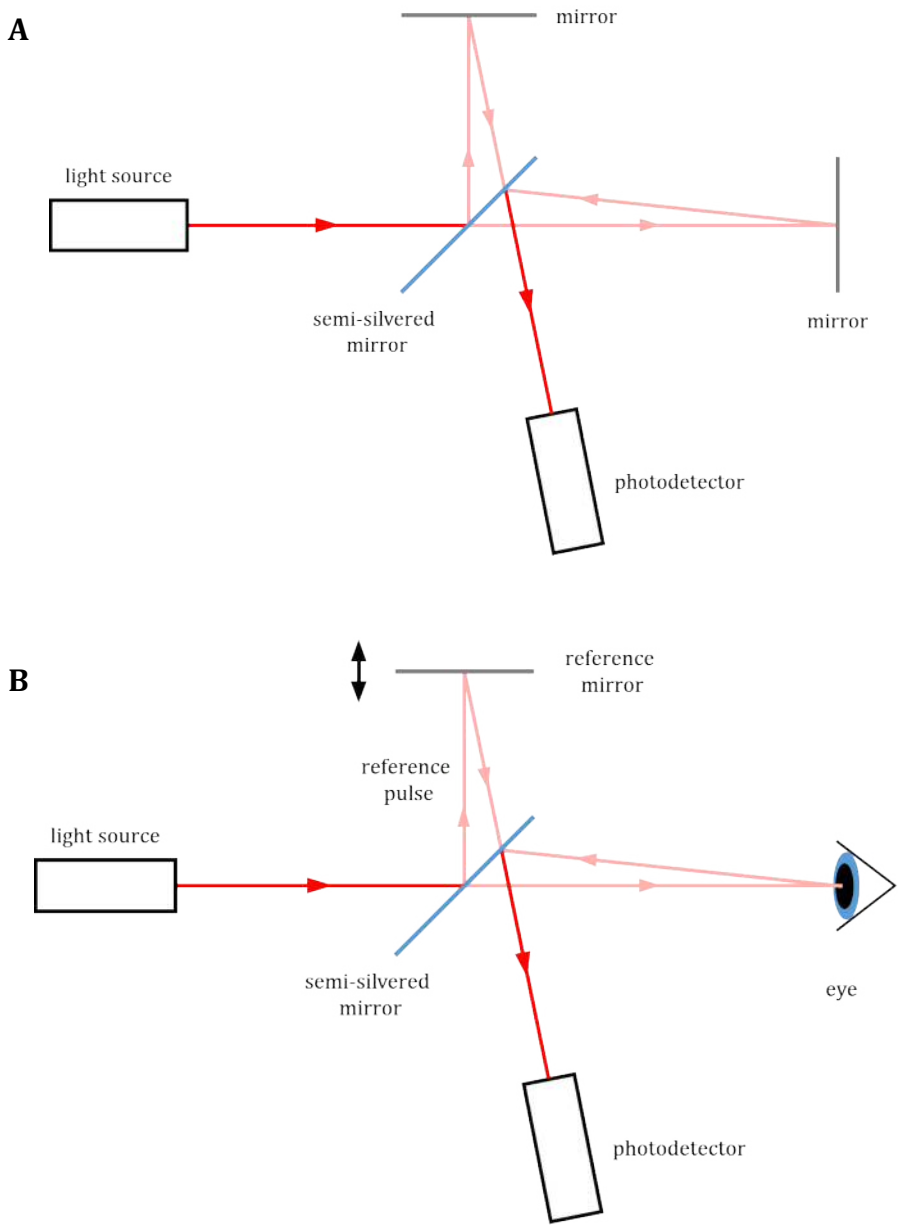

Figure 1.13 Schematic diagram of (A) a Michelson interferometer, and (B) optical coherence tomography. The return paths and photodetector are shown off-axis for demonstrative purposes. Image adapted from Terry (2017).

1.5.2 Resolution

Several parameters define how useful an imaging modality is, for both clinical and research purposes. One of the main advantages of using OCT for medical imaging is the complete decoupling of axial (depth) resolution and transverse (lateral) resolution (Hitzenberger 2003). The axial resolution is determined by the coherence length of the light used and, unlike scanning laser ophthalmoscopy, is not influenced by the numerical aperture of the eye nor aberrations arising from the

cornea or lens. Transverse resolution is defined by the size of the focussed transverse spot of the optical beam.

Axial image resolution is important for visualising individual layers of the retina, and is related to the spectral bandwidth of the imaging light source used as described in Equation 1.1 (Drexler 2004).

Equation 1.1

where:
Δz is the axial resolution,
Δλ is the spectral bandwidth of the light source,
λ is the centre wavelength of the light source used for imaging (assuming a Gaussian spectrum).

Commercial OCT instruments commonly use broad-bandwidth superluminescent diode (SLD) light sources, emitting ~50 nm bandwidths centred at ~850 nm, resulting in ~5 μm axial resolution in tissue (n=1.4). Schmitt (1999) identifies three parameters as requirements for the ideal OCT light source; emission in the near infrared spectrum, a high irradiance, and a short temporal coherence length. The coherence length is a finite distance over which light maintains some degree of coherence, and is inversely proportional to the spectral bandwidth of the light source. Although SLDs satisfy the first two of these parameters and are relatively cheap to manufacture, they have a long coherence length, which limits the axial resolution. To overcome this limitation, ultrabroad-bandwidth, solid state femtosecond Titanium:sapphire lasers have been used, which provide excellent resolution but are very expensive and less portable than SLDs, limiting their use to research rather than clinical application.

As previously mentioned, transverse resolution for OCT imaging is defined by the size of the focussed transverse spot of the optical beam (Equation 1.2; Drexler 2004).

Equation 1.2

where:

Δx is the transverse resolution
d is the spot size on the objective lens
f is the focal length of the objective lens
λ is the centre wavelength of the light source used for imaging (assuming a Gaussian spectrum)

High transverse resolution images can be obtained by using a high numerical aperture (i.e. a reduced spot size) at the expense of a reduced depth of focus. Transverse image resolution of the retina is generally limited by pathological or normal ageing changes to the intraocular media (i.e. cataracts) and ocular aberrations, although this can be minimised using adaptive optics techniques (see Drexler and Fujimoto (2008) for a comprehensive review).

Other important parameters of OCT for research and clinical use are data acquisition time (must be short to minimise motion artefacts and maximise patient comfort and exposure safety), detection sensitivity (often compromised in order to keep acquisition time to a minimum), image penetration depth in tissue, and image contrast (Drexler and Fujimoto 2008).

1.5.3 Types of OCT

Early clinical devices were 'Time Domain OCT', although these have been almost entirely superseded by the newer generation 'Frequency Domain OCT', with the recent introduction of swept-source systems bringing new opportunities in imaging of the deeper structures. OCT angiography has also become commercially available, allowing enhanced imaging of vascular structures by using adapted image processing techniques in conjunction with conventional OCT imaging, to detect blood flow. An explanation of each type of OCT and their advantages and limitations are outlined in the following section.

1.5.3.1 Time Domain OCT

The method of adjusting the reference mirror to measure the reflectivity at each data point is known as Time Domain OCT (TD-OCT). The need for manual movement within the system results in slow image acquisition (~4000 a-scans/sec) and hence difficulty in collecting sufficient data to allow for 3-D imaging (Drexler 2004; Povazay et al. 2007). This was a major limitation of the early commercial instruments, such as the Stratus OCT (Carl Zeiss Meditec, Inc., Dublin, CA) system, which is now considered obsolete. Furthermore, TD-OCT displays an inverse relationship between axial resolution and signal-to-noise ratio (SNR), limiting the resolution attainable by this method of imaging (Choma et al. 2003).

1.5.3.2 Frequency Domain OCT

The alternative to TD-OCT is Frequency (or Fourier) Domain OCT (FD-OCT). This modality assesses the interferometry data in the frequency domain, using Fourier transforms to directly obtain the depth-reflectivity profile. FD-OCT measures reflectivity along an entire a-scan simultaneously rather than sequentially, negating the requirement of a mobile reference mirror. Consequently, FD-OCT has a substantially higher a-scan acquisition rate (by approximately 50 times; Leitgeb, Hitzenberger and Fercher 2003; Drexler 2004; Povazay et al. 2007), facilitating the acquisition of 3-D images in a clinically feasible time period (~5 seconds). FD-OCT has been demonstrated as having higher sensitivity than TD-OCT to macular pathologies, including AMD, diabetic macular edema (DME), and uveitis-related maculopathies (Choma et al. 2003; Gupta et al. 2008; Forooghian et al. 2008; Sayanagi et al. 2009; Cukras et al. 2009; Major et al. 2014).

There are two different methods of acquiring the interferometry data in FD-OCT; Spectral Domain (SD-) and Swept Source (SS-) OCT. Both use Fourier transforms to produce depth-reflectivity profiles which comprise the final OCT image (van Velthoven et al. 2007). These techniques are described in more detail in the following section.

Spectral Domain OCT

The first of these methods (SD-OCT) uses a broadband light source with a spectrometer as the detector. The spectral components are spatially encoded rather

than time encoded (as in TD-OCT), and a dispersive element is used to spectrally distribute the different wavelengths from the light source. The interferometer encodes the depth information from the sample across the spectrum, before it is spectrally dispersed and imaged by a high speed camera. A single exposure of light can be used to build a full-depth scan, resulting in a higher acquisition speed than TD-OCT.

Swept Source OCT

SS-OCT uses a photodiode detector and a rapidly tuned light source to acquire the spectral signature from the sample. Conversely to SD-OCT, the spectral components are time encoded rather than spatially encoded, but without the need for a mobile reference mirror as in TD-OCT. The use of this type of detector results in a higher acquisition rate, reducing image acquisition time whilst maintaining the use of 3-D imaging. Swept source technology is utilised in the latest generation of OCT devices; for example, the DRI OCT Triton (Topcon Corp, Tokyo, Japan) has a scan rate of 100,000 a-scans/sec, whereas its predecessor, the spectral domain Topcon 3D OCT-2000, operates at half this rate (50,000 a-scans/sec).

Additionally, the sensitivity (defined as the SNR for a perfect sample reflector) is independent of both scan depth and source bandwidth, unlike other modalities (Choma et al. 2003). This allows visualisation of deeper structures with more clarity. The DRI OCT Triton provides choroidal thickness maps for operators to evaluate choroidal thickness with minimal time and effort (Hirata et al. 2011). This is potentially useful for monitoring choroidal thickness in pathologies known to affect choroidal thickness, such as CSC, AMD, pathologic myopia, and angioid streaks (Ellabban et al. 2012; Jirarattanasopa et al. 2012; Ohno-Matsui et al. 2012).

Klaver et al. (2012) conducted a population-based study on retinal and choroidal thickness measured by SS-OCT. A total of 111 participants aged 55 and over were included from the Rotterdam Study (Hofman et al. 2007), and 93% of scans acquired were deemed to be of high quality. They concluded that the long-wavelength SS-OCT was fast and relatively easy to use, and provides opportunities for evaluating retinal and choroidal thickness in large studies. A disadvantage of these swept source systems is the cost to manufacture, and hence the cost to the end user.

1.5.3.3 OCT angiography

Optical coherence tomography angiography (OCTA) is a recently developed approach to non-invasive vascular imaging. It employs motion contrast to identify blood flow, by comparing backscattered signal between rapidly acquired sequential OCT images. Point by point signal correlation is used to identify spatial change between the images. Areas of no difference between repeated scans are deemed stationary, whilst differences in signal are attributed to motion of erythrocytes in the blood vessels (Ferrara et al. 2016). Both the retinal and choroidal microvasculature may be viewed with OCTA. The acquisition time of an OCTA scan is typically 2-4 times that of an SS-OCT volume scan (~2 seconds), and is comparable to a conventional SD-OCT volume scan (~5 seconds). To ensure consistency between sequential images, eye tracking and image registration techniques are typically employed.

Injection of contrast material is not required for this technique, providing an advantage over the current gold standard angiography techniques; fluorescein angiography and indocyanine green angiography. Furthermore, OCTA acquires volumetric data, unlike the 2-D photography used in traditional angiography. Different layers of the vasculature can therefore be isolated and viewed independently with OCTA. For example, the retinal vasculature can typically be separated into the superficial plexus and deep plexus, and the choriocapillaris can often be visualised. However, since the majority of OCTA devices are adapted from conventional OCT devices, the wavelength at which they operate limits visualisation of the structures beneath the RPE (see Section 1.6.1.1).

Since OCTA requires motion to identify vasculature, stationary fluid leakage is not easily detectable, as with traditional angiography. Artefacts are inherent in OCTA imaging, which commonly arise from eye motion, or overlying vascular structures or media opacities (for more detail on artefacts in OCTA, see Spaide et al. 2015). Unlike other angiography methods, OCTA provides an image representing a single time-point, where all vessels are visualised simultaneously. This cannot be differentiated into vascular filling and emptying stages (e.g. arteriovenous phase, laminar venous phase), as can be investigated from the time-course following injection of contrast material.

Despite these limitations, OCTA has been shown to be capable of detecting changes in choroidal blood flow, indicating the presence of CNV in AMD, and capturing microvascular abnormalities in diabetic eyes and vascular occlusions (Jia et al. 2014; de Carlo et al. 2015). Although OCTA shows promise for future use in clinical identification of vascular changes in pathology, it was not utilised in this thesis for a number of reasons. Firstly, this technology was not commercial available at the outset of this work. Secondly, it is not optimised for imaging the deeper structures, and the SNR of the deeper choroid is often low. Finally, areas of particularly high or low flow velocity have been shown to generate signals outside the detection range of the device, resulting in artefacts (Spaide et al. 2015; Ferrara et al. 2016). The effect of AMD on blood flow and the impact this has on OCTA imaging is not yet fully understood. Since the aim of this thesis was to identify structural changes to the vasculature in AMD, it seemed pertinent to utilise an established imaging technique based on structure reflectivity rather than blood flow.

1.6 OCT imaging of the choroid

Since choroidal imaging *in vivo* is a relatively new technique, protocols for quantifying the vasculature are not well established. The following section contains an overview of OCT optimisation for imaging deeper structures, including the choroid. This is followed by a review of histological studies of the choroid in AMD, and explores how these quantification techniques may be used to inform study design for *in vivo* choroidal analysis.

1.6.1 Optimisation of OCT for choroidal imaging

There are limitations that should be considered when imaging the choroid with conventional SD-OCT instruments. For example, there is a decrease in imaging sensitivity with increased depth in the structure, termed 'signal roll-off'. Additionally, light scattering by the ocular tissue and optical media results in a reduction of the OCT signal. These factors limit the SNR, and ultimately the sensitivity of the imaging system. In an attempt to overcome these limitations,

alterations to conventional OCT have been made to optimise visualisation of the deeper structures, including long-wavelength OCT and enhanced depth imaging.

1.6.1.1 Light source wavelength

The majority of commercial SD-OCT instruments utilise a light source with a central wavelength of ~800-860 nm. A table of the specifications of several commercial OCT devices can be found in Appendix A. More recently, OCT instruments utilising a longer wavelength light source in the region of 1050 nm have been developed. These provide better visualisation of the deeper structures, particularly beneath the RPE. The RPE has a high concentration of melanin pigment, which is highly scattering and absorbing. However, the optical properties of melanin are strongly wavelength-dependent, with longer wavelengths suffering less from scatter and absorption. This allows improved visualisation of the choroid with long-wavelength OCT devices. This may be clinically useful for diagnosing early stage pathologies known to affect the choroid including AMD, particularly when accompanied by choroidal neovascularisation (Povazay et al. 2003; Unterhuber et al. 2005).

Long-wavelength OCT also has the advantage of reduced image degradation due to scatter caused by opacities in the intraocular media, such as cataracts and corneal opacities (since these are also wavelength-dependent), resulting in a higher SNR. This enables clinically useful data to be collected in a wider range of subjects, particularly those with other age-related ocular conditions such as AMD or diabetic retinopathy (Povazay et al., 2007; Drexler and Fujimoto 2008). Additionally, since 1050 nm is not visible to the human eye, patients will not exhibit the reflex to track the scanning line during image acquisition, which is commonly reported with conventional-wavelength OCT.

Assuming the water content of the vitreous to be ~90% and the average human axial eye length to be ~25 mm, one can estimate the comparative OCT signal loss at various wavelengths. There is a reduction of detectable signal from the retina from ~89.4% at 800 nm to ~48.4% at 1060 nm (Hammer et al. 1995; Unterhuber et al. 2005). This is largely due to the absorption spectrum of water (Figure 1.14). This may be compensated for by increasing the power of the light source, although not

exceeding standards for continuous corneal irradiance (ANSI 2000; ICNIRP 2013). Images obtained at 1050 nm have been shown to penetrate ~200 μm deeper into the choroid than those obtained at 800 nm (Unterhuber et al. 2005).

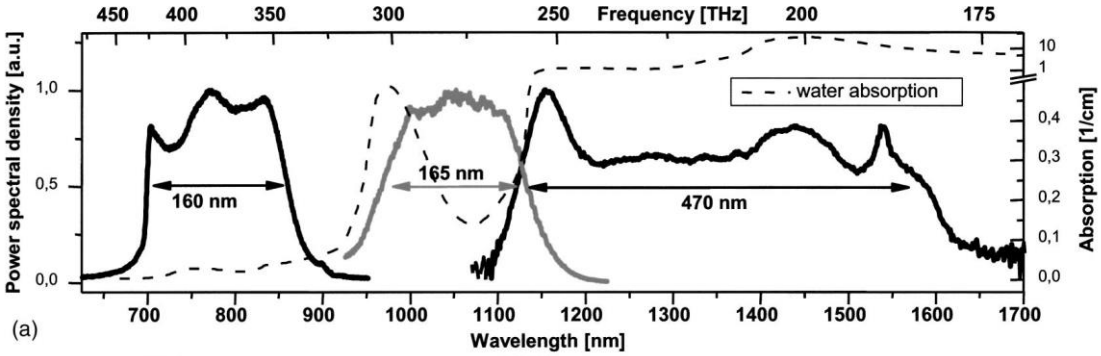

Figure 1.14 Output spectra of three different lasers: Ti:sapphire laser (black line, left), photonic crystal fiber-based source (grey line, centre), and a MenloSystems laser (black line, right), overlaid with a water absorption spectrum (broken line). Image from Drexler (2004).

The water absorption spectrum has two wavelength regions where absorption is relatively low; below ~950 nm, and a narrow band between 1040-1100 nm. Three different lasers are also shown in Figure 1.14, displaying the suitability of two of these for use in posterior eye imaging, with corresponding water absorption minima of ~800 nm and ~1050 nm. The third laser (MenloSystems) is clearly unsuitable for this purpose. However, this fiber laser may have clinical applications for *in vivo* imaging of the anterior segment, where the path of light through water-filled cavities is shorter prior to reaching the target structure (Drexler 2004). The Visante OCT (Carl Zeiss Meditec, Inc., Dublin, CA) uses an SLD at 1310 nm for anterior eye imaging, including the anterior segment, cornea and lens (e.g. to collect clinical data for LASIK or intraocular lens (IOL) surgery).

1.6.1.2 Enhanced depth imaging

Prior to the introduction of commercial long-wavelength OCT devices, alterations in acquisition techniques were made to optimise visualisation of the deeper structures using conventional-wavelength OCT systems (Spaide et al. 2008). These techniques are collectively known as enhanced depth imaging (EDI).

SD-OCT inherently suffers from depth-dependent signal roll-off; this is a reduction in the SNR with increasing distance from the 'zero delay line' (the depth of highest image sensitivity). In clinical OCT imaging, the retinal structures are

typically of most interest, and therefore are positioned close to the zero delay line. However, this limits the capabilities of SD-OCT for imaging the choroid, which is located further from the zero delay line. In EDI, the position of the reference mirror is adjusted to invert the image, bringing the choroid closer to the zero delay line. EDI is available in the acquisition software of many newer commercial OCT instruments (Regatieri et al. 2012b). EDI has been shown to be effective for imaging the choroid in healthy individuals as well as those with choroidal abnormalities, including AMD, CSC, and CNV in high myopia (Fujiwara et al. 2009; Imamura et al. 2009; Margolis and Spaide 2009; Sigler and Randolph 2013).

However, OCT devices optimised for imaging the deeper structures (e.g. long-wavelength light sources) are likely to outperform conventional SD-OCT instruments with EDI. Visualisation of the deeper structures can be further enhanced with image processing techniques, which are discussed further in Section 2.3.

1.6.2 Comparison to histology

Histology is considered the gold standard method of informing and validating OCT measurements of the retina and choroid (Toth et al. 1997; Yabushita et al. 2002; Drexler and Fujimoto 2008). Pre-dating OCT, histology has contributed a large amount to the pool of knowledge on the physiology of the posterior pole, including the choroidal vasculature (McLeod and Lutty 1994). Light microscopes have a far higher spatial resolution than OCT (~0.2 μm versus ~5 μm), allowing for repeatable measurements of small features, including the thickness of Bruch's membrane (~3 μm) and lumen diameters within the choriocapillaris (~8 μm; Ramrattan et al. 1994).

To investigate choroidal vasculature *in vivo*, methods of quantifying structures can be adapted from previously used *ex vivo* techniques. There have been several publications using histological analysis to investigate changes to the choroid in AMD (Sarks 1976; Ramrattan et al. 1994; Spraul et al. 1996; Spraul et al. 1999; McLeod et al. 2002; McLeod et al. 2009; see Section 1.4.5). These studies utilise light microscopy to visualise the choroidal vasculature, and quantify based upon vessel diameter and density.

Ramrattan et al. (1994) studied histologic sections of 95 normal human maculae and 25 maculae with various stages of AMD. Thickness of Bruch's membrane was measured, as well as length and cross-sectional diameter of the capillary lumen in the choriocapillaris (measured parallel and perpendicular to Bruch's membrane respectively), in addition to total choroidal thickness (Figure 1.15). These were measured 8 times at regularly spaced intervals of 140 μm, and averaged. Although measurements of these small structures are possible using histology, this feature size is below the resolution limit of current OCT instruments and hence cannot currently be measured *in vivo*. However, it may be possible to transfer the concept of lumen length and diameter measurements used in this study to the deeper, larger choroidal vessels which can be resolved. Spraul et al. (1996; 1999) followed a similar approach, extending their histological analysis of the choriocapillaris to incorporate diameters of the larger choroidal arteries and veins.

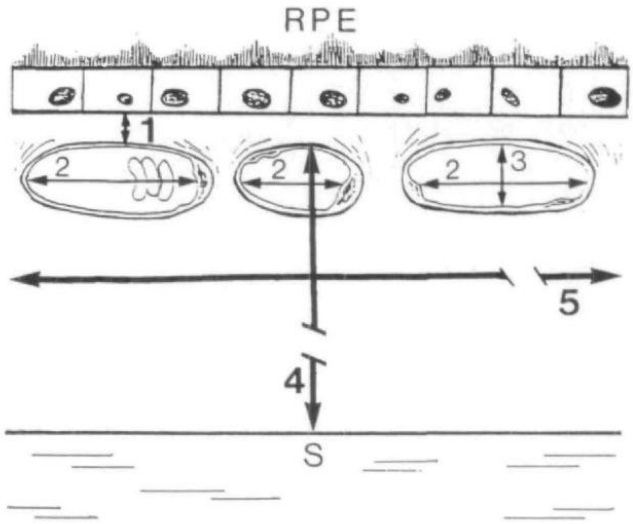

Figure 1.15 Diagram illustrating the measurements performed on histologic sections of choroid: (1) thickness of Bruch's membrane; (2) capillary lumen length; (3) capillary diameter; (4) choroidal thickness; (5) total distance (1120 μm) along which measurements were made at 140 μm intervals. Bruch's membrane has been exaggerated for demonstrative purposes. Image from Ramrattan et al. (1994).

To ensure that these measurement techniques are transferrable to OCT images, the imaging modalities must be comparable (i.e. the areas or relative high or low reflectivity on OCT must relate directly to retinal or choroidal structures on light microscopy). Several studies have demonstrated the comparability of OCT imaging and histology (Gloesmann et al. 2003; Anger et al. 2004; Curcio et al. 2011; Figure 1.16).

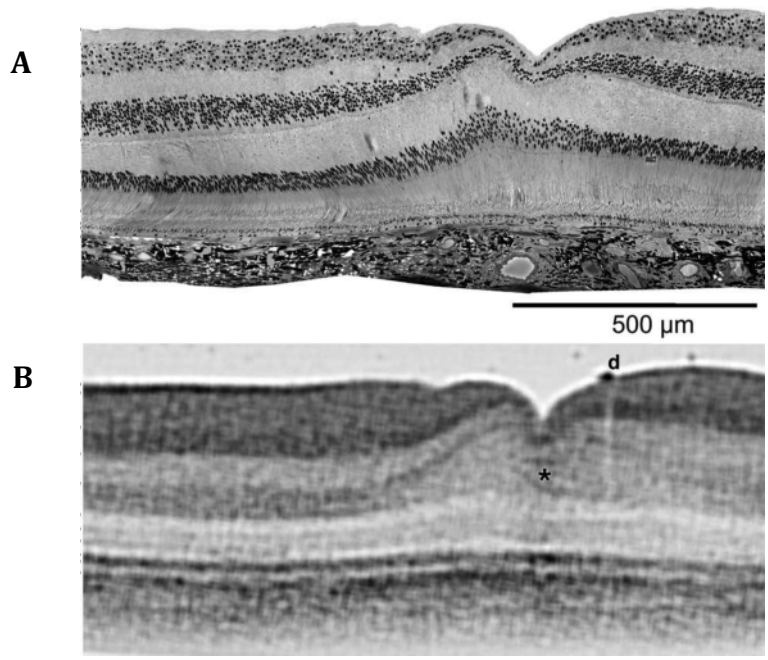

Figure 1.16 Ex vivo section of monkey fovea imaged using (A) light microscopy and (B) UHR-OCT. Image adapted from Anger et al. (2004).

Curcio et al. (2011) manually measured thickness of 21 physiological layers of retina and choroid (including the choriocapillaris and choroid) at 25 lateral locations, in 18 donor eyes. These locations were distributed nasally and temporally within the central 6 mm of posterior pole, centred on the foveal pit. Measurements were made perpendicularly to the RPE, using the 'lengths' tool in IPLab, a commercial image analysis program (Scanalytics, Fairfax, VA). The histologic measurements and boundary selection were compared to that of *ex vivo* OCT (Spectralis). The measurement methods were very different between the two techniques, however the authors concluded that newer OCT systems can accurately identify retinal and choroidal layer boundaries, with good agreement to histologic measurements with light microscopy.

It should be noted that whilst histology provides high-resolution images, there are significant limitations. Firstly, availability of donor eyes is limited, particularly those from young individuals. Secondly, histology is an *ex vivo* technique, requiring an excised eye with no circulation. When considering visualisation of the choroid, a highly vascular structure, histology may not be the most appropriate approach, since the structure can be expected to change without blood flow.

For example, the mean macular choroidal thickness of healthy eyes measured using histological methods has been reported as 125.7 ± 44.1 μm (Curcio et al. 2011) and 139 ± 51 μm (Spraul et al. 1999). This is far lower than the published literature on mean choroidal thickness measured using *in vivo* OCT imaging (ranging 196 to 354 μm; see Section 1.2.5). The same is true for the mean diameter of the large choroidal vessels, reported as 37.1 μm with histological examination (Spraul et al. 1999), and ranging from 123 to 160 μm with *in vivo* OCT imaging (Bittencourt et al. 2014; Park and Oh 2014). Curcio and colleagues (2011) identified a mean difference between histological and OCT retinal volume measurement of 14.5%, attributed to tissue shrinkage during the histological sample preparation process. Tissue shrinkage in the choroid was not investigated due to the poor visibility of the choroid-scleral boundary in the OCT images. Based on the differences in mean choroidal thickness and vessel diameters between the methods reported in the literature, the preparation process of histological samples is likely to have a substantial effect on the choroidal structure. In fact, choroidal thickness has been shown to reduce to approximately half its *in vivo* value following histologic fixation (Li et al. 2016; Figure 1.17).

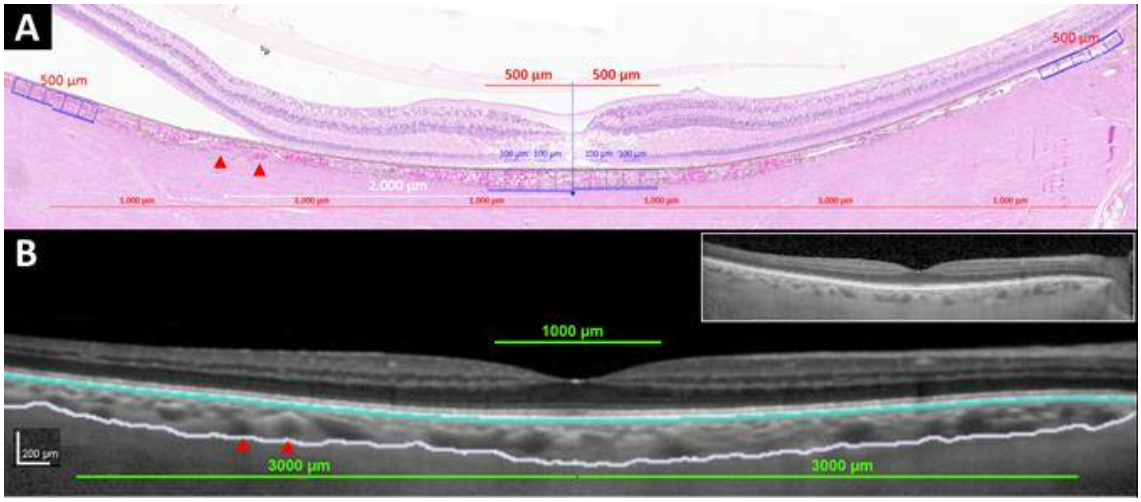

Figure 1.17 Horizontal macular sections comparing histological preparation (post-enucleation; A) with in vivo EDI OCT imaging (B). The choroid was found to be half the thickness following enucleation, with a reduction in the large choroidal vessel diameter (arrowheads). Image from Li et al. (2016).

In summary, although we are well informed about *ex vivo* choroidal structure from histological techniques, *in vivo* techniques such as OCT can provide information regarding choroidal vasculature in the functioning eye, and in a clinical setting. OCT is an established and effective method of imaging the human retina *in vivo*, comparable to histology (albeit with a reduced resolution, and allowing for

tissue shrinkage). More recent developments in OCT imaging, such as EDI and long-wavelength light sources, facilitate optimised visualisation of the choroidal structure. The technique is non-invasive, and allows for quick and easy acquisition of high resolution 3-D images of the posterior pole, in both clinical and research settings. However, the majority of clinical analysis of these images is qualitative, with only minimal quantitative analysis available on commercial systems (generally limited to retinal layer thickness maps and manual calliper measurements). Section 1.7 describes various image analysis techniques that may be employed to quantify structural features within OCT images.

1.7 Image analysis techniques

To gain useful information from a clinical image, structural features must undergo evaluation (for example, assessing the integrity of the retinal layers). This may be a qualitative evaluation by a skilled clinician, or may involve manual or automated analysis to quantify the features. There are two stages to image analysis: image preparation and data extraction. The first of these aims to optimise image quality, typically with regard to noise reduction and feature enhancement. This is followed by data extraction, which may be qualitative or quantitative, depending on the purpose of the analysis. In clinical assessment, this is often qualitative analysis, whereby clinicians will screen images for signs of pathology (e.g. identifying intra- or sub-retinal fluid in OCT images). In research, quantitative analysis is more common, for example comparing retinal or choroidal thickness between disease and control groups.

These two processes are collaborative, with image preparation being tailored to the type of data to be extracted. For example, enhancement of certain features is commonly applied to improve their visualisation. Conversely, the type of data to be extracted is also limited by the images themselves; image resolution being a common limiting factor. This section explores approaches to data extraction from OCT images, including manual parameters, automated segmentation, and machine learning techniques. With consideration to these approaches, image preparation techniques are discussed in Section 2.3.

1.7.1 Manual choroidal vasculature quantification

For a parameter to be effective at describing the vascular structure, it should meet a set of criteria. For clinical feasibility, it should be easily applicable to existing imaging techniques (e.g. OCT), with minimal processing time and user input (to minimise inter-observer variation). Parameters should be sensitive to detecting differences between groups, for example, between disease and control groups (for diagnosis), or over time (for monitoring). For biological parameters, this is often difficult to achieve due to large variations between individuals, and between repeat measurements, often due to confounding factors. For instance, subfoveal choroidal thickness has high variability between individuals, and is affected by many short-term factors including time of day and caffeine intake (see Section 1.3). Parameters should therefore also demonstrate good intra- and inter-session repeatability.

The parameter most commonly used to describe the choroid is choroidal thickness. This is typically measured subfoveally, or at defined locations relative to the foveal pit or ONH, using digital callipers. Alternatively, it may be obtained using automated segmentation algorithms (see Section 1.7.2). Other vascular parameters have been evaluated to describe the vasculature itself, including vessel diameter (Yang et al. 2013; Park and Oh 2014), thickness of the choroidal sublayers (Haller's and Sattler's layer; Park and Oh 2014; Esmaeelpour 2014b), and assessment of the ratio of vessel lumen to surrounding stromal tissue (Branchini et al. 2013; Sonoda et al. 2015).

1.7.1.1 Vessel diameter

Vessel diameter has been investigated as a potential parameter to describe the choroidal vasculature in pathological and healthy eyes (Yang et al. 2013; Bittencourt et al. 2014; Park and Oh 2014). Yang et al. (2013) performed manual diameter measurement of the largest visible vessel with a zone of width 4500 μm, centred on the fovea (Figure 1.18). This was measured perpendicularly to Bruch's membrane at the widest point of the lumen. Two masked observers performed the measurements, and measurements were re-performed if the inter-observer difference was >15%. In cases with a difference ≤15%, the mean of the two values was used. Line scans (average of 100 b-scans) acquired using the Spectralis OCT were utilised in this study. This parameter was used to demonstrate vascular

engorgement in CSC, both in the affected and fellow eye (vessel diameters of 305 ± 101 μm and 251 ± 98 μm respectively, versus 140 ± 40 μm in the control group). However, only a single vessel per eye was used in analysis, with small sample sizes (n=15 per group). The measurement protocol provides no assessment of changes to the smaller choroidal vessels.

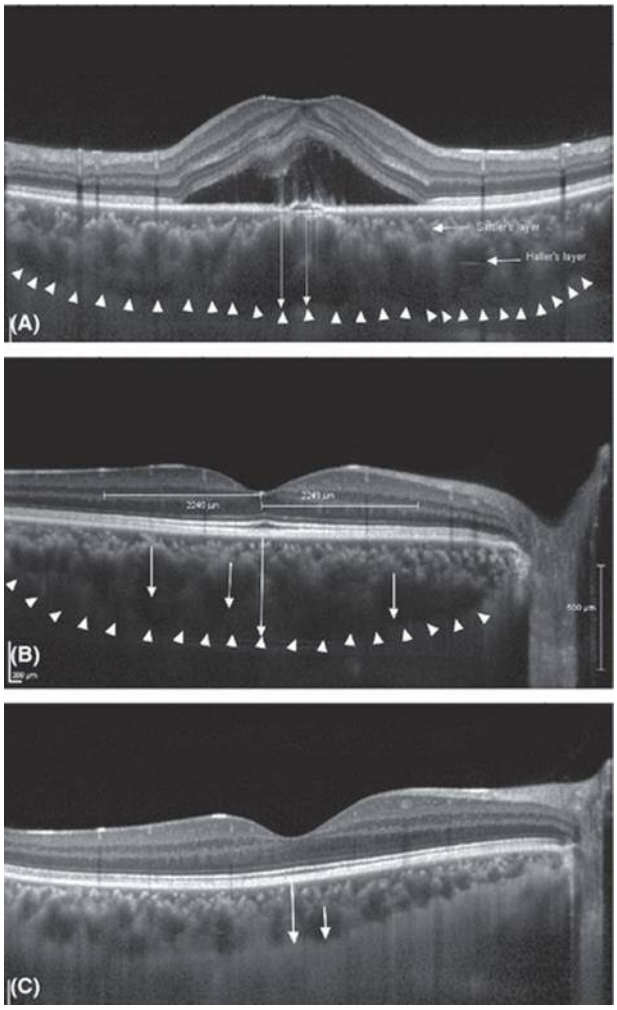

Figure 1.18 Example OCT b-scan from an eye with CSC (A), the fellow eye (B), and a healthy control eye (C). Arrowheads denote the posterior choroidal boundary, and subfoveal choroidal thickness is shown by the long white arrows. The shorter vertical arrows represent the diameter of the largest vessel lumen. Image from Yang et al. (2013).

Bittencourt et al. (2014) measured vessel diameter in Haller's layer at 3 locations within a single foveal b-scan (subfoveal, 2 mm nasally and 2 mm temporally). This was repeated for two further b-scans, 2 mm superior and 2 mm inferior to the foveal b-scan. A mean was calculated from these measurements, and was shown to be smaller in eyes with chronic posterior non-infectious uveitis than healthy controls (123 ± 37 μm and 160 ± 32 μm respectively). Park and Oh (2014) followed a similar protocol, and measured the diameter of large choroidal vessels at

locations 750 μm nasal, temporal, inferior and superior of the fovea. Large vessels were defined as measuring ≥100 μm in adults, and ≥80 μm in children, based upon unpublished pilot data. Mean choroidal vessel diameters were 123 ± 21 μm (age 30.7 ± 4.3 years) and 103 ± 16 μm (age 6.7 ± 1.9 years). This difference was statistically significant, despite there being no significant difference in choroidal thickness between the groups.

1.7.1.2 Haller's and Sattler's layer thickness

Although these measurement protocols include multiple vessels per eye, limitations associated with sampling selection (i.e. representation of the population within those structures sampled) are inherent. To minimise the effects caused by individual vessel quantification, several studies have used choroidal sublayer thicknesses to quantify the choroidal vasculature (Sim et al. 2013; Branchini et al. 2013; Park and Oh 2014; Esmaeelpour 2014b; Adhi et al. 2015; Lu et al. 2016). This is based upon differentiation of the large and medium vessel populations, i.e. Haller's layer and Sattler's layer.

The thickness of these two choroidal sublayers has been documented in healthy eyes. Park and Oh (2014) found the large vessel layer thickness to be 238.3 ± 55.9 μm and the medium vessel layer to be 88.5 ± 28.4 μm in adult eyes. These values are similar to the findings of Branchini et al. (2013), who measured layer thicknesses of 204.3 ± 65.9 μm and 52.9 ± 20.6 μm respectively. These digital calliper measurements were taken from three locations; subfoveal, and 750 μm nasally and temporally. This same manual measurement protocol was utilised to demonstrate significant thinning of both vascular layers in diabetic retinopathy and geographic atrophy (Adhi et al. 2013; Adhi et al. 2014). The control groups in these studies consisted of healthy eyes, with good agreement in vessel layer thicknesses to previous findings. However, these measurement protocols required manual calliper measurement at several pre-defined point locations in the image, again introducing sampling limitations. To further minimise this limitation, segmentation of the choroidal boundaries was used to obtain thickness measures averaged over a defined region, for example ETDRS subfields.

Sim et al. (2013) assessed the repeatability and reproducibility of a novel segmentation protocol to identify the large and medium vessel layers, in eyes with DR. Two observers manually segmented three boundaries; outer border of RPE, choroidoscleral junction, and the Haller-Sattler layer boundary (Figure 1.19). This intra-choroidal boundary was defined as the top of the hypo-intense areas of large vessel lumen (the Haller layer). The Sattler layer included the choriocapillaris, as this was deemed indistinguishable due to its small thickness. High reproducibility in choroidal thickness within a standard ETDRS grid was found, with a mean inter-observer difference of 4.1 μm and 13.7 μm for the Haller and Sattler layers respectively. Intra-observer repeatability was also assessed, resulting in coefficients of repeatability (CoR) of 35.2 μm (29.6%) and 29.2 μm (26.0%) respectively. The authors concluded that the choroidal vascular sublayers can be quantified in eyes with DR, with good repeatability and reproducibility. A similar segmentation protocol was used to demonstrate a reduction in the area of Sattler's layer (as a percentage of total choroidal area) in intermediate AMD (41.1%), when compared to early AMD and healthy controls (Lu et al. 2016). No significant difference was found between eyes with early AMD (47.6%) and healthy controls (47.2%).

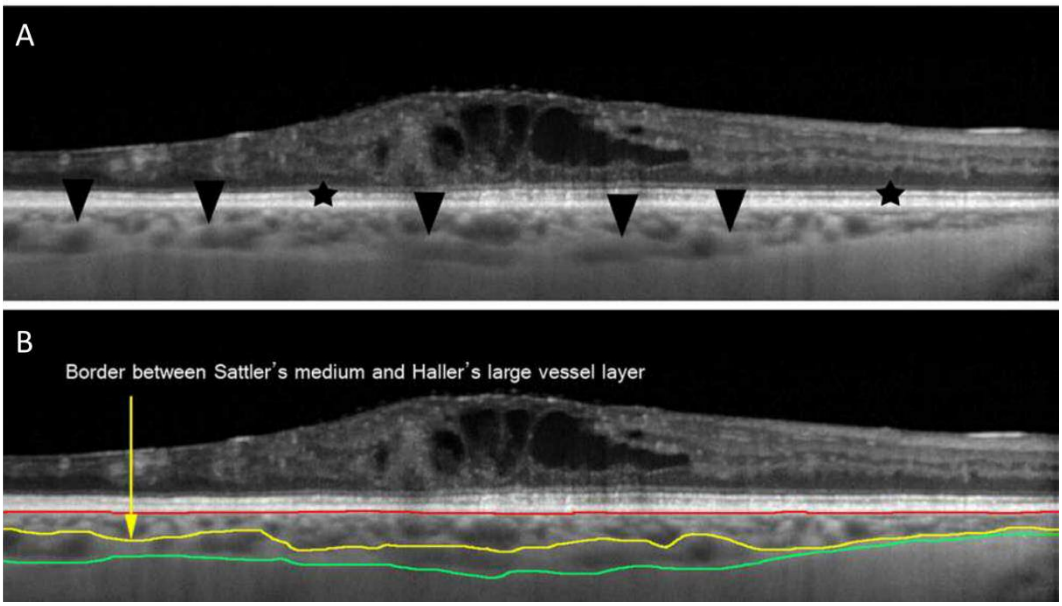

Figure 1.19 Example b-scan with manually segmented boundaries within the choroid. Black arrowheads (A) and yellow line (B) indicate the boundary between the Haller and Sattler layers. Black stars (A) denote areas with ambiguous boundary definition. Image adapted from Sim et al. (2013).

Esmaeelpour et al. (2014b) developed an automated algorithm to segment the Haller and Sattler layers in images acquired with a long-wavelength OCT, in eyes with and without dry AMD. Mean thickness of Haller's layer and Sattler's layer

within a standard ETDRS grid were calculated. For healthy eyes, intra-session CoR (as a percentage of mean thickness) were 18% and 23% for Haller's and Sattler's layer respectively, whilst inter-session CoR were 19% and 26%. For the AMD group, intra-session CoR were 22% and 44% respectively, whilst inter-session CoR were 21% and 34%. This is comparable to the repeatability of manual segmentation in diabetic eyes reported by Sim and colleagues (2013). Both vascular layers were found to be significantly thinner in intermediate AMD with nAMD fellow eye diagnosis, when compared to healthy eyes and to bilateral intermediate AMD (Esmaeelpour 2014a). There was no difference between the eyes with intermediate AMD and the nAMD fellow eye, although both layers were thinner in the nAMD eyes than the healthy group. Although this algorithm showed feasibility for automated segmentation of the choroidal sublayers, it is not currently available outside the institution in which it was developed.

1.7.1.3 Thresholding and binarisation

In OCT images, varying intensity is representative of reflectivity of the imaged structure. Structures with high reflectivity appear bright (e.g. pigment), whilst those with low reflectivity appear dark (e.g. fluid). In the choroid, the vessel lumen have low reflectivity and appear darker than the surrounding stromal tissue, which has higher reflectivity. This relative difference in intensity can be used to distinguish between the vessel lumen and stroma, within the choroidal structure. By defining a 'cut-off' intensity value, greyscale images may be converted to binary images, with pixels below this intensity threshold becoming black and pixels above the threshold becoming white. This technique is known as thresholding, and can be used to identify lumen and stroma within a choroidal image. From these binary images, the percentage lumen or stroma can be easily ascertained.

Thresholding of OCT images has been applied in several investigations of choroidal structure *in vivo* (Branchini et al. 2013; Sonoda et al. 2015; Agrawal 2016a; Kuroda et al. 2016). Two main methods of automated thresholding have been utilised; Otsu global thresholding and Niblack's autolocal thresholding (Otsu 1979; Niblack 1986). Otsu's method determines a single threshold value applied to every pixel within the image, using an iterative method to minimise intra-class variance. Branchini et al. (2013) applied this method to OCT scans of healthy eyes

(n=42), to determine the ratio of choroidal stroma to vessel lumen. A ratio of 0.27 ± 0.08 was found, suggesting a greater proportion of vessel lumen in the choroidal layer. This was conducted for a single averaged b-scan through the foveal pit, and therefore included vessels from all depths within the choroid. This was conducted on a conventional-wavelength OCT (Cirrus HD-OCT; Carl Zeiss Meditec, Inc., Dublin, CA), prior to the advent of EDI; the authors suggest that the use of long-wavelength OCT may be beneficial to this methodology. Otsu thresholding has since been applied to enface images (at a constant depth beneath the RPE; see Section 2.3.3) acquired with the Topcon DRI OCT Triton (Kuroda et al. 2016). These images were of healthy eyes (n=26) and eyes with CSC (n=40). Vascular area (defined as the percentage of vessel lumen in the binarised image) was found to be significantly higher in eyes with CSC, although the authors acknowledge that the protocol of threshold selection was gross, and should be improved to distinguish stroma from lumen.

Niblack's autolocal thresholding defines a threshold based upon mean and standard deviation pixel intensity within a predefined neighbourhood size. The threshold is therefore not consistent across the image. This method accounts for fluctuation in mean intensity across the image (i.e. regions of relative high or low intensity). This is particularly pertinent to the use of OCT images, as areas of low relative contrast may result from overlying media opacities or retinal features (e.g. CNV). Sonoda et al. (2014) outlined a protocol for thresholding OCT cross-sectional scans using a modified Niblack method. The luminal and stromal areas were automatically calculated for 20 healthy eyes and 15 eyes with active nAMD pre- and post- photodynamic therapy (PDT). A variation of this protocol has been verified on healthy eyes (Figure 1.20), and a parameter was developed to quantify the vascular status of the choroid, termed choroidal vascular index (CVI; Agrawal et al. 2016a). This was calculated by dividing luminal area by total choroidal area; on average, approximately 66% of the subfoveal choroid was found to be vascular in healthy eyes. This analysis has since been used to investigate the choroidal vasculature in several ocular diseases, including nAMD, CSC, VKH disease, panuveitis, and diabetes, with promising results (Wei et al. 2016; Agrawal 2016b; Agrawal 2016c; Agrawal et al. 2016d; Tan et al. 2016; Koh et al. 2017).

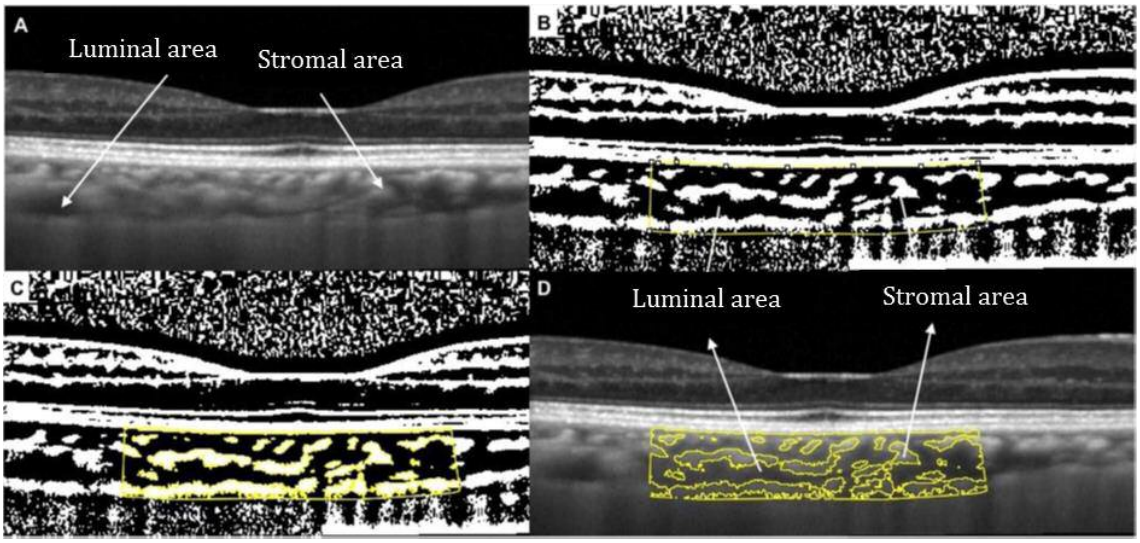

Figure 1.20 Niblack's autolocal thresholding applied to a cross-sectional SD-OCT scan of a healthy eye. Luminal (dark) and stromal (bright) areas are identified (A). A central region of interest (1.5 mm in width) is identified (B). The binarised image is used to produce segmented vessels (C). Vessel segmentation overlay on original b-scan (D). Image adapted from Agrawal, Gupta, et al. (2016).

1.7.2 Automated segmentation

The resolution of modern OCT systems allows visualisation of several intra-retinal layers and individual choroidal vessels. The number of studies utilising OCT has created a demand for fast, automated methods of segmentation (boundary identification) and quantification of features. Retinal layer segmentation has a clear clinical use in gaining a quick insight into the health and integrity of the retinal layers, with many commercial OCT instruments now providing reliable and repeatable on-board segmentation software (Giani et al. 2010; Terry et al. 2016; Hanumunthadu et al. 2017). This information is often presented to the clinician as layer thickness maps, which are quickly generated, relatively easy to interpret, and can be compared to a database of healthy, age-matched individuals. However, segmentation of the well-defined retinal layers and the somewhat less-defined choroidal vessels and posterior choroidal boundaries are very different tasks, each presenting unique obstacles to overcome. The following section briefly outlines recent developments in automated layer segmentation software and choroidal vessel segmentation algorithms (for examples, see Figure 1.21).

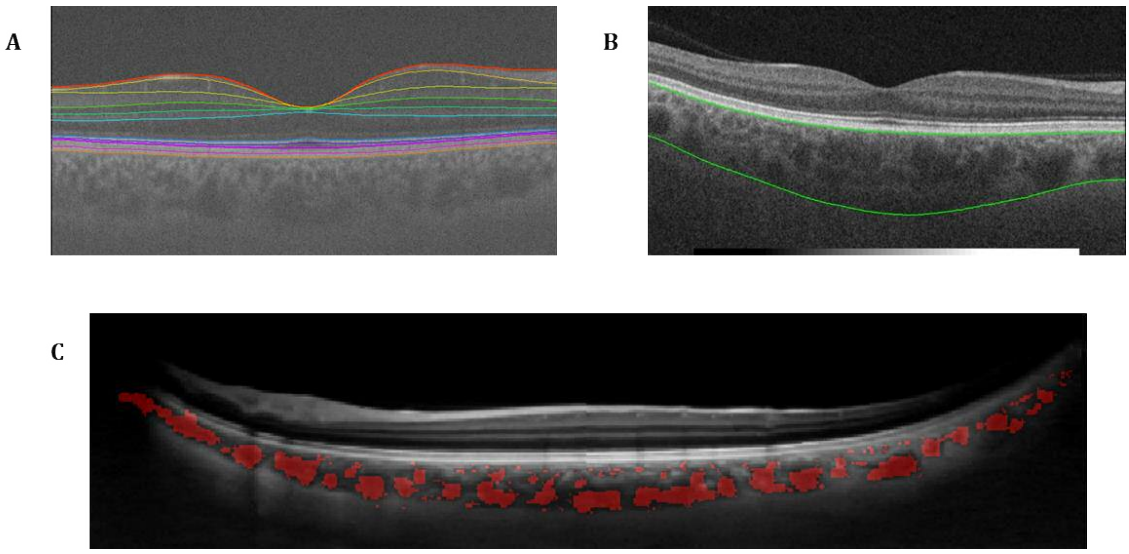

Figure 1.21 Examples of automated feature segmentation on OCT images. (A) Intra-retinal layer segmentation with the Iowa Reference Algorithms. (B) Choroidal layer segmentation with the DRI OCT Triton (Topcon) on-board analysis software. (C) Choroidal vessel segmentation; image from Kajić et al. (2013). Images in A and B acquired by L. Terry during conduct of this study.

1.7.2.1 Choroid and intra-retinal layer segmentation

Commercial OCT devices are supplied with on-board analysis software, which is usually capable of producing automated segmentation of the retina, and often a number of intra-retinal layers. The definition and number of layers varies greatly between devices, with some now even incorporating automated choroidal layer segmentation, for example the Topcon DRI OCT Triton (Figure 1.21B). The repeatability of this particular algorithm is assessed in Section 3.4. Although these algorithms are convenient for fast clinical review of acquired images, this on-board software is almost universally restricted to use on images acquired by the parent device, limiting its application in a research capacity.

Beyond on-board OCT analysis software, there are a number of fully automated intra-retinal layer segmentation algorithms have been developed. These have mostly been developed at research institutions, and are device-independent (i.e. allow input of images from multiple OCT devices). This section outlines these segmentation algorithms, including their potential applications and limitations. Each algorithm is assessed against a list of criteria, including number of layers, availability of the software, and ongoing development; a summary can be seen in Table 1.3. The published accuracy and reproducibility of each algorithm is discussed, where this information is available.

Table 1.3 Comparison of intra-retinal layer segmentation algorithms.

Algorithm/ software	Number of intra-retinal layers	Choroidal segmentation?	Free to use?	Continued development?
Iowa Reference Algorithms	11	Yes	Yes	Yes
DOCTRAP	7	No	Unknown	Yes
Orion	7	No	No	Yes
OCTSEG	6	No	Yes	No

Iowa Reference Algorithms

The Iowa Reference Algorithms (Retinal Image Analysis Lab, Iowa Institute for Biomedical Imaging, Iowa City, IA) contains OCT Explorer for viewing and annotating images, and OCT Segmenter which is capable of segmenting 11 retinal layers and 2 choroidal layers in 3-D macula OCT images (Abràmoff et al. 2010; Zhang et al. 2015; Sonka and Abràmoff 2016; Figure 1.21A). It can import images exported from several commercial OCT devices, as well as standard image formats including '.tif' and '.jpg'. These algorithms are based on graph-theory and contextual information from neighbouring b-scans, and are documented in detail by Abràmoff et al. (2010). They were adapted for SD-OCT by Garvin et al. (2009) from an algorithm by Li et al. (2006), originally designed for TD-OCT.

Garvin and colleagues (2009) validated the intra-retinal layer segmentation using images from 24 healthy eyes, manually segmented by two experienced ophthalmologists as a reference standard. A software boundary positioning error of 5.69 ± 2.41 μm was found, which was very comparable to the inter-observer variability of 5.71 ± 1.98 μm. Philip et al. (2016) validated the choroidal segmentation on healthy eyes (n=18), demonstrating good agreement between SD-OCT and SS-OCT, with automated and manual boundary placement. At the time of writing, these algorithms are still undergoing further development, and support is available from the developers (https://www.iibi.uiowa.edu/content/iowa-reference-algorithms-human-and-murine-oct-retinal-layer-analysis-and-display; accessed 11th January 2017).

DOCTRAP

An alternative segmentation algorithm is the Duke Optical Coherence Tomography Retinal Analysis Program (DOCTRAP; Duke University, Durham, NC). This algorithm is also based on graph theory, and is capable of segmenting 7 layers

in normal eyes, as accurately as expert graders (Chiu et al. 2010). The software has been shown to produce automated thickness values with good agreement with the on-board segmentation of Spectralis and Cirrus HD-OCT in DME (Lee et al. 2013a; Willoughby et al. 2017). It has also been shown to accurately and reproducibly segment retinal boundaries in images containing drusen and GA, producing potentially useful metrics representing RPE changes in AMD (Chiu et al. 2012). Srinivasan et al. (2014a) applied this software to OCT images of mice retinae with and without pathology, and found the software to accurately segment retinal layer boundaries when compared to manual segmentation. The DOCTRAP software package also has the facility for manual segmentation, although it is not widely available outside the institution in which it was developed (https://olv.duke.edu/tech/3383; accessed 11th January 2017).

Orion

Orion is a device-independent 7 layer segmentation software package produced by California-based company Voxeleron. This automated algorithm has been shown to have good agreement with manual segmentation by experts, and has excellent repeatability across all reported layers (Oakley et al. 2014). To date, the majority of studies utilising this algorithm aimed to investigate retinal changes in optic neuritis and multiple sclerosis, rather than retinal pathology (Saidha et al. 2011; Syc et al. 2012). This software was released commercially in 2014, and is undergoing further development (http://www.voxeleron.com/orion; accessed 11th January 2017).

OCTSEG

The Optical Coherence Tomography Segmentation and Evaluation GUI (OCTSEG) is a MATLAB-based retinal layer segmentation algorithm under development at The Pattern Recognition Laboratory (University of Erlangen-Nuremberg, Germany). The output from this software has been shown to be comparable to manual segmentation results on normal and glaucomatous eyes (Mayer et al. 2010). However, the focus of the currently published work is on glaucoma and the ONH, and only the retinal nerve fibre layer (RNFL) is discussed in any detail. This suggests that the algorithm may not be optimised for application to macular scans. Development on this algorithm has now ceased, and no technical

support is available (https://www5.cs.fau.de/research/software/octseg; accessed 11th January 2017).

To conclude, each of these algorithms has limitations, and are likely optimised for differing applications, dependent on which structure or layer is intended for assessment. It is important to note that none of these algorithms are approved for clinical use, and are currently intended for research use only. Of these algorithms, the Iowa Reference Algorithms is capable of segmenting the most intra-retinal layers, and is the only one to include automated choroidal segmentation. Lastly, it is freely available for download and use, and support from the developers is available. Further detail on this software, as well as an evaluation of repeatability and agreement with on-board segmentation of two commercial OCT systems (Topcon 3D-OCT 1000 and Zeiss Cirrus HD-OCT), can be found in Section 3.1 (and Terry et al. 2016; Appendix G).

1.7.2.2 Choroidal vessel segmentation

Until recently, limitations in commercial OCT technology have restricted analysis of the choroid to calliper measurement or manual segmentation. Advancements such as long-wavelength light sources and EDI have been accompanied by a limited number of publications describing algorithms to allow automated choroidal vessel segmentation (Zhang et al. 2012; Duan et al. 2013; Kajić et al. 2013). These have used a variety of techniques to differentiate the vessel lumen from surrounding stromal tissue.

Zhang et al. (2012) modelled choroidal vessels as 3-D tube-like objects to aid vessel detection, and segmented vessels by thresholding voxels (3-D pixels) obtained by the vessel detection algorithm. The authors showed this automated method to have high reproducibility, but the sample size was relatively low (n=24), and restricted to healthy individuals. Furthermore, only around half of the repeat scans (24 of 43) were of sufficient image quality to warrant further analysis. For clinical application of this technique, further optimisation would be required. This study was conducted using a Cirrus HD-OCT, although the authors suggested that the use of a long-wavelength OCT may result in a larger percentage of images providing useful measurements.

Duan et al. (2013) produced enface images at a constant depth beneath the RPE, and applied algorithms to filter noise and threshold. This was combined with segmentation of overlying retinal vessels to remove resulting shadows from the binarised image, before vessel diameter and thickness analyses were conducted. This methodology was found to not be reliable for the choriocapillaris, and processing times were fairly extensive (~20 minutes per volume scan), limiting their application to large datasets. Furthermore, the images used in this study were of a small number of healthy eyes (n=8) and there is no published data on its performance in eyes with pathology.

Kajić et al. (2013) developed a fully automated vessel segmentation algorithm using 3-D edge filtering and projection of probability cones to determine the likely position of a vessel core (Figure 1.21C). Images from a non-commercial long-wavelength OCT were used, and the authors claimed that the algorithm could produce results even in tomograms with a low SNR. The applied processing took 5-10 minutes per volume scan on an average desktop machine (2 GHz, 8 GB RAM), and the algorithm was tested successfully on both healthy eyes (n=45), and eyes with dry AMD (n=10; Esmaeelpour et al. 2014b). The authors cautioned that since the technique was developed using images from a non-commercial OCT, it would be expected that the algorithms would require adapting for optimised performance on commercial OCT devices.

In summary, each of these approaches to choroidal analysis appear to have different strategies of segmenting and assessing choroidal vasculature, with associated limitations. At present, none of these algorithms are at a stage of development to be released outside the institutions in which they were produced, or to be applied clinically. These algorithms are therefore not utilised in this thesis. However, a custom thresholding protocol of enface choroidal images is evaluated in Section 3.2. The development of OCTA has led to a migration in research interest for many groups investigating choroidal vasculature from conventional OCT to OCTA (see Section 1.5.3.3). However, analysis of these images is typically qualitative at this stage, as quantitative analysis is limited (Koustenis et al. 2016).

1.7.3 Machine learning

Machine learning is the study and construction of algorithms that are capable of learning from and making predictions on data. Training data is used to form the basis of the algorithm, providing features from which predictions are based when novel data is encountered. This technique is ideal for big data, where designing and programming explicit algorithms for each given task is unfeasible. There are many established methods of feature extraction, algorithm training, and validation; a detailed description and evaluation of these can be found in Chapter 5.

All of the image analysis methods described in Sections 1.7.1 and 1.7.2 are limited by visualisation of the choroid in OCT images. This can largely be attributed to limited SNR and the relatively low contrast of the choroidal vessels caused by signal roll-off (although averaging could ameliorate this to some extent). In similar cases, machine learning approaches have been utilised, to identify more complex textural features within a region of poor contrast (Wernick et al. 2010; Alpaydin 2014; de Bruijne 2016). The simplest way to assess the viability of such a method is to determine whether texture changes are detectable with advancing disease. This approach is based on mathematically extracting shape and orientation information from images, which reflect the underlying physiological structure.

Clinical classifications are established for AMD (see Section 1.4.7), and can be used to establish the 'true' classification of data, upon which to train the learning algorithms. This is known as the ground truth, and is used for testing the accuracy of the algorithms. Successful classification of novel images into disease groups (based on severity or subtype) indicates that differences are detectable in the structure between groups or with advancing disease, and that automated classification is feasible using machine learning algorithms. To the author's knowledge and at the time of writing, no automated techniques have been developed to classify images by AMD disease severity, based on choroidal appearance (keyword searches for "machine learning" AND "choroid" on PubMed, Web of Science, and Scopus; 28th April 2017). Therefore, studies described in this section fall into two categories; applying machine learning techniques to the detection of AMD from OCT images, and to the classification of AMD from retinal photographs. See Chapter 5 for more detail on the techniques described here.

1.7.3.1 AMD detection from OCT images

Only one study has applied machine learning principles to automated classification of OCT images based solely on choroidal appearance (Koprowski et al. 2013). A retrospective analysis of 1000 OCT images was conducted. Morphological and texture features were extracted from the choroidal region, and were used to build a classifier using 'decision trees' from 600 of the images. The remaining 400 were used for validation and testing. The random forest classifier (RFS) uses a series of weak (only slightly better than chance) binary decision trees; a majority decision from multiple trees is utilised for the final classification (Breiman 2001). The features were based upon number of 'objects' in the image, average position of the centre of gravity in the x- and y-axis, and standard deviation of the mean brightness of pixels within the objects. Ophthalmological diagnosis into one of three groups was used as the ground truth, to assess accuracy of the classifier. The three groups used were nAMD or DME, ischemia of the inner retinal layers, and scarring fibrovascular tissue. Classification accuracy was 73%, 83% and 69% respectively. In this study, the choroid layer was defined as all portions of the image posterior to the RPE, which included the sclera. Furthermore, since this was a retrospective analysis, the images were not optimised for choroidal visualisation during acquisition. Crucially, the feature classification was, at least in part, dependent on differences in choroidal appearance caused by overlying retinal features, rather than solely changes to the choroidal morphology. For instance, the authors comment that the neovascular group displayed characteristic shadows in the choroid caused by retinal changes, and a global reduction in brightness was evident in the ischaemic group. From this, no conclusion could be drawn with regard to differences in the choroidal vasculature between disease groups.

Srinivasan (2014b) extracted features from 45 OCT images, using multiscale Histograms of Oriented Gradient (HOG) descriptors. This essentially describes the shape of objects by assessing the strength and orientation of the spatial gradients in the image (Dalal and Triggs 2005). These features were used to train a support vector machine (SVM)-based classifier to identify images into one of three groups; normal, dry AMD, or DME. SVM is based on the theoretical mapping of features in space and determination of the optimal plane to best separate the data into classes based upon these features (Cortes and Vapnik 1995; Kim et al. 2002). Classification accuracies of 86.7%, 100% and 100% were achieved for the normal, dry AMD, and

DME groups respectively. Srinivasan and colleagues describe the insufficiency of a single b-scan for diagnosing retinal diseases, hence volume scans were utilised for this study. Within a single volume scan, a representation of 33% b-scans of a single disease state was found experimentally to be the optimum cut-off for detection rate (i.e. if a third or more of the b-scans were classified as AMD, a final classification of AMD was given for that eye). Prior to feature extraction, images were cropped axially to 40 pixels above and 5 below the mean lower boundary of the retina. This excluded the majority of the choroid from this analysis.

Albarrak et al. (2016) also utilised HOG descriptors for automated detection of AMD from OCT volume scans. This feature detection methodology avoids segmentation-based methods which rely on high contrast features and are generally time consuming. Similarly to the work of Srinivasan and colleagues, SVM classifiers were trained for automated classification, although this time there were only 2 groups; AMD (n=72) and normal (n=68). Parameters relating to feature extraction refinement were experimentally optimised, achieving a classification performance ranging from 86% to 100%. The Area Under the Receiver Operator Characteristic Curve (AUC) was used to assess performance in this study. This method of assessing performance is independent of the decision threshold chosen, and demonstrates increased sensitivity in ANOVA tests (Bradley 1997). Unlike the other methods discussed in this section, Albarrak and colleagues utilised 3-D feature extraction, rather than considering 2-D b-scans individually. However, due to the requirement of non-excessive computation time, parameters were constrained to a relatively small range.

Artificial neural networks are a commonly used approach to computational classification, modelled on biological neural networks, such as those behind image recognition in the human brain (Lippmann 1987; Specht 1990). This is a 'deep learning' technique, and features are self-learnt by the classifier through a series of feed-back and feed-forward loops. This negates the need for 'hand-crafted' features such as the HOG descriptors described previously, which can introduce an element of bias. However, very large datasets are typically required to train a classifier with high accuracy (Krizhevsky et al. 2012). The largest study to date to apply these techniques to classification of OCT images is Lee et al. (2017). Convolutional neural networks (CNN) were used to automatically classify normal (n=1259) versus AMD

(n=347) based on retinal appearance, achieving a sensitivity of 88.6% and specificity of 87.8%. Apostolopoulos et al. (2016) applied CNN to a smaller dataset; n=269 intermediate AMD, and n=115 without AMD. Their 'RetiNet C' algorithm achieved an AUC of 99.7%. From these studies, CNN appears to be a promising technique for automated screening and computer-aided diagnosis of AMD using volumetric OCT images.

1.7.3.2 AMD classification from retinal photographs

Machine learning techniques have also been applied to automated detection and classification of AMD from retinal photographs. Parvathi and Devi (2007) optimised algorithms for drusen detection, using log-Gabor filters for feature extraction. This is an established texture-based technique, using a series of linear filters of varying frequency and orientation to localise and extract information (Jain and Farrokhnia 1990).

Kankanahalli et al. (2013) advanced from disease detection, and evaluated automated classification by AMD severity. A subset of 600 subjects from the AREDS study were selected for analysis (divided equally between nAMD, GA, and control patients). Visually salient features (relatively prominent textural features) were extracted from retinal photographs, and used to train random forest classifiers for 4 different severity classes; AREDS categories 1-4 (AREDS 2001a). For a 3-class severity problem (i.e. combining categories 1 and 2), an accuracy of 91.8% was achieved. Priya and Aruna (2011) also attempted to classify images into disease groups, although this time by type of disease rather than severity. A Kirsch operator (another method of edge detection) was used to extract features, predominantly describing blood vessels visible in the retinal photographs. These were used to train a probabilistic neural network to classify into 3 groups; normal, dry AMD, and wet AMD. This method achieved sensitivity of 94% and specificity of 95%. However, these were coarse groups with distinct differences in retinal appearance, so a high classification accuracy was to be expected.

In summary, machine learning techniques have been applied to detection of AMD from OCT images, as well as disease severity classification from retinal photographs. The results show potential for automated disease detection using a

variety of feature extraction techniques (e.g. Gabor filters, HOG descriptors) and classifier training methodologies (e.g. random forest, SVM, and neural networks). Since the choroid is known to be implicated in the pathogenesis of AMD, but methods of quantifying the vasculature have significant limitations (see Section 1.7.1), machine learning should be explored as an alternative approach to analysis. To date, no algorithms have been optimised for automated classification of AMD by disease severity (early- and late-stage AMD) based upon textural appearance of the choroid.

1.8 Project overview and aims

It is clear from the literature that structural changes to the choroid have been identified in AMD, although these are not typically detectable in the early disease stage. However, the hypoxia theory of AMD suggests that changes to the choroid are linked to signs of early disease, such as drusen development (Feigl 2007). A number of factors make detecting these changes difficult *in vivo*. Firstly, choroidal thickness is the most common parameter used to quantify the structure. The normal variation in this parameter is large, and differences in mean thickness between disease groups would therefore need to be large to reach statistical significance. Furthermore, relatively small changes in early disease may be masked by other factors shown to cause fluctuations in choroidal thickness, difficult to control for in experimental study design (e.g. smoking and cardiovascular associations such as hypertension).

Other parameters have therefore been explored to describe the vessels themselves, such as vessel diameter and choroidal vascularity index. Although imaging technology now allows for optimised visualisation of the choroid, inherent image noise and signal lost to the overlying structure continue to limit the ability to differentiate vessel lumen from surrounding tissue. The main aim of this thesis was therefore to determine whether structural changes to the choroidal vasculature in AMD are detectable using long-wavelength OCT imaging, and whether they have any potential clinical value in detecting or monitoring AMD. This was addressed by evaluating methods for vessel quantification, adapted from previously described protocols (Sohrab et al. 2012; Bittencourt et al. 2014; Sonoda et al. 2014). This included assessment of the repeatability of vascular parameters.

Since the majority of these analysis techniques require input from an observer, they are often time consuming, limiting their clinical application. Machine learning algorithms have been shown to be capable of automated classification of medical images (Wernick et al. 2010). Once classifiers have been developed using a training set of images, no further subjective input is required to establish a classification of a previously unseen image. This makes machine learning algorithms ideal for integration into clinical image analysis software. As an example, on-board OCT image analysis software could be made capable of producing a likely disease diagnosis from a newly acquired image, providing a fast and accurate tentative diagnosis for triaging busy hospital clinics. This could ensure that clinical assessment and treatment be delivered to those requiring most urgent care and minimise false positive referrals into secondary care.

As a step towards this ultimate aim, the feasibility of these techniques for classifying choroidal OCT images by AMD disease severity was evaluated. Following classifier training, features with the strongest relationship with disease stage (i.e. contributing to classification) were extracted to provide information on how the vasculature differs between disease states. For example, different spatial frequencies may peak in each disease stage, which could be linked to changes in vessel diameter or density. Relating the features to vascular parameters may further our understanding of vascular changes in AMD, and the role of the choroid in the pathogenesis of the condition.

The main aim of this thesis is to determine whether structural changes to the choroidal vasculature in AMD are detectable using *in vivo* OCT imaging.

To achieve this, three supplementary aims are as follows:

1) To optimise protocols for image acquisition and processing for enhanced visualisation of the choroidal vasculature.
2) To evaluate parameters describing the choroidal vasculature, including assessment of inter-session repeatability.
3) To explore the feasibility of applying machine learning techniques to automated classification of AMD by disease severity, based on choroidal appearance.

2 Development of image acquisition and processing protocols

Advances in OCT imaging and analysis techniques, particularly the advent of long-wavelength OCT, have facilitated reliable imaging of the choroid *in vivo*. However, given the novelty of choroidal OCT imaging, definitive imaging protocols and analysis methods have not yet been established. The best approach to these tasks is not evident from the literature, with published approaches typically tailored to the immediate aims of each study. This chapter discusses the development of imaging and analysis protocols utilised in the studies in this thesis. An overview of the imaging system and techniques used in this thesis is provided, followed by the image processing steps undertaken following acquisition. The results of two pilot studies are then presented, which were used to inform protocol design for further data collection.

2.1 Long-wavelength (1040 nm) OCT system

The investigations presented in this thesis have utilised a non-commercial long-wavelength (1040 nm) SD-OCT to produce 3-D images of the posterior pole. This system was selected to benefit from the long-wavelength light source, which can penetrate deeper into the retinal structures (including the highly pigmented RPE). This provides improved visualisation of the choroid and choroid-scleral junction, in comparison with conventional systems. Furthermore, penetration through media opacities such as cataracts is improved (Povazay et al. 2007), which are prevalent in the elderly target population. This wavelength also has the benefit of being outside the visible spectrum, preventing the common observer response of tracking the scanning line during image acquisition. See Section 1.6 for more detail on long-wavelength OCT and imaging the choroid. An overview of the specifications of this system are shown in Table 2.1.

This OCT system also allows the scanning parameters to be freely adjusted, including scan width, number of a-scans per b-scan, spacing of b-scans, number of b-scans per volume, and horizontally- or vertically-oriented raster scanning. This is in contrast to most commercial devices, which restrict image acquisition to pre-set

parameters with only limited customisability, likely to maximise compatibility with the on-board software analysis. This customisability allows for acquisition of a range of image types, from small, very highly sampled images to wide scanning areas, covering more retina than the majority of commercial OCT systems. Additionally, an 800 600 pixel LCD micro-display is used to present a fixation target, which can be customised for each patient. For example, a large cross or peripheral fixation target can be used for a patient with a central scotoma.

Table 2.1 Specifications of the long-wavelength OCT system utilised in this thesis.

Central wavelength (λ_c)	~1040 nm
Imaging rate	47,000 a-scans/sec
Axial resolution	~5 μm in tissue (RI=1.4)
Lateral resolution (theoretical)	~6 μm
Refractive error range	Up to ± 6.00 dioptres

Whilst this non-commercial device provides a number of distinct advantages, the limitations must also be considered. Firstly, the graphical user interface (GUI) for image capture is not designed for commercial use and consequently is not easily accessible to inexperienced users. The system requires considerable training to be used effectively. The focus of the instrument must be manually adjusted, and is calculated from the patient's biometry and refractive error. Manual alignment of the eye with the imaging system is based solely on the live OCT image, whereas alignment on commercial devices is usually supplemented by a live infrared image, making the process easier for the operator. The image capture software has an enface OCT facility enabling visualisation of an image following acquisition, to ensure the absence of gross eye movements and blinks, providing an opportunity to repeat an image if necessary. There is no capacity for instant review or analysis of images, as is commonly incorporated in commercial devices. Images must be exported and manually processed prior to analysis, and subsequent analysis such as thickness maps must be produced by other means, which can be time consuming. This is extremely limited in comparison to most on-board commercial review software that enable near-instant review and analysis.

Eye tracking systems are becoming increasingly common in newer commercial systems (e.g. Cirrus HD-OCT). These track the location of the eye, and

attempt to correct for small eye movements. They may pause a scan during blinks or gross eye movements, and resume once fixation has been re-established. This is particularly valuable for patients with poor fixation or a high blink rate, and can minimise patient discomfort caused by refraining from blinking for a period of time. However, this facility was not incorporated in this OCT device. Other limitations of this non-commercial system include higher rates of instrument down-time to allow for repairs and alterations, and a restricted availability of such devices. Although a commercial long-wavelength instrument became available during the course of this work (Topcon DRI OCT Triton), to date there are only a handful of these devices in clinical use in the UK. This is likely due to the current cost of this device, which exceeds that of its conventional OCT counterparts, due in part to the addition of swept-source technology.

At the outset of this project, the light source of the non-commercial device had been in use for approximately 5 years, and in this time had lost ~25% of its power. A noticeable reduction in image quality over this period was observed, due to restricted imaging penetration depth of the system. To address this issue, a new 'identical' light source was installed, following completion of the repeatability study (Chapter 3) but prior to commencement of data collection from patients with AMD (Chapter 4 onward).

The 1040 nm OCT is able to acquire a volumetric scan in ~5 seconds; a duration widely considered clinically acceptable. During this time, the patient is required to fixate a target and avoid eye movements and blinking. A longer acquisition time would allow for either image averaging or higher scan density, improving image quality and/or SNR. However, since dry eye is particularly prevalent in the elderly population, increasing the acquisition time is an unrealistic approach. Experience suggests the standard acquisition time of 5 seconds may potentially be challenging for patients with a reduced tear break-up time, although artificial tears can be used to reduce discomfort during image acquisition.

2.2 Scan parameters

An advantage of the 1040 nm non-commercial system is the ability to control the scanning parameters (e.g. scan angle). In comparison, the majority of

commercial OCT devices are limited to a small range of pre-set scan parameters, the most common being 6 6 mm, or 20° 20° (512 128 pixels) as found on Topcon and Zeiss instruments respectively. Unless otherwise stated, all studies in this thesis utilise 20° 20° isometric scans, consisting of 512 a-scans per b-scan, and 512 b-scans per volume. This provided equal spatial sampling in the X and Z planes (Figure 2.1). To allow comparison between devices, averaging in the Z-plane was used to produce equivalent volumes (512 128 pixels) where appropriate. However, images of this size were under-sampled, limiting image resolution. This is discussed further in Section 2.4.2.

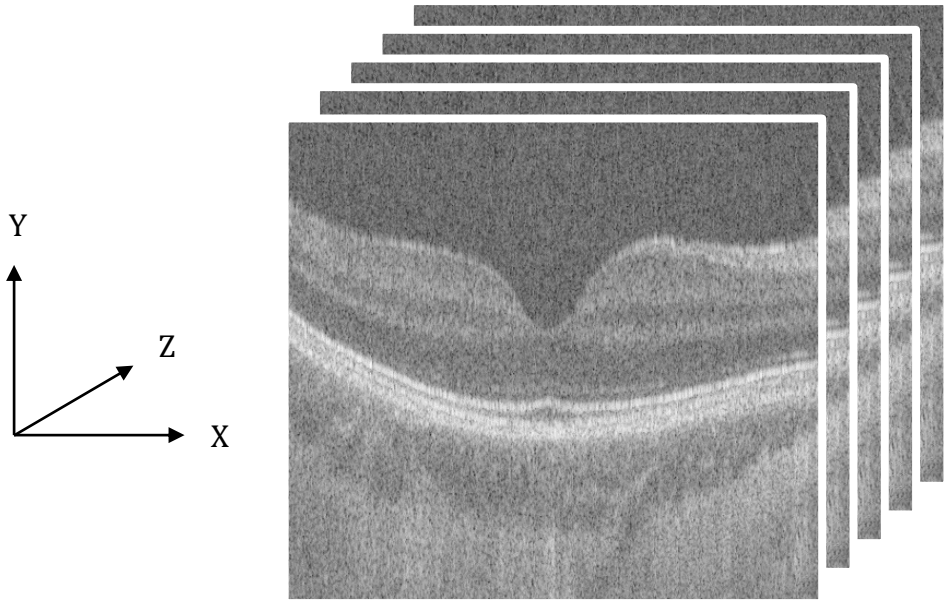

Figure 2.1 Series of consecutive b-scans within a 20° 20 (512 512) macular volume scan.

In addition, an averaged line scan through the fovea was collected to provide an image with a high SNR. This was 36° (4096 a-scans) in width to encompass visualisation of the ONH, and was an average of 16 b-scans of the same region. The volume scans would ideally also undergo averaging to a similar extent, however this would require increased acquisition time or loss of sampling, and suffer from the challenges associated with 3-D image registration (Markelj et al. 2012; Lee et al. 2015). Since instant review of images was not possible, multiple images of each type were collected from each individual, to ensure high image quality. Table 2.2 outlines the parameters of the standard images collected as part of this thesis. Some parameters required optimisation to address the aims of the studies in this thesis; these preliminary studies are presented in Section 2.5.

Table 2.2 Scan parameters used in this thesis for the 1040 nm OCT device. Parameters requiring further investigation with preliminary studies are indicated in the final column.

Parameter	Volume scan	Line scan	Further investigation required?
Scan size	20° 20°	36°	Yes – volume scans under-sampled
Scan dimensions (pixels)	512x512x1024	4096x1024	No – consistent with literature
Repeat images	3	3	No – sufficient to exclude outliers
Wavelength	1040 nm	1040 nm	No – extensive literature
Power output	<2.5 mW	<2.5 mW	Yes – ensure safety and quality

Although the scan sizes described above are generally accepted as the clinical norm for retinal imaging, choroidal imaging is a relatively new field and few established imaging protocols have been developed. A pilot study in Section 2.5 describes the development of a protocol for maximising choroidal visualisation with long-wavelength OCT imaging. However, it is first necessary to consider the post-processing steps and measurement techniques to be applied to the acquired images.

2.3 Post-processing

Following acquisition, all long-wavelength OCT images were saved as proprietary (spectral) data files (.FD1) and required pre-processing before viewing and/or analysis. The following describes the processing steps applied to all images obtained using the long-wavelength OCT in this thesis (Figure 2.2), and image scaling considerations made during the analysis process.

2.3.1 Conversion from spectral data to image data

All long-wavelength OCT images were converted from spectral data (.FD1) to image data (.TIF). This was performed using customised software written in MATLAB (The MathWorks, Inc., Natick, MA). During this process, images underwent dispersion correction. The purpose of this correction was to address a mismatch between the two arms of the interferometer within the OCT system. Since different wavelengths of light travel at different speeds through a material, the light is dispersed (in time rather than in space) when it returns to the photodetector. To correct for this, a rectangular region of interest (ROI) was manually selected, ideally through a high-contrast section of retina and choroid. From this region, a factor to

correct the dispersion was calculated and applied across the entire image stack. A high-specification computer (Intel Core i7-4790 CPU at 3.6 GHz, with 16 GB RAM) was used to minimise processing time (approximately 5 minutes per 512 512 volume scan).

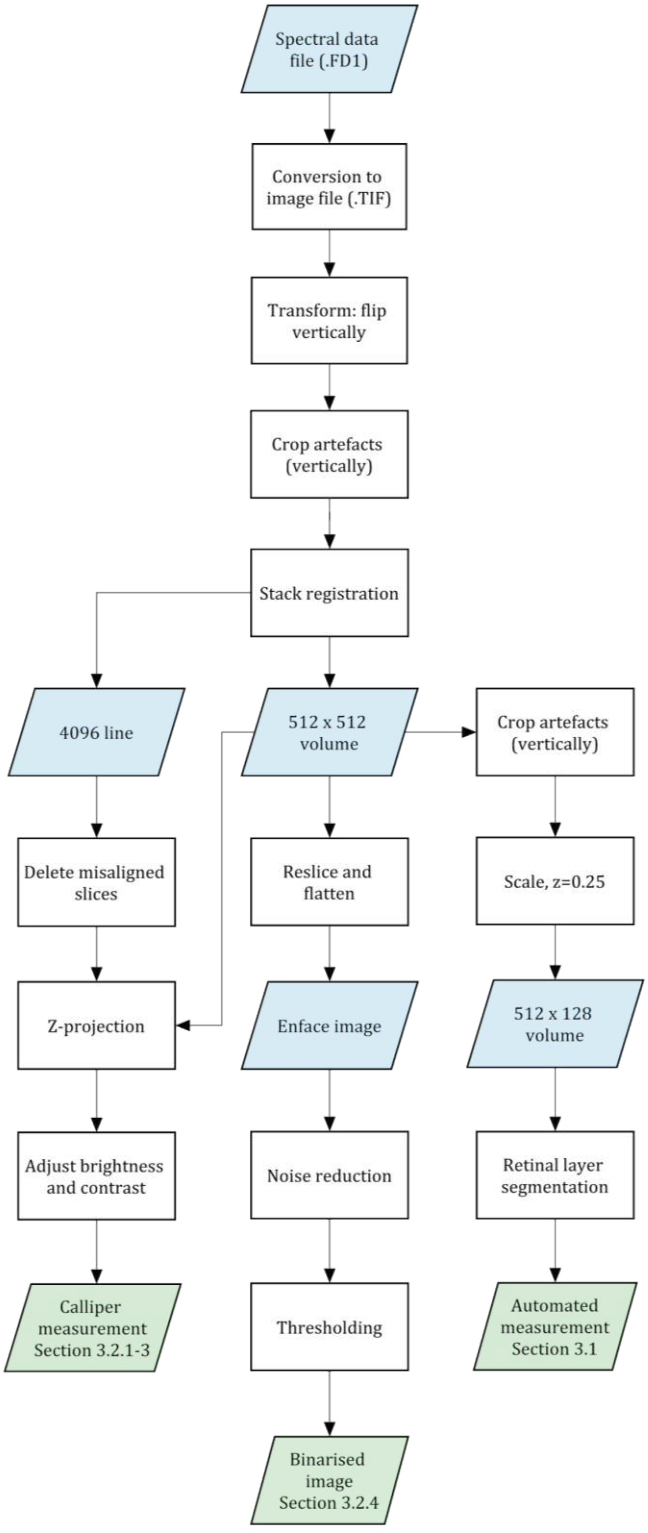

Figure 2.2 Series of image pre-processing steps (white rectangles) that all scans acquired with the 1040 nm OCT device underwent. Blue rhombi represent image types; green rhombi represent outcome measure categories, and the section in which they are investigated is specified.

2.3.2 Image preparation and artefact correction

Although images were optimised during the acquisition process, inevitably artefacts and noise were inherent. Artefacts were commonly a result of poor fixation or ocular motion during acquisition, or due to the optics of the eye and the instrument itself (e.g. low levels of stray light within the imaging system). The effects of such artefacts may be minimised using post-processing techniques. The following processes were carried out sequentially to all long-wavelength OCT images using the Java-based image processing package Fiji, an open source distribution of ImageJ (Rasband; National Institute of Health, USA; Schindelin et al. 2012).

2.3.2.1 Transform and crop

Images were collected using a technique similar to EDI (see Section 1.6), positioning the choroid close to the zero delay line during acquisition. This optimised visualisation of the choroidal vessels, however images appeared inverted (choroid at the top of the image and retina below). Images underwent vertical transformation (inverting to place the retina above the choroid) for consistency with the format familiar to users of commercial OCT devices, and to allow for image input into automated retinal layer segmentation software (see Section 3.1).

Vertical cropping of images was used prior to stack registration, to remove reflection artefacts likely due to stray light within the imaging system. This had the added benefit of reducing file size, by removing portions of the image containing structures irrelevant to the analysis (i.e. excess vitreous and post-choroid). This reduced processing times for subsequent steps described here.

2.3.2.2 Stack registration

Due to the raster-scanning pattern used during acquisition of the volume scans, small involuntary eye movements resulted in misalignments between adjacent b-scans within the volume. Stack registration was therefore used to align all b-scans according to a 'global anchor' (Figure 2.3). The StackReg plugin (Thévenaz et al. 1998) allowed the user to define the global anchor slice; for these images, the b-scan corresponding to the centre of the foveal pit was used as the global anchor. The algorithm used common features between adjacent b-scans to

register all slices within the volume to the selected slice. This registration was essential for viewing enface images and prior to averaging of adjacent b-scans.

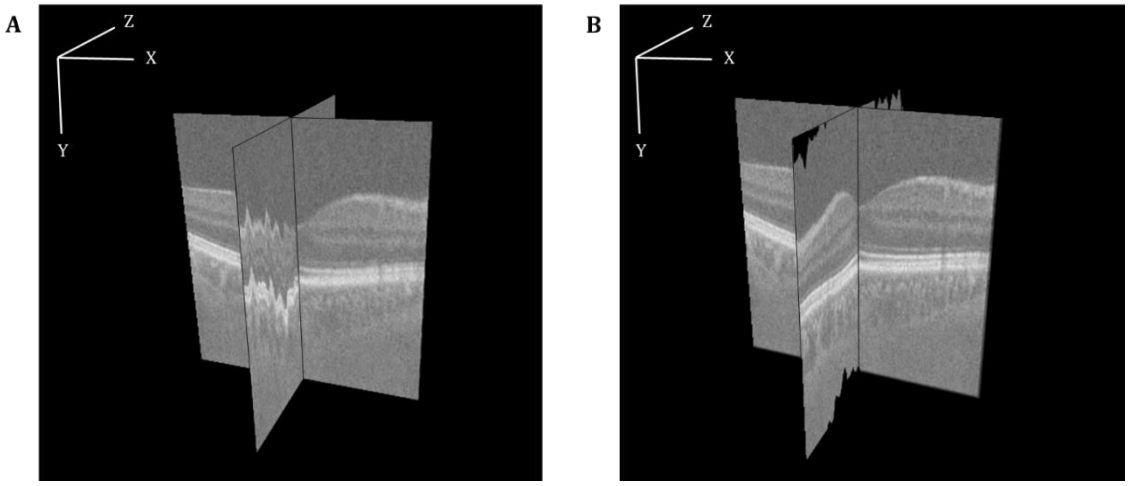

Figure 2.3 Macular volume scan without stack registration (A) and with stack registration (B). Note the misalignment of b-scans in the Z-direction pre-registration, and the artefacts at the top and bottom of the image post-registration, caused by vertical translation to align each b-scan.

Artefacts in the image as described above could provide strong features for alignment by the algorithm. This would lead to inappropriate registration, as these artefacts may not be present in the exact same location in each b-scan. To overcome this, these artefacts were removed prior to stack registration, using cropping. Translational transforms (images moved only in the X and Y plane) were used for these images, to prevent magnification or rotation of the b-scans, as would occur in alternative forms of transformation, such as scaled rotation.

2.3.3 Noise reduction and image enhancement

The preceding steps were applied to all images acquired with the 1040 nm OCT (both volume and line scans), to produce images in TIFF format for further analysis. The following describes processing steps applied to reduce noise, or enhance certain features within the image. The processing steps applied were selected to optimise the image with respect to the desired outcome measure, and were therefore dependent on the particular feature(s) to be assessed (Figure 2.2).

2.3.3.1 Z-projection and image scaling

Z-projection was utilised to average adjacent b-scans within a volume scan, reducing noise to enhance visualisation of the choroidal layer and vessel boundaries (Figure 2.4). This produced 2-D representations of the volume, which were used for manual calliper measurement of choroidal thickness or vessel size. Typically, 5 adjacent b-scans centred on the foveal pit were included in this averaging, equating to a total separation between b-scans of ~50 μm. This minimised noise whilst maximising spatial resolution; averaging over a greater number of b-scans (i.e. a higher total separation between slices) resulted in a decrease in boundary definition due to varying location of the boundary in image space.

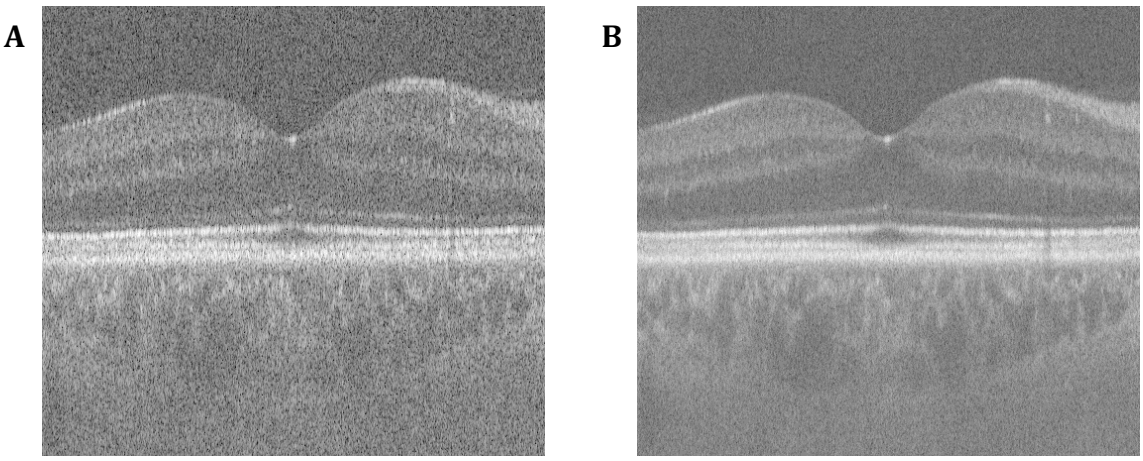

Figure 2.4 Single b-scan through the foveal pit (A), taken from a 20° 20° (512 512) volume. Following z-projection of 5 consecutive b-scans (B), much of the high-frequency noise has been removed and the retinal and choroidal structures are more easily distinguished.

There were several potential projection types, including the use of a maximum, minimum, or median intensity, or summing the intensities across adjacent b-scans. Speckle (a type of high frequency noise) is inherent in OCT images, causing corresponding pixels in consecutive slices to vary in intensity (these may be higher or lower than the average intensity). If minimum, maximum, or sum of pixel intensities were applied, each pixel was considered in the averaging process, regardless of its representative value. To prevent inclusion of erroneous pixel intensities, the median intensity was used. The limitation of Z-projection was the loss of spatial localisation, since adjacent b-scans were not of the exact same retinal location.

Z-projection was also used for the line scans, to produce high quality line scans through the foveal pit by averaging several b-scans. This was equivalent to

highly averaged line scan processing on the majority of commercial OCT devices. The number of averaged b-scans varies between commercial devices; those with a faster acquisition rate and retinal tracking (to compensate for small eye movements) generally average a larger number of b-scans (up to 100). Since the non-commercial device used in this thesis did not have retinal tracking, any misaligned slices following stack registration were manually identified and excluded prior to averaging of line scans.

Image scaling was also used to make the 1040 nm OCT volume scans (512 512) comparable in size to commercial equivalents (typically 512 128; Section 3.1). This involved decreasing the number of slices in the image, by averaging every 4 slices (i.e. Z=0.25 scaling using averaged down-sampling). This technique used the neighbourhood of known pixel values surrounding the unknown pixel to calculate an interpolated value for the pixel in question.

2.3.3.2 Reslice and flatten

Stack reslice was used to construct orthogonal slices through an image, generating a 'side-view' of adjacent b-scans. This was used to produce enface images from the acquired volume scans. This allowed visualisation of choroidal cross-sections of a fixed depth below the retina, from a perspective akin to retinal photography. Stack registration was crucial prior to this step, to ensure alignment of adjacent b-scans within the volume.

Despite this process, the images often retained a residual curve due to the optics of the visual system. Producing an enface image from this would be of inconsistent depth in the choroid (Figure 2.5). To overcome this, a custom program written in MATLAB was used to 'flatten' the b-scans prior to stack reslice (see Appendix B). Several points lying on the RPE-choroid boundary were manually identified on 5 predetermined b-scans throughout the stack. This boundary was selected as it was well-defined and easy to identify in the images (unlike the posterior choroidal boundary), and was consistent in shape across the foveal pit (unlike the inner retinal layers). The program interpolated between the identified points on each b-scan to produce semi-automated segmentation of the anterior choroidal boundary. This was then interpolated between slices to produce a

boundary for each b-scan in the stack. Vertical translation of pixel columns (a-scans) was automatically applied to align the segmented boundaries to a flat plane. Again, scaled rotation was not used, to prevent the introduction of transverse scaling errors.

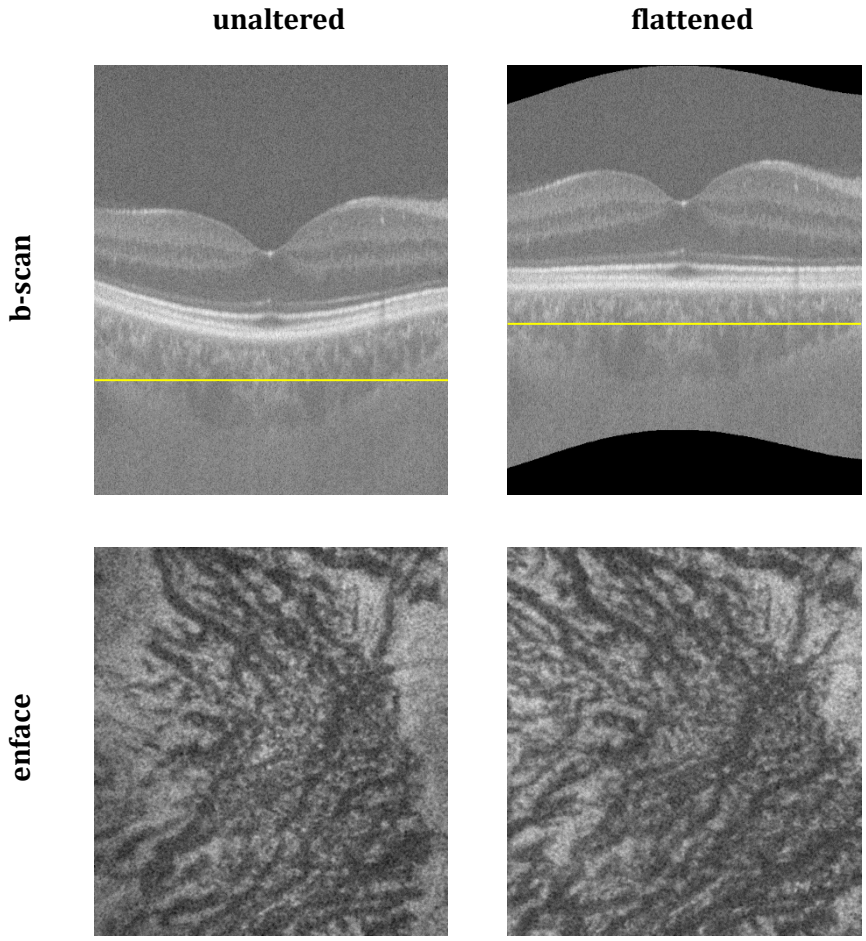

Figure 2.5 Flattening images using semi-automated segmentation of the anterior choroidal boundary ensured greater consistency of choroidal depth in the enface view. In the unaltered image, the reslice plane (yellow line) incorporates sclera towards the edges of the b-scan. The brightness and contrast of the enface images have been manipulated to enhance the vessels.

2.3.3.3 Noise reduction

Applying a mean or median filter replaces each pixel with the mean or median value of its neighbours, including itself. This has the effect of eliminating pixel values which are unrepresentative of their surroundings i.e. noise reduction. A convolution filter is based on a kernel system, which describes the shape, size and weighting of the neighbouring pixels to be represented in the average. More weighting can be given to the central pixel to limit the influence of surrounding pixels on the outcome. The effects of various kernels can be seen in Figure 2.6. A

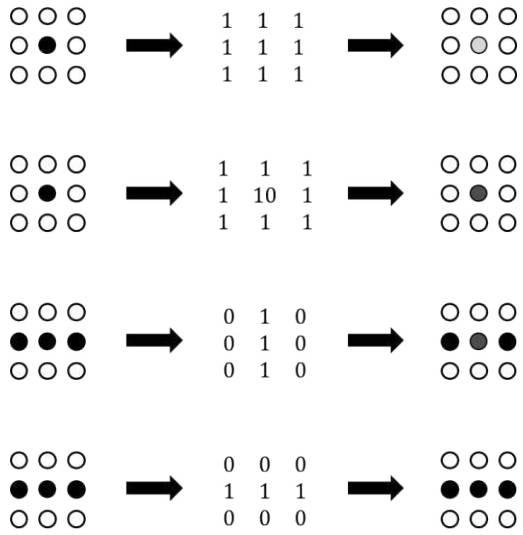

Figure 2.6 Examples of kernels commonly used in convolving filters, and the effects they have on the central pixel.

3 3 square kernel with equal weighting given to each pixel was applied to the enface OCT images to reduce the effect of unrepresentative pixel intensities caused by speckle (Figure 2.7).

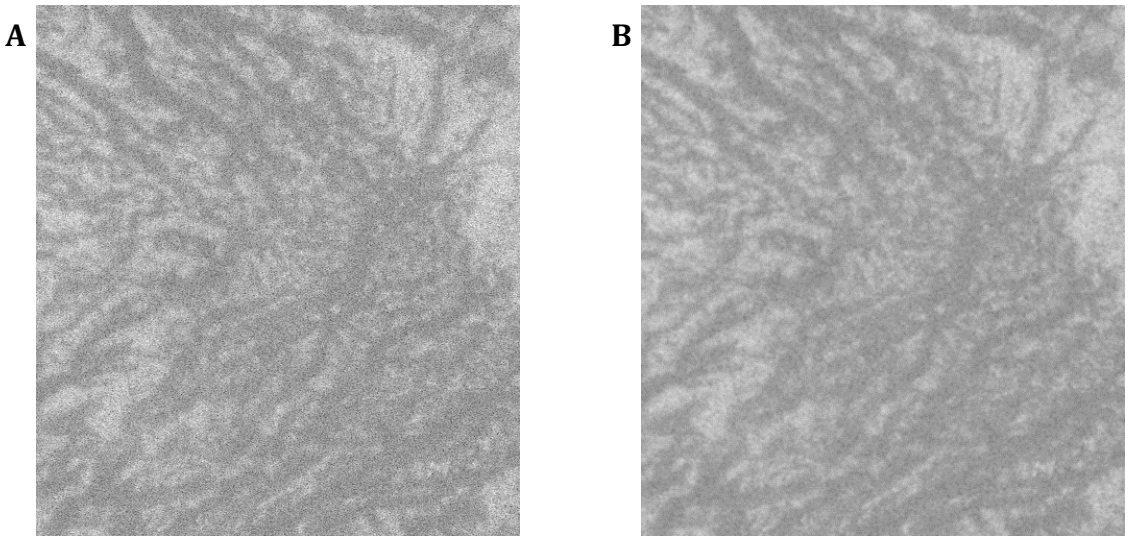

Figure 2.7 Enface choroidal OCT image before (A) and after (B) application of convolution blur. A 3 3 kernel with equal pixel weighting was used to reduce high frequency noise (speckle).

Larger kernels (e.g. 5 5) will give smoother, less noisy images, however this will result in the loss of high-frequency image information. Anisotropic kernels can also be applied solely in one direction (X or Y), to average pixels in a single orientation. This could be of potential benefit for OCT imaging, due to the decoupling of axial and transverse resolution (see Section 1.5.2). An anisotropic kernel could be applied to enhance retinal layers by applying averaging horizontally only, in b-scan view. For this thesis however, enhancement of retinal layers was not required, so this directional process was not applied.

2.3.3.4 Brightness and contrast

Adjusting the brightness of an image adds or subtracts a bias to every pixel within the image, altering the overall perceived intensity, whilst maintaining the absolute differences between pixels. Brightness was manually adjusted to subjectively improve visualisation of the retinal layers and choroidal structures. Contrast adjustment alters the proportional luminance according to the relative intensity of each pixel. Since this can result in saturation of boundaries such as the RPE, which may have led to errors in interpreting exact boundary positions, contrast adjustment was not used in image quantification.

2.3.4 Magnification and scaling

OCT images are affected by magnification in the transverse plane; therefore to ensure accurate quantifiable measurements the images required scaling. The magnification effect results from the optics of the imaging instrument and the subject's eye. Transverse OCT dimensions should be corrected for axial length to counter this effect (Odell et al. 2011).

To appreciate the potential magnitude of this effect, we consider two eyes; one with an axial length of 20 mm (likely a hyperope), and one with an axial length of 28 mm (likely a myope). Using Equation 2.1, the first of these eyes will have a magnification factor of 0.80x, the second will have a magnification factor of 1.16x. Therefore, for a retinal feature of 100 μm, the measured size would be calculated as 80 μm and 116 μm respectively; an error of up to 20 μm, which would be considered significant.

Prior to the correction of any magnification effects, the size in microns was calculated from the size in pixels measured from the image. A lateral scaling factor was calculated for each image using the following equations (Littmann 1982; Bennett et al. 1994):

Equation 2.1

where:

N_p = number of pixels in the scan

A = input scan angle (°)

R = retina to nodal point distance, or vitreous chamber depth (mm)

R can be calculated as follows:

Equation 2.2

where:

A = axial eye length (AEL; mm)

1.6 mm is the cornea to principle plane distance (from Bennett et al. 1994)

1.34 is the assumed group refractive index of the eye

From Equations 2.1 and 2.2, a 20° 20° (512 512) volume scan obtained from an eye with AEL = 24 mm would have lateral scaling of 11.38 µm/pixel. At least 2 adjacent pixels are required to resolve an edge, which in this case would have a combined size of 22.76 µm. This is larger than the lateral resolution limit of the OCT (~6.3 µm), and would therefore be under-sampled. A 5° 5° scan of the same dimensions on the same eye would have lateral scaling of 2.85 µm/pixel, which would be over-sampled. Over- and under-sampling are explained in more detail in Section 2.5.1. For this research, lateral scaling was calculated from the measured AEL of each eye, and used to convert image size in pixels to feature size in microns. A detailed investigation of the effect of AEL-dependent lateral scaling is outlined in Section 3.1.

Since the axial scaling is determined by the bandwidth of the light source (Huang et al. 1991; Drexler and Fujimoto 2008), the axial component of an OCT image is independent of AEL, and is the same for all eyes. However, an axial scaling factor must still be applied to convert the number of image pixels to a physical size in microns. For the long-wavelength OCT, the axial scaling in air was empirically determined to be 2.66 µm/pixel, which equated to 1.90 µm/pixel in tissue (n=1.4). Therefore, an axial scaling factor of 1.90 µm/pixel was applied to all images from the long-wavelength device.

2.4 Measurement techniques

Histological measures, as outlined in Section 1.6.2, are considered the gold standard for informing quantification of OCT images. This section describes the development of measurement techniques used in this thesis, and the associated limitations of such quantification.

2.4.1 Manual measurement approaches

For this thesis, manual measurement of choroidal thickness and vessel diameter were carried out using digital callipers in Fiji. All non-foveal retinal locations were identified considering transverse magnification, as described in the previous section. Measurements were taken vertically on the image, regardless of the slope of the retina, for ease of axial scaling conversions. However, since the retina typically follows a convex curve in OCT images, axial measurements may not be truly representative, particularly in locations further from the foveal pit (Figure 2.8). To minimise the effects of this, images were acquired with the retina as 'flat' as possible, through careful alignment of the imaging system. The program to translationally align a-scans to a flat plane (RPE) was therefore only required for images to be viewed enface.

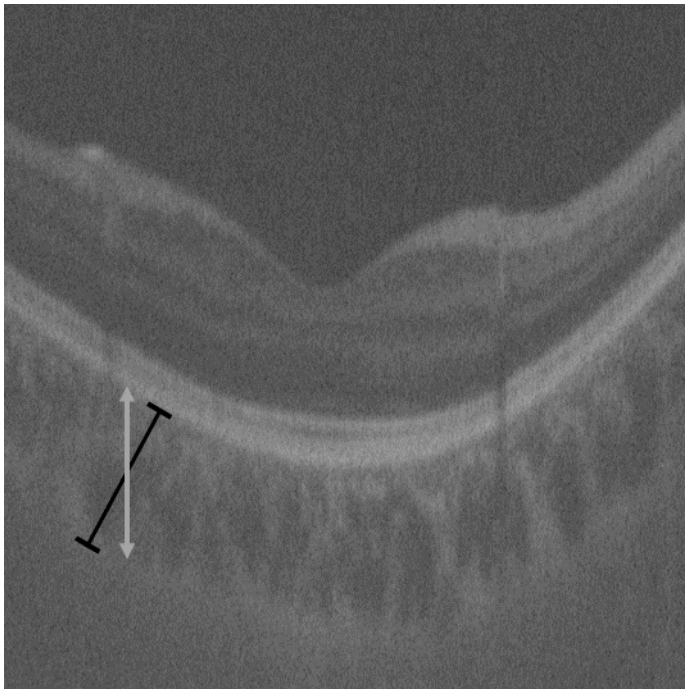

Figure 2.8 Choroidal thickness was manually measured axially (grey arrow). For curved images, this was not the same as choroidal thickness perpendicularly to the RPE, particularly further from the foveal pit (black line; exaggerated).

The choroid was defined as the area enclosed by the posterior boundary of the RPE and the choroid-scleral boundary, identified by the visible bright sclera and the outer border of the choroidal stroma. This was selected as the posterior choroidal boundary, as it has been shown to be more reproducible than alternative boundaries, such as the outer border of the choroidal lumen, or the inner border of the sclera, as shown in Figure 2.9 (Vuong et al. 2016).

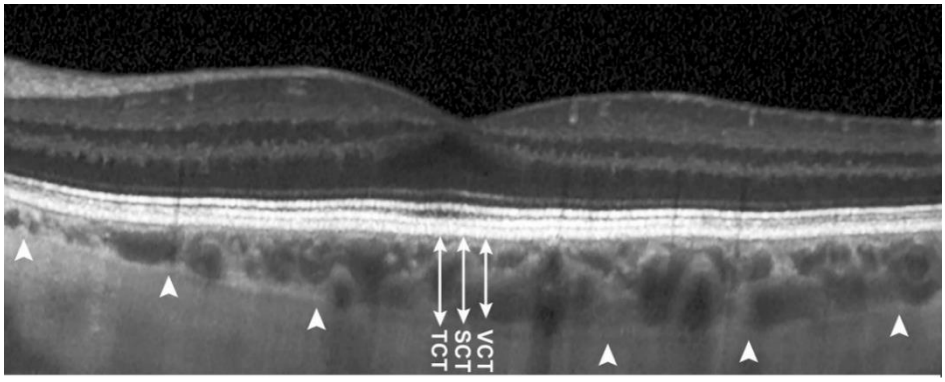

Figure 2.9 Horizontal averaged b-scan from a Spectralis OCT, with three potential posterior choroidal boundaries displayed. Vascular choroidal thickness (VCT) uses the outer border of the vessel lumen. Stromal choroidal thickness (SCT) uses the outer border of the choroidal stroma. Total choroidal thickness (TCT) uses the inner border of the sclera (arrowheads), which was found to be visible in only 43% of participants. Image from Vuong et al. (2016).

In terms of quantifying the choroidal vascular structure itself, there were several approaches that could be taken. The first approach was manual calliper measurement of vessel diameters (Figure 2.10A). Again, these were measured axially for ease of scaling conversions. As an alternative, manual segmentation of the vessels was a possibility (Figure 2.10B), to obtain vessel area, vessel density, and a ratio of vessel to surrounding tissue.

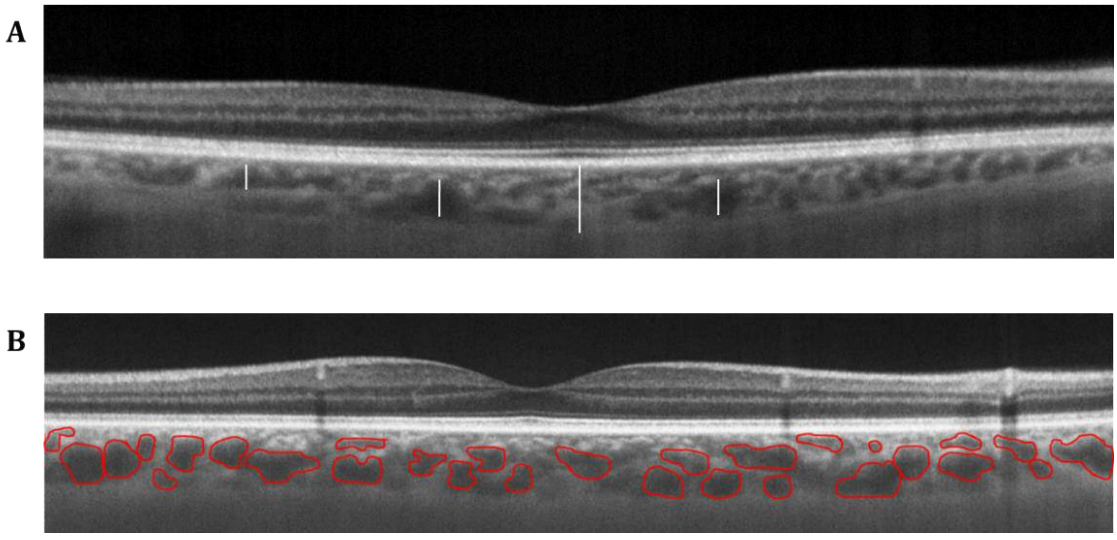

Figure 2.10 Potential manual choroidal parameter measurements. (A) Calliper measurements; subfoveal choroidal thickness (longest white line) and vessel diameters (three shorter white lines). (B) Hand segmentation of the vessel lumen.

Another approach was to use the enface view for quantification, providing visualisation of a fixed depth across the choroid simultaneously. Again, calliper measurements or hand segmentation could be used, yielding similar parameters to those discussed previously. Alternatively, thresholding techniques could be applied to binarise the images (Figure 2.11). The ratio of black to white (i.e. vessel lumen to surrounding tissue) could then be established with image processing software, and provide an output representative of the entire choroid at a single plane of set depth in the choroid. This limited potential misrepresentation through sampling individual vessels.

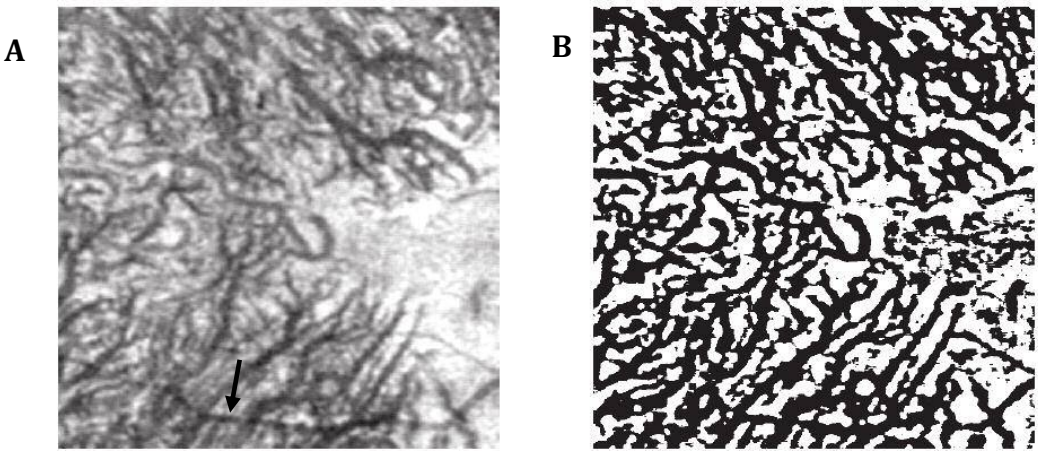

Figure 2.11 Example of an enface image of choroidal vessels (A) and the same image having undergone binarization using thresholding techniques (B). Note the artefact from an overlying retinal vessel (arrow). Image from Duan et al. (2013).

2.4.2 Limitations of manual measurements

Whilst these manual techniques are simple and easy to apply, they are associated with significant limitations. The choroid is a 3-D dense vascular network, however only a 2-D section through this structure is visualised in each tomogram. Therefore these images lack perspective of the angle at which any given vessel has been 'sectioned'. If vessels are sectioned obliquely, a true vessel cross-section is not visible, although it may have a similar shape (see Figure 2.12). Vessel diameters will tend to be over-estimated using this method.

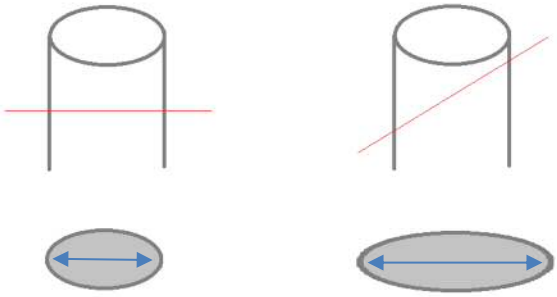

Figure 2.12 The angle at which a vessel is bisected (red lines) has a great effect on the resulting apparent vessel 'diameter' (blue arrows). Without knowledge of the directionality of the vessel relative to the 2-D plane being viewed, it is difficult to ensure appropriate measurement.

Furthermore, from a 2-D section in isolation it was not possible to assess whether the apparent cross-section is simply a segment through an arching vessel (see Figure 2.13). Unlike the retina, the choroidal structure varies greatly between individuals. There is no regular structure akin to retinal layers, and the blood vessels do not appear to follow set patterns like that of the vascular arcades supplying the inner retina. It was therefore not possible to select a corresponding vessel on each individual, and there was no simple way to ensure that sampled vessels were representative of the entire choroid. The use of enface images addressed this limitation in-part, by encompassing all vessels at a predetermined depth below the RPE. However, these were still 2-D samples of the volume, and in addition suffered from other limitations such as artefacts from overlying structures (e.g. retinal blood vessels as demonstrated in Figure 2.11).

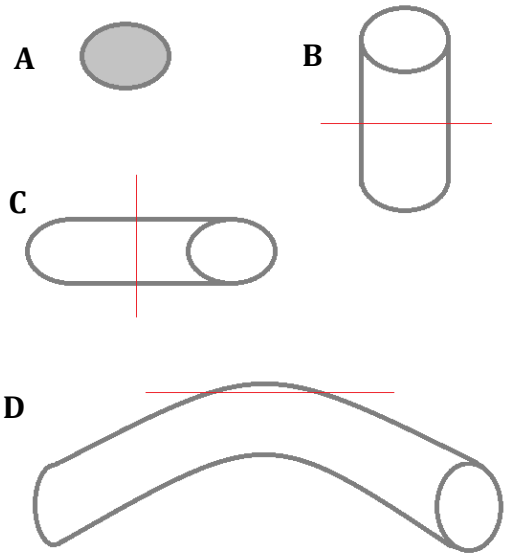

Figure 2.13 Without perspective from surrounding slices, a 2-D vessel section (A) can arise from bisection of a vessel of unknown directionality (B and C), or a section through an arching vessel (D). The red lines indicate the plane at which the vessel in each example could be bisected to produce a similar 2-D luminal shape.

To minimise the impact of these issues, established histological techniques often utilise sampling approaches, for example, averaging measurements across multiple vessels. Although this usually improves measurement repeatability, the method of vessel selection is still associated with known limitations of sampling, including potential bias and misrepresentation. To overcome these limitations, the entire choroidal volume within the scan region should be included in the analyses. However, averaging techniques used to reduce noise are limited (e.g. Z-projection), and the individual b-scans remain relatively noisy. In similar cases, texture analysis has previously been used to extract information in an attempt to quantify structure (Koprowski et al. 2013; Srinivasan 2014b; Albarrak et al. 2016).

Finally, as with the majority of manual quantification techniques, the measurements described here are time-consuming, and can inherently suffer from significant inter- and intra-observer variability. This greatly limits the potential clinical value of such measurements. To overcome these limitations, the employment of automated analysis methods should be considered. As discussed in Section 1.7.3, machine learning techniques are a powerful tool for this type of analysis (see Chapter 5).

2.5 Optimising scan parameters and protocols

When collecting data of this type, a protocol must be established detailing the parameters of the images acquired. This ensures consistency within the dataset, and optimises the dataset for the purpose for which it was collected. These parameters include (but are not limited to) scan angle, a-scans per b-scan, b-scans per volume, and number of repeat images acquired. In addition, the higher the power of the light source in the imaging device, the better the image quality. For safety reasons however, power output must be capped at a pre-defined level for ocular imaging (ANSI 2000; ICNIRP 2013). The following section outlines pilot studies undertaken for parameter selection and imaging protocol development, including investigations of image sampling and light source power.

2.5.1 Pilot study 1: Effect of lateral sampling on choroidal vessel visualisation

2.5.1.1 Background

Although long-wavelength OCT allows visualisation deeper into the choroidal structure, contrast of this region is often limited due to signal roll-off. One potential method to increase visualisation is to increase the sampling density of the scan (i.e. increase the number of a-scans per unit area of choroid), and thus utilise the full optical resolution of the device. Increasing the number of a-scans per b-scan, and b-scans per volume would have this effect, but would also greatly increase the image acquisition time. Therefore, reducing the scan angle would be the preferable option to achieve this.

The theoretical resolution limit of this non-commercial OCT system is ~6 μm. This is inherent to the optics of the human eye, and will be the limiting factor of image resolution for images with sampling exceeding this level (i.e. over-sampling). If an image is sampled below this limit, image resolution is further limited by the sampling rate; this is called under-sampling. Since a minimum of two adjacent pixels are required to resolve an edge, sampling rate must be at least half the resolution limit to resolve the edge (~3.09 μm/pixel).

A list of sampling rates for a range of scan widths can be seen in Table 2.3, calculated using Equation 2.1, and a standard AEL of 24 mm. The conventional scan size of commercial OCT devices is typically 20° 20° which is substantially under-sampled, limiting the lateral image resolution. The smaller the scan angle, the greater the sampling (i.e. the fewer microns of structure represented per image pixel). Greater degrees of over-sampling allow for more averaging during post-processing without loss of spatial information from the image. However, the limitations of decreasing the scan size are the reduction in number of vessels within the imaging field, and the loss of localisation information. The ideal scan size for visualising the choroidal vasculature would maximise lateral image resolution whilst maintaining a reasonable field of view. Beyond the point where the sampling rate is equal to the theoretical resolution limit of the system (equating to ~5.6° scan width), no further improvement in image quality would be expected, since the resolution is limited by optics of the eye.

Table 2.3 Lateral sampling rates for different sized scans, assuming a scan size of 512 512 pixels of an eye with an AEL of 24 mm. The sampling rate approximately equal to half the theoretical resolution of the imaging system is highlighted in grey.

Scan width (°)	Lateral sampling rate (µm/pixel)	Under/over sampled?
20	11.33	Under
10	5.66	Under
9	5.10	Under
8	4.53	Under
7	3.97	Under
6	3.40	Under
5.6	3.09	Equal
5	2.83	Over
4	2.27	Over

The aim of this study was to demonstrate the effects of lateral sampling, and to investigate the extent to which these effects impact OCT image quality. To achieve this, images with a range of scan sizes underwent both objective and subjective image quality analysis. The scan sizes assessed represented images with a lateral sampling rate close to the theoretical resolution limit of the device (from Table 2.3). Three observers familiar with OCT images were enrolled to grade image quality based on pre-defined criteria. The agreement between observers was assessed to ensure grading consistency.

2.5.1.2 Methods

Participants

Young, healthy participants (n=9) were recruited for this study from staff, students, and volunteers at the School of Optometry and Vision Sciences, Cardiff University. Mean age (±SD) was 25.9 ± 2.8 years. AEL was measured using an average of 5 readings from an IOLMaster (Carl Zeiss, Jena, Germany). Mean AEL and refractive error (mean sphere) were 24.7 ± 1.8 mm and -2.00 ± 2.77 D respectively. All participants had visual acuity of 0.1 logMAR (6/7.5) or better.

Image acquisition and preparation

Each participant underwent long-wavelength OCT imaging of the right eye. 512 512 macular volume scans were obtained, for scan sizes from 8° 8° to 4° 4°, in 1° intervals. In addition, 512 512 macular volume scans of 20° 20° visual angle were acquired (the clinical standard; to be used for reference only). Participants did not undergo pupil mydriasis, and all images were acquired under minimal room lighting.

Following conversion from spectral data to image data, a predetermined set of processing steps were followed to prepare the images for assessment (see Figure 2.14). This included vertical cropping and stack registration, as described in Section 2.3.2. To enable visualisation of both the large- and medium-sized choroidal vessels in this task, depths of 75% and 50% of the choroidal thickness beneath the foveal pit were isolated. An area was selected with a height of 5 pixels and the full width of the scan, centred on each of the two depths, and resliced to produce two enface views of 5 consecutive slices each. A convolving filter was applied to reduce speckle, using a 3 3 kernel of equal weighting. Each set of 5 slices were then averaged using

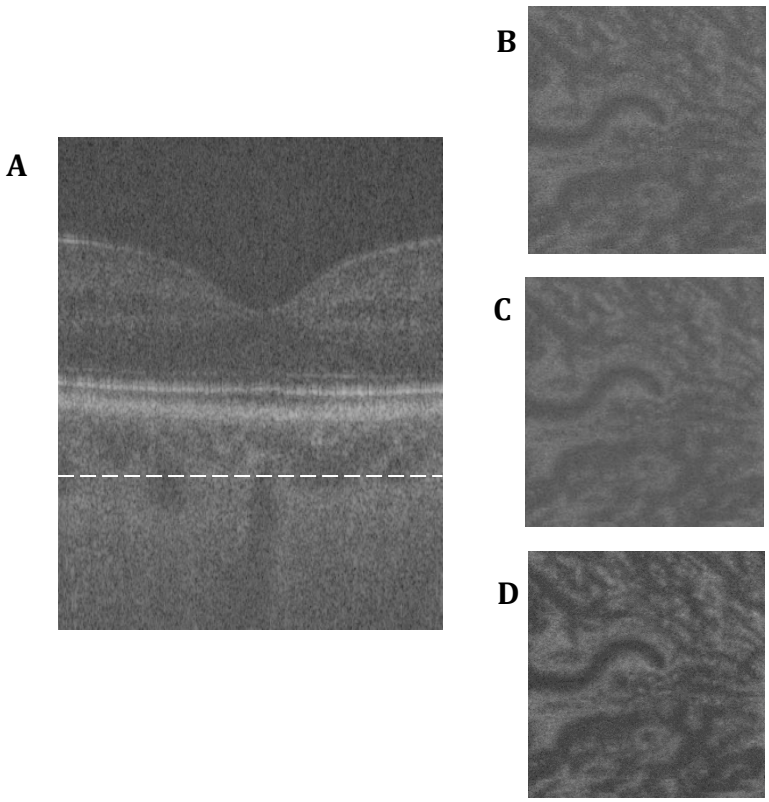

Figure 2.14 Image processing protocol. (A) A single b-scan through the foveal pit, with minimal processing, showing 75% depth in the choroid (dashed line). (B) Enface view of the choroid at this depth. (C) Convolving blur applied to the enface view. (D) Average of 5 consecutive images in the stack with convolving blur, and adjusted brightness.

Z-projection, and the resulting images were converted to 8-bit to allow manual adjustment of brightness, to subjectively maximise visibility of the choroidal vessels. The result was two enface images, at 75% and 50% choroidal depth respectively. Image contrast was not adjusted, as it was to be used as one of the quality grading criteria.

It was important to consider the effects of image magnification during presentation. It was likely that a more 'zoomed out' image (i.e. the wider scans), would be perceived as better quality, due to the presence of more vessels, and the lack of visibility of smaller vessels, which may be masked by background noise. To control for this effect, the central 3° of each image was isolated, and scaled to 410 410 pixels (the number of pixels in the 4° image following cropping to 3°). A size of 3° was selected to prevent bias from identification of the true 4° scans by the presence of misalignments surrounding the image caused by the stack registration process. Images were scaled up in size rather than down to prevent pixel averaging that may artificially improve perceived image quality. An example is shown in Figure 2.15. During presentation for grading, the screen resolution was set such that images were presented over 410 410 screen pixels, removing the possible effects of aliasing (spatial sampling of pixels during image presentation).

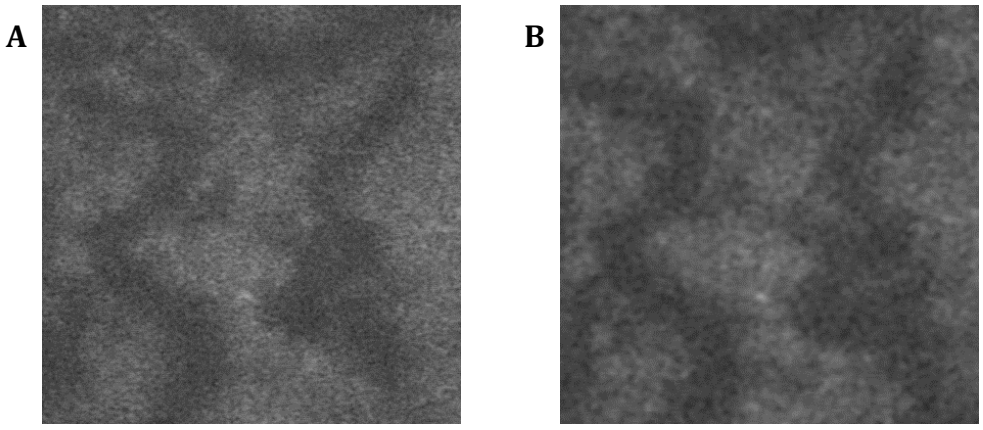

Figure 2.15 The same area of choroid sampled at 75% depth, imaged using (A) 4° and (B) 8° scanning protocols. The central 3° of visual angle of each image has been cropped and scaled to 410 410 pixels. The 8° scan has a more pixelated appearance, and the extent of over-sampling of the 4° scan is evident when comparing the perceived quality of the images.

Grading protocol

Three independent observers who were masked to the images and were not involved in the collection of the images were used for grading image quality. These

were experienced optometrists familiar with viewing similar ophthalmological images. A total of 45 enface choroidal OCT images at 75% depth (5 scan widths per eye) were presented three times each in a random order (135 presentations in total). In cases where two identical images were randomised into consecutive order, the latter image was swapped with the following image.

The graders were provided with simple instructions (see Appendix C) a day prior to the grading sessions, to familiarise themselves with the protocol. The grading session began with a training session, in which 5 test images with a variety of image qualities were presented. The graders were encouraged to record a grade for these images, although these results were not included in the analysis. These test images were collected from the fellow eye of a subset of participants, and hence were not included in the main presentation, but were of similar quality for training purposes.

Graders were given unlimited time to record grades for two criteria; overall contrast of the image, and edge definition of the vessels (described below). Graders were not permitted to return to previous images once they had been graded. Both criteria were graded on a 5-point scale (Ludewig et al. 2010), as follows:

1. Poor
2. Restricted
3. Sufficient
4. Good
5. Excellent

The overall contrast of the image was graded according to the difference in luminance between the vessel lumen and surrounding tissue. Edge definition was based upon the apparent luminance profile, with a distinct edge receiving a higher grade. Diagrammatic examples, which were included in the grading instructions, are shown in Figure 2.16.

This entire process was repeated for the 50% depth images on a different day, to minimise fatigue effects. The same computer monitor was used by the three graders on both days to ensure consistent image presentation, and negating the need for monitor calibration.

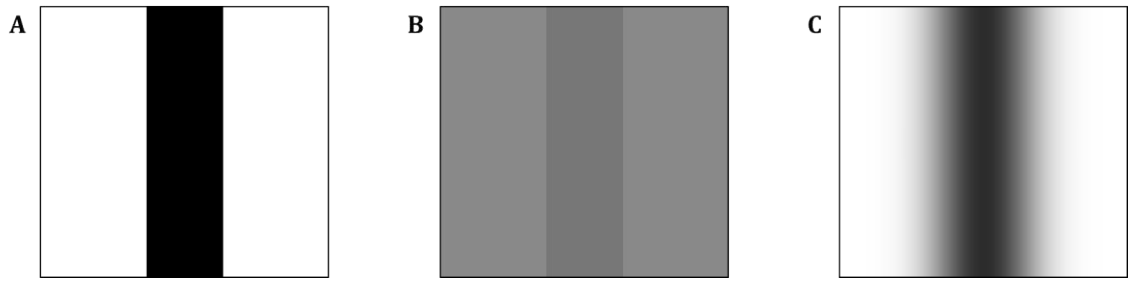

Figure 2.16 Schematics demonstrating both criteria: (A) optimum image quality, Grade 5; (B) low contrast; (C) low edge definition.

Objective quality assessment

As an objective measure, the number of misalignments due to image registration failure were counted for each unscaled image at 75% choroidal depth. This was not repeated at 50% depth, as the number of misalignments would be consistent at any depth. Due to the size of the larger vessels, misalignments were likely to be more evident at 75% depth. Misalignments were classed as visible horizontal lines of poor continuity in the enface view (Figure 2.17). This was carried out independently of the subjective quality grading, by a single observer who was masked to the randomised images.

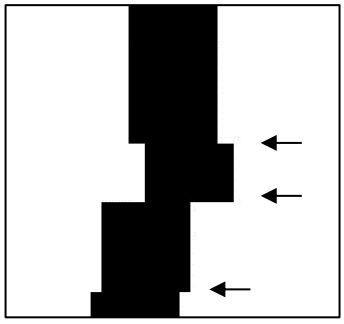

Figure 2.17 Schematic demonstrating poor continuity in an enface image, due to 'failings' of the stack registration process. Each arrow indicates one misalignment.

Statistical analysis

The data were checked for normality using a Shapiro-Wilk test ($P>0.05$). A repeated measured ANOVA was used to determine whether the differences in subjective grades between the scan sizes were statistically significant ($P<0.05$). A post-hoc Bonferroni correction was applied to ascertain where the significant differences were, at a 95% significant level. Where normality could not be assumed

(Shapiro-Wilk P≤0.05), a Friedman test was used, with a post-hoc Wilcoxon signed ranks test.

To assess observer repeatability and inter-observer agreement, single measures intra-class correlation coefficients (ICC) were calculated. These coefficients were interpreted as follows: 0.01-0.2, slight agreement; 0.21-0.4, fair agreement; 0.41-0.6, moderate agreement; 0.61-0.8, substantial agreement; >0.8, almost perfect agreement (Landis and Koch 1977).

2.5.1.3 Results

Subjective assessment

The mean subjective image quality results from the three graders can be seen in Table 2.4. For 75% choroidal depth, smaller scan angles were generally associated with higher grading scores for contrast and edge definition of the vessels. The mean scores for edge definition were consistently poorer than contrast. For the 50% choroidal depth, there was no obvious association between scan angle and subjective image quality. For both grading criteria, inter-observer variability was similar for each of the scan sizes, and there was a similar level of variability for each of the criteria (Figure 2.18). However, there was a higher degree of inter-observer variability for both criteria at 50% depth than at 75% depth (as represented by the error bars).

Table 2.4 Mean subjective image quality grade (1=poor; 5=excellent) for images of varying scan size, by three observers.

Scan size (°)	**Mean image quality grade**			
	Overall contrast		*Edge definition*	
	75% depth	*50% depth*	*75% depth*	*50% depth*
4	2.77	2.47	2.74	2.36
5	2.53	2.38	2.43	2.36
6	2.54	2.53	2.26	2.58
7	2.31	2.44	2.07	2.40
8	2.21	2.41	1.88	2.04

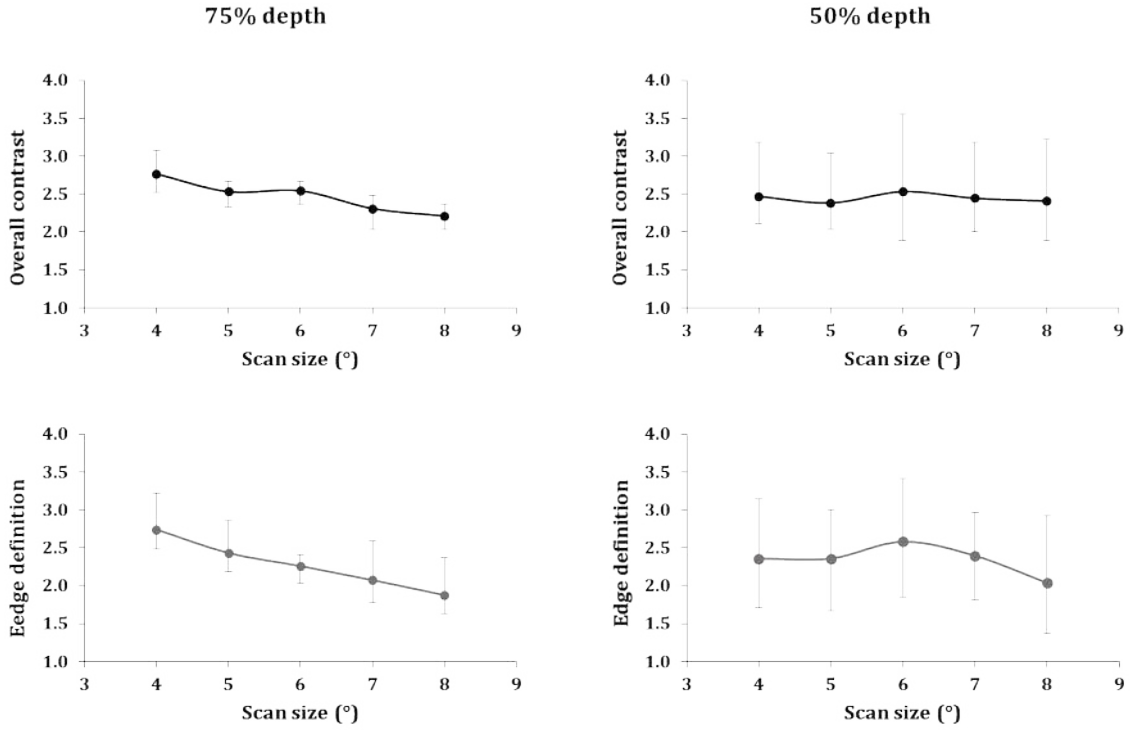

Figure 2.18 Mean grades (1=poor; 5=excellent) for varying scan sizes. Mean data from the three independent observers is presented at 75% and 50% depth, for both grading criteria. Error bars represent the range of grades assigned by the three observers.

For 75% choroidal depth, a repeated measures ANOVA determined that the difference in mean contrast grade between scan sizes was statistically significant ($P<0.05$). With Bonferroni correction, a difference in contrast grade was found only between the 4° and 8° scans. Since normality could not be assumed for edge definition grades (Shapiro-Wilk, $P < 0.05$), a Friedman test was used. A post-hoc Wilcoxon signed ranks test identified a significant difference between all sizes, with the exception of consecutive sizes, e.g. 4° and 5° (Table 2.5). For 50% choroidal depth, a repeated measures ANOVA determined that there were no significant differences in the contrast and edge definition grades for different sized scans ($P=0.926$ and $P=0.252$, respectively).

Table 2.5 Pairwise comparison of mean grades of contrast (black) and edge definition (grey) at 75% depth, following a repeated measures ANOVA with post-hoc Bonferroni correction, and a Friedman test with post-hoc Wilcoxon signed ranks test, respectively. The significance values for each comparison are included in the table.

Scan size (°)	4	5	6	7	8
4	-	0.656	0.905	0.193	0.029*
5	*0.106*	-	1.000	0.338	0.649
6	*0.024**	*0.398*	-	0.440	0.127
7	*0.012**	*0.049**	*0.271*	-	0.440
8	*0.012**	*0.012**	*0.018**	*0.271*	-

***significant at the 0.05 level**

Statistical analysis showed substantial to almost perfect intra-observer agreement for all three graders at both choroidal depths (Table 2.6). At 50% depth, edge definition grades had a higher consistency than contrast grades for all observers, however at 75% depth this was only substantial for Grader 2. Inter-observer agreement was almost perfect for both grading criteria at 75% depth, and substantial for both criteria at 50% depth (Table 2.7).

Table 2.6 Intra-class correlation coefficient (ICC) for intra-observer consistency in both grading criteria, for both choroidal depths.

Grader	Intra-class correlation coefficient			
	Overall contrast		*Edge definition*	
	75% depth	*50% depth*	*75% depth*	*50% depth*
1	0.846	0.794	0.850	0.888
2	0.652	0.623	0.813	0.758
3	0.728	0.698	0.740	0.719

Table 2.7 Intra-class correlation coefficient (ICC) for inter-observer consistency between the three graders in both grading criteria, for both choroidal depths.

Intra-class correlation coefficient			
Overall contrast		*Edge definition*	
75% depth	*50% depth*	*75% depth*	*50% depth*
0.859	0.774	0.860	0.800

Objective assessment

The largest scans had, on average, 2.8 ± 2.5 misalignments, compared to 5.7 ± 3.2 for the smallest scans (Table 2.8). Scans ≥6° in size demonstrated less variability in the number of misalignments (failure of image registration) between individuals, as shown by the error bars in Figure 2.19.

A repeated measures ANOVA determined that mean number of misalignments differed significantly between scan sizes ($P<0.05$). However, with Bonferroni correction, no statistically significant differences were found in the number of misalignments between any of the scan sizes. Least significant difference adjustment was then applied, producing statistically significant differences at a 95% significance level in the number of misalignments between 4° and 6°, 4° and 7°, 4° and 8°, 5° and 7°, and 5° and 8° scans (Table 2.9).

Table 2.8 Number of misalignments per image for each participant (A-I), for a single observer.

Scan size (°)	Number of misalignments									Mean	Standard deviation
	A	*B*	*C*	*D*	*E*	*F*	*G*	*H*	*I*		
4	4	9	6	8	2	2	10	2	8	5.7	3.2
5	4	4	6	8	1	0	9	1	13	5.1	4.3
6	5	4	4	5	0	2	5	0	6	3.4	2.2
7	2	3	5	3	2	0	3	0	7	2.8	2.2
8	3	2	4	6	0	0	2	1	7	2.8	2.5
Total	18	22	25	30	5	4	29	4	41		

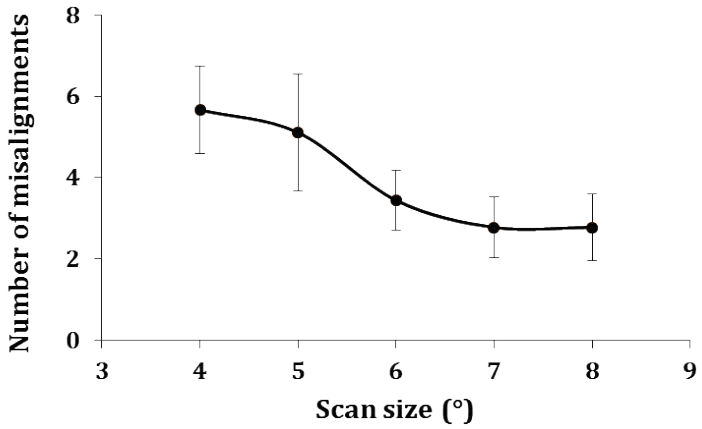

Figure 2.19 Mean (± SE error bars) number of misalignments of image registration for various scan sizes. Smaller scan sizes result in a higher average number of misalignments in the stack registration software.

Table 2.9 Pairwise comparisons of number of misalignments, following a repeated measures ANOVA with post-hoc least significant difference adjustment (equivalent to no correction). Post-hoc Bonferroni correction shown in grey boxes (italics). The significance values for each comparison are included in the table.

Scan size (°)	4	5	6	7	8
4	-	0.540	0.010*	0.008*	0.012*
5	*1.000*	-	0.105	0.029*	0.023*
6	*0.100*	*1.000*	-	0.282	0.242
7	*0.080*	*0.294*	*1.000*	-	1.000
8	*0.117*	*0.232*	*1.000*	*1.000*	-

***significant at the 0.05 level**

2.5.1.4 Discussion and conclusions

For 75% choroidal depth, wider scan angles were associated with poorer subjective image quality on both criteria assessed. This indicates that an increase in sampling rate (i.e. a smaller scan), provides higher perceived image quality. At 50% depth, no significant association was found between subjective image quality and scan size, potentially due to crowding effects caused by a higher density of vessels per image (i.e. higher spatial frequency). This may be perceived as a less prominent 'background' in the image, arising from a higher ratio of vessel lumen to surrounding tissue at this depth (Figure 2.20). Furthermore, it is more likely that at this depth, some smaller vessels may not be resolved due to the optical limits of the OCT, resulting in a perceived increase in noise in the image background. This may also have the effect of lowering the background luminance, reducing the perceived contrast of the image. High frequency noise (inherent to this imaging technique) likely reduced the ability of the observer to appreciate differences in image quality between the scan sizes, which may explain the findings at 50% choroidal depth, where the typical feature size (i.e. vessel size) was smaller.

The number of vessels visible in the smaller scans was relatively low, particularly when factoring in patient misalignments and the parts of the image lost to the stack registration process. Furthermore, image acquisition was more difficult for the smaller scans, due to limited field of view when aligning the imaging system.

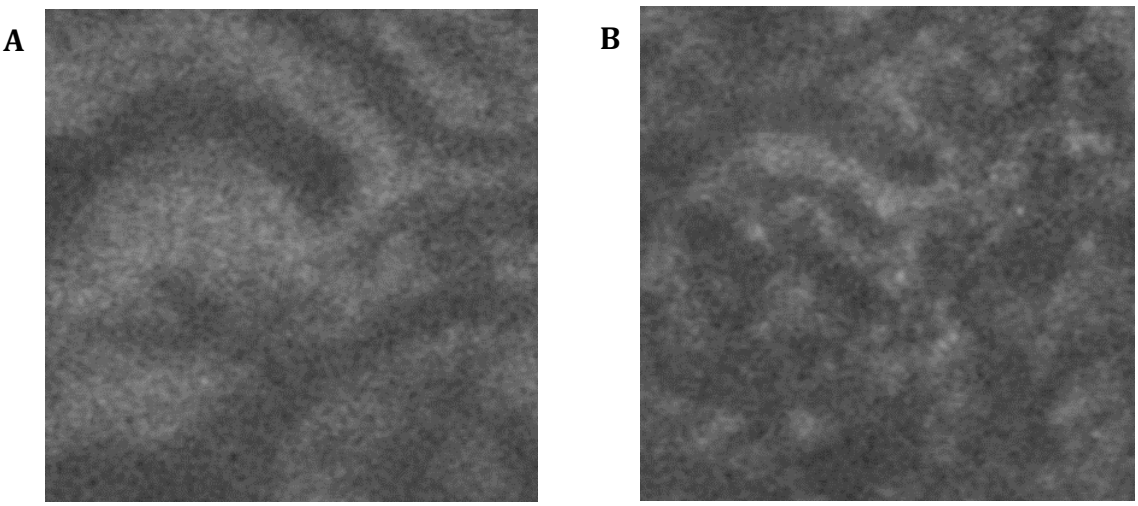

Figure 2.20 The same 7° scan sampled at (A) 75% depth, and (B) 50% depth. The image at 50% depth has a higher vessel density, and a higher apparent ratio of visible lumen to background.

For the objective analysis, scans ≥6° in size demonstrated more consistent stack registration. Statistical analysis revealed significantly fewer misalignments in 6° images when compared to smaller images, whilst no further improvement beyond this was identified ($P<0.05$). With a Bonferroni correction however, these differences were not significant. The 7° and 8° images displayed a similar number of misalignments due to stack registration as the 6° images. These results suggested that an image of 6° or greater was optimal for minimising the number of misalignments due to stack registration. This was consistent with the expectations of stack registration, since images of a smaller area of choroid were likely to have fewer similar features between b-scans, and were therefore more prone to registration failures.

Statistical analysis showed strong intra-observer agreement for each of the three graders. When comparing the grades from the three observers, both grading criteria showed near-perfect agreement. This consistency allowed more confidence in the reliability of the results produced by the graders.

The use of a 5-point grading scale is a potential limitation. This allowed for grader indecisiveness i.e. assigning a grade of 3. A forced choice grading scale (e.g. a 4-point or 6-point scale) may have eliminated any effects of this central-tendency bias. A 4-point scale may not have provided a spread of data wide enough to distinguish between images of reasonable and good quality, so a 6-point grading scale may have been preferable. However, other studies have defended the use of 5-

point grading scales similar to the one used in this study, such as the well-established Likert scale (Likert 1932; Ludewig et al. 2010).

Overall, larger vessels had higher subjective image quality with a higher sampling rate (i.e. smaller scan size) in terms of contrast and vessel definition. Although this subjective difference was statistically significant, it was small and unlikely to be clinically significant. For smaller vessels, there was no difference between any of the scan sizes, suggesting that different imaging protocols were not required for visualising vessels of different sizes.

Considering all the findings of this pilot study, a medium-sized scan equivalent to the theoretical resolution limit of the imaging system (~6°) would be optimal to balance optimal subjective image quality with field of view, whilst minimising misalignments of the stack registration software. The 6° scan size had the additional benefit of ease of alignment during image acquisition, whilst maintaining the majority of the perceived benefits related to over-sampling.

In summary, this pilot study has demonstrated the effects of image sampling on perceived image quality, with the optimum scan size found to be 6°. The clinical standard for volume scans is 20° 20°, and the majority of commercial devices do not allow absolute flexibility in scan size (typically limited to a handful of pre-set specifications). Furthermore, the macula is defined clinically as the central 6 mm centred on the fovea, which approximately equates to the central 20° of visual angle. It is possible that scans smaller than this may fail to represent the clinical appearance of macular pathology, as defined by clinical classification systems (AREDS 2001a). For these reasons, the standard 20° scan angle will be primarily utilised in this thesis. However, since these images are under-sampled, 36° line scans comprising 4096 pixels will also be used to provide an over-sampled image, with a wide field of view. A comparison of these two types of image for quantifying the choroidal vasculature can be found in Section 3.2.

2.5.2 Pilot study 2: Light source power output

2.5.2.1 Background

Another variable which has a direct effect on image quality is the power output of the imaging light source. Typically, the higher the power output, the better the image quality. However, this is limited by guidelines outlined by the International Commission on Non-Ionizing Radiation Protection (ICNIRP 2013) and the American National Standards Institute (ANSI 2000), which describe the safety standards for ocular exposure to a laser beam of a given wavelength, assuming a pupil size of 7 mm.

A change in the power output of the light source could directly affect both the penetration depth and the relative intensity of the structures imaged (Drexler and Fujimoto 2008). To ensure consistency between OCT images, particularly for the purpose of comparison, it was important that the imaging parameters and conditions remained as similar as possible between imaging sessions. Consequently, it was deemed necessary to investigate the power output characteristics of the light source within the long-wavelength OCT system over time. Any trends or variations in the power output may be taken into account when establishing the imaging protocol, to maximise the reliability and repeatability of the images.

2.5.2.2 Methods

A handheld PM100D energy meter (Thorlabs, Newton, NJ) was used to measure the power output of the long-wavelength OCT light source over a 5 hour period. The initial measurement was taken following light source activation and completion of the system self-calibration (lasting approximately 90 seconds). Measurements were obtained at a distance of 30 mm from the anterior surface of the OCT system's objective lens, as this is the approximate distance between the instrument and the patient's eye during image acquisition. A subsequent measurement was obtained every 5 minutes for 150 minutes (2.5 hours), at which stage the measurement frequency was reduced to 30 minute intervals for a further 150 minute period. The power output was assessed over a 300 minute period (5 hours), since this was the upper limit of likely use per day throughout this research.

For safety reasons, the imaging beam was blocked at the objective lens using an infra-red card between readings, in line with the standard operating procedures of the device, and ethical approval. A control measurement was also taken with the

equipment *in situ*, with the infra-red card blocking the beam. The detector of the meter was set to measure the power output at 1040 nm; the wavelength of the light source. Room lighting was minimal, to mimic the conditions of image acquisition.

2.5.2.3 Results

Following initialisation of the light source, a steep decline in power output was observed over the first 30 minutes. The rate of decline then slowed over the subsequent 20 minutes, until reaching an equilibrium at around 70 minutes (Figure 2.21). The power output did not fluctuate after this point.

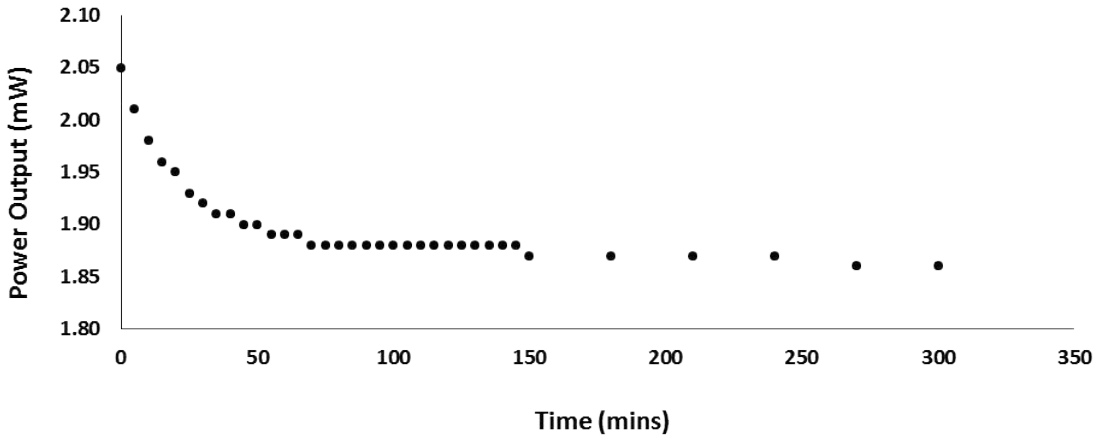

Figure 2.21 The power output of the long-wavelength OCT light source declined steeply over a 30 minute period following initialisation (Time = 0), after which time it stabilised.

2.5.2.4 Discussion and conclusions

As the light source power output declined most steeply during the first 30 minutes, imaging should be avoided during this period. Although images obtained during this period would have a greater reflectivity and appear to be of 'better quality', they would not be directly comparable to images collected after this period, due to intensity change. After this initial 'warming up' period, the change in power output was minimal over the following 4 hours.

Furthermore, all power measurements were within the recommended safe levels for a light source at 1040 nm (2.5 mW of continuous corneal irradiance; ANSI 2000). As long as this limit is observed, this light source is safe for imaging human participants.

To conclude, all imaging protocols in this thesis included a 30 minute latency period following light source activation, prior to image acquisition. This minimised variation between imaging sessions attributed to power output of the imaging light source.

2.5.3 Image acquisition and processing summary

The aforementioned image acquisition, processing and potential analysis protocols are summarised in Table 2.10. The image acquisition protocols for use in this research have been described, including the imaging system and scan parameters. A series of image processing steps have been defined, but are dependent on the structure or parameter to be investigated. With regard to image analysis, a number of limitations of conventional analysis methods, such as manual calliper measurements, have been outlined. An evaluation of such parameters is conducted in Section 3.2. A machine learning approach to analysis with potential to overcome these limitations is developed and validated in Chapter 5.

Table 2.10 Summary of the image acquisition, processing, and potential analysis protocols used in this research. Protocols requiring further investigation are discussed in Chapter 3.

Variable	**Protocol**
Imaging system	1040 nm non-commercial OCT
Scan size	20° 20° (512 512 1024 pixels) 6° 6° (512 512 1024 pixels) 36° (4096 1024 pixels)
Number acquired	3 repeat images of each type
Initialisation time	30 minutes
Pupil size	≥ 5 mm (mydriasis with 0.5% Tropicamide)
Image pre-processing protocol	See flowchart in Figure 2.2 Series of image pre-processing steps (white rectangles) that all scans acquired with the 1040 nm OCT device underwent. Blue rhombi represent image types; green rhombi represent outcome measure categories, and the section in which they are investigated is specified.
Choroidal parameters (to be developed)	Choroidal thickness (digital calliper) Vessel diameters (digital calliper) Percentage vessel lumen (thresholding) Choroidal volume (automated segmentation) Automated texture analysis (machine learning)
AMD disease clinical classification	Adapted protocol required

3 Evaluation of analysis techniques

A number of parameters for describing the choroid and the choroidal vasculature have previously been described (see Section 1.7). The majority of the literature evaluating these parameters used images acquired with conventional-wavelength (~850 nm) OCT devices. This chapter evaluates several of these parameters on images from a non-commercial long-wavelength (~1040 nm) OCT device, as well as introducing a novel parameter to quantify the vessel structure. All studies conducted here were on healthy eyes, to establish the repeatability of parameter measurement prior to application in disease. The importance of ocular biometry for lateral scaling of OCT images is also explored.

3.1 Effect of lateral scaling on OCT quantification

The transverse size of any retinal or choroidal feature in an OCT image can be calculated using the appropriate ocular biometry and instrument meta-data (Littmann 1982; Bennett et al. 1994). The following describes a study investigating the importance of lateral scaling considerations for quantifying OCT images.

3.1.1 Background

Commercial OCT devices are generally manufactured with on-board retinal layer segmentation software. Contemporary software is commonly limited to retinal thickness and a small number of intra-retinal layers, and is almost universally restricted to use on images acquired by the parent device. Furthermore, on most contemporary OCT devices (e.g. Topcon 3D OCT-1000, and Zeiss Cirrus HD-OCT), this software does not make lateral scaling compensation for ocular biometry (i.e. AEL). Differences in the definition of the posterior retinal boundary, along with the diversity of segmentation methods, also makes quantitative comparisons between the devices difficult.

The Iowa Reference Algorithms (Retinal Image Analysis Lab, Iowa Institute for Biomedical Imaging, Iowa City, IA) are a publically available, graph theory-based

approach to 3-D segmentation of the retinal layers in spectral domain OCT images (Garvin et al. 2009; Abràmoff et al. 2010; Antony et al. 2011). The software has previously been shown to be capable of identifying 7 retinal layer boundaries, providing results comparable to hand segmentation by two ophthalmologists (Garvin et al. 2009). OCT Explorer version 3.5 is capable of segmenting 10 intra-retinal layers in addition to providing conventional retinal thickness values (inner limiting membrane (ILM) to RPE). These algorithms have been shown to generate layer thicknesses, comparable to a retinal specialist, in healthy participants using Cirrus HD-OCT 5000 images (Lee et al. 2010). Furthermore, it has been shown to produce comparable results to the on-board Spectralis OCT software on images from participants with diabetic macular edema (Sohn et al. 2013).

A lateral scaling factor for any OCT image can be determined using:

(i) An estimate of the retina to principal plane (a hypothetical plane at which all the refraction in the lens system can be considered to happen) distance, taken as AEL minus 1.6 mm for the purposes of this study (representing the cornea to principal plane distance, from Gullstrand's exact schematic eye; Bengtsson and Krakau 1992).
(ii) The scan angle of an image in air.
(iii) An estimate of the bulk ocular refractive index.

The on-board software of two commercial (Topcon and Zeiss) instruments used in this study provide only a single lateral scaling value for all patients regardless of AEL, resulting in an error in the reported size of the image which scales with AEL. This error manifests as a discrepancy between the fixed size ETDRS grid (which does not compensate for AEL) and the AEL-dependent image size. Therefore, the position of retinal layer measurements and hence the regional thickness values become AEL-dependent; an important consideration when comparing different OCT instruments. Converting all image files to a compatible TIFF format allowed input of an independently calculated, AEL-dependent lateral scaling into the Iowa Reference Algorithms, for images from all devices.

The following study had one primary and two secondary aims:

Primary aim:

1) To investigate the importance of biometric considerations and image scaling by comparing the segmentation of the Iowa Reference Algorithms on images from various (conventional and long-wavelength) OCT devices using both fixed-AEL and AEL-dependent scaling.

Secondary aims:

2) To evaluate the inter-session repeatability of the intra-retinal layer segmentation performed by the Iowa Reference Algorithms and the on-board commercial segmentation software, on healthy eyes.
3) To assess agreement in retinal thickness values generated by the Iowa Reference Algorithms and the on-board commercial segmentation software.

Since the primary aim is the most pertinent to this thesis, it will be discussed here in detail. A detailed report addressing the two secondary aims (not directly relevant to this work) can be found in Terry et al. (2016) and Appendix G.

3.1.2 Methods and protocols

Participants

Healthy participants (n=25) were recruited from staff, students and volunteers at the School of Optometry and Vision Sciences, Cardiff University. All participants had a corrected visual acuity of 0 logMAR (6/6) or better using an ETDRS chart and a refractive error (mean sphere) of less than ±6.00 dioptres in the test eye.

Exclusion criteria included: posterior ocular pathology such as age-related macular degeneration and glaucoma; ocular hypertension (>21 mmHg); narrow iridocorneal angles (grade 1 or less assessed by Van Herick); and significant corneal or lenticular opacities (Lens Opacities Classification System III grade 4 or more for any criteria; Chylack et al. 1993). Grade 4 was selected due to the enhanced imaging performance of long-wavelength OCT in the presence of media opacities (Povazay et al. 2007). Participants with systemic conditions including diabetes, uncontrolled

hypertension and neurological disease were also excluded, as were those taking medication known to affect retinal function.

One eye was selected as the test eye for each participant; this was the eye with the better visual acuity (or lower refractive error if one eye was outside the refractive range). An average of 4 IOP measurements were taken using non-contact tonometry (Topcon CT-1), and one drop of tropicamide 0.5% was instilled into the test eye of each participant prior to imaging. Retinal photographs were obtained to ensure participants did not have posterior eye disease. AEL (anterior corneal surface to RPE) was measured using optical biometry (IOLMaster).

OCT imaging

Following mydriasis, all participants underwent OCT imaging using a non-commercial long-wavelength (1040 nm) SD-OCT, a Topcon 3D-OCT 1000, and a Zeiss Cirrus HD-OCT 5000. Imaging undertaken with the long-wavelength OCT was performed below the recommended maximum power limit for a 10 second exposure (less than 2.5 mW at the cornea; ANSI 2000).

Volume scans centred on the fovea were acquired using each device. To allow comparison, all images from the commercial instruments were obtained from a 20° 20° field of view, comprised of 512 128 a-scans, and were acquired by a single trained operator.

Data analysis

The long-wavelength OCT images underwent dispersion correction to convert the raw spectral data (FD1 file format) to logged image data (TIFF file format), using custom software in MATLAB. The images were then exported to Fiji, where they were converted to 8-bit and cropped along the Y-axis to remove artefacts. The images then underwent translational stack registration, and further y-axis cropping to remove artefacts from this process (omitting this step resulted in misidentification of these artefacts as retinal layer boundaries by the Iowa algorithms). The images were then imported to the Iowa Reference Algorithms, along with the images from the two commercial instruments which were unaltered. In addition, the commercial device images were converted to TIFF format using Fiji

and re-imported to the Iowa Reference Algorithms, to allow for manual scaling input.

All OCT images underwent automated retinal layer segmentation using the Iowa Reference Algorithms. Retinal thickness was taken as the distance from the most anterior hyper-reflective line (corresponding to the ILM) to the posterior of the most posterior hyper-reflective line (corresponding to the outer boundary of RPE). Mean thickness values for the retina and 10 intra-retinal layers were obtained for the foveal subfield and the inner and outer rings of a standard ETDRS grid on all images (see Figure 3.1).

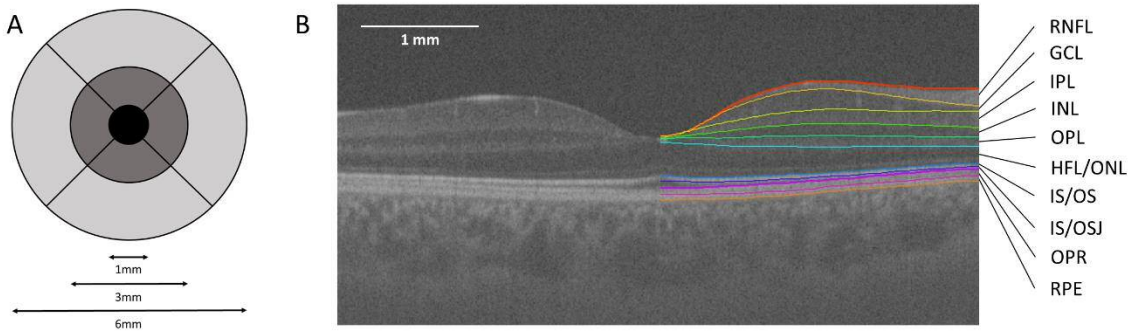

Figure 3.1 ETDRS grid and example 10 intra-retinal layer segmentation. (A) Standard ETDRS grid showing the foveal subfield (black). The inner ring is an average of the four parafoveal subfields (dark grey) and the outer ring of the four perifoveal subfields (light grey). (B) 10 layer (11 boundary) segmentation of a long-wavelength OCT image, produced by the Iowa Reference Algorithms. The left half of the image shows the image prior to segmentation. Image from Terry et al. (2016).
Layers 1-10 (top to bottom; as defined by the software): retinal nerve fibre layer (RNFL); ganglion cell layer (GCL); inner plexiform layer (IPL); inner nuclear layer (INL); outer plexiform layer (OPL); outer plexiform layer-Henle fibre layer to boundary of myoid and ellipsoid of inner segments (HFL/ONL); photoreceptor inner/outer segments (IS/OS); inner/outer segment junction to inner boundary of outer segment photoreceptor/retinal pigment epithelium complex (IS/OSJ); outer segment photoreceptor/retinal pigment epithelium complex (OPR); retinal pigment epithelium (RPE).

For the commercial instruments, the metadata supplied by the manufacturer was used in determining voxel (3-D equivalent of pixel) size, in order to demonstrate the importance of correct lateral scaling. In all other cases, including the long-wavelength OCT images, lateral scaling factors were calculated from the scan angle, AEL and an assumed bulk ocular index of 1.336 (Littmann 1982; Bennett et al. 1994). The axial scaling of each pixel was calculated assuming a mean refractive index of the retinal layers of 1.4, 1.38, and 1.36 for the long-wavelength, Topcon, and Zeiss instruments respectively (Sidman 1957; Terry et al. 2016). These represent the assumptions for refractive index made for each device, and were provided by

the manufacturers of the commercial devices. The percentage differences between the fixed-AEL and AEL-dependent scaled measurements were calculated for the two commercial devices.

The mean differences in total retinal thickness between the commercial devices and the long-wavelength OCT (assumed as ground truth for this analysis) were calculated. This was performed for both fixed-AEL scaling and AEL-dependent scaling for the commercial devices. The relationship between retinal thickness discrepancies of the scaling methods and AEL was evaluated using Spearman's rank correlation.

3.1.3 Results

Twenty-five eyes from 25 participants were included in the study. The mean age of the participants was 34.9 ± 13.5 years (range 20 to 62 years). Sixteen participants were female (64%). The mean AEL and refractive error (mean sphere) were 23.7 ± 1.3 mm (range 21.6 to 26.6) and -0.58 ± 1.93 dioptres (range -4.50 to +3.00) respectively. The maximum cylindrical power was 3.00 dioptres.

Table 3.1 Total retinal thickness measurements (mean ± SD; µm) using AEL-dependent and fixed-AEL scaling (with the exception of the 1040 nm OCT images). The percentage difference between the two scaling methods is shown.

		Fovea	Inner ring	Outer ring
AEL-dependent scaling	1040 nm	270.9 ± 16.8	335.2 ± 17.4	294.0 ± 20.6
	Topcon	284.6 ± 17.0	342.2 ± 18.2	293.2 ± 21.6
	Zeiss	284.8 ± 17.6	347.6 ± 18.3	300.6 ± 21.0
Fixed-AEL scaling	Topcon	281.5 ± 16.9	342.8 ± 18.0	295.2 ± 21.8
	Zeiss	280.8 ± 17.5	347.0 ± 18.0	302.0 ± 21.4
Percentage difference	Topcon	1.1%	0.2%	0.7%
	Zeiss	1.4%	0.2%	0.5%

Mean retinal thickness measurements produced with both scaling methods can be seen in Table 3.1. The images from the long-wavelength device only underwent AEL-dependent scaling, to serve as the 'ground truth' for comparison to the other devices. Correcting for individual AEL with the Iowa Reference Algorithms yielded mean differences of less than 2% in total retinal thickness in all cases, when

compared to the fixed-AEL scaled thickness measurements. This difference was largest in the foveal subfield. In general, the measured retinal thickness was greatest for the Zeiss images, followed by the Topcon, and finally the long-wavelength OCT.

The Iowa Reference Algorithms returned automated segmentation of 10 intra-retinal layers for all images. These values underwent AEL-corrected lateral scaling as described previously. The percentage difference of these corrected values from the fixed-AEL scaling values ranged from -15% to +26% (corresponding to Topcon GCL layer/Zeiss RNFL, and Zeiss GCL layer respectively, both in the foveal subfield; Table 3.2).

Table 3.2 Mean thickness (µm) of 10 intra-retinal layers produced by segmentation using the Iowa Reference Algorithms with AEL-dependent scaling. Percentage difference from fixed-AEL scaling shown in italics, to the nearest percentile (commercial devices only). The largest percentage differences are highlighted in grey.

Layer	Fovea			Inner ring			Outer ring		
	Topcon	**Zeiss**	**1040 nm**	**Topcon**	**Zeiss**	**1040 nm**	**Topcon**	**Zeiss**	**1040 nm**
RNFL	7.0 *-7%*	5.9 *-15%*	5.2 -	25.5 *0%*	25.2 *0%*	24.2 -	39.3 *-9%*	40.9 *-7%*	39.3 -
GCL	17.0 *-15%*	13.4 *26%*	17.2 -	48.5 *0%*	52.4 *1%*	50.5 -	24.7 *3%*	27.2 *7%*	29.3 -
IPL	29.3 *1%*	27.5 *-4%*	24.4 -	42.5 *1%*	40.7 *-2%*	39.9 -	35.3 *3%*	37.3 *0%*	36.0 -
INL	17.7 *-10%*	22.5 *-4%*	18.9 -	37.8 *-1%*	43.2 *-1%*	37.5 -	28.1 *0%*	32.9 *1%*	29.6 -
OPL	23.0 *3%*	20.7 *0%*	20.3 -	29.6 *1%*	28.0 *0%*	30.0 -	26.2 *2%*	24.1 *2%*	28.4 -
OPL-HFL ~ BMEIS	120.8 *0%*	122.3 *0%*	116.5 -	95.5 *1%*	96.9 *1%*	90.3 -	79.7 *1%*	79.4 *1%*	71.6 -
IS/OS	13.9 *0%*	11.7 *0%*	14.8 -	12.6 *2%*	10.3 *1%*	13.7 -	12.5 *-1%*	10.2 *-1%*	13.0 -
IS/OSJ ~ IB_RPE	17.0 *1%*	19.7 *1%*	17.3 -	11.7 *0%*	14.0 *0%*	12.6 -	10.3 *0%*	15.5 *-2%*	15.8 -
OPR	20.1 *-1%*	20.7 *-1%*	20.6 -	19.8 *1%*	21.3 *0%*	20.7 -	18.5 *1%*	17.8 *2%*	15.2 -
RPE	18.6 *1%*	15.5 *0%*	15.6 -	18.6 *0%*	15.5 *-1%*	15.5 -	18.6 *-1%*	15.3 *-1%*	15.5 -

Discrepancies in fixed-AEL scaled retinal thickness measurements between the commercial and long-wavelength devices showed a strong correlation with AEL, for the commercial instrument data, in both the foveal subfield and the outer ring (Spearman rank $\rho>0.50$, $P<0.05$ in all cases), although only moderate to weak for the inner ring (Spearman $\rho<0.50$). In all cases, the correlation was reduced to an insignificant level when the AEL-dependent scaling was used in the comparisons between data from the three devices (Figure 3.2).

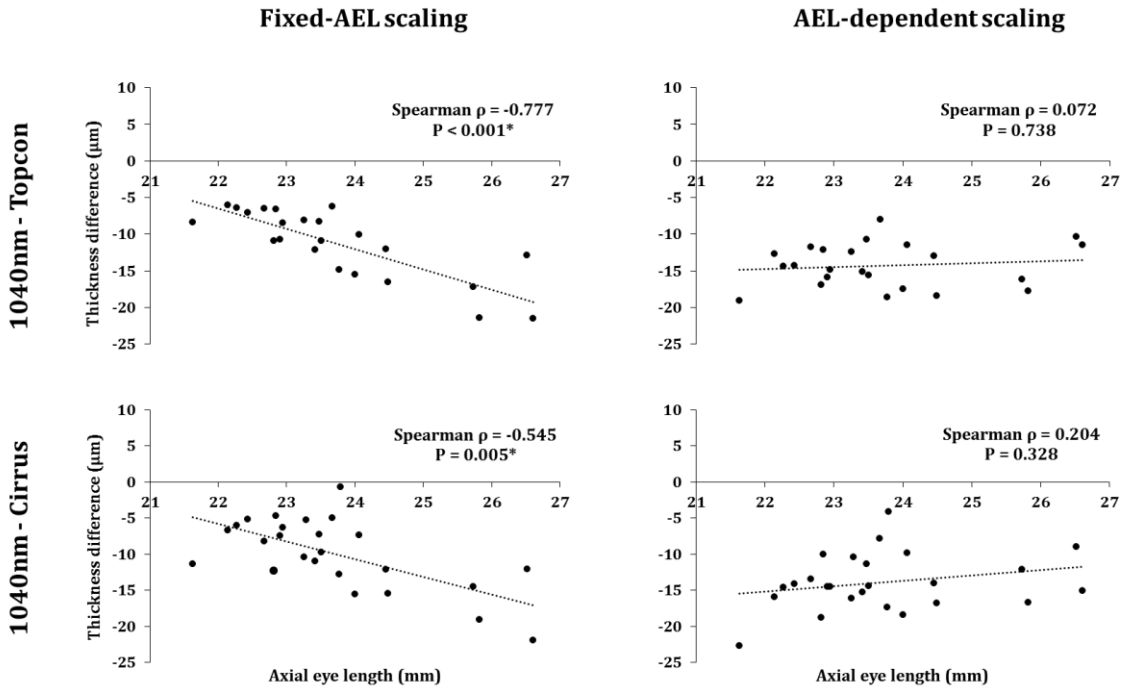

Figure 3.2 Difference in retinal thickness measurements between devices (µm) versus AEL (mm) for the foveal subfield, as produced by the Iowa Reference Algorithms using both scaling methods. The 1040 nm OCT images underwent AEL-dependent scaling only, and serves here as ground truth.

***significant at the 0.05 level**

3.1.4 Discussion

The Iowa Reference Algorithms produced automated segmentation of 10 intra-retinal layers on all images from all three devices. A substantial impact of AEL-corrected lateral scaling on mean intra-retinal layer thickness values was demonstrated, particularly for the inner retinal layers. If an AEL-dependent lateral scaling is not used, the ETDRS grid (defined in mm units at the retinal surface) will overlay a smaller or larger area of retina, depending on the AEL. The ETDRS subfield sizes could vary by up to 30%, assuming a normal AEL range of 20 - 28 mm which is

a little larger than for the cohort of this study. Due to the physiological shape of the retina (particularly at the foveal pit), a relative difference in size of the ETDRS grid would impact the mean thickness measurements of a given region (Figure 3.3). This is reflected in the percentage differences in thickness between the two scaling methods, shown in Table 3.2. Appropriate scaling to account for AEL is therefore an important consideration for any quantitative retinal thickness analysis, particularly in cross-sectional applications.

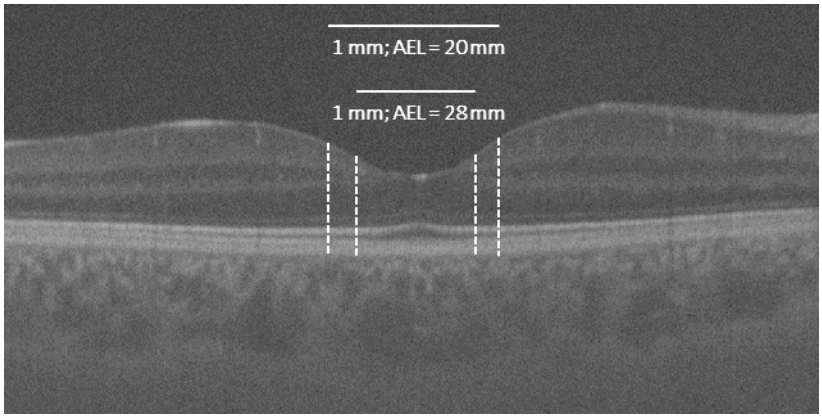

Figure 3.3 Differences in AEL-dependent scaling result in a larger or smaller area of retina residing within each region of the ETDRS grid (dashed lines). Difference in foveal subfield size shown (1 mm in diameter) for lateral scaling assuming an AEL of 20 mm and 28 mm.

Refractive index assumptions for retinal tissue used by each device could result in a small difference in axial scaling. Knowing the assumption made by each device, a difference in absolute thickness values between instruments of between 1.4% and 2.9% would be expected, with largest thickness values from the Zeiss images (n=1.36), then Topcon images (n=1.38), and finally the long-wavelength OCT (n=1.4). This expectation was consistent with the findings in Figure 3.2.

Discrepancies in retinal thickness measurement between images from the long-wavelength and commercial systems were significantly correlated with AEL for the foveal and outer ring subfields, using the fixed-AEL scaling. When the AEL-dependent scaling was used throughout this analysis, all these correlations were reduced and were no longer significant (Figure 3.2). This effect is consistent with the expected transverse magnification error that arises when fixed-AEL scaling is used for images from either of the commercial instruments. The Iowa Reference Algorithms allow for direct input of transverse scaling factors prior to image segmentation which should be used, where possible, to reduce these demonstrated magnification errors.

To conclude, lateral magnification errors affect the consistency and reliability of generated thickness values, and are therefore an important consideration in quantitative OCT retinal layer analysis. Furthermore, the Iowa Reference Algorithms provide a convenient mechanism to apply an accurate AEL-dependent lateral scaling to images from any OCT device. This approach should be followed where any quantitative analysis with a lateral aspect (i.e. not solely axial measurements) is undertaken. These findings are directly applicable not only to retinal analysis, but also to choroidal analysis, the principle topic of this thesis. Although the likely effect of this error is relatively small, AEL-dependent scaling will be incorporated wherever appropriate.

3.2 Choroidal parameter development

A number of methods of quantifying the choroidal vasculature have been previously assessed (see Section 1.7.1). To be an effective parameter, measures must be feasible, repeatable, and sensitive to detecting difference between groups (cross-sectional) or change over time (longitudinal). Since the images in this thesis were acquired using a non-standard OCT device, previously used parameters must be validated on these images, prior to application to disease. This section includes an evaluation of a number of previously described choroidal measures for feasibility and repeatability. These include subfoveal choroidal thickness, vessel diameter, and proportion of vessel lumen. The use of a novel parameter describing structure complexity is also assessed in Section 3.2.4.

Inter-session repeatability was established using the dataset described in Section 3.1, comprising volume and line scans of healthy eyes, which underwent pre-processing as described in Figure 2.2. All study participants were asked to refrain from drinking tea or coffee on the days of data collection, to control for any potential effect of caffeine intake on the choroidal structure (see Section 1.3). To minimise the effect of diurnal variation, both imaging sessions were conducted at the same time of day. Bland-Altman plots and CoR were used to assess repeatability. A comparison is made between the use of volume scans and line scans for the measurement of these parameters, where appropriate. Measurement protocols for each parameter are described in the following sections, and were performed by one observer, who

was masked to previous measurements. All processing steps were undertaken using Fiji, unless otherwise stated.

3.2.1 Subfoveal choroidal thickness

The first parameter assessed was subfoveal choroidal thickness (SFCT). This is the most commonly described and applied parameter in the literature, and is one of the simplest to perform through manual digital calliper measurement.

3.2.1.1 Methods

SFCT was defined as a vertical measurement beneath the lowest point of the foveal pit, from the posterior border of the outermost hyper-reflective line (RPE) to the posterior choroidal stroma, as described by Vuong et al. (2016). For the volume scans, surrounding b-scans were used to localise the deepest point of the foveal pit, and this b-scan was used for the measurement. The zoom and adjust brightness functions were freely used to enhance visualisation of the anterior and posterior choroidal boundaries. A single digital calliper measurement was manually performed for each volume scan and line scan in the dataset.

3.2.1.2 Results

Volume and line scans were acquired from 25 participants at 2 sessions. As discussed in Sections 2.2 and 2.5.1, the line scans were over-sampled and underwent greater averaging, providing a higher SNR than the volume scans. Of the 25 eyes imaged, visibility of the posterior choroidal boundary in the volume scans was poor for 4 of the eyes. These 4 eyes were excluded from all volume scan analysis. However, this boundary was visible in the line scans of all 25 eyes; hence no eyes were excluded from the line scan analysis. For comparison between the scan types, a separate analysis of the line scans was performed, excluding the same 4 eyes. The demographics of the study participants can be found in Table 3.3. In general, the eyes excluded from the volume scan analysis had a shorter AEL and were more hyperopic than the included eyes, although this was based on only 4 excluded eyes and it is therefore difficult to assess the significance of this observation.

Table 3.3 Demographics (mean ± SD) of all study participants, and subdivided into those that were included and excluded from the analysis of the volume scans.

	All participants	Included	Excluded
n	25	21	4
Age (years)	34.9 ± 13.5	36.4 ± 14.1	26.8 ± 4.3
AEL (mm)	23.7 ± 1.3	23.9 ± 1.3	22.7 ± 1.0
Refractive error (mean sphere; dioptres)	-0.60 ± 1.9	-0.80 ± 1.9	0.44 ± 1.8

Mean SFCT of all eyes measured from the line scans was 341.1 ± 132.0 μm, although this reduced to 297.1 ± 91.1 μm following exclusion of 4 eyes (Table 3.4). SFCT of the excluded eyes (measured from the line scans) ranged from 537 μm to 595 μm. When the same 4 eyes were removed from the line scan analysis also (for comparison only), SFCT was very comparable between scan types (paired t-test, P=0.769). Inter-session repeatability was very similar for volume and line scans (CoR ~7%). The variation in SFCT between individuals was very high, ranging from 85.5 to 594.7 μm. There was no significant difference in SFCT between Session 1 and Session 2 (paired t-test, P>0.05 in all cases).

Table 3.4 Mean (± SD) subfoveal choroidal thickness (SFCT) and inter-session CoR in μm and as a percentage of the mean SFCT. The larger dataset of line scans is shown separately.

Scan type	Mean SFCT (μm)	Range (μm)	CoR (μm)	CoR (%)
Volume (n=21)	295.3 ± 87.8	88.0 - 448.7	20.5	6.9
Line (n=21)	297.1 ± 91.1	85.5 - 457.9	21.1	7.1
Line (n=25)	341.1 ± 132.0	85.5 - 594.7	24.1	7.1

3.2.1.3 Discussion

Mean SFCT in this cohort was 341.1 ± 132.0 μm. This is similar to the findings of Rahman et al. (2011), who reported a mean thickness of 332 ± 90 μm in a healthy cohort of similar age (38 ± 5 years) imaged using Spectralis OCT. The variation in thickness between eyes was greater in the present cohort, as was the age range of participants (20-62 versus 30-49 years). This may in part account for the variation in choroidal thickness, since the choroid has been shown to thin with age (see Section 1.3.1). As a result of the demonstrated large variation between healthy individuals, large differences in mean choroidal thickness between disease groups

(or a large sample size) would be required to reach statistical significance. This parameter may therefore not be sensitive to small differences between groups.

Conversely, a number of studies have reported a lower mean SFCT than these findings (Ding et al. 2011; Lee et al. 2013c). The majority of participants in the present study were Caucasian, whilst these two studies were of Asian eyes, which are typically more myopic and have a longer AEL, where one would expect thinner choroids (see Section 1.3.2). For instance, Lee et al (2013c) reported a mean SFCT of ~270 μm, with a mean AEL of 25.11 ± 1.43 mm and a mean refractive error of -3.27 ± 2.48 D. The difference in mean SFCT between studies could be explained by the demographics of the cohorts.

The inter-session CoR of SFCT was ~24 μm; this represents the normal variability that can be expected between imaging sessions with this measurement technique in a young, healthy population. Changes between sessions of greater than this value may indicate change in the structure beyond normal variation, which could be associated with pathology. Rahman et al. (2011) assessed the repeatability of SFCT measurements in young, healthy participants (n=50). Intra-observer CoR was found to be 23 μm, whilst inter-observer CoR and intra-session CoR were 32 μm and 34 μm respectively. Inter-session repeatability was not assessed, but in the present study was found to be slightly lower than these values. This may be due to the OCT devices used in the studies; Rahman et al. acquired images using a conventional-wavelength commercial OCT with EDI, whilst a long-wavelength OCT was used in this study. This long-wavelength device may therefore provide an advantage over the conventional commercial OCT devices in terms of repeatability of SFCT measurement.

Inter-session repeatability of SFCT was very similar for volume and line scans acquired from the same eyes. However, 4 of the 25 eyes were excluded from the volume scan analysis due to poor visibility of the posterior choroidal boundary. These eyes had the greatest SFCT of the sample (all >530 μm), therefore suffered most from the inherent signal roll-off with depth in the images. The SNR was low at the posterior choroidal boundary, causing the boundary to be poorly defined and not possible to accurately locate. This boundary could be visualised on the line scans of all four of these eyes, likely due to the reduced image noise resulting from averaging during image processing.

There was minimal difference in SFCT measurements acquired from the line scans and volume scans. Measurements from these scan types are therefore directly comparable. However, since the posterior choroidal boundary was visible in a higher proportion of the line scans, this scan type is preferable for use in manual measurement of SFCT.

Since SFCT is a sampled measurement (i.e. measured at a single location), it may not be representative of the sub-macular choroid as a whole. An averaged measurement of choroidal thickness over a defined area is likely to be more suitable for this task. However, since this requires manual segmentation of the anterior and posterior choroidal boundaries, it is time consuming and therefore not feasible for clinical application. Methods of automated segmentation for fast regional choroidal thickness measurement are explored in Section 3.4.

3.2.2 Visible vessel diameter and vessel ratio

Vessel diameter has been described in the literature as a method for quantifying the choroidal vasculature. Approaches to measurement technique vary, with some authors measuring the largest visible vessel within a given distance from the fovea (Yang et al. 2013), whilst others measure the largest vessel at a predefined distance and direction from the fovea (Bittencourt et al. 2014; see Section 1.7.1). However, these measurements are susceptible to high inter-observer variability. For instance, Yang et al. (2013) defined the limit of acceptable measurement difference between observers as 15%. Since the mean vessel diameter of their control group was 140 μm, this equates to a difference of ~21 μm. In an attempt to minimise the effects of this potential error, this section evaluates the use of multiple measurements to produce a mean value for visible vessel diameter (VVD).

In addition to vessel diameter, Bittencourt et al. (2014) outlined the use of a ratio of vessel diameter to choroidal thickness in describing the vasculature. This parameter is also evaluated in this section, and will be referred to here as 'vessel ratio'.

3.2.2.1 Methods

VVD was defined as a vertical measurement of the hypo-reflective vessel lumen, taken at the point of maximum diameter. For the volume scans, surrounding b-scans were used to localise the deepest point of the foveal pit, and this b-scan was used for the measurement. The zoom and adjust brightness functions were freely used to enhance visualisation of the vessel lumen boundaries. A single digital calliper measurement was manually performed for each of the three largest visible vessels within 3000 μm nasally and temporally of the fovea (Figure 3.4). This ensured that the same area of choroid was included in the volume scans (width ~6000 μm) and line scans (width ~11000 μm). The vessel ratio (VR) was also calculated (VR=VVD/SFCT).

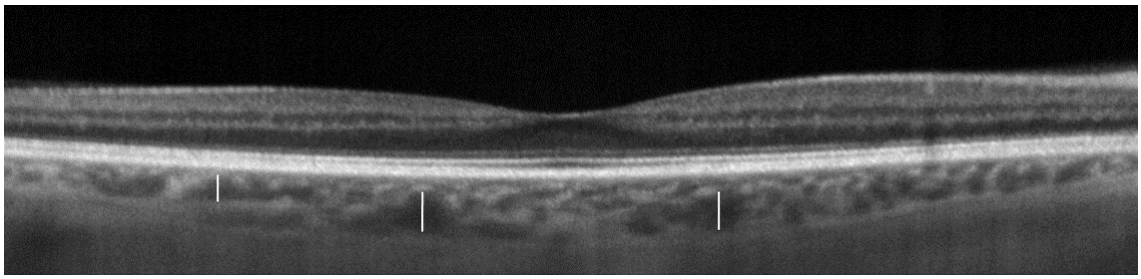

Figure 3.4 Measurement of VVD from a line scan. The three largest vessels were manually measured vertically, at the point of maximum diameter (white lines) using digital callipers. The mean of these was taken as VVD.

3.2.2.2 Results

Of the 25 participants, 4 were excluded from the volume scan analysis due to poor visibility of the choroidal vessels. These were the same 4 eyes as were excluded from the SFCT analysis (see Section 3.2.1). It was possible to obtain VVD measurements from the line scans of all 25 participants.

Mean VVD measured from the line scans of all eyes was 152.8 ± 35.7 μm, although this reduced to 142.7 ± 28.3 μm following exclusion of 4 eyes (Table 3.5). VVD of the excluded eyes (measured from the line scans) ranged from 187 μm to 231 μm. When these eyes were excluded from the line scan analysis, mean VVD was still significantly larger in the line scans than the volume scans (paired t-test, $P<0.05$). Inter-session repeatability was slightly better for the measurements from the line scans than the volume scans (CoR of 14.7% versus 21.2%). There was no

significant difference in VVD between Session 1 and Session 2 (paired t-test, P>0.05 in each case).

Table 3.5 Mean (± SD) visible vessel diameter (VVD) and inter-session CoR in µm and as a percentage of the mean VVD. The larger dataset of line scans is shown separately.

Scan type	Mean VVD (µm)	Range (µm)	CoR (µm)	CoR (%)
Volume (n=21)	122.6 ± 28.8	58.9-185.2	25.9	21.2
Line (n=21)	142.7 ± 28.3	99.8-186.8	24.0	16.8
Line (n=25)	152.8 ± 35.7	99.8-231.2	22.4	14.7

The mean ratio of VVD to SFCT (vessel ratio) was 0.49 ± 0.17 (Table 3.6). The vessel ratio of the 4 excluded eyes ranged from 0.33 to 0.39 (due to the high SFCT). The CoR of this parameter was lower for the line scans than the volume scans.

Table 3.6 Mean (± SD) vessel ratio and inter-session CoR (also as a percentage of the mean vessel ratio). The larger dataset of line scans is shown separately.

Scan type	Mean VR	Range	CoR	CoR (%)
Volume (n=21)	0.44 ± 0.10	0.30-0.67	0.15	34.6
Line (n=21)	0.52 ± 0.17	0.32-1.18	0.10	19.1
Line (n=25)	0.49 ± 0.17	0.32-1.18	0.09	18.4

The relationships between these parameters and SFCT can be seen in Figure 3.5. A strong positive correlation was found between the variables, with thicker choroids generally having a larger VVD (Spearman's $\rho>0.5$; $P<0.05$). One outlier was identified in the VR correlation and was removed from further analysis. A strong negative correlation was found between SFCT and vessel ratio (Spearman's $\rho>0.5$, $P<0.05$).

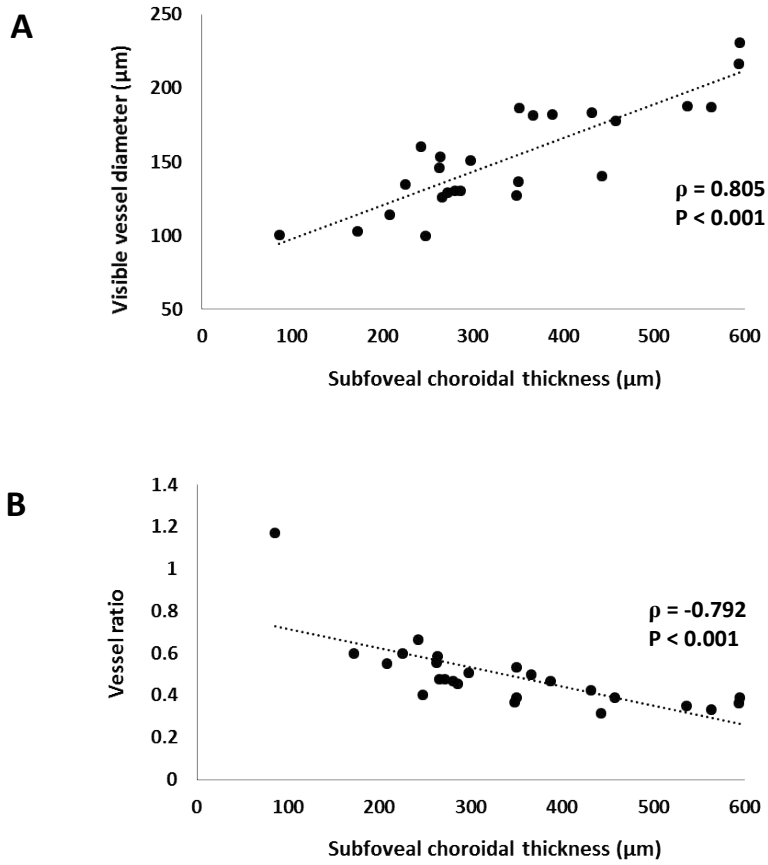

Figure 3.5 Scatter plots showing the relationship between (A) mean visible vessel diameter and (B) vessel ratio, as a function of subfoveal choroidal thickness. Spearman's rho (ρ) and significance value (P) given. The outlier in plot B was removed prior to correlation testing but is included here for demonstrative purposes.

3.2.2.3 Discussion

Based on these repeatability findings, a change in VVD of >22.4 µm is required to indicate change in the structure beyond normal inter-session variation. Although this is a large difference given the mean vessel diameter, differences exceeding this value have been demonstrated with OCT imaging between disease and control groups, in both central serous chorioretinopathy (CSC) and posterior uveitis (Yang et al. 2013; Bittencourt et al. 2014). The mean absolute difference in VVD between sessions was 9.0 µm, which equates to ~5.9% of mean vessel diameter. This is far lower than the 15% acceptance criteria employed by Yang et al. (2013).

Vessel measurements obtained from the line scans were significantly larger than those from the volume scans, even when the same 4 images were excluded from both sets (paired t-test, $P<0.05$). Measurements of VVD are therefore not directly comparable between scan types. The cause of this discrepancy is unclear,

although it may be associated with the averaging of multiple b-scans during image processing of line scans. If the b-scans are misaligned, spatial resolution is reduced. It is possible that if the stromal space between vessel lumen is small, it may be lost during averaging of misaligned b-scans. Although care was taken to ensure this error was minimised during image processing, it is likely that a small amount of misalignment remained, which may in part explain these findings. The mean VVD of the line scans was 152.8 ± 35.7 μm, which is consistent with the healthy control group of previous studies; for example the findings of Yang et al. (2013) and Bittencourt et al. (2014), who reported mean vessel diameters of 140 ± 40 μm, and 160 ± 32 μm respectively.

A strong positive correlation was found between SFCT and VVD. This suggests that, in general, the maximum choroidal vessel size is larger in thicker choroids. This is consistent with the findings of Park and Oh (2014), who identified a strong positive correlation between these variables in both adults and children. Additionally, a strong negative correlation was identified between SFCT and VR; i.e. the vessel ratio was lower for thicker choroids. The mean VR in the total sample (n=25) was 0.49; therefore the mean diameter of the 3 largest choroidal vessels was approximately half of the SFCT. This is lower than the VR of 0.61 reported by Bittencourt et al. (2014) on 23 healthy, young participants, despite similar mean vessel diameter values. The difference is attributable to the mean SFCT between the studies (261.6 ± 45.6 μm versus 341.1 ± 132.0 μm). The far greater variation in choroidal thickness in the current cohort (particularly in the upper range) may contribute to the difference in VR.

One outlier was identified in the correlation of SFCT and VR (Figure 3.5 Scatter plots showing the relationship between (A) mean visible vessel diameter and (B) vessel ratio, as a function of subfoveal choroidal thickness. Spearman's rho (ρ) and significance value (P) given. The outlier in plot B was removed prior to correlation testing but is included here for demonstrative purposes. B). This participant had a particularly thin choroid (SFCT of 85.5 μm). The largest vessels were identified to measure VVD, however these were typically not located directly beneath the fovea. In this case, the largest vessels were located elsewhere, in a location where the choroid was thicker than beneath the fovea. Since the choroid is typically physiologically thickest beneath the fovea, the VR is usually less than 1.

However, the VR of this participant was 1.2, as the VVD was larger than the SFCT. Since this study was on a healthy cohort and this measure did not follow the physiological norm, this measure was classed as an outlier and removed from the correlation analysis. However, it should be noted that the vessel ratio may exceed 1 in pathological eyes, particularly in cases of subfoveal choroidal atrophy.

Inter-session repeatability of VVD was better for the line scans than the volume scans. Due to the averaging applied during processing of the line scans, the SNR is higher, and the vessel lumen appear more defined than in the volume scans. This allowed greater accuracy in localisation of the lumen boundaries, which likely explains the difference in CoR between the scan types. The 4 eyes excluded from the volume scan analysis were those with high SFCT (>530 μm) in which visualisation of the posterior choroidal boundary was not possible. It was large vessels that were of interest for this evaluation, which are located in the outer choroid (Haller's layer), and hence suffer most from signal roll-off in those with a thicker choroid, limiting visualisation of the vessel lumen. Despite this, VVD measurements (and hence VR calculations) were feasible on all eyes using the line scans. Line scans are therefore preferable for manually quantifying vessel diameter in this manner.

3.2.3 Choroidal area, luminal area, and choroidal vascularity index

The measurements evaluated in Sections 3.2.1 and 3.2.2 were 1-dimensional, i.e. lengths. They therefore suffer from the limitations of sampling, since a measurement of a single location (or an average of multiple locations) is used to describe the structure. These protocols also consider only axial measures for ease of image scaling. To minimise the effect of sampling, 2-dimensional measurements have previously been considered, including choroidal area and luminal area. These are the 2-dimensional counterparts to choroidal thickness and vessel diameter respectively, but consider the entire choroid visible in the b-scan, rather than at fixed locations. A protocol for obtaining these parameters from OCT line scans using image binarization has been described by Sonoda et al. (2014), and has been applied to several ocular pathologies (see Section 1.7.1.3).

Considering VR (the ratio of VVD to SFCT), the corresponding 2-D measurement is the ratio of luminal area to choroidal area. This parameter has been

previously described by Agrawal et al. (2016a), and termed Choroidal Vascularity Index (CVI). This section evaluates the application of these methods to line scans of healthy eyes acquired using a non-commercial long-wavelength OCT device.

3.2.3.1 Methods

The protocol described by Sonoda et al. (2014) was applied to measure choroidal area, luminal area and stromal area, with minor modifications. Firstly, the image was cropped to a rectangular area 3000 µm wide (equivalent to the inner ring of the ETDRS grid), centred on the deepest point of the foveal pit. The zoom and adjust brightness functions were then used freely to enhance visualisation of the boundaries of the choroid. The boundaries of the central 1500 µm of choroid were selected from the basal margin of the RPE to the choroidal-scleral border, using the polygon selection tool (Figure 3.6A). This area was added to the 'ROI manager' in Fiji.

Three large choroidal vessels were identified (it was not possible for these to all exceed 100 µm in this dataset, as stated in the original protocol). The mean brightness of these vessel lumen was measured, within a circle of 9 pixel diameter, using the oval selection tool. The image minimum brightness was adjusted to this value to minimise noise (Figure 3.6B), and the image was converted to 8-bit.

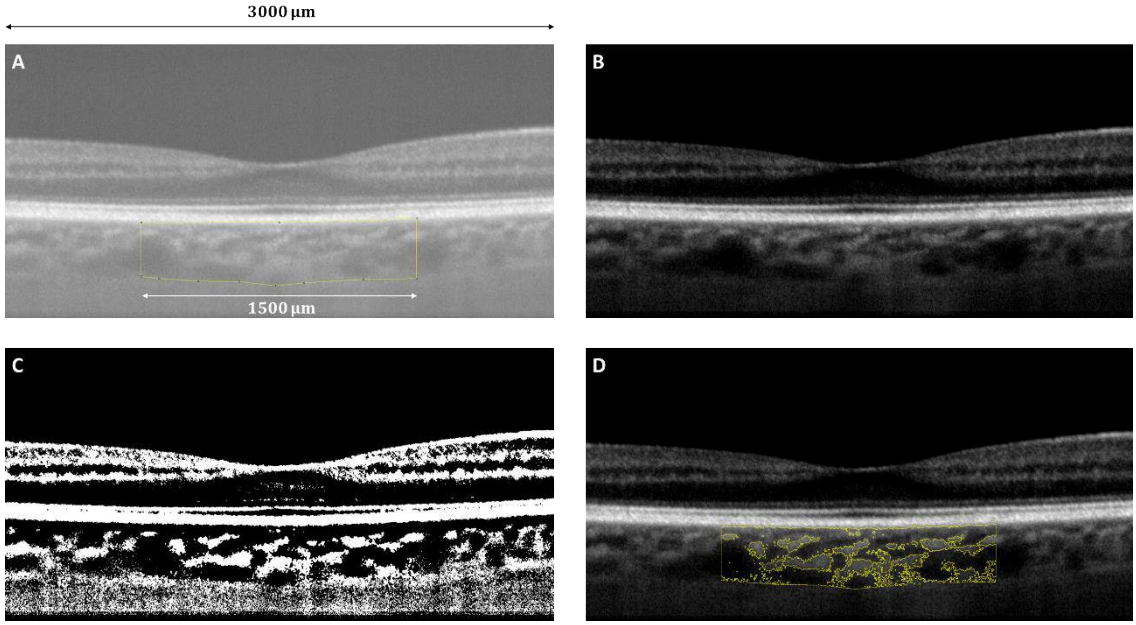

Figure 3.6 Protocol summary for image binarization and parameter measurement. (A) Area selection. (B) Adjustment of brightness. (C) Niblack auto local thresholding* (Niblack 1986). *(D) Overlay of binarised image perimeter.

Prior to thresholding, a median filter was applied to minimise remaining speckle in the image. This was not included in the original protocol, which was optimised for images acquired with the Spectralis OCT. Since the images in the current dataset were acquired on a non-commercial device, only minimal post-processing had been applied, and some high frequency noise remained. Following the median filter, images underwent Niblack autolocal thresholding (Niblack 1986; Figure 3.6C). The binarised image was then converted to a RGB image to allow use of the 'threshold color' tool. This tool was used to produce an automated outline of the binarised perimeter across the image (i.e. the luminal areas). This selection was added to the ROI manager, and was combined with the previous selection to produce an outline of the luminal areas in the central 1500 μm of choroid only (Figure 3.6D).

Automated measurements of the choroidal area (CA) and luminal area (LA) were then produced using the Analyse>Measure tool in Fiji (with the sum of the black areas in pixels taken as LA). The stromal area (SA) was then calculated from these values (SA=CA-LA). These values were in pixels, and were converted to mm^2 by multiplying by both the axial and transverse scaling factors. The choroidal vascularity index (CVI) was also calculated (CVI=LA/CA) for each image.

3.2.3.2 Results

All 25 participants were included in this analysis. Mean choroidal area within the central 1.5 mm was 0.484 mm^2, of which vessel lumen accounted for 0.367 mm^2 (75.8%). Variation in CA between eyes was high, and ranged from 0.14 to 0.87 mm^2. CVI ranged from 0.683 to 0.900. There was no significant difference between Session 1 and Session 2 for any of the parameters (paired t-test, P>0.05 in all cases). Inter-session repeatability of each parameter is shown in Table 3.7.

Table 3.7 Mean (± SD) choroidal area (mm^2), luminal area (mm^2), stromal area (mm^2), and choroidal vascular index (CVI). Inter-session CoR is given for each parameter, including as a percentage of the mean value.

Parameter	Mean ± SD	Range	CoR	CoR (%)
Choroidal area	0.484 ± 0.178	0.142-0.865	0.051	10.51
Luminal area	0.367 ± 0.148	0.118-0.730	0.042	11.53
Stromal area	0.117 ± 0.047	0.024-0.221	0.033	29.01
CVI	0.758 ± 0.055	0.683-0.900	0.048	6.39

The correlation of LA and CVI with CA can be seen in Figure 3.7. A strong positive correlation was found between CA and LA, with thicker choroids generally having a larger LA (Spearman's $\rho>0.5$; $P<0.05$). There was no linear correlation between CA and CVI (Spearman's $\rho=-0.193$).

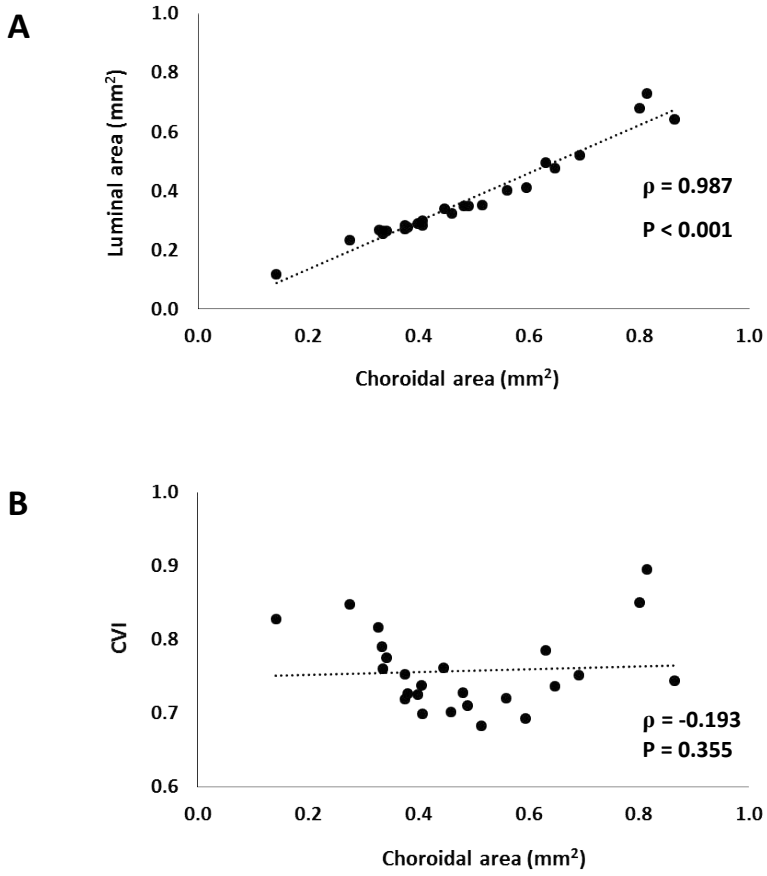

Figure 3.7 Scatter plot showing relationship between (A) luminal area and (B) choroidal vascular index (CVI), as a function of choroidal area. Spearman's rho (ρ) and significance value (P) given.

3.2.3.3 Discussion

Mean CA in the central 1.5 mm^2 was 0.484 ± 0.178 mm^2. This is comparable to the findings of Gupta et al. (2017), who reported a value of 0.452 ± 0.094 mm^2 in healthy eyes (n=273). On average, vessel lumen accounted for 75.8% of choroidal area, although this value ranged from 68.3 to 90.0% between individuals. This is higher than the mean values of 65.4% reported by Sonoda et al. (2014) and 65.6 ± 2.3% (range 60.1 to 71.3%) by Agrawal (2016a), on healthy individuals using this protocol. Following the same protocol, Gupta et al. (2017) reported a CVI of 55.5%, which is far lower than the present study. However, this was on an older cohort with

a mean age of 60.1 ± 6.8 years, which may explain some of the difference between these findings.

This protocol was optimised for images from the Spectralis OCT, whereas the current study utilised a non-commercial long-wavelength device. The images from the commercial device undergo pre-processing, including averaging of 100 b-scans to improve SNR. This may contribute to the discrepancy between these values of CVI. Branchini et al. (2013) reported a light to dark pixel ratio of 0.27, which equates to a CVI of 78.7%. This is a more similar value to the findings of the current study. Images in that study were acquired on a Cirrus OCT device, and utilised an alternative thresholding method, which may contribute to the difference in findings between studies.

Both CA and LA had a reasonable CoR (0.051 mm^2 and 0.042 mm^2 respectively). A change in CA of >0.051 mm^2 (or luminal area of > 0.042 mm^2) would suggest structural change beyond normal variation. Following the same measurement protocol, Sonoda et al. (2014) identified a mean difference between eyes with AMD and healthy controls of ~0.049 mm^2 in CA and ~0.033 mm^2 in LA, which is slightly lower than these values. However, mean differences exceeding these CoR values have been demonstrated in CSC and diabetic retinopathy (Agrawal 2016b; Gupta et al. 2017).

There was a strong positive correlation between CA and LA, which is unsurprising given the relationship between SFCT and VVD demonstrated previously. There was no correlation between CA and CVI. This indicates that there is no relationship between SFCT and proportion of vessel lumen. This is in contrast to the VR parameter evaluated in Section 3.2.2, which showed a strong negative correlation. However, this finding is in agreement with Wei et al. (2016) who found CVI to not be influenced by choroidal thickness.

In conclusion, all the parameters evaluated are feasible for application to line scans acquired by the non-commercial long-wavelength OCT device. All parameters demonstrated reasonable inter-session repeatability. However, CVI should be used with caution due to limited agreement with the published literature, and the use of a protocol not optimised for use with this OCT device.

3.2.4 Enface analysis

The previous method of quantifying vessel area ratio considered the entire choroidal depth in a single b-scan. This includes a spectrum of vessel sizes, from the small vessels of the choriocapillaris to the large vessels of Haller's layer. During image thresholding, fine detail from the anterior choroid is often lost (as can be seen in Figure 3.6D). Pathology primarily affecting this smaller vasculature may therefore not be detectable using this method. An alternative measurement method would be to quantify all vessels at a predefined depth in the choroid. Sohrab et al. (2012) analysed enface OCT images of the choroid at varying depth, producing a parameter they termed 'choroidal vascular density'. This was defined as the ratio of black pixels (representing vessel lumen) to total image pixels (similarly to CVI at a fixed choroidal depth), following a custom thresholding protocol. Due to the ambiguity of this term (density may be taken to represent vessels per unit area), this parameter will be referred to here as 'luminal area ratio'.

Measuring vessel lumen area relative to total area does not provide information on the size of features in the image, in this case vessels. For instance, a choroid containing many small vessels may produce a similar luminal area ratio to a choroid with fewer large vessels. A novel parameter was therefore evaluated for describing feature complexity. The perimeter of the vessel lumen in a binarised image is relatively simple and easy to obtain, and can be reported as a proportion of total image pixels, termed 'luminal perimeter ratio'. This section evaluates the feasibility and repeatability of quantifying the vasculature at a set choroidal depth using enface OCT images.

3.2.4.1 Methods

As outlined in Section 2.3.3.2 (and Appendix B), all volume scans were flattened to the outermost hyper-reflective line (RPE) to ensure that a consistent choroidal depth was selected across the image. To account for the large variation in SFCT in this cohort, a percentage depth from RPE to posterior choroidal boundary was utilised, rather than an absolute depth beneath the RPE. An arbitrary depth of 50% was selected to ensure sufficient vessel resolution (i.e. to avoid inclusion of the small vessels of the choriocapillaris). This depth also minimised inclusion of sclera

at the edges of the enface image, caused by the physiological thinning of the choroid with increased distance from the fovea (as seen in Figure 3.8).

The processing steps are summarised in Figure 3.8. Firstly, a rectangular region was selected at 50% choroidal depth, of full image width and height of 5 pixels. This was resliced then underwent median Z-projection to produce an enface image. The artefacts from stack registration were cropped from the image. The image was then duplicated, and a median filter applied to each image, one with a radius of 4 pixels (to remove high frequency noise) and the other with a radius of 50 pixels. The first image was then divided by the second to control for any large intensity fluctuation across the image. This step was necessary to prepare the image for application of a global Otsu threshold to produce a binarised image.

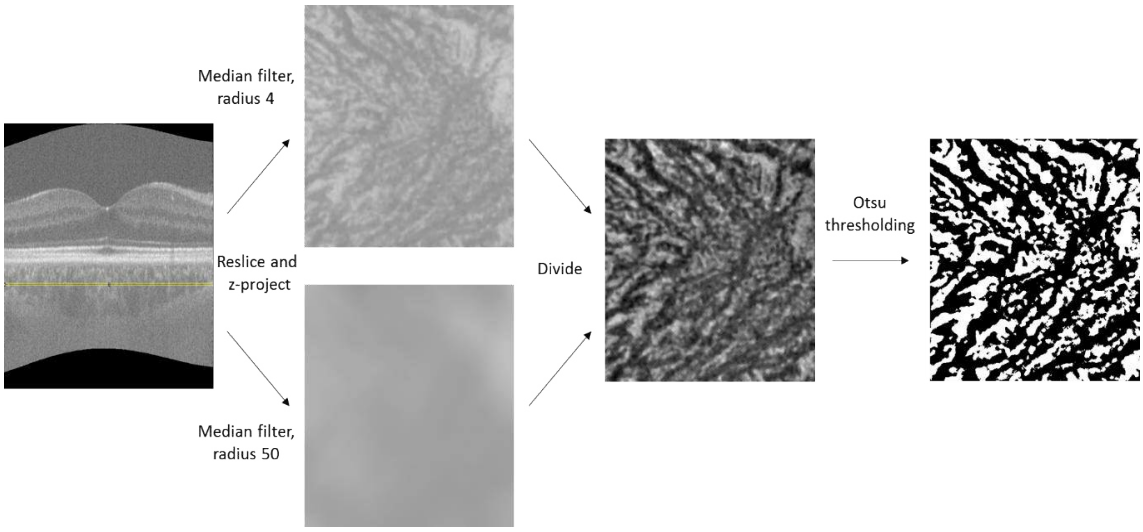

Figure 3.8 Summary of protocol for producing binarised enface images at 50% choroidal depth.

The luminal area ratio (LAR) was calculated by dividing the number of black pixels by total image pixels. Similarly to the measurement of LA in the previous section, the image was converted to RGB, and 'color threshold' tool was used to measure the perimeter of the luminal area. The perimeter was divided by total image pixels to produce luminal perimeter ratio (LPR), a gross measure of feature complexity.

To test the discriminative abilities of the parameters, different choroidal depths were used as a proxy for different disease states. The above protocol was therefore repeated to produce an additional set of enface image at 25% choroidal depth from the RPE, where vessels should appear anatomically different (Spraul et

al. 1999). A Wilcoxon signed ranks test was used to test whether the difference between depths was statistically significant.

3.2.4.2 Results

Since this analysis was using the volume scans, the 4 eyes with poor visualisation of the choroidal vessels were excluded (as for the previous analyses). The mean LAR at 50% choroidal depth was 0.595 ± 0.031. The mean LPR was 0.113 ± 0.002. There was no significant difference between Session 1 and Session 2 for either parameter (Wilcoxon, P>0.05). Inter-session repeatability is shown in Table 3.8.

Table 3.8 Mean (± SD) luminal area ratio and luminal perimeter ratio at 50% depth. Inter-session CoR given for each parameter, including as a percentage of the mean value.

Parameter	Mean ± SD	Range	CoR	CoR (%)
Luminal area ratio	0.595 ± 0.031	0.527 - 0.644	0.033	5.48
Luminal perimeter ratio	0.113 ± 0.002	0.096 - 0.156	0.012	10.75

A representative example of the binarised enface images at 25% and 50% choroidal depth can be seen in Figure 3.9. In general, the images at 50% displayed larger vessels. A comparison between choroidal depths at Session 1 can be seen in Figure 3.10. The mean LAR at 50% and 25% depth was 0.599 ± 0.031 and 0.594 ± 0.030 respectively. This difference was not statistically significant (Wilcoxon, P=0.970). The mean LPR at 50% and 25% depth was 0.111 ± 0.017 and 0.125 ± 0.012 respectively. This difference was statistically significant (Wilcoxon, P<0.001).

Figure 3.9 Binarised enface OCT images from the same eye show larger vessels at 50% depth (A) than at 25% depth (B) beneath the RPE.

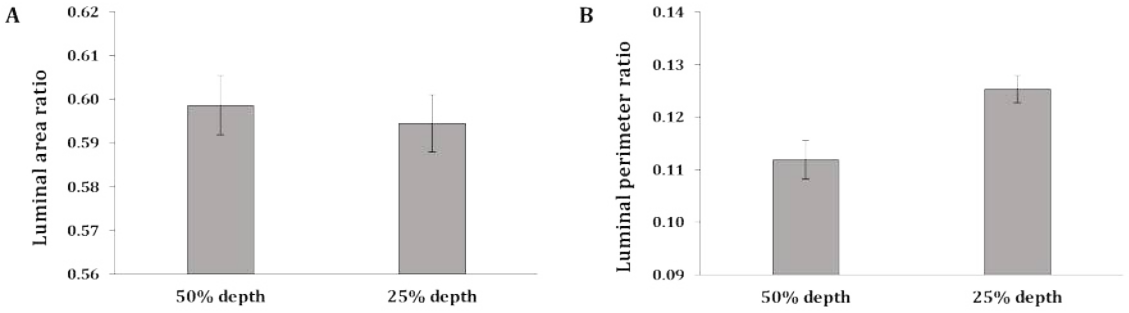

Figure 3.10 Comparison of Session 1 mean luminal area ratio (A) and mean luminal perimeter ratio (B) for enface slices at 50% and 25% choroidal depth. Error bars represent the standard error of the mean. The difference between depths was not significant for luminal area ratio (P=0.970), but was significant for luminal perimeter ratio (P<0.001).

3.2.4.3 Discussion

On average, vessel lumen accounted for 59.5 ± 3.1% of choroidal tissue at 50% depth. This is similar to the findings of Kuroda et al. (2016), who reported a value of 53.8 ± 4.3% on healthy eyes. This was using a similar protocol, including Otsu thresholding, and was conducted on images acquired using a commercial long-wavelength OCT device. However, these values are lower than those reported by Sohrab et al. (2012). Following a custom analysis program to process and threshold images, they found vessel lumen to constitute 75.9 – 88.4% of the middle vessel layer and 79.3 – 87.2% of the outer vessel layer. This study was conducted on images from a Cirrus HD-OCT. The difference in values between the studies is likely attributable to the differences in thresholding protocol and OCT device (and therefore image scaling) used.

Both LAR and LPR had a reasonable inter-session CoR (0.033 and 0.012 respectively). Therefore to indicate structural change beyond normal variation, an increase in these values of >3.3% and >1.2% would be required. When applying the protocol to eyes with early AMD, the mean difference between the disease and control groups was 3.3% in the middle vessel layer (Sohrab et al. 2012). To date, it has not been applied to late-stage AMD. Kuroda et al (2016) identified a large mean difference in this parameter between their CSC and control groups (~11.0%). It is therefore feasible for this difference to be detectable in pathology. To the author's knowledge, no previous studies have investigated LPR in choroidal OCT imaging, or in AMD patients.

When comparing the two different depths in the choroid, there was no significant difference in LAR. This indicates that either there is no difference between these depths, or that this parameter is not sensitive enough to detect a small difference between the two choroidal depths. Given the physiology of the choroidal structure, and the detectable difference in vessel appearance perceived by the observer (as seen in Figure 3.9), one can assume that there is truly little difference in LAR between 50% and 25% choroidal depth. However, since these are healthy eyes, it is possible that a change in this parameter would be detectable between disease and control eyes, attributed to vessel changes such as dropout (e.g. AMD) or engorgement (e.g. CSC).

Conversely, LPR was significantly higher at 25% than 50% depth in the choroid. This novel parameter provides a gross measure of feature complexity, with finer detail features (i.e. multiple small vessels) yielding a higher ratio. This may therefore be useful in quantifying differences in feature complexity between disease and control groups, which could be attributable to structural change such as vessel dropout, known to occur in AMD (Ramrattan et al. 1994; Chirco et al. 2016).

In conclusion, both parameters evaluated are feasible for application to enface images acquired with this non-commercial long-wavelength OCT device. Both parameters demonstrated reasonable inter-session repeatability. It should be noted that the use of LAR alone does not fully describe the features within the enface image, and it is possible for two images with obvious differences in vessel structure to yield similar results. LPR can therefore be used alongside this parameter as a gross measure of vessel complexity.

3.2.5 General discussion

In this section, a total of eight parameters (including one novel parameter) were evaluated for feasibility and inter-session repeatability on a dataset comprising images of 25 healthy eyes, acquired with a non-commercial long-wavelength OCT device. All parameters were feasible and demonstrated reasonable repeatability (CoR ranging from 5.5% to 18.4%). Each parameter will therefore be applied to a dataset comprising images of early and late-stage AMD, along with

healthy age-similar controls, to assess their sensitivity to detecting difference in structure between disease stages (see Section 4.4).

Several parameters were measured on both line and volume scans, to identify which scan type was more appropriate to use. Although the inter-session repeatability was usually similar between scan types, 4 eyes were excluded from some of the volume scan analyses due to poor visualisation of the vessels. No eyes were excluded from the analyses of the line scans. Therefore, line scans should be used (where possible) to conduct 1-D or 2-D measurements of the b-scans. However, volume scans are required for the production of enface images, and hence the enface parameters that were evaluated. Therefore, both scan types should be collected for the AMD dataset, and quantified according to Table 3.9.

Table 3.9 Summary of parameters for quantification of choroidal vasculature using each scan type.

Line scan	Volume scan
Subfoveal choroidal thickness (SFCT)	Luminal area ratio (LAR)
Visible vessel diameter (VVD)	Luminal perimeter ratio (LPR)
Vessel ratio (VR)	
Choroidal area (CA)	
Luminal area (LA)	
Choroidal vascular index (CVI)	

3.3 Three-dimensional analysis of choroidal vasculature

The OCT volume scans acquired represent the choroid in three-dimensions. The low contrast and low SNR inherent to these choroidal images would be expected to make 3-D structural analysis difficult. However, given the availability and value of many 3-D techniques in other areas (e.g. 3-D skeletonization/connectivity; Kohjiya et al. 2006; Reif et al. 2012; Jin and Kim 2017), it was necessary to further explore the feasibility of a 3-D analysis approach.

The first stage of 3-D analysis is to identify the features of interest within an image, in this case the choroidal vessel lumen throughout the volume scan. Most simply this could be achieved using a manual segmentation approach. However, this is time-consuming and open to subjectivity, and was therefore not considered a feasible approach for a large numbers of volume scans. Therefore, automated

segmentation of the choroidal vessels, similar to the approaches described in Section 1.7.2.2 (Zhang et al. 2012; Kajić et al. 2013), was attempted using Fiji. To maximise the likelihood of success and limit the impact of low contrast and poor SNR previously identified, it was decided that the 6° volume scans would be used, which were shown to provide optimum image quality due to greater image sampling (see Section 2.5.1).

Images were resliced to produce an enface view, and underwent noise reduction (median filtering), as described in Section 3.2.4 (enface analysis). Otsu thresholding was then applied to the enface images to automatically identify the vessel lumen. To evaluate the feasibility of this technique as a precursor to 3-D analysis, the results from individual binarised image frames were compared to manual segmentation by a clinical observer familiar with OCT images of the choroid (an example is shown in Figure 3.11).

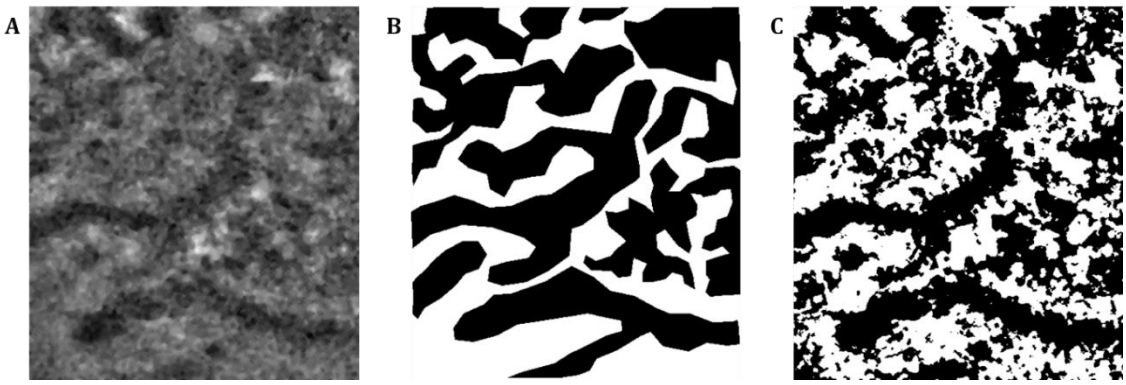

Figure 3.11 Comparison of choroidal vessel identification methods. An enface image was produced from a 6° volume scan, which underwent noise reduction (A). From this image, the vessel lumen were manually segmented (B) and automatically segmented using Otsu thresholding (C).

Although there was similarity between the binarised images produced through manual and automated segmentation, the Otsu thresholding resulted in a large number of high frequency noise artefacts, particularly in low contrast regions of the image. In an attempt to minimise this, a median filter was used to remove outliers, which were defined as clusters of black or white pixels with a radius ≤2 pixels. Despite this, some regions remained (visible particularly in the lower part of Figure 3.11C). These regions were generally not consistent between neighbouring image frames, and hence produced poor continuity during attempted construction of a 3-D model (Figure 3.12).

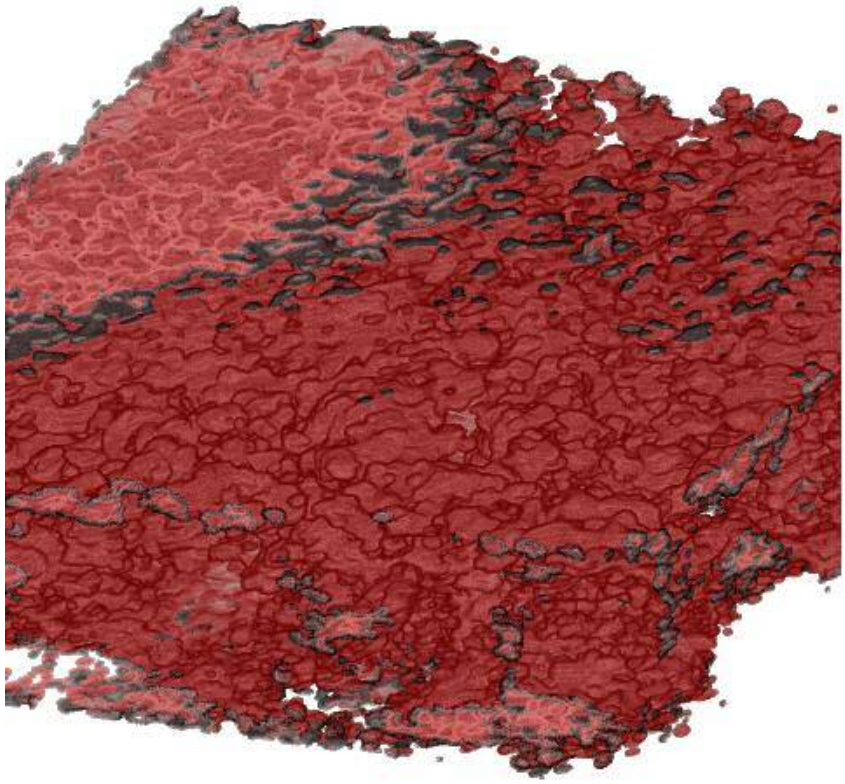

Figure 3.12 A 3-D model of the choroidal vasculature in the 6° 6° volume scan, produced using automated Otsu thresholding to identify the vessel lumen. The vascular structure is largely obscured by high frequency noise in the binarised image.

Unlike the highly-averaged line scans used to establish choroidal area in Section 3.2.3, these volume scans did not undergo averaging, resulting in maintained spatial resolution but a relatively low SNR. Furthermore, the contrast between the vessel lumen and surrounding tissue was low, despite the image enhancement during post-processing (median filtering). This resulted in inconsistent vessel segmentation between image frames, which was not sufficient for subsequent 3-D analysis. It was therefore decided that 3-D structural analysis of the choroidal vasculature was not feasible on this dataset. However, this should be revisited with the advent of swept source long-wavelength OCT, which demonstrates reduced signal roll-off and a higher scanning rate (see Section 1.5.3), facilitating the acquisition of higher quality images than those acquired for this study.

Texture analysis has been shown to be an effective technique for automated extraction of shape and orientation information from OCT images with relatively low contrast and SNR (Koprowski et al. 2013; Srinivasan 2014b; Albarrak et al.

2016). The application of this technique to describing changes to the choroidal structure in AMD is explored in Chapter 5.

3.4 Automated choroidal segmentation

Since the majority of parameters described in Section 3.2 required manual measurement, they were time consuming, relied on an experienced observer, and are likely limited by inter-observer variability (see Section 2.4.2). This in turn limits the feasibility of application of these parameters to clinical assessment. This section therefore evaluates two methods for automated segmentation of the choroidal layer, as a means of producing fast, automated choroidal thickness and volume measurements, with a view to clinical application.

The majority of data presented in this thesis were obtained using a non-commercial long-wavelength OCT, principally due to control of scan parameters (a facility generally restricted on commercial devices) and the increased penetration necessary for choroidal imaging. However, the Topcon DRI OCT Triton was released in Europe in March 2015; after commencement of this work. With the availability of a commercial equivalent of the equipment described in this thesis, it can reasonably be expected that future work would be conducted using such a device, particularly for applications in a clinical setting. The following therefore describes a short investigation of the imaging system capabilities, and the on-board analysis of this device, as well as the performance of a device-independent segmentation software on these images.

3.4.1 Background

As described in Section 3.1, the Iowa Reference Algorithms is device-independent software for multi-layer segmentation of OCT images. In 2015 (version 4.0), a choroidal segmentation module was added, allowing automated choroidal thickness values to be produced for images from multiple OCT devices. Since the commercial devices used in Section 3.1 were not optimised for choroidal imaging, the capabilities of this segmentation were not evaluated. However, a commercial long-wavelength OCT dataset would be ideal for this purpose, since it is optimised for choroidal visualisation in a clinical setting.

The on-board analysis software of the DRI OCT Triton is capable of producing automated segmentation of the choroidal layer on images acquired on the device, within minutes of image acquisition. This can be used to generate choroidal thickness maps which can be reviewed by the clinician.

The aim of the following study was to investigate the intra-session repeatability of both choroidal segmentation algorithms on images from a commercial SS-OCT device, and to determine the agreement in automated choroidal thickness measurements.

3.4.2 Methods and protocols

Healthy participants (n=24) were recruited from staff, students and volunteers at the School of Optometry and Vision Sciences, Cardiff University. All participants had no known ocular pathology. Two 20° 20° (512 256) macular volume scans were acquired from the same eye within a 15 minute period, using the Topcon DRI OCT Triton ($\lambda_c \approx 1050$ nm). Participants did not undergo mydriasis prior to imaging, and images were acquired under minimal room lighting.

All images underwent fully automated choroidal segmentation with the on-board analysis software. AEL data for each participant (measured using an IOLMaster) was entered into the electronic patient record prior to image acquisition, and a correction for biometry was then made automatically by the system during lateral image scaling. The exact correction made is unknown, as this information has not been made available by the manufacturer. All images were also exported from the software, and underwent automated choroidal segmentation using the Iowa Reference Algorithms. Again, AEL-dependent scaling was used to minimise errors associated with ETDRS grid positioning (see Section 3.1).

Mean choroidal thickness in 9 ETDRS subfields was produced for each image using both segmentation methods (Figure 3.13). Bland-Altman plots and CoR were used to assess intra-session repeatability and agreement of automated choroidal thickness measurements produced by the algorithms. The relationship between the absolute choroidal thickness difference between algorithms and mean choroidal thickness was investigated. A least squares linear regression was used to assess the statistical significance of the relationship between mean choroidal thickness and

agreement between segmentation methods (F statistic; P<0.05). A paired samples t-test was also used to determine if the thickness values produced by each algorithm were significantly different (P<0.05). With no correction for multiple comparisons, the chance of finding one or more significant differences in 9 tests was 37%. Therefore, a Bonferroni adjustment was made to account for these multiple comparisons, by reducing the critical value from 0.05 to 0.006 (for n=9 comparisons; Altman 1991).

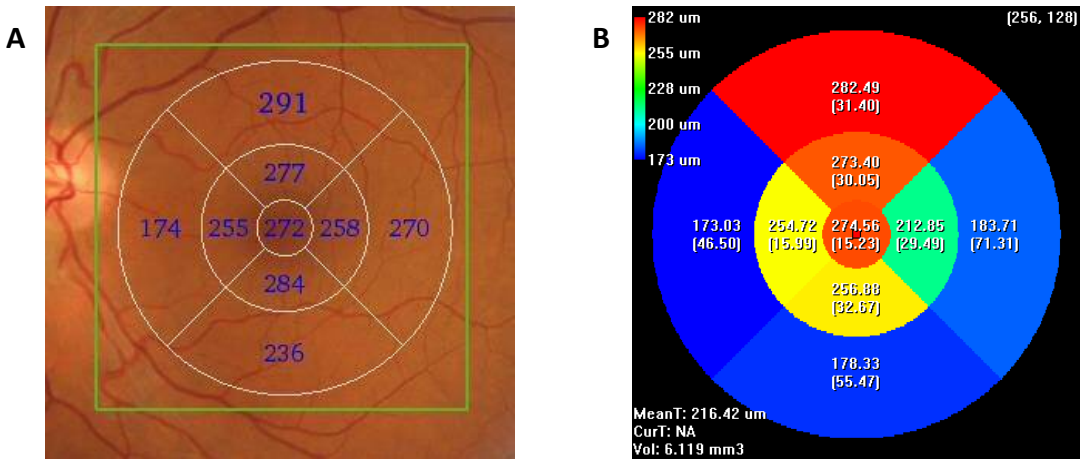

Figure 3.13 Example ETDRS grid overlays from (A) Triton on-board software; mean thickness (µm), and (B) Iowa Reference Algorithms; mean thickness (and SD; µm).

3.4.3 Results

Twenty-four eyes from 24 participants were included in the study. The mean (± SD) age of participants was 34.3 ± 13.5 years (range 19 to 63 years). Thirteen participants were female (54%). An automated segmentation result was produced for all images, by both algorithms.

Mean choroidal thickness for 9 ETDRS subfields is shown in Table 3.10. The Triton on-board segmentation produced greater mean choroidal thickness values than the Iowa Reference Algorithms, in all subfields. The mean difference between algorithms was greater in the temporal and superior subfields, than the nasal and inferior subfields. However, the difference between algorithms was only statistically significant for the S2 subfield, and was no longer significant when a Bonferroni adjustment was applied.

Table 3.10 Comparison of mean choroidal thickness (CT; µm) produced by the two segmentation methods.

ETDRS subfield	Mean CT (Triton on-board segmentation; µm)	Mean CT (Iowa Reference Algorithms; µm)	P (t-test)
F	268	245	0.074
N1	246	232	0.156
N2	193	188	0.511
I1	259	236	0.103
I2	244	220	0.075
T1	268	238	0.061
T2	260	227	0.055
S1	281	245	0.053
S2	275	237	0.033*

***significant at 0.05 level**

There was no significant bias in choroidal thickness in the first and second set of acquired images, for either algorithm (paired t-test; P>0.05 in all cases). The CoR of both segmentation methods is shown in Figure 3.14. CoR was consistently lower for the Triton on-board segmentation than the Iowa Reference Algorithm segmentation, with the exception of the foveal subfield. A representative example of the Bland-Altman plots for each algorithm is shown in Figure 3.15.

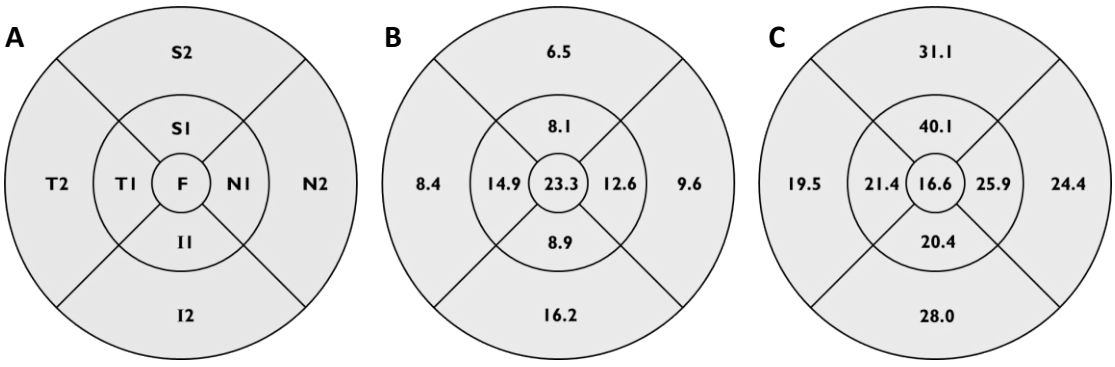

Figure 3.14 (A) ETDRS subfields; F=Foveal, N=Nasal; T=Temporal; S=Superior; I=Inferior. CoR (µm) for mean choroidal thickness values produced by (B) the Triton on-board software, and (C) the Iowa Reference Algorithms.

In general, the CoR was higher for thicker choroids. However, the relationship between absolute difference and mean thickness was only statistically significant for a subset of ETDRS subfields (Table 3.11). These subfields were not

consistent across both segmentation algorithms (N2 for the Triton on-board segmentation, and F and I1 for the Iowa Reference Algorithms).

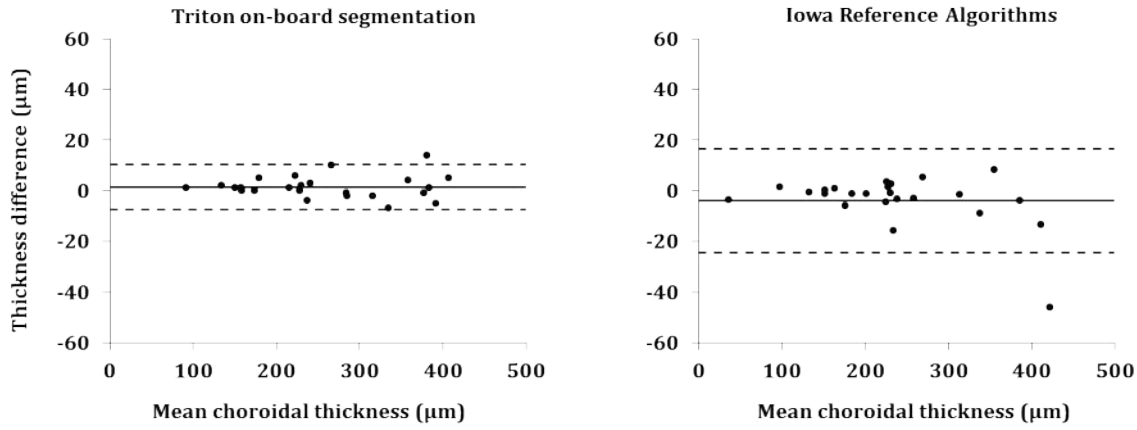

Figure 3.15 Example Bland-Altman plots for intra-session repeatability of both segmentation algorithms; subfield I1 (representative of the 9 subfields). Solid line = mean difference; dashed lines = 95% limits of agreement.

Table 3.11 Mean difference (bias; µm) and 95% limits of agreement (µm) for mean choroidal thickness produced by each segmentation algorithm. P values represent statistical significance of the relationship between mean thickness and absolute difference between algorithms.

ETDRS subfield	Mean difference (µm)	Limits of agreement (µm)	P (F statistic) Triton on-board	P (F statistic) Iowa Ref Algorithms
F	22.3	-91.8 to 136.4	0.019*	0.002**
N1	13.7	-76.1 to 103.6	0.008*	0.232
N2	4.4	-58.7 to 67.5	0.005**	0.148
I1	22.7	-105.6 to 151.0	0.039*	0.004**
I2	23.3	-97.1 to 143.8	0.023*	0.469
T1	29.9	-115.6 to 175.3	0.031*	0.465
T2	33.2	-124.2 to 190.6	0.122	0.887
S1	35.8	-132.6 to 204.2	0.090	0.479
S2	38.1	-123.5 to 199.9	0.179	0.033*

***significant at 0.05 level**

****significant with Bonferroni adjustment**

3.4.4 Discussion

The Triton on-board software demonstrated better repeatability than the Iowa Reference Algorithms for these images. This was likely a result of optimisation

of the segmentation algorithms for images from the parent device. The Iowa Reference Algorithms segmentation failed to accurately identify the posterior choroidal boundary on a number of images (Figure 3.16), resulting in an overall underestimation of mean choroidal thickness and a poorer repeatability. The difference in choroidal thickness between segmentation methods was not statistically significant, although was likely large enough to be considered clinically significant (ranging from 4.4 to 38.1 μm). This bias was more prominent for thicker choroids in several subfields (Table 3.11), where signal roll-off had a greater effect (i.e. it was more difficult to visualise the choroid-scleral boundary). In addition, the mean thickness difference between algorithms was lower in regions where the choroid is physiologically thinner (particularly subfield N2, due to its proximity to the ONH), providing further support for this argument.

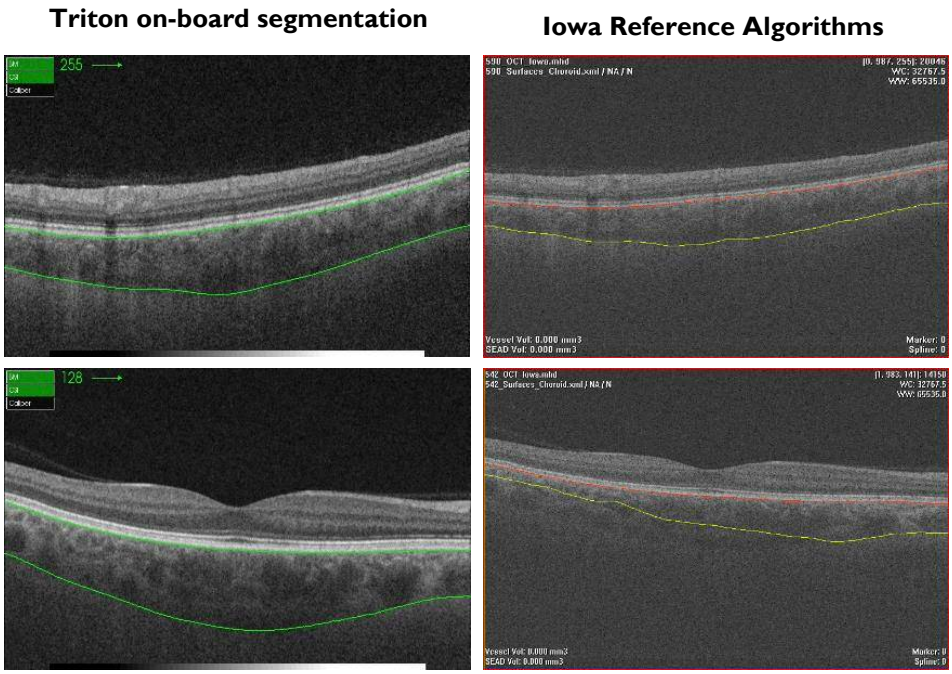

Figure 3.16 Example choroidal segmentations, demonstrating good agreement between algorithms (top row) and poor agreement (bottom row). The images in the left column were exported directly from the Triton on-board review software, where they had undergone automated image enhancement for viewing purposes. The raw image files were imported into the Iowa algorithms (right column); this is why the contrast appears different between segmentation methods.

To summarise, the Triton on-board segmentation produced automated choroidal thickness values with high intra-session repeatability. It is therefore a potential method of automated segmentation of the choroid in healthy eyes, in future work. The Iowa Reference Algorithms had a relatively high frequency of posterior choroidal boundary misplacement, and is therefore not suitable for

automated segmentation of images from the Triton device at this time. It may be possible to optimise the algorithm for these images, or conversely that the images could be manipulated to achieve repeatable segmentation (e.g. image brightness/contrast), although this would require further investigation. It should be noted that the version of the Iowa Reference Algorithms with the facility for choroidal segmentation (version 4.0.0 beta) is an experimental release, undergoing continued improvements. It is investigational software only, and is not approved for clinical use at this time.

The majority of studies within this thesis utilised images acquired using a non-commercial device, which these segmentation algorithms have not been optimised for, and hence would be likely to perform poorly. Additionally, this study included only healthy eyes; a lower repeatability for segmentation of eyes with retinal pathology would be expected, due to reduced visibility of the choroidal boundaries. Therefore, all choroidal segmentation in this thesis was conducted using a manual segmentation protocol, as described and validated in Section 5.1.1.

4 Manual quantification of choroidal vasculature in AMD

Having evaluated the feasibility and inter-session repeatability on healthy eyes (Section 3.2), the eight manual choroidal parameters could now be applied to a dataset of long-wavelength OCT images acquired from individuals with various stages of AMD. By doing this, these parameters could be assessed for their ability to quantify the choroidal structure throughout the disease process (furthering our knowledge of choroidal involvement in the pathogenesis of AMD), and for their diagnostic potential. This chapter describes the process of constructing this dataset, including participant identification and data collection (Section 4.1). A custom protocol for clinical classification of AMD disease severity, adapted from the AREDS classification system (AREDS 2001a), is then described and evaluated (Section 4.2). The results of a demographic analysis of the participants are presented in Section 4.3. All statistical analyses were performed in SPSS (version 20; SPSS Inc., Chicago, IL), unless otherwise stated. Finally, the results from the application of the manual choroidal parameters to the dataset are presented and discussed, in relation to detecting and classifying AMD disease stage based on choroidal vascular structure (Sections 4.4 and 4.5).

4.1 Participants and preliminary measurements

The following section describes the identification and recruitment of participants for this study, as well as the methodology for the preliminary measurements collected. This cohort was used for all analysis in this chapter and Chapter 5; the participant demographics are also described in this section.

4.1.1 Power calculation

To estimate the sample size required to detect a significant difference between the disease groups, a power calculation was performed. Since vessel diameter was a relatively simple parameter, this was used to estimate the required sample size. No published data was available on changes in vessel size in AMD assessed with *in vivo* imaging, therefore the minimum significant difference and

assumed standard deviation were based on histological data. Spraul et al. (1996) reported a mean difference of ~8.5 μm in choroidal vessel diameter between eyes with AMD and age-matched controls. This difference is theoretically possible to detect with the long-wavelength OCT device used, with an axial resolution of ~5 μm in tissue. In the same study, the within-group standard deviation was ~10 μm. This calculation used the Altman Nomogram (Altman 1991) and the following values:

Minimum significant difference (δ): 8.5 μm
Assumed standard deviation (s): 10 μm
Significance level: 95%
Power: 90%

Using these values, the standardised difference (δ/s) was calculated as 0.85. Given the assumptions made in the calculation of standardised difference, a higher power than 80% was selected to increase the probability of correctly rejecting the null hypothesis, if the alternative hypothesis was true (i.e. to correctly identify a difference between disease groups, if such a difference exists). From the Altman Nomogram, a sample size of 25 participants per group was therefore required to detect a significant difference between groups, with a power of 90%, and significance level of 95%.

For validation, a further calculation was performed, based on published data on choroidal thickness measurement from long-wavelength OCT images of eyes with intermediate AMD, nAMD, and healthy controls (Esmaeelpour 2014a). The differences between the disease and healthy groups were 110 μm and 88 μm respectively, the smaller of these differences was used in this calculation, as well as the largest standard deviation of the groups (the healthy group; 95 μm). This yielded a standardised difference of 0.93, resulting in a slightly smaller sample size of 23 participants per group, using the same significance level and power as the previous analysis. Therefore, a sample size of 25 eyes per group was deemed appropriate for the purpose of this research.

4.1.2 Participant identification and recruitment

4.1.2.1 Ethical approval

Ethical approval for this study was received from the South East Wales Research Ethics Committee (Panel D). All participants were provided with a copy of the Participant Information Sheet (Appendix D) prior to deciding whether to take part in the research. There was no time limit between receiving the information and participation in the study (until the end of the data collection period). Written informed consent was obtained from all participants on the day of data collection. The study adhered to the tenets of the Declaration of Helsinki.

4.1.2.2 Participant recruitment

Participants with AMD were primarily identified from patients attending scheduled outpatient appointments in the medical retinal clinic of Mr Ayed Al-Bermani, at the University Hospital of Wales. Additional participants were recruited from Cardiff University Optometrists. Healthy participants who acted as controls for the study were recruited from Cardiff University Optometrists, or were research volunteers at Cardiff University.

4.1.2.3 Inclusion and exclusion criteria

A set of criteria for inclusion in the study, and exclusion criteria, are outlined below. For inclusion in the study, all participants had to meet all inclusion criteria and none of the exclusion criteria.

Inclusion criteria

- Aged 55 years or over
- Male or female
- With or without clinical signs or diagnosis of AMD
- Willing and able to give consent and participate in the study

Exclusion criteria

- Any of the following ocular conditions: glaucoma; ocular hypertension (>21 mmHg); narrow anterior chamber angles (≤Grade 1 with Van Herick);

significant cataract (≥Grade 4 on any criterion with LOCS III); significant corneal or other media opacity; non-AMD related fundus changes.

- Any of the following systemic conditions: diabetes mellitus; neurological disease (e.g. Alzheimer's disease, Parkinson's disease, epilepsy).
- Currently taking medication known to affect retinal function (e.g. chloroquine, tamoxifen).
- Refractive error ≥ ±6.00 dioptres in the most powerful meridian, or astigmatism > 3.00 dioptres.
- Consumption of caffeinated tea or coffee on the day of data collection.

4.1.3 Preliminary measurements

To ensure that participants were suitable for inclusion in the study, a series of preliminary measurements were obtained. The following section is a list of the tests or procedures that were performed prior to OCT image acquisition, in chronological order. All tests were performed on both eyes, where possible, and by a single registered optometric researcher.

Consent, medical and ocular history

Firstly, written informed consent was obtained. Participants were then asked a series of questions about their general health, medication, and ocular history, to ensure that they did not meet any of the exclusion criteria listed in Section 4.1.2.3. The patient's sex, age, and ethnicity were also recorded to ensure that the disease and control groups were demographically similar (see Section 4.3). Patients were also asked to report their history of smoking and anti-VEGF therapy.

Visual acuity

Visual acuity (VA) was measured monocularly using a standard ETDRS logMAR letter chart (Ferris et al. 1982). This was performed at 3 m (the distance for which the chart was calibrated), and reduced to 2 m or 1 m if the patient was unable to read any letters at the standard distance. Participants were encouraged to read as many letters as possible on the chart, and the acuity was measured on an individual letter basis, and recorded in conventional logMAR notation (i.e. each letter was equivalent to 0.02 logMAR).

Anterior chamber angle and pupil mydriasis

The anterior chamber angle was assessed using the Van Herick technique (Van Herick et al. 1969), adjacent to the temporal limbus. To minimise risk of angle closure glaucoma induced by pupil mydriasis, participants with narrow anterior chamber angles (Grade 0 or 1) did not undergo mydriasis, and were excluded from the study. For those with Grade 2 or above, both pupils were dilated using 1 drop of Tropicamide 1%. The drug expiry date, batch number, and time of instillation were recorded.

Media assessment

The intra-ocular media (cornea, anterior chamber, lens, and anterior vitreous) were assessed for clarity using slit lamp biomicroscopy. The LOCS III grading system (Chylack et al. 1993) was used to quantify the extent of any opacities in the crystalline lens (nuclear, cortical and posterior subcapsular opacities were graded separately). Eyes with LOCS III Grade 4 or above in any criterion were excluded, as were those with significant corneal opacities. This relatively high grade was selected due to the enhanced performance of long-wavelength OCT in the presence of media opacities, when compared to conventional-wavelength OCT (Povazay et al. 2007).

Axial eye length

Axial eye length (AEL) was measured using optical biometry (IOLMaster). An average of 5 measurements was calculated to ensure measurement accuracy. AEL was used to establish accurate lateral scaling of OCT images for each eye (see Section 3.1).

Refractive error

An objective measure of refractive error was obtained using autorefraction (KR-7500 Autokeratorefractor; Topcon, Tokyo, Japan). An average of 3 measurements was used and the spherical and cylindrical components of the refraction were recorded. The mean spherical refraction was calculated as the spherical component plus half of the cylindrical component. Eyes with a refractive error over ±6.00 dioptres in the most powerful meridian, or astigmatism over 3.00 dioptres, were excluded from the study.

Intra-ocular pressure

Intra-ocular pressure (IOP) was measured as an average of 4 reading acquired using a non-contact tonometer (CT80; Topcon, Tokyo, Japan). Eyes with an IOP >21 mmHg were classed as outside the normal range, as defined by the NICE guidelines (National Institute for Health and Care Excellence 2009), and were excluded from the study.

Retinal photography

Retinal photographs were obtained using a Topcon 3D-OCT 1000 (Topcon, Tokyo, Japan). Images were 45° in diameter, centred on the fovea. These photographs were used to establish the disease classification of each eye in the study, according to the protocols described in Section 4.2.

Blood pressure

Blood pressure (BP) was measured using an automated sphygmomanometer (Omron M5-I; Omron Corporation, Kyoto, Japan). A total of 3 readings from the left arm were averaged (systolic and diastolic), following a 5 minute seated rest period. This directly preceded image acquisition using the long-wavelength OCT.

Study eye selection

If one eye of a participant met any of the exclusion criteria, the other eye was automatically selected as the study eye. If both eyes met none of the exclusion criteria, one eye was randomly selected as the study eye. Disease classification of the fellow eye was noted, but was not used for selection of the study eye (other than in the healthy control group, where neither eye had a classification of AMD).

4.2 Clinical classification methodology

As discussed in Section 1.4.7, imaging technology, understanding of AMD pathophysiology, and clinical requirements have changed since the development of the majority of classification systems (Klein et al. 1991; Bird et al. 1995; AREDS 2001a; Ferris et al. 2013; Danis et al. 2013). Some aspects of these systems are now either inappropriate or not feasible for use in the contemporary clinical/research environment (e.g. stereoscopic retinal photography). Furthermore, OCT is an

imaging modality ideal for cross-sectional visualisation of the retina, and is now commonplace in the clinical environment, but is yet to be incorporated into a widely used classification system. The following section describes the protocol developed for categorising participants into disease groups for this thesis.

The proposed protocol utilised three sources of data available to the researchers; retinal photography, OCT imaging, and ophthalmological diagnosis, with categorisation based on established AREDS definitions (AREDS 2001a). The definitions of macular regions and retinal features were kept largely in line with those established by the AREDS classification system, to maximise consistency and comparability with existing literature and practice.

4.2.1 Retinal photography

Retinal photographs (45°) obtained with a Topcon 3D-OCT 1000, centred on the fovea, were inspected. The photographs were viewed in a randomised order in PowerPoint (Microsoft, Richmond, WA). The image size could be adjusted at user discretion using the zoom function, and no time limit was set for assessing each image. Overlays of predetermined sizes were provided that could be moved freely across the images (but not resized). These were used to display the macula regions

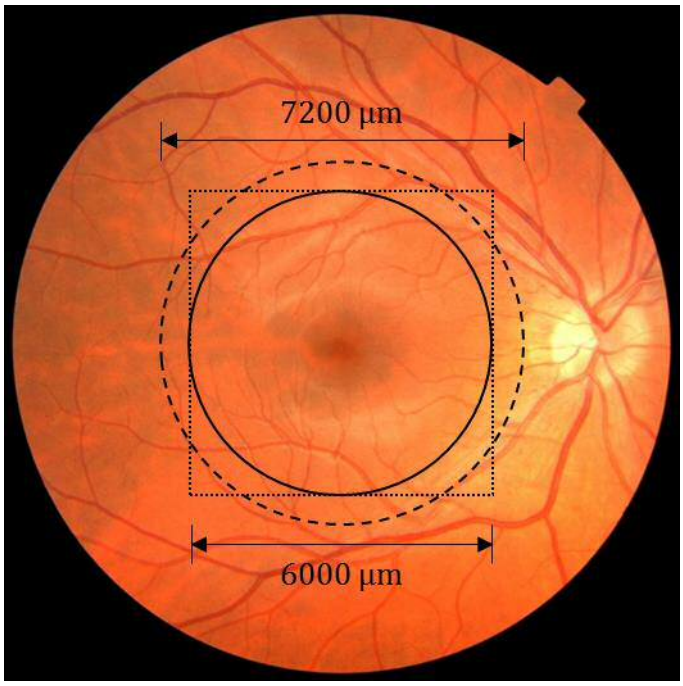

Figure 4.1 A 45° retinal photograph showing the outer boundary of the ETDRS grid, as defined by AREDS (solid line) and AREDS2 (dashed line). The size of a 20° 20° OCT volume scan is shown by the dashed square, assuming an AEL of 24.5 mm.

defined by the ETDRS grid, and to determine the size of retinal lesions, such as atrophy, drusen or pigmentary disturbances. These overlays were sized according to the definitions set out by the AREDS classification (AREDS 2001a). AREDS2 definitions were not used, as these define the macular region as 7200 μm in diameter, which is larger than the OCT images collected as part of this dataset (Figure 4.1).

4.2.2 OCT imaging

The second step was inspection of 20° 20° (512 512) long-wavelength (1040 nm) OCT images, centred on the fovea. These were presented in Fiji software, in conjunction with the corresponding retinal photograph, for verification purposes. This was to ensure that signs of AMD not detected in the retinal photograph (particularly subtle signs of nAMD) were not overlooked due to lack of stereopsis. Again, the zoom function could be used freely, as could adjustment of brightness and contrast. Two optometrists were selected to grade a total of 149 images, and were masked to patient identity and data. In cases of disagreement, a classification by a third optometrist was used, and the three graders met to discuss each case and determine a final classification. If agreement could not be reached, the image was deemed ungradable. The classification criteria based on retinal appearance for both imaging modalities are shown in Table 4.1.

Since the aim of this research was to assess parameters for their ability to quantify the choroidal structure with advancing disease, the severity groups used in the clinical classification were intentionally coarse. Furthermore, the exclusion criteria for media opacities in this study was not particularly stringent (LOCS III, Grade 4 or above), possibly resulting in a subset of retinal photographs of sub-optimal quality to allow accurate grading with the 9-point scale utilised in the AREDS system (Davis et al. 2005). The disease status of the fellow eye was not considered during the classification process (as in the AREDS simplified severity scale; Ferris et al. 2005).

Table 4.1 Classification criteria for the three disease groups. Area definitions from AREDS (2001a): I-1 = 180 µm diameter; C-1 = 125 µm diameter; C-0 = 63 µm diameter.

Class	AREDS Level	Photograph Criteria	OCT Criteria
Neovascular AMD (nAMD)	4 (advanced)	Presence of **ANY** of the following: Fibrovascular/serous PED, Serous sensory retinal detachment, Subretinal/RPE haemorrhage, subretinal fibrous tissue, Photocoagulation for AMD	Presence of **ANY** of the following: Fibrovascular/serous PED, Serous sensory retinal detachment, Subretinal/RPE haemorrhage, subretinal fibrous tissue, Photocoagulation for AMD
Geographic atrophy (GA)	4 (advanced)	Sharply demarcated depigmentation in central subfield, area > I-1 **AND** no signs of nAMD	Depigmentation at fovea, diameter > 11 pixels laterally **AND** no signs of nAMD
Early AMD	2 and 3	No signs of GA or nAMD **AND** drusen max size ≥ C-0 **OR** drusen total area ≥ C-1 **OR** pigmentary changes, area ≥ C-1	No signs of GA or nAMD **AND** presence of drusen, max size ≥ 4 pixels laterally **OR** pigmentary changes, area ≥ 7 pixels laterally
Normal	1	No signs of GA or nAMD Drusen max size < C-0 **AND** drusen total area < C-1	No signs of GA or nAMD **AND** no drusen ≥ 4 pixels laterally in size present
Ungradable	N/A	Unable to determine a classification	Unable to determine a classification

4.2.3 Ophthalmological diagnosis

The final aspect of this classification protocol was diagnosis by a consultant ophthalmologist. This was only used to determine a classification of inactive nAMD, following anti-VEGF treatment. In some cases, these patients have very few or no remaining signs of a previous neovascular episode, and may be misclassified as early AMD or even healthy if a classification is based solely on retinal appearance. This was used to override classification by the graders in these cases.

4.2.4 Evaluation of classification system

A total of 149 eyes of 77 participants were classified using this approach, to evaluate the robustness of the classification system. Each eye was classified according to the above protocol, and assigned to one of five categories; normal, early

AMD, nAMD, GA, or ungradable (as defined in Table 4.1). Agreement of the two primary graders was achieved on 122 of these eyes (~82%; Table 4.2). Almost half of the images were of the non-study eye, which were classified to allow further sub-analysis of fellow eye diagnosis. Since fellow eyes were not subject to the exclusion criteria used for the study eye (e.g. media clarity), images from these eyes were often of sub-optimal quality and more likely to be ungradable.

Table 4.2 Inter-grader agreement for classification of all eyes classified during the evaluation of this grading system (n=149). Areas of agreement between graders are highlighted in grey.

		Grader 1				
		Normal	Early AMD	nAMD	GA	Ungradable
Grader 2	Normal	43	4	0	0	0
	Early AMD	3	31	5	1	0
	nAMD	0	1	38	2	3
	GA	0	3	4	7	0
	Ungradable	0	1	0	0	3

The study eye of each participant was selected as described in Section 4.1.3 (n=75). Considering the classification of these eyes only, agreement between the primary graders was achieved on 64 of 75 eyes (~85%; Table 4.3). The largest source of disagreement between graders was the early versus nAMD classification; 5 of the eyes that were classified as nAMD by Grader 1 were classified as early AMD by Grader 2. A potential source of these disagreements was the misclassification of large confluent drusen as drusenoid PED in the OCT images, and the differentiation of inactive nAMD (following anti-VEGF therapy) from early disease. These were the main sources of discussion between the three graders concerning disagreements, prior to final classification decisions.

This final classification stage rendered this classification system suitably robust for use in this research. Following the group discussion, there were 25 eyes classified into each group (healthy, early AMD, and nAMD), agreed upon by all graders. Eyes classified as GA or ungradable were not used in further analysis.

Table 4.3 Inter-grader agreement for classification of the 75 study eyes used in further analysis. Areas of agreement between graders are highlighted in grey.

		Grader 1				
		Normal	Early AMD	nAMD	GA	Ungradable
Grader 2	Normal	25	1	0	0	0
	Early AMD	2	22	5	0	0
	nAMD	0	0	17	1	0
	GA	0	1	1	0	0
	Ungradable	0	0	0	0	0

4.3 Participant demographics

A summary of participant demographics is shown in Table 4.4. There were a total of 25 participants classified in each group, all of which self-identified as 'white British'. There was no statistically significant difference in the proportion of males in each group, nor the proportion of right eyes, pseudophakic eyes, or participants with a history of smoking (Chi-squared test; $P>0.05$). There was also no statistically significant difference in age, AEL, refractive error, IOP, systolic BP, diastolic BP, or time of day of image acquisition between groups (1-way ANOVA or Kruskal-Wallis test; $P>0.05$ in all cases).

VA was significantly poorer in the nAMD group than the other two groups (Kruskal-Wallis test; $P<0.001$), although there was no significant difference between the healthy and early AMD groups. Many of the participants in the early AMD group may therefore be asymptomatic and, without having undergone ophthalmological examination, may have been unaware of their condition. This highlights the importance of thorough macular assessment in this age group, to identify those at risk of developing nAMD, and to inform clinical advice and monitoring.

Table 4.4 Summary of participant demographics for the 3 groups. Binary parameters are given as a percentage, and were tested for significance using a Chi-squared test. Other parameters are given as mean ± SD, and were tested for significance using a 1-way ANOVA (parametric) or Kruskal-Wallis test (non-parametric#). For VA, post hoc Dunn-Bonferroni analysis revealed that the nAMD group was significantly greater than the other two groups.

Parameter	Healthy	Early AMD	nAMD	p
n	25	25	25	-
Ethnicity (% Caucasian)	100	100	100	-
Sex (% male)	44	48	36	0.683
Test eye (% right eye)	48	60	48	0.618
Pseudophakic (%)	12	28	32	0.215
History of smoking (%)	48	52	44	0.852
Age (years)	73.3 ± 7.9	76.3 ± 7.6	77.7 ± 8.3	0.141
AEL (mm)	23.44 ± 0.63	23.45 ± 0.95	23.52 ± 0.95	0.927
Refractive error (dioptres)#	1.19 ± 1.66	0.30 ± 1.58	0.88 ± 1.82	0.342
VA (logMAR)#	0.05 ± 0.14	0.06 ± 0.14	0.37 ± 0.37	<0.001*
IOP (mmHg)	13.8 ± 2.2	14.2 ± 3.7	15.0 ± 2.8	0.356
BP - systolic (mmHg)#	143.0 ± 23.3	149.0 ± 22.6	145.1 ± 23.0	0.773
BP - diastolic (mmHg)#	77.0 ± 13.2	77.4 ± 9.1	79.1 ± 10.3	0.594
Time of day#	11:37 ± 01:26	12:08 ± 01:28	12:11 ± 01:36	0.284

***significant at 0.05 level**

#non-parametric statistical test applied

In the nAMD group, the mean number of anti-VEGF injections to the study eye was 10.2 ± 5.9 (range 0 to 25). Of the 25 eyes, 23 were currently undergoing anti-VEGF therapy; this is high due to the method of participant identification. It is unknown which anti-VEGF agent(s) were used to treat each eye, as well as the treatment duration. The remaining 2 eyes were treatment-naïve. Since access to treatment records were not available for this study, this data was based on self-reported treatment history, and should therefore be interpreted with caution.

Where possible, the fellow (non-study) eye was also classified according to the classification protocol described in Section 4.2. A summary of these is presented in Table 4.5. In total, 8 fellow eyes were ungradable. In the healthy group, this was due to presence of epiretinal membrane (n=3), or atypical retinal appearance not attributed to AMD (n=2). In the AMD groups, these represented previous trauma (n=1), toxoplasmosis scar (n=1), or retinal appearance atypical of AMD (n=1). A total of 4 fellow eyes did not undergo classification, since no OCT images were available.

This was due to refractive error outside the imaging capabilities of the OCT device (n=1), previous trauma resulting in no fundus view (n=1), or unilateral imaging at the request of the participant (n=2).

Over half of the participants in the early AMD group had a fellow eye classification of nAMD. This was likely due to the primary source of participant recruitment, since the majority of patients attending the ophthalmology clinic had a diagnosis of nAMD and were receiving anti-VEGF therapy. However, if changes to the choroid precede development of CNV, these may be evident bilaterally, and may therefore have an effect on the appearance of the vascular structure in the fellow eye. Analysis of fellow eye diagnosis was therefore performed to investigate this potential effect.

Table 4.5 Fellow eye status for all participants included in the study. Bilateral classifications (i.e. both eyes with the same disease stage) are highlighted in grey.

		Study eye		
		Healthy	Early AMD	nAMD
Fellow eye	Healthy	18	4	6
	Early AMD	0	7	0
	nAMD	0	12	13
	GA	0	0	3
	Ungradable	5	1	2
	Not classified	2	1	1
Total		25	25	25

4.4 Manual choroidal vasculature quantification results

4.4.1 Between-group comparison

The parameters described in Section 3.2 were obtained from all images in the dataset described in Section 4.3 (n=75) by a single observer. To maximise the accuracy of measurements, an observer experienced with acquiring and analysing long-wavelength OCT images was selected. Although this observer was an optometrist with experience in interpretation of OCT images, they were masked to the disease classification of the images (as established in Section 4.2) to minimise any bias in quantification. The order in which images were analysed was randomised for each choroidal parameter evaluated.

The mean value (±SD) of each parameter for each disease group is shown in Table 4.6. These are presented as bar charts in Figure 4.2, with error bars representing standard error of the mean (SE), and significant differences between groups indicated with an asterisk (*).

Table 4.6 Mean (±SD) measurement for each parameter describing the choroidal vasculature, for the three disease groups. Significance was tested using a 1-way ANOVA (parametric) with post-hoc Bonferroni, or Kruskal-Wallis test (non-parametric#) with post-hoc Dunn-Bonferroni. The significant differences were between the healthy and nAMD group, and the early AMD and nAMD group, in all cases where P<0.05. SFCT = subfoveal choroidal thickness; VVD = visible vessel diameter; VR = vessel ratio; CA = choroidal area; LA = luminal area; CVI = choroidal vascularity index; LAR = luminal area ratio; LPR = luminal perimeter ratio.

Parameter	Mean (±SD) measurement			p
	Healthy	Early AMD	nAMD	
SFCT (μm)	237.2 ± 88.9	255.7 ± 103.1	163.2 ± 61.8	0.001*
VVD (μm)	133.8 ± 33.6	140.7 ± 35.0	118.4 ± 30.0	0.056
VR#	0.606 ± 0.157	0.609 ± 0.185	0.780 ± 0.214	0.001*
CA (mm^2)	0.311 ± 0.103	0.317 ± 0.106	0.225 ± 0.086	0.002*
LA (mm^2)	0.223 ± 0.076	0.230 ± 0.078	0.158 ± 0.064	0.001*
CVI#	0.718 ± 0.031	0.725 ± 0.048	0.698 ± 0.064	0.308
LAR	0.560 ± 0.040	0.567 ± 0.042	0.552 ± 0.052	0.519
LPR	0.112 ± 0.009	0.110 ± 0.011	0.107 ± 0.011	0.197

***significant at 0.05 level**

#non-parametric statistical test applied

SFCT was significantly lower in the nAMD group than both the healthy and early AMD groups (Figure 4.2A). There was no statistical significance between the healthy and early AMD groups. VVD was also lower in the nAMD group than the other two groups; although this did not reach statistical significance (Figure 4.2B; P=0.056). VR was significantly higher in the nAMD group than the healthy and early AMD groups (Figure 4.2C). Again, there was no significant difference between the healthy and early AMD groups.

In the 2-D analysis (Figure 4.2D-F), choroidal area and luminal area were significantly lower in the nAMD group than both the healthy and early AMD groups. There was no significant difference between the healthy and early AMD groups. CVI was lowest in the nAMD group, although this difference did not reach statistical significance (P=0.308).

In the enface analysis (Figure 4.2G-H), LAR was not significantly different between the three groups. LPR showed a general negative trend with advancing disease stage, although this did not reach statistical significance (P=0.197).

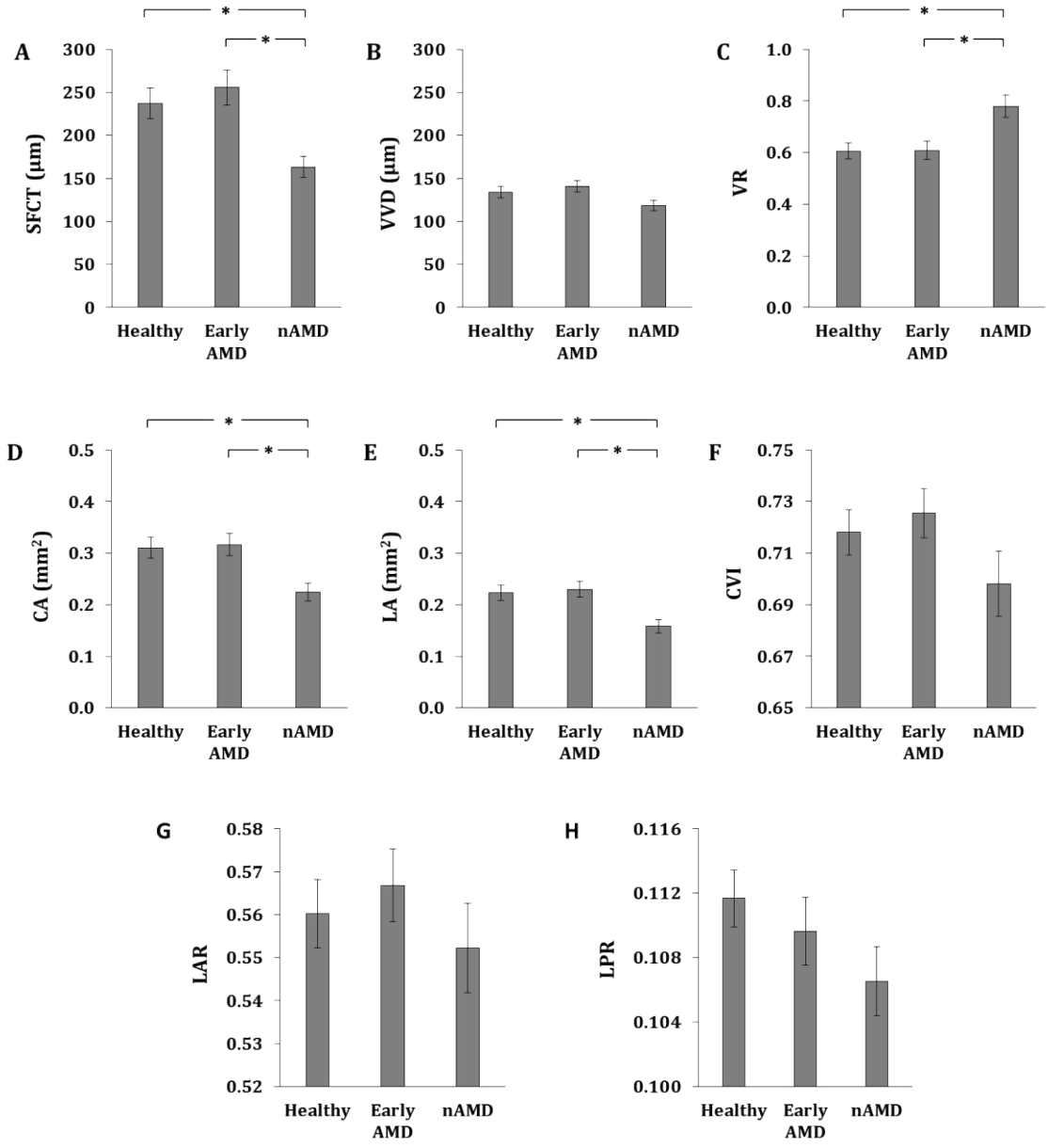

Figure 4.2 Mean values (± SE error bars) for (A) SFCT, (B) VVD, (C) VR, (D) CA, (E) LA, (F) CVI, (G) LAR, and (H) LPR, for the three disease groups. SFCT = subfoveal choroidal thickness; VVD = visible vessel diameter; VR = vessel ratio; CA = choroidal area; LA = luminal area; CVI = choroidal vascularity index; LAR = luminal area ratio; LPR = luminal perimeter ratio. *significant at 0.05 level.

4.4.2 Relationship with fellow eye diagnosis

To investigate the relationship with fellow eye status, the early AMD group was subdivided into three subgroups based on diagnosis of the fellow eye; no AMD

(n=4), early AMD (n=7), and nAMD (n=12). The parameters showing a significant difference (or near-significant in the case of VVD) between disease groups in the previous analysis were compared between these subgroups, to identify the presence or absence of a gross relationship between fellow eye diagnosis and choroidal structure. Since the groups were small, between-group differences were evaluated subjectively, and no statistical analyses were performed.

The mean value of each parameter for each disease subgroup is shown in Figure 4.3, with error bars representing standard error of the mean. In general, SFCT was higher for early AMD eyes with healthy fellow eyes, than for bilateral early AMD or fellow eye nAMD. VR was lowest for the healthy fellow eye subgroup. There was little difference between subgroups for VVD, CA, or LA. There was also little difference between those with a fellow eye status of early AMD or nAMD, for any of the parameters.

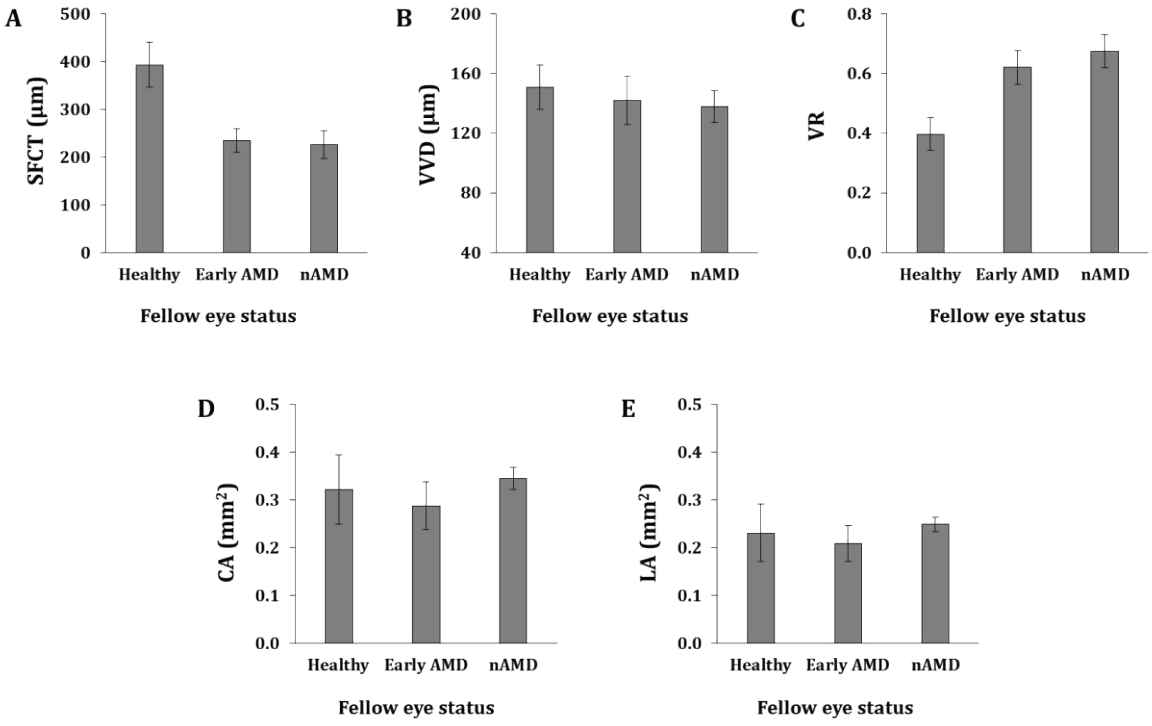

Figure 4.3 Mean values (± SE error bars) for eyes in the early AMD group, sub-divided by fellow eye diagnosis. SFCT = subfoveal choroidal thickness; VVD = visible vessel diameter; VR = vessel ratio; CA = choroidal area; LA = luminal area.

4.4.3 Diagnostic potential

To investigate the diagnostic ability of the parameters, receiver operating characteristic (ROC) curves were produced (Figure 4.4). ROC curves are for dichotomous data (i.e. two groups), although this study had three disease groups. A one-versus-all approach was therefore used; since there was little difference in the parameter means and standard deviations between the healthy and early AMD groups (Table 4.6), these were pooled into a single group for this analysis. The ability to differentiate between nAMD and non-nAMD would likely be of greatest clinical value, since treatment is currently available only for the neovascular subtype. Reliable identification of this subtype through choroidal structure could be of potential benefit in triaging patients through referral refinement schemes, or in monitoring stable AMD in 'virtual' macular clinics in the hospital eye service. This could theoretically enhance prioritisation of patients requiring further ophthalmological assessment and/or treatment, whilst minimising the number of 'false positive' referrals into secondary care.

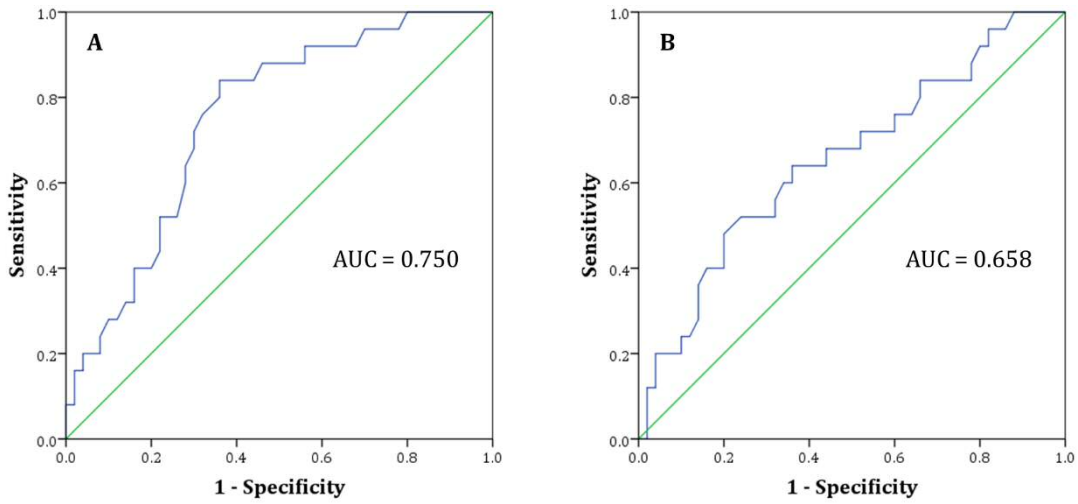

Figure 4.4 Example receiver operating characteristic (ROC) curves assessing diagnostic potential for (A) SFCT and (B) VVD. AUC = area under the curve; SFCT = subfoveal choroidal thickness; VVD = visible vessel diameter.

This analysis was performed only on those parameters with statistically significant differences (or near-significant in the case of VVD) between disease groups. A total of 5 parameters were therefore investigated further; SFCT, VVD, VR, CA, and LA.

The diagnostic potential of each parameter to predict a classification of nAMD on the entire dataset (n=75) was assessed using the area under the curve (AUC). AUC ranged from 0.762 for VR to 0.658 for VVD. The optimum cut-off for

prediction of nAMD with each parameter was determined subjectively as the point maximising sensitivity and specificity (i.e. the point on the ROC curve closest to the top left corner). These values are presented in Table 4.7.

Table 4.7 The optimal cut-off value for each parameter to predict a classification of nAMD with maximum accuracy. Parameters are ordered by AUC (descending). SFCT = subfoveal choroidal thickness; VVD = visible vessel diameter; VR = vessel ratio; CA = choroidal area; LA = luminal area.

Parameter	AUC	Optimal cut-off	Sensitivity (%)	Specificity (%)
VR	0.762	0.635	80	66
SFCT	0.750	198.8 μm	84	64
LA	0.748	0.198 mm^2	76	64
CA	0.743	0.263 mm^2	76	68
VVD	0.658	127.4 μm	64	64

4.5 Discussion

A total of eight parameters describing the choroidal vascular structure were applied to a dataset of long-wavelength OCT images acquired from eyes without AMD (n=25), with early AMD (n=25), and with nAMD (n=25). A significant difference between the nAMD group and the other two groups was identified in the SFCT, VR, CA, and LA parameters. The difference in VVD between groups was nearing statistical significance (P=0.056). No significant difference between the healthy and early AMD groups was identified with any parameter evaluated.

Considering SFCT firstly, the choroid was significantly thinner in the nAMD group than the healthy group (163.2 ± 61.8 μm and 237.2 ± 88.9 μm respectively; Figure 4.2A). This was equivalent to a mean difference between groups of ~75 μm (~32%); comparable to previously reported values of ~53 μm (Chung et al. 2011), ~88 μm (Esmaeelpour 2014a), and ~95 μm (Lu et al. 2016). However, it should be noted that the majority of participants in the nAMD group of the present study were undergoing (or had previously undergone) anti-VEGF therapy. This study was limited by the lack of treatment history data; the number of injections were self-reported, and anti-VEGF agent and treatment duration were unknown.

Anti-VEGF therapy has been associated with a reduction in choroidal thickness, with reported mean decreases in thickness of 10-25 μm following a 12 month treatment period (Yamazaki et al. 2012; Ting et al. 2016; Section 1.4.6). This

reduction in choroidal thickness was identified in the first 6 months of treatment only, with no further change over the following 6 months. The mean number of anti-VEGF injections in these studies after the 12 month period were 5.8 ± 2.9 and 5.6 ± 2.1 respectively, although there was no relationship between number of injections and decrease in choroidal thickness over time. However, it is unknown if this trend would extend to the mean number of injections in the present study (10.2 ± 5.9). Although the mean difference in SFCT between the treated nAMD and healthy groups of the present study (~75 μm) exceeded these reported longitudinal changes, it is not possible to separate choroidal changes associated with the pathology from changes resulting from pharmacological intervention. Any conclusions regarding the aetiology of the choroidal changes observed in the nAMD group would therefore be speculative. Further work would be required to investigate the effects of anti-VEGF therapy on choroidal structure and to differentiate these from changes associated with the underlying pathology.

In keeping with previous literature, no difference in SFCT was identified between early AMD (255.7 ± 103.1 μm) and healthy age-similar controls (Wood et al. 2011; Kim et al. 2011; Lee et al. 2013b; Jonas et al. 2014; Lu et al. 2016). The mean and standard deviation of SFCT were comparable to previously reported values for healthy and early AMD groups (Wood et al. 2011), and for all three disease groups (Esmaeelpour 2014a), with both studies utilising a non-commercial long-wavelength OCT device, similar to the one used in this thesis.

The mean difference in VVD between the healthy and nAMD groups was ~15 μm (~11%), although this did not reach statistical significance (Figure 4.2B). This may be due to the large within-group variation in VVD, and more data would likely be required to investigate this parameter further. The mean VVD in the healthy group was 133.8 ± 33.6 μm; this is similar to the control group of previous studies of vessel diameter in CSC, with reported mean values of 140 ± 40 μm (Yang et al. 2013) and 160 ± 32 μm (Bittencourt et al. 2014). The mean ages of these groups were 47 and 30 years respectively, whereas the mean age of the healthy group in the present study was 73 years. This difference may explain the lower mean vessel diameter in this thesis, since age has been shown to negatively correlate with vessel diameter (Bittencourt et al. 2014).

Since the mean differences between groups were not known at the start of this research, the power calculation was performed using an estimate of this value and the within-group standard deviation (see Section 4.1.1). To detect such a small difference between groups with high standard deviation, with the power and significance level used, a far larger sample size would be required. Given the difference in the mean VVD between the healthy and nAMD groups of the present study (~15 μm), and the within-group standard deviation (~33 μm), a sample size of 75 participants per group would be required for a power of 80% and a 95% significance level (Altman 1991).

The VR was significantly higher for the nAMD group than the other two groups (Figure 4.2C). In nAMD, the mean diameter of the largest choroidal vessels was 78% of the SFCT, compared to 61% in both the healthy and early AMD groups. The mean VR of the healthy group was very similar to a previously reported value of 61 ± 1% in healthy eyes (Bittencourt et al. 2014). There is no published data on vessel diameter or vessel ratio measured *in vivo* in AMD for comparison.

Considering the 2-D analysis (Figure 4.2D-F), CA and LA were both significantly lower in the nAMD group than the other two groups. The mean CA was ~28% lower in the nAMD group than the healthy group, whilst the mean LA was ~29% lower. CVI was also lowest for the nAMD group, although this difference did not reach statistical significance. Again, this may be due to large within-group variation.

Comparing to the existing literature, mean values of CA and LA in the healthy group (0.311 mm^2 and 0.223 mm^2 respectively) were similar to values reported by Gupta et al. (2017) of 0.452 mm^2 and 0.241 mm^2 respectively, following the same measurement protocol. The lower CA in the present study may be explained by the lower mean SFCT (237 ± 89 μm versus 302 ± 63 μm) or the higher mean participant age (73 ± 8 versus 60 ± 7 years). Wei et al. (2016) found CVI to be reduced in eyes with nAMD by an average of 0.026, compared to the fellow eye with early AMD. This is highly comparable to the current study, where a mean difference of 0.027 was found between the early and nAMD groups. However, the absolute mean value and within-group variation of CVI in the nAMD group were higher in the present study (0.698 ± 0.064 compared to 0.601 ± 0.046). Since the same measurement protocol was followed, this difference may (in part) be attributed to the different OCT devices

used in these studies, possibly due to the wavelength-dependent reflectivity properties of the choroidal structures.

For the enface analysis, no significant difference was found between any of the three groups, for both LAR and LPR (Figure 4.2G-H). However, there was a general decrease in LPR with advancing disease stage. Again, the within-group variation was high in relation to the between-group variation, which is likely why this difference did not reach statistical significance. An arbitrary depth of 50% in the choroid was used for this analysis, to ensure sufficient vessel resolution (i.e. to avoid inclusion of the small vessels of the choriocapillaris nearing the resolution limit of the OCT), and to minimise inclusion of the sclera at the edges of the enface image (see Section 3.2.4). However, the use of this fixed percentage depth would not be sensitive to disease-related changes in vessel structure localised to other choroidal depths, for example at the level of choriocapillaris. Since these vessels are too small to resolve with this OCT, the parameters evaluated here would not be suitable for quantifying the vascular structure. Other image analysis methods such as texture analysis may be utilised for this purpose, as explored by Sohrab et al. (2012). This approach is employed in the machine learning methodology, as a way of extracting feature information from the OCT images (see Section 5.1.2).

The early AMD group was sub-divided by fellow eye diagnosis, to investigate a potential relationship between fellow eye diagnosis and choroidal structure in this cohort. There was little difference between the three subgroups for VVD, CA, or LA. This suggests that fellow eye diagnosis did not influence these parameters, although the power of the sub-analysis is greatly reduced. However, the choroid was thicker in eyes with no signs of AMD in the contralateral eye than the other two groups. Assuming these individuals had relatively few signs of early AMD in the study eye (mild degenerative changes) compared to those with bilateral early AMD (including intermediate degeneration), this may indicate a level of symmetry in choroidal vessel changes with progression of early AMD. There was little difference between eyes with bilateral early AMD and those with fellow eye nAMD. If vessel abnormality is part of the pathogenesis of nAMD, choroidal changes would be expected to be more advanced in cases of fellow eye nAMD. This is the basis for the AREDS simplified scale, which takes into account fellow eye diagnosis for 5-year risk prediction (Ferris et al. 2005). However, this was not the case for this cohort. The

high proportion of fellow eye nAMD in this sample is therefore unlikely to contribute significantly to the inter-group findings. However, it should be noted that these subgroups were small, and larger sample sizes would be required to investigate this relationship further.

The five parameters assessed diagnostically provided reasonable ability to predict a classification of nAMD (AUC ranging from 0.658 to 0.762; Table 4.7). The parameters showing greatest diagnostic potential were SFCT and VR. The optimal SFCT cut-off to predict a classification of nAMD was 200 μm, achieving a sensitivity of 84% and specificity of 64%. These values are not feasible for a clinical test, due to the frequency of false positives and negatives. However, SFCT is simplest and quickest measurement to perform, and provides one of the most accurate predictions of the parameters evaluated. Although it is of limited potential as a standalone biomarker, it may be a useful parameter to be used in conjunction with other clinical information to inform clinical follow-up (i.e. monitoring of those individuals likely to develop CNV). Further work would be required to investigate the optimum combination of potential structural and functional parameters for this purpose. However, it should also be noted that the majority of eyes in this group were of treated nAMD, and the change in choroidal structure in the nAMD group was likely attributed (at least in part) to anti-VEGF therapy rather than pathological change. This was therefore not a test of true diagnostic ability (which would be based on treatment-naïve eyes).

The other structural parameters assessed in this chapter were limited in their ability to predict the disease classification, due to their relatively low sensitivity and specificity for a clinical test. Additionally, they require manual measurement of the vessels, which may not be practical for a clinical setting and may result in high inter-observer variability, and they offer no distinct advantage over the measurement of SFCT. To automate the disease group predictions, and to maximise sensitivity and specificity, the use of machine learning is explored in Chapter 5. This allows the development of a more complex model for predicting disease classification, which may also be sensitive to subtle differences in choroidal structure in the early disease stage, not detectable with the parameters evaluated in this chapter.

5 Automated disease stage classification using machine learning

As discussed in Sections 2.4.2 and 3.2.5, manual choroidal parameter measurement is limited by several factors, including intra- and inter-observer variability, 2-D sampling of the 3-D vessel structure, and clinical feasibility of time-consuming measurement protocols. This section describes the development of machine learning protocols for automated classification of AMD by disease severity, as outlined in Figure 5.1.

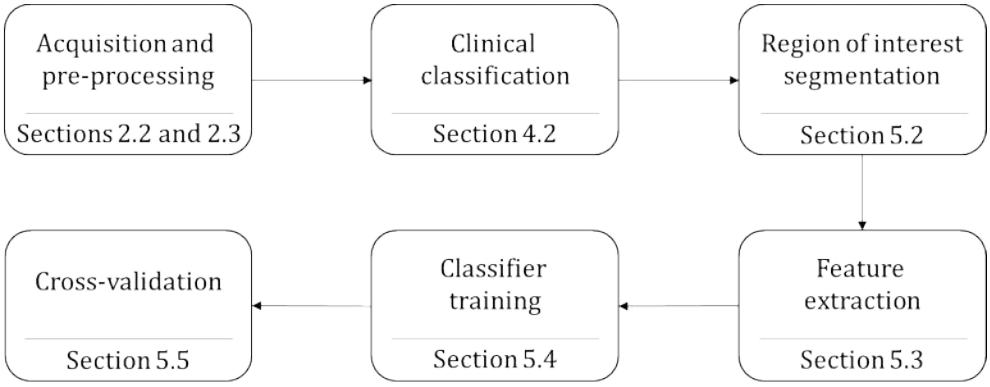

Figure 5.1 Flowchart depicting the development of automated classification protocols, along with the section of this thesis in which they are discussed. OCT images were acquired and processed, classified using a modified AREDS classification (AREDS 2001b), and the choroid was manually segmented. Textural features were extracted and used to train classifiers. These were evaluated for accuracy using cross-validation.

5.1 Methodology

Firstly, images were acquired and pre-processed as described in Sections 2.2 and 2.3, producing stack-registered volume scans (512 512). All images were then manually classified by AMD disease severity using a custom protocol (described in Section 4.2), adapted from the AREDS classification system (AREDS 2001a). This was used as the ground truth for automated classification.

Manual segmentation was then used to distinguish the choroid from other structures in the OCT image (Section 5.1.1). Textural information was then extracted from this region, to describe and quantify features of the choroidal vasculature (Section 5.1.2). Various machine learning techniques were tested for automated classification of AMD by disease stage, based upon textural features within the choroid (Section 5.1.3). Finally, the accuracy of the classifiers was assessed using

cross-validation (Section 5.1.4). All steps in the machine learning process (feature extraction, classifier training, and cross validation) were undertaken using custom programs written in MATLAB, unless otherwise stated. The methods in Sections 5.1.2 to 5.1.4 were performed by collaborators from the Department of Computer Science, Swansea University (Dafydd Ravenscroft; Jingjing Deng; Xianghua Xie).

5.1.1 Region of interest segmentation

Since only the choroidal region of the OCT images was to be included in the automated classification, this region required identification in each image. As discussed in Section 3.4, at the time of writing, there was no validated method of automated choroidal segmentation. Hence, manual segmentation of the choroid was required (n=75 OCT images).

5.1.1.1 Manual segmentation protocol

Due to the time-consuming nature of manual segmentation, three observers were used to identify the ROI. For consistency, all observers followed the same protocol for segmentation (depicted in Figure 5.2). All observers were masked to the clinical classification of the images, and underwent training on a minimum of 2 volume scans in order to familiarise themselves with the style of images and the segmentation protocol. A custom program in MATLAB was used to view images and manually identify the boundaries of the choroid. To improve visualisation, particularly of the posterior choroidal boundary, a rolling average of 10 consecutive b-scans was applied (for visualisation purposes only; Figure 5.2A-B).

Starting in the lower left-hand corner of the first b-scan, observers identified the posterior choroidal boundary first, by manually selecting several points along the boundary. This was primarily defined as the choroidal-scleral junction, or the posterior vessel lumen if the junction was not visible. A minimum of 5 points was suggested, although it was at the observers' discretion whether more points were deemed necessary. The minimum suggested value was implemented to produce a good approximation to the curvature of the choroidal boundary, using higher order polynomial interpolation (e.g. cubic and quartic polynomials; Figure 5.3).

A

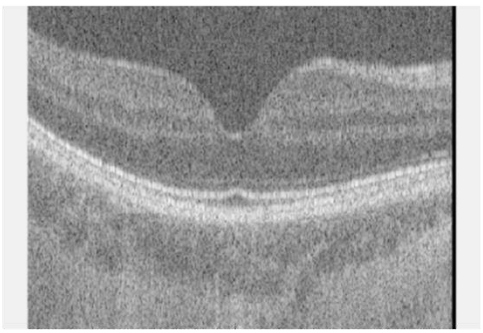

D

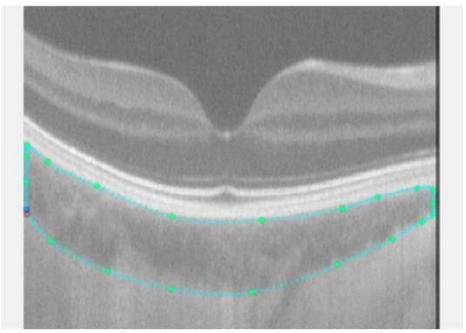

B

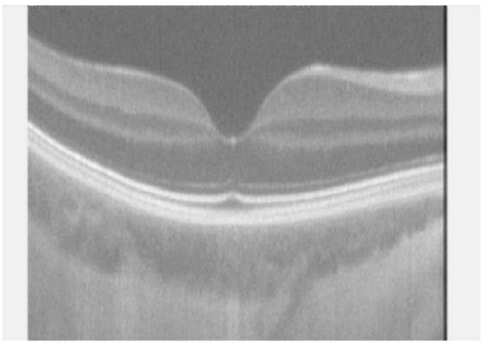

E

	X Coordinate	Y Coordinate
1	8	247
2	74	195
3	165	136
4	285	140
5	352	149
6	434	183
7	478	214
8	481	228
9	480	247
10	479	253
11	437	243
12	318	224
13	200	226
14	105	264
15	52	299
16	7	333
17	7	320
18	6	285
19	6	254

C

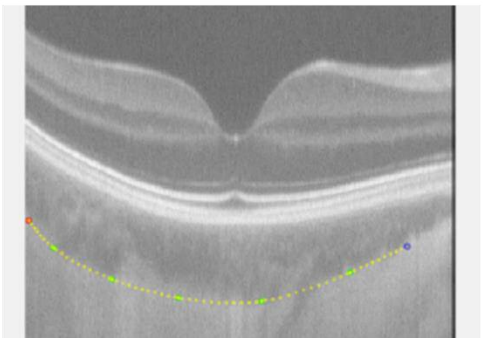

Figure 5.2 Steps (A-E) in the protocol for manual identification of the choroidal ROI, using a custom program in MATLAB. Volume scans were loaded into the program (A), and averaged to enhance boundary visualisation (B). The posterior choroidal boundary was manually identified (C), followed by the anterior boundary, creating a closed contour (D). This process was repeated for every tenth b-scan in the volume, and the Cartesian coordinates in image space of each identified boundary point were saved as a list for each b-scan (E).

Following identification of the posterior choroidal boundary, observers continued labelling the contour by identifying the right hand edge of the visible choroid (this varied due to lateral shift of b-scans during the preceding stack registration process). This was then extended to the anterior choroidal boundary, defined as the posterior of the most hyper-reflective line (RPE), and finally the left hand boundary of the visible choroid (Figure 5.2C-D).

Interpolation was used to join consecutive points within a segmented boundary to produce a closed contour, which was then saved in a coordinate system. This process was repeated at intervals of 10 b-scans throughout the image stack. A total of 51 b-scans per volume were therefore segmented (Figure 5.2E). Interpolation between b-scans was applied to produce an approximated segmentation of the choroid for all b-scans within each volume.

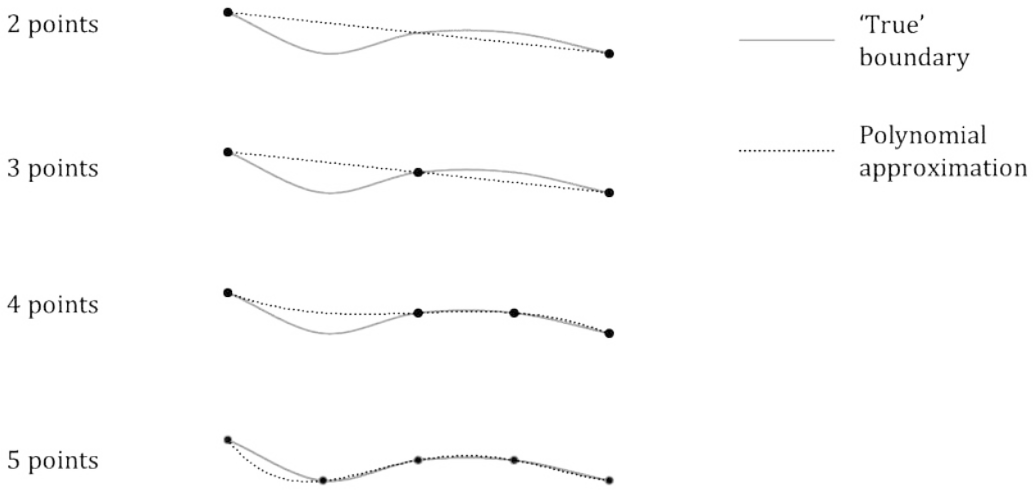

Figure 5.3 Demonstration of the effect of the number of identified points on the accuracy of the curvature approximation, using polynomial interpolation.

5.1.1.2 Inter-observer validation

Images were assigned to one of three observers (two clinical and one non-clinical) to identify the choroidal ROI. The non-clinical observer underwent training and their performance was validated by one of the clinical observers. However, due to the complex clinical appearance of late-stage AMD, the non-clinical observer was restricted to assessing images classified as healthy or early AMD. Images in the nAMD class generally displayed poorer visibility of the choroidal boundaries caused by overlying retinal features (i.e. areas of relative low contrast caused by highly reflective neovascular membranes or fibrovascular scarring). This limitation in assignment methodology was a potential source of bias between classes, due to differences in segmentation technique between observers. To ensure this bias was not significant, a subset of images were segmented again by a different observer, masked to disease classification and previous segmentation results. The following section describes this validation process.

Quality control/validation method

A total of 15 volume scans (5 per disease class) were randomly selected to undergo validation (i.e. to ensure consistency in segmentation between observers). Of the 51 b-scans that were segmented (every 10th b-scan in the original volume), 10 b-scans were randomly selected. Each volume was then randomly assigned to a different observer to the initial segmentation, and the same segmentation protocol was followed for the subset of 10 b-scans identified for validation per volume scan.

Following segmentation by the second observer, the identified regions of interest were compared between the two observers, for each selected b-scan. The boundaries of the ROI identified for each b-scan were stored within a coordinate system. To quantify agreement between observers, a program written in MATLAB (see Appendix E) was used to establish the percentage overlap of the two regions. This was calculated using the number of common pixels between regions identified by each observer (Equation 5.1; top row), and the maximum number of pixels encompassed by the two regions (Equation 5.1; bottom row).

$$\frac{\text{}}{\text{}}$$

Equation 5.1

This parameter was chosen to ensure that the regions identified by both observers were consistent in size and location (Figure 5.4A). The median and interquartile range (IQR) of percentage overlap were calculated across all randomly

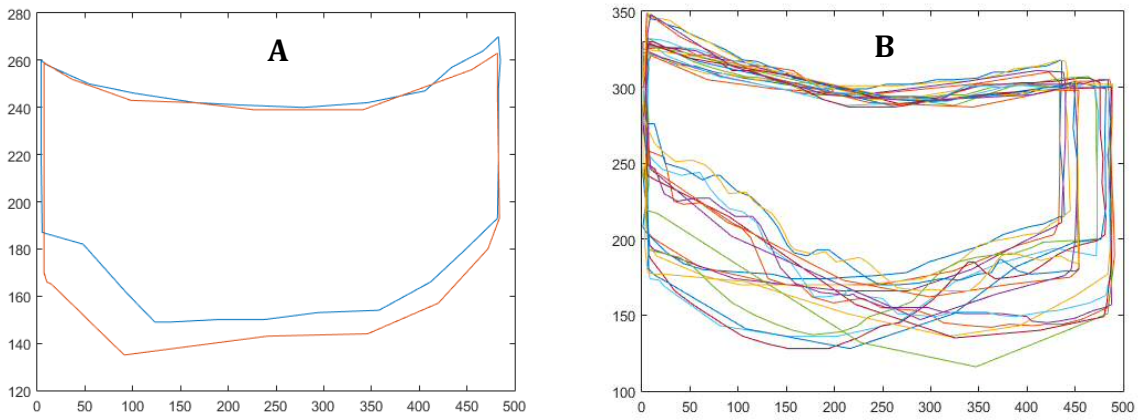

Figure 5.4 Example ROI from the same b-scan from a healthy eye, identified by two observers (A). Percentage overlap in this case was 84.3%. Demonstration of variability in choroidal size and shape across a single volume scan (B); 10 b-scans are shown, each segmented by two observers. Particularly note the variation in position of the right hand vertical boundary, due to the preceding stack registration process.

selected b-scans within each disease group (a total of 50 b-scans per group). Figure 5.4B highlights the need to label b-scans throughout the 3-D stack, since the size and shape of the choroidal region varied greatly across the volume scan from a single eye.

Results

An example of the identified ROIs within a single volume, by 2 observers, can be seen in Figure 5.4B. There was substantial variation in choroidal size and shape between b-scans within a single volume scan, most notably in the position of the posterior choroidal boundary, and the vertical boundary on the right of the image. Median percentage overlap between the two observers was 88.4%, 86.3% and 76.8% for the healthy, early AMD, and nAMD groups respectively. The range and IQR were similar between the healthy and early AMD group, but there was far more variation in percentage overlap within the nAMD group (Figure 5.5).

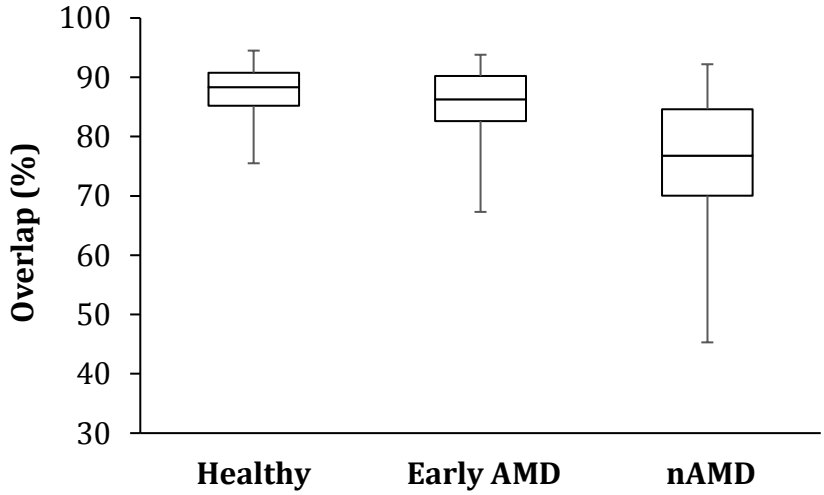

Figure 5.5 Box plots showing the median, IQR and range of percentage overlap of the ROI between observers, for each disease group.

Discussion

Variation between b-scans in vertical boundary placement on the right of the images was caused by the preceding stack registration process (see Figure 5.6). It was imperative to eliminate any such artefacts from the images, to prevent inclusion of these regions in the training and testing data. Since this boundary was well

defined, there was little disagreement on the position between observers (for example, Figure 5.4A). The bold contrast in reflectivity between the RPE and the anterior choroid made the anterior choroidal boundary relatively easy to identify accurately, although this was poorer in eyes showing disruption to the RPE resulting from pathological changes. The majority of disagreements between observers originated in the position of the posterior choroidal boundary. This boundary had the smallest difference in reflectivity between layers (i.e. between the posterior choroid and sclera), making it difficult to accurately locate in some cases. Due to its physiological location posterior to the retina and RPE, this boundary also suffered most from signal roll-off, causing it to be poorly defined and difficult to identify in some eyes.

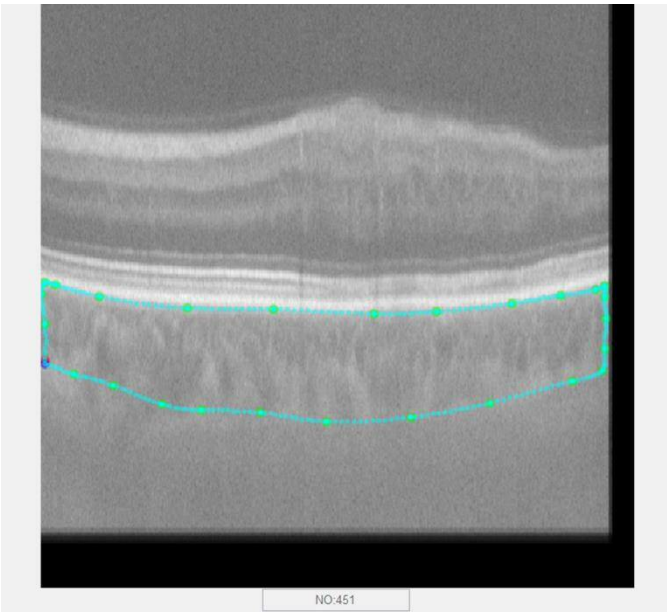

Figure 5.6 Artefacts from stack registration process (dark areas) visible around lower and right side of image. These were excluded from the identified ROI to ensure they were not used during classifier training.

The percentage agreement was lower in the nAMD group, although this was to be expected due to reduced visibility of the choroidal boundaries caused by a relative increase in reflectivity from overlying retinal features. However, this may have an effect on the training of neural networks used in further analysis. If regions of choroid were falsely being included or excluded preferentially from one group (in this case, the nAMD group), the training data may not be truly representative of the choroid in that disease stage. The posterior choroid was the region most likely to be excluded (or conversely, the anterior sclera to be included) during identification of the ROI. Since these regions had relatively low contrast (the main reason for

boundary misplacement), it was unlikely that they would contribute strong representation within the neural networks. It was therefore probable that this limitation would not have a large direct effect on the automated classification results.

Overall, the percentage overlap was reasonable, suggesting that observers were consistent in identifying the ROI. Since the purpose of this protocol was to identify a region of the image to be isolated for further analysis, the agreement did not need to be as high as would be required for direct quantitative analysis of the segmentation region (e.g. choroidal area). This protocol for manual segmentation of the choroidal layer was therefore suitable for use in this study.

5.1.2 Feature extraction

The next step in the classification process was to extract textural information from the ROI. This aim of this was to condense the image data in the ROI (i.e. pixel locations and intensities) into summarised textural information, such as spatial arrangement of pixel values. Assuming the OCT image accurately depicts the structure, the mathematically extracted shape and orientation information represents the underlying vascular structure. Although several methods for feature extraction have been described, Gabor filters are relatively simple to apply, and have been shown to perform well against alternative methods in textural analysis problems (Monadjemi 2004; Gonzalez-Lopez et al. 2015). They have been successfully applied to retinal image analysis, including retinal vessel and choroidal layer segmentation, drusen detection, and RNFL defect detection (Soares et al. 2006; Hayashi et al. 2007; Parvathi and Devi 2007; Gonzalez-Lopez et al. 2015; see Section 1.7.3).

A 2-D Gabor filter is a linear filter consisting of a sine wave grating multiplied by a Gaussian kernel function (Figure 5.7). A number of gratings of predefined spatial frequency and orientation are produced to form a Gabor filter bank (Figure 5.8). This technique is therefore a multi-channel filtering approach, similar to that described by Jain and Farrokhnia (1990). The theory is based upon the deconstruction of images into a number of filtered images, each representing a narrow range of frequencies and orientations. This is analogous to early

descriptions of perception in the human visual system (Campbell and Robson 1968), with Gabor filters comparable to the simple cells of the visual cortex, responding primarily to oriented edges and gratings.

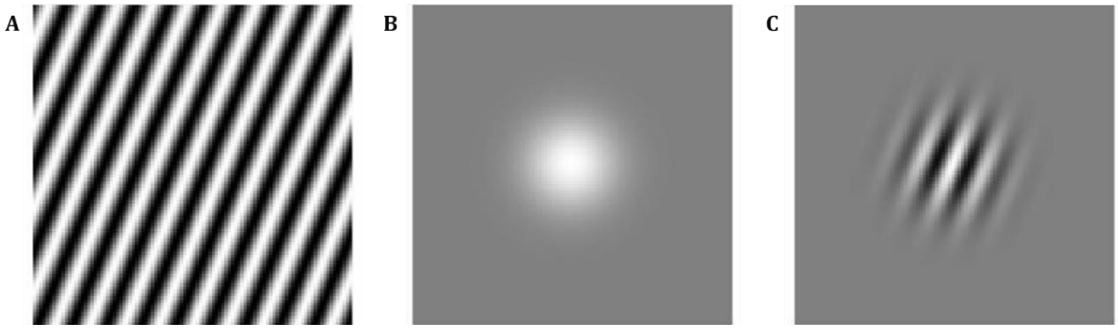

Figure 5.7 The product of (A) a sine wave grating and (B) a Gaussian blob is (C) a Gabor patch. In this case, a wavelength of 10 pixels and an orientation of 22.5° from vertical are used.

Theoretically, a range of spatial frequencies is useful for detecting vessels of different diameters, for example the smaller vessels of the anterior choroid, and the larger vessels of Haller's layer. The grating size giving the strongest response should correspond to the predominant vessel size in the image. Changes to the vessel sizes throughout the AMD disease process may therefore be detectable using these filters of varying spatial frequency.

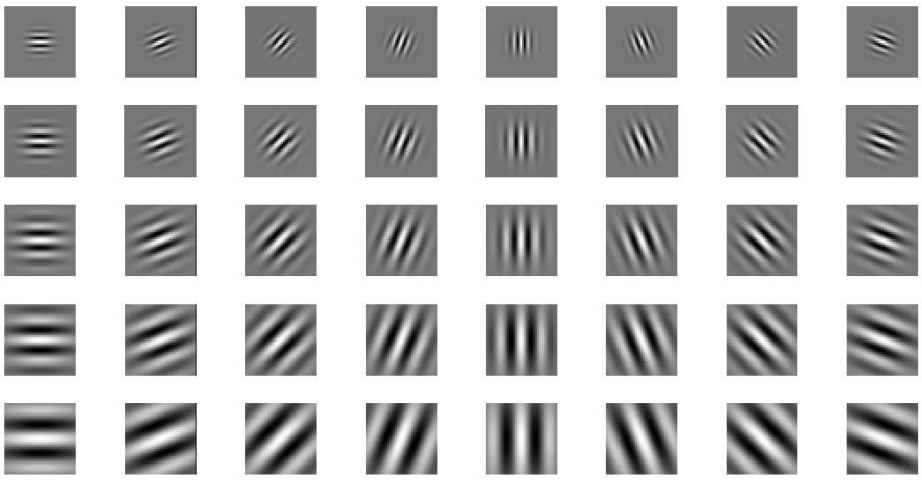

Figure 5.8 Visual representation of the Gabor filter bank used in this analysis. From top to bottom, the wavelength of the gratings are 6, 8, 10, 12 and 18 pixels, and orientations rotate from horizontal by 22.5° (left to right).

Since the choroid comprises a range of vessel sizes, the wavelengths (λ) of the sine wave gratings were selected to reflect this. The optimum wavelength required to detect a vessel would be double that of the vessel diameter, assuming the vessel diameter is equal to the spacing between vessels. However, due to the

decoupling of axial and lateral scaling in OCT, these wavelengths will equate to different vessel sizes in the two directions. For instance, a grating of λ = 8 pixels (λ/2 = 4 pixels) would equate to vessel diameters of ~8 μm axially and ~46 μm laterally. This grating would therefore be sensitive to different vessel sizes in each meridian. To account for this, a range of wavelengths were employed in the Gabor filter bank; λ/2 = 3, 4, 5, 6, and 9 pixels. This equates to a range of vessel diameters of ~6 to 17 μm axially, and ~34 to 102 μm laterally (assuming an AEL of 24 mm). Therefore, changes to the small vessels should produce differences in the horizontally oriented filters, and changes to the large vessels should produce differences in the vertically oriented filters. Orientations between these two axes were also used to complete the Gabor filter bank (every 22.5°), and account for the vessels between these sizes. A total of 40 filters were used (8 orientations of 5 spatial frequencies), each 39 39 pixels in size.

During feature extraction, each of the filters in the Gabor bank was convolved across the image, producing a series of filtered images with limited spectral information. The aim of this was to determine the 'energy' of each filtered image required to reconstruct the input image. As described by Jain and Farrokhnia (1990), the relative importance of each filtered image was represented in a histogram (Figure 5.9; Deng et al. 2016). Each image pixel was assigned to one of 11 equally sized energy 'bins', each of which represented a discrete range of energy responses (shown along the x-axis). The relative frequency of pixels assigned to each bin (normalised from 0 to 1) defined the y-axis.

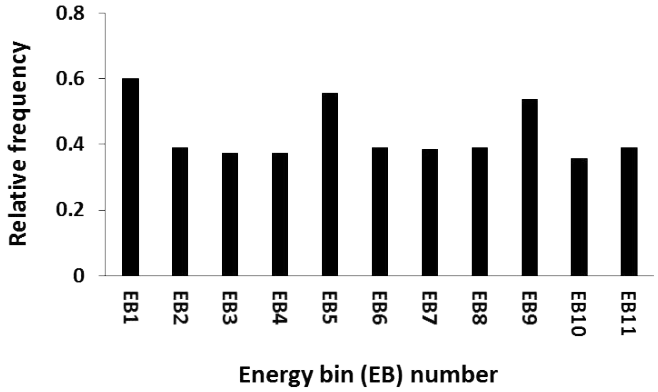

Figure 5.9 Example energy histogram from an image produced by a single Gabor filter. The y-axis represents relative frequency of each discrete 'energy bin', shown along the x-axis (a total of 11 bins were used). Image adapted from Deng et al. (2016).

This filtering process was repeated for all 40 filters in the Gabor bank (8 orientations 5 spatial frequencies), and the energy histograms were concatenated to form a total of 440 feature descriptors (40 filters 11 bins), for each b-scan. These feature descriptors were then used as input to train and test the classifiers (described in Section 5.1.3 and 5.1.4 respectively).

5.1.3 Classifier training

Since the data used in classifier training was pre-classified into disease group by clinicians, this was a 'supervised' classification problem. The aim was to train classifiers to sort images into one of three groups; healthy, early AMD, or nAMD. The input to the classifiers was the feature descriptors described in Section 5.1.2, along with the ground truth classification (Section 4.2). The output was one of the three disease groups. A subset of the data was used for training purposes, whilst the remaining data was used to test the classifiers for accuracy (see Section 5.1.4).

Each b-scan within a volume was assigned the same class during the clinical classification. All b-scans from a single eye were given equal weighting in the classification, regardless of their proximity to the fovea, or signs of overlying retinal degeneration visible on the OCT scan. This was based on the assumption that vessel changes in AMD are uniform across the central 20° 20° of sub-macular choroid. Since the aim of this research was to establish the feasibility of applying machine learning to automated disease severity classification, this assumption was made for ease of classifier training. Reasonable accuracy of a simple classifier acts as proof of concept, as well as indicating structural change to the choroidal vasculature throughout the disease process. Following this, the classifiers would require optimisation on a far larger dataset, to maximise accuracy of automated disease classification prior to clinical application. This optimisation process may include weighting of b-scans in the classification with relation to location or retinal features. The implications of this assumption are discussed further in Section 5.3.

Three established types of classifier were evaluated on this dataset; K-nearest neighbour (KNN), random forests (RFS), and support vector machines (SVM). Although all three classifiers have been shown to produce accurate classification of medical tomographic images (Koprowski et al. 2013; Bhuvaneswari

and Therese 2015; Albarrak et al. 2016), it was unknown which would have the best performance in this classification task. All three classifiers were therefore evaluated, and their performance is compared in Section 5.2. A study of the latter two of these methods applied to a preliminary dataset comprising OCT images of eyes with varying stages of AMD is described in Deng et al. (2016). The following sections are a description of the models and predictions made by each classifier type. A comprehensive explanation of each type of classifier, along with additional information, can be found in Alpaydin (2014).

5.1.3.1 K-nearest neighbour (KNN)

KNN is a relatively basic classifier, which makes predictions directly from the entire training set. For a previously unseen image, the K-most similar images ('nearest neighbours') in the training set are identified and summarised to produce a classification for the new image (Figure 5.10). To measure similarity between the input and training set, distances in Euclidian space between images were calculated for each of the 440 feature descriptors. This distance was used to produce a weighted score, with the nearest neighbour having the highest weighing. The final classification of the new image was based on a majority vote from the K-highest weighted scores. For this analysis, K was set to 5 to maximise accuracy, whilst minimising over-fitting.

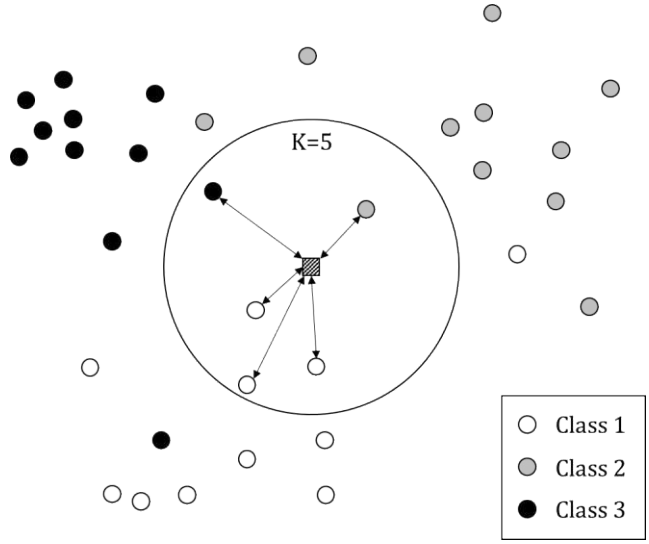

Figure 5.10 K-nearest neighbour predicts the class of a new input (shaded square) by identifying the K-most similar data in the training set. The classification is determined by the most frequent class in this neighbourhood (in this case, Class 1).

Over-fitting is a common limitation of machine learning, referring to a classifier with high sensitivity to the training data, but poor accuracy when classifying previously unseen test data. This occurs when random patterns or noise in the test sample are learned by the classifier, and used as a basis for classifying data from a different sample during testing. This is often the case in relatively small datasets, resulting in poor generalisation of the model to previously unseen data in the population. The extent of over-fitting of all classifiers used was assessed using cross-validation (testing the classifiers by sampling previously unseen data; see Section 5.1.4).

5.1.3.2 Random forests (RFS)

A random forest classifier is a type of ensemble machine learning, combining a large number of weak classifiers ('decision trees') to create an accurate predictive model. A decision tree is a method of classifying data into discrete groups, using a series of successive binary criteria. Data is input at the top of the tree, and passes down each layer until it reaches an end node at the bottom of the tree, where a classification is output. The path followed (and hence the end node reached) is dependent on multiple split points in the tree, each based on a binary criterion designed to divide the data. These criteria generally determine whether a variable is less than or greater than a predefined threshold. An example of simple decision tree architecture is shown in Figure 5.11.

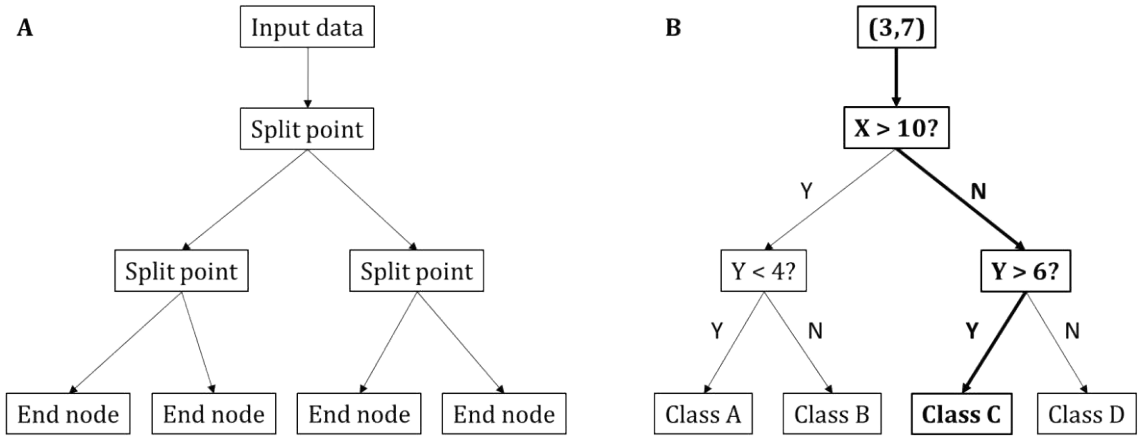

Figure 5.11 (A) Simple decision tree architecture, showing the possible paths of input data, through a series of split points, leading to an end node denoting a classification. (B) An example of a simple decision tree, with binary criteria at each split-point. In this case, input data (X = 3, Y = 7) was allocated to Class C.

In this study, RFS classifier training involves constructing decision trees to classify into the disease groups, based on the labelled training data. These trees are sensitive to the specific data on which they are trained, and therefore are prone to over-fitting (resulting in poor classification accuracy on previously unseen data). Bootstrap aggregation ('bagging') can be used to minimise this problem; at each node within the tree, a random subset of all possible features for the binary criterion are made available to the learning algorithm. From this subset, the feature and threshold combination which produces the most discriminative data split are selected and assigned to that split-point. The size of the subset was set to 21 in the present study, calculated as the square root of the number of feature descriptors ($\sqrt{440}$; Breiman 2001). Trees are allowed to grow until a minimum number of samples at each split-point is reached (this was set to 3 in the present study to minimise overfitting). The result is a decision tree with multiple split points to separate data into the classes.

This process was repeated with a different random subset of features, producing another decision tree based on different combinations of features and thresholds (due to the bagging process). This was repeated until a total of 50 trees were constructed, which were combined to form the decision forest (Figure 5.12). For previously unseen (test) data, the probability of the sample belonging to each class was assigned at the end node of each tree. The final classification was determined by combining weighted predictions from each tree in the forest.

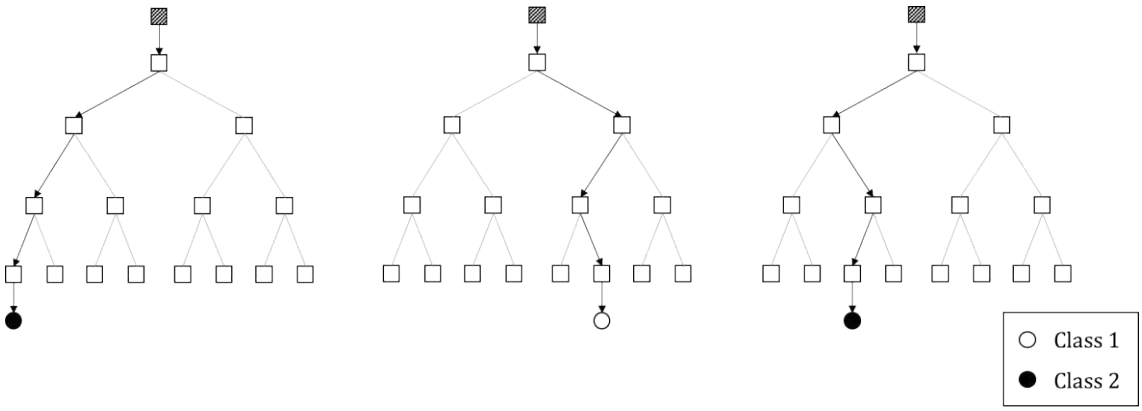

Figure 5.12 Random forest classifiers consist of multiple decision trees (n=3 shown here), each with a number of binary split-points (white squares). New data (shaded square) is entered at the top of each tree, and is classified at the end node. The final classification is based on the combined weighted predictions from each tree (in this case, Class 2).

5.1.3.3 Support vector machines (SVM)

This classifier describes how training data plotted in n-dimensional space (n representing the number of feature descriptors) can be separated by a 'hyperplane'. This describes the plane that best separates the training data into two known classes. The position of this hyperplane is learned from the training data and used to determine the class of a new input; its mapped location in relation to the hyperplane is used to predict the classification.

SVM is based upon the hypothetical 'maximal-margin' classifier. The maximal-margin hyperplane is the term given to the optimal hyperplane separating the classes. The 'margin' is defined as the perpendicular distance from the nearest correctly classified point of each group to the hyperplane (Figure 5.13). The smaller the margin (i.e. the closer the input is to the hyperplane), the less confidence the model gives to the class prediction. The points with the smallest margin (i.e. the closest correctly classified points to the hyperplane) are called the support vectors, and are used to define the hyperplane, and hence the construction of the classifier.

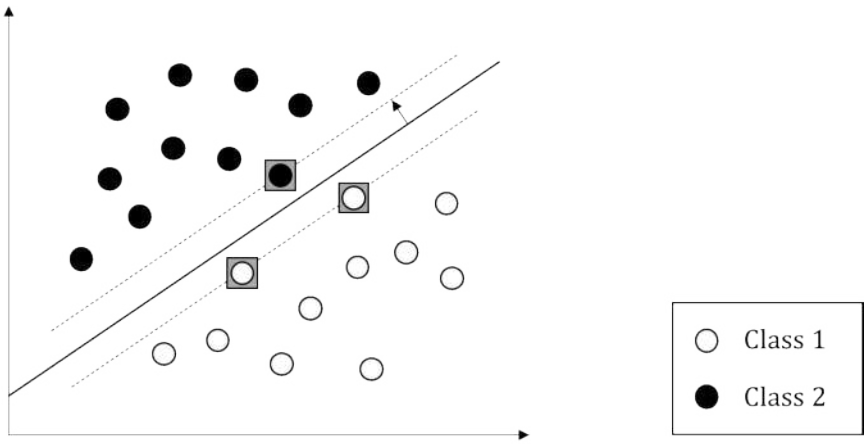

Figure 5.13 A support vector machine uses a hyperplane (solid line) to define the best separation between data belonging to two classes, shown here in 2-D space for simplicity. The support vectors (marked in grey boxes) are the correctly classified data points closest to the hyperplane, and the perpendicular distance from these to the hyperplane is known as the margin (black arrow). Image adapted from Cortes and Vapnik (1995).

With real data however, there will often be some overlap in space between classes; therefore a hyperplane may not perfectly separate all training points in the classes. The 'soft margin' classifier is used to relax the constraints of the hyperplane, allowing some points in the training data to violate the separating line (Cortes and Vapnik 1995). This accounts for outliers in the training data, and aids in reducing model over-fitting to these outliers.

In practice, the SVM algorithm is implemented using a kernel, defining the similarity between new data and the support vectors. This kernel may be linear, polynomial, or radial, to best separate the classes (allowing for curved or more complex hyperplanes). The present study used the established radial basis function (RBF) kernel, also known as the Gaussian kernel (Equation 5.2). This was capable of creating complex regions within the feature space, and hence maximise classification accuracy.

Equation 5.2

where:
$(x - x')^2$ is the squared Euclidian distance between vectors
σ is a free parameter to be determined by the algorithm

SVM was developed for binary classification (i.e. separating data into two classes only). Since there were three classes in this dataset, a one-against-all approach was used (Kim et al. 2002). In turn, each class was tested against all data from the remaining two classes combined. This produced multiple SVMs, of which the one with the strongest prediction (i.e. the maximal margin) for a particular input was used.

5.1.3.4 Convolutional neural networks (CNN)

In addition to these traditional classifiers, the use of neural networks for automated classification into disease groups was evaluated. This did not require the feature extraction techniques described in Section 5.1.2, and the results are therefore presented and discussed separately to the other classifiers (Section 5.2.3).

Artificial neural networks are a commonly used approach to computational classification, modelled on biological neural networks, such as those behind image recognition in the human brain (Lippmann 1987). Convolutional neural networks (CNN) are a powerful machine learning technique, often applied to object recognition problems (LeCun et al. 2015). Unlike traditional neural network techniques, a CNN preserves the spatial relationship between pixels, to prevent loss

of spatial structure from the image during the learning process. A CNN is designed to learn and generalise features from an input image, in order to classify a previously unseen image. The input data for the CNN was intensity and spatial location of all pixels in the choroidal ROI. The 'hand-crafted' features used to train the other classifiers (produced by the Gabor filters) were therefore not required for this analysis.

A CNN typically has a complex architecture, with three types of layers (from input to prediction); convolutional layers (typically coupled with normalisation layers), pooling layers, and fully-connected layers (Figure 5.14). The convolutional layers are comprised of filters, with the aim of extracting textural information from the image. The filters are a square of fixed size, known as a receptive field, which are convolved across the input image (in a similar manner to the Gabor filters described in Section 5.1.2). This is a method of combining pixels with their neighbours, accentuating or masking certain image features, depending on the kernel used. A predefined number of filters are used, which are initially randomised, but then undergo optimisation by the algorithm using back-propagation in the network. The output from the first layer is called a feature map, and forms the input for the next convolutional layer. A new set of optimisable features are then convolved across the feature map, the output of which feeds into the next layer, and so on.

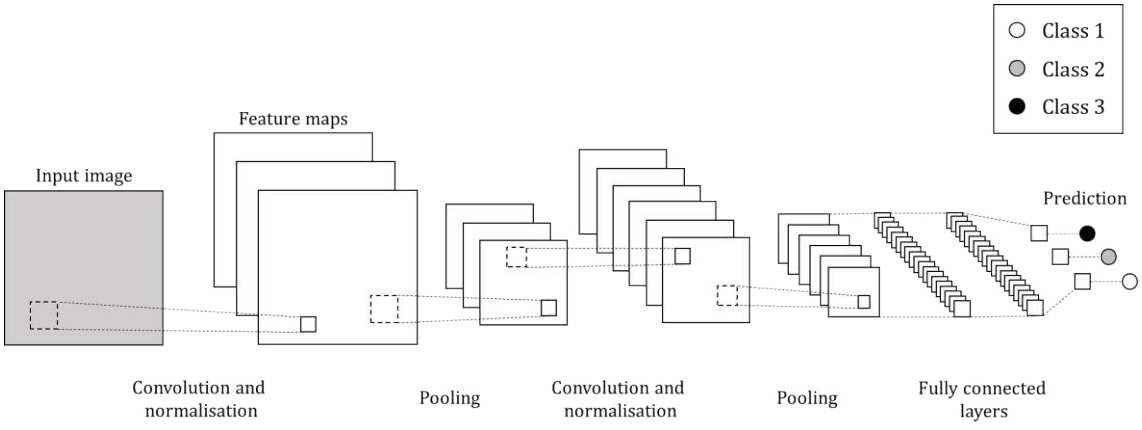

Figure 5.14 Schematic of a simplified convolutional neural network. Convolutional, normalising and pooling layers are used for extracting and generalising textural features within the image. Fully connected layers are used as a classifier to predict the class of a previously unseen image. Image adapted from Lawrence et al. (1997).

Normalisation layers are often utilised between convolutional layers, for spatial smoothing of the feature maps, following filtering. A commonly used type of normalisation is the 'rectified linear unit' (ReLU), which normalises values over a local region of defined size (LeCun et al. 2015).

Pooling layers follow the convolutional layers, and down-sample the feature maps from the previous convolutional layer. These layers aim to consolidate and generalise the textural features across all input data, to reduce the effect of over-fitting of the model to the training sample. Fully connected layers are implemented at the end of the network, to create non-linear combinations of features, for class prediction by the model.

CNN typically relies on all input images being the same size. However, this was not true for the choroidal ROIs, which varied greatly in size and shape. Therefore, 50 patches were randomly selected from the ROI for this analysis, each 40 40 pixels in size. These patches were used as the input for the CNN.

The CNN used in this analysis was comprised of the following 21 layers, from input to prediction (architecture shown in Figure 5.15):

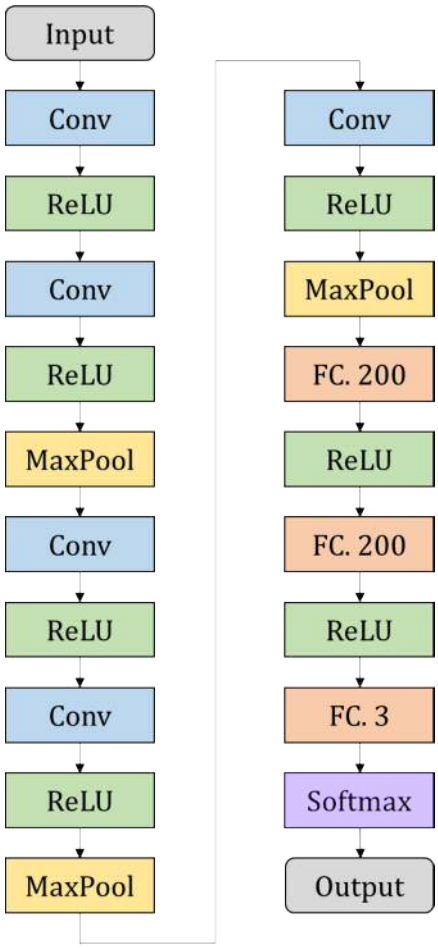

Figure 5.15 Network architecture of the CNN, from input to prediction. Conv = convolutional layer; ReLU = 'rectified linear unit' normalisation layer; MaxPool = maximum pooling layer; FC. X = fully connected layer with X neurons; Softmax = layer to carry out error calculations in class prediction.

- 5 convolutional layers, each with 128 filters with receptive field (kernel) size 3 3 pixels. Although the number of filters was specified, the actual filters used were determined by the algorithm (Figure 5.16). A ReLU normalisation layer was used after each convolutional layer for spatial smoothing prior to entering the next layer.
- 3 pooling layers, to select the maximum pixel values in the feature maps, in a 2 2 pixel neighbourhood. This compressed the feature information, minimising the computational demand of the classifier.
- 3 fully connected layers to separate images into the classes based on the feature maps. The first two of these consisted of 200 neurons and were followed by a ReLU normalisation layer, whilst the final layer consisted of 3 neurons (one for each class).
- A 'Softmax' layer was added to the end of the network to carry out error calculations in class predictions. This layer outputs a 'confidence score', akin to the probability of each input sample belonging to each of the three classes. The largest confidence score was used to determine the final classification of each b-scan.

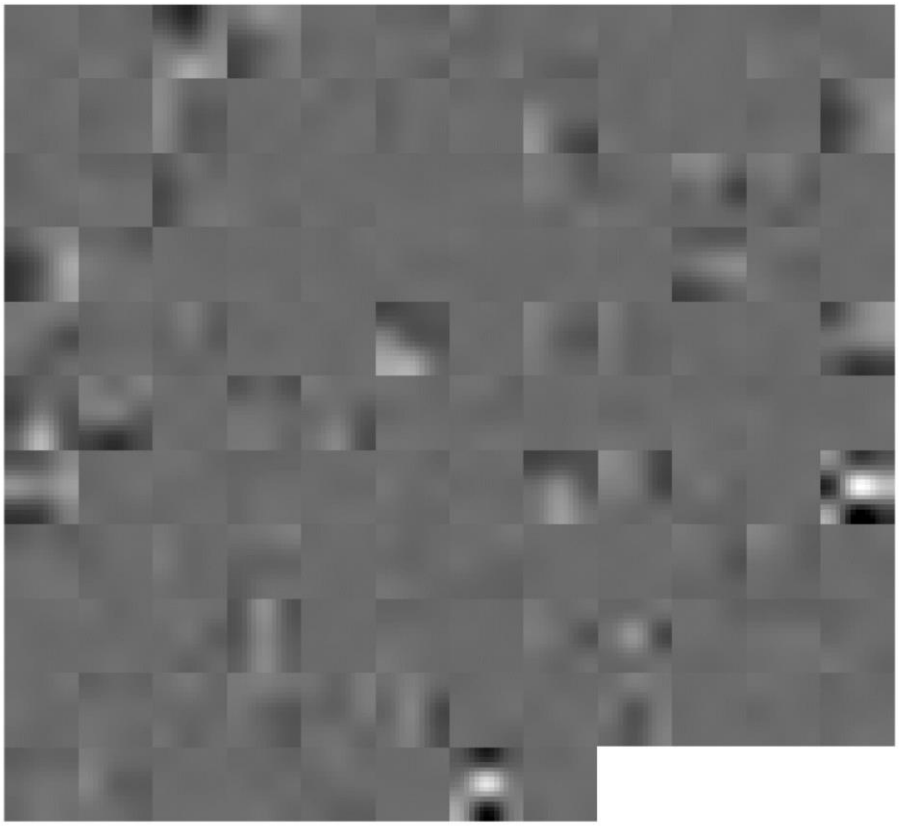

Figure 5.16 The output of the 128 filters that were created by the first convolutional layer of the CNN (3 3 kernels convolved across an image patch 40 40 pixels in size). These were randomly generated filters, and included bar gratings and diagonal gradients, with a range of contrasts. Image adapted from Ravenscroft (2016).

5.1.4 Cross-validation

For this analysis, each volume scan was separated into individual b-scans, each of which was treated as a single image. All 512 b-scans per volume were included in the analysis. Every b-scan in the volume scan was labelled with the class established by the protocol in Section 4.2; this was taken as the ground truth. This was repeated for all 75 volume scans. This produced a dataset of 38,400 labelled b-scans, equally divided between three disease groups.

To evaluate the accuracy of the classifiers, a proportion of the images were set aside as test data. This data was not used during the training process, and was therefore previously unseen by the classifiers. Each classifier was then used to classify these test images, and the accuracy of the classifiers was established (i.e. the percentage agreement between automated classification and ground truth). This process was called cross-validation. Three methods of cross-validation were conducted, based upon the proportion of data devoted to training and testing; 10-fold, 2-fold, and leave-one-out (Figure 5.17).

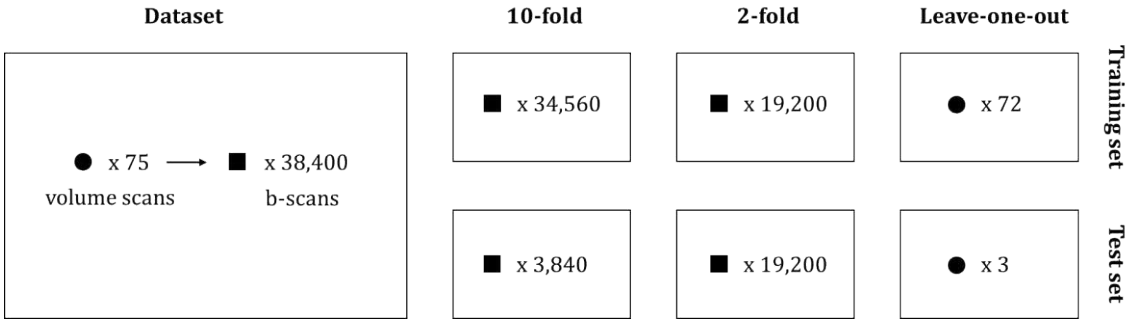

Figure 5.17 The total dataset comprised of 75 volume scans from 75 eyes, each consisting of 512 b-scans. In the first run, one tenth or half of the b-scans were randomly selected for the test set, in 10-fold and 2-fold cross-validations respectively. The remainder were used to train the classifiers. For the leave-one-out cross-validation, all b-scans from 3 eyes (one per disease group) were used as the test set. This was repeated using each subset for testing, for a total of 10, 2, and 25 runs for the 10-fold, 2-fold and leave-one-out cross-validation respectively.

For 10-fold cross-validation, the 512 b-scans from each eye were randomly distributed amongst 10 equally sized groups. Nine of these groups were used for training, and the final group was used for testing. During cross-validation, the algorithmic prediction was compared to the clinical classification, and the percentage agreement between classification methods (automated and clinical) was established. The classifiers were then retrained, this time removing one of the other 9 groups from the training phase, to be used for testing. The classification accuracy

was again assessed. This was repeated for a total of 10 'runs' (each using a different subset for testing), and the mean accuracy was calculated. The agreement between classification methods was averaged across all runs, and presented in a 'confusion matrix'. An example confusion matrix with fictional data is shown in Table 5.1, for interpretation guidance. These matrices are presented in Appendix F, and are summarised in Section 5.2.1 (for KNN, RFS, and SVM), and Section 5.2.3 (for CNN).

A 2-fold cross-validation was also conducted, in which the data was randomly divided in half; the training and test datasets were therefore equal in size. There were two runs in this cross-validation, using each half of the dataset for training and testing. This is generally a more robust measure of classifier accuracy, since more data is used in the testing phase.

Finally, a leave-one-out cross-validation was used. For this, all b-scans from 3 eyes (one per disease group) were set aside for testing. All b-scans from the 72 remaining eyes were used to train the classifiers. During testing, each b-scan from the test eyes were classified individually. The class of highest frequency amongst the b-scans was taken as the final classification for each eye (i.e. a majority vote). This was repeated for a total of 25 runs, with a different random eye from each class being removed in turn for testing. This form of cross-validation is the most robust, and mimics the clinical scenario of classifying images from eyes previously unseen by the classifiers.

Table 5.1 Fictional confusion matrix for interpretation guidance. Ground truth (analogous to clinical classification) is divided by column and algorithmic prediction is divided by row. 80% of group B were correctly classified by the algorithm, whilst 15% were classed as group A, and 5% were classed as group C.

		Ground truth (clinical classification)		
		A	B	C
Algorithmic prediction	A	100%	15%	0%
	B	0%	80%	10%
	C	0%	5%	90%

To summarise, the methodology for automated classification of images using machine learning has been presented in this chapter. A method for manually

segmenting the choroidal region of interest was described, along with a study of the inter-observer variability of this method. Following this, the use of Gabor filters for feature extraction was outlined, with a view to producing automated quantification of textural features within the choroid. Three types of classifier (K-nearest neighbour, random forest, and support vector machine) were then described, each of which are designed to predict the class of a previously unseen image, based on training data. The accuracy of these three classifiers can be assessed using cross-validation (10-fold, 2-fold, and leave-one-out). The accuracy of each classifier at predicting AMD disease severity is presented in the following sections, along with a discussion of their performance relative to each other, and to the literature. The feasibility of applying a further classifier, not requiring the hand-crafted feature extraction process (convolutional neural network), is also explored.

5.1.5 Methodology summary

The methods described in Section 5.1 were applied to a dataset of long-wavelength OCT images acquired from individuals at different stages of AMD. The training and testing of the classifiers was performed with collaborators from the Department of Computer Science, Swansea University (Dafydd Ravenscroft; Jingjing Deng; Xianghua Xie). Interpretation of the results (including association of image features to the choroidal structure), and a discussion of subsequent clinical implication, was undertaken by the author of this thesis.

The aim of this analysis was to evaluate the feasibility of applying machine learning techniques to automated classification of AMD by disease severity, based on choroidal appearance. By proxy, successful classification would indicate that changes to the texture of the choroidal region of OCT images, with advancing disease severity, are detectable *in vivo*. A successful classification was defined as high classification accuracy achieved using 10-fold and 2-fold cross-validation, in conjunction with reasonable accuracy with leave-one-out cross-validation (which was expected to be lower due to the limited size of the training dataset). The results of the classifications are presented in this chapter, with results from the convolutional neural network (CNN) presented separately due to the difference in feature extraction method. The discriminative features that were considered important to the classification are explored, and are compared to the vascular

changes described in the literature. Additional results can be found in Appendix F, including confusion matrices of each classifier, for each cross-validation method used.

5.2 Results

5.2.1 Cross-validation

The choroidal ROI from OCT images (n=75) was used to train and test classifiers to predict AMD disease severity by classification into three groups; healthy, early AMD, or nAMD. The accuracy (percentage agreement between classifier and ground truth) of each classifier, evaluated with 10-fold cross-validation, is shown in Table 5.2. Support vector machine (SVM) was the best-performing classifier, with mean accuracy of 98.3%. K-nearest neighbour (KNN) also performed well, with 94.9% mean accuracy, and random forest (RFS) was the poorest of the three classifiers in this analysis, with 89.2% mean accuracy. For KNN and SVM, the healthy class had the highest accuracy, whilst with RFS and SVM, the early group had the lowest accuracy.

Table 5.2 Classification accuracy (%) of 10-fold cross-validation for each classifier. KNN = K-nearest neighbour; RFS = random forest; SVM = support vector machine.

	Healthy	Early AMD	nAMD	Mean
KNN	97.3	94.6	92.9	**94.9**
RFS	90.9	85.1	91.7	**89.2**
SVM	98.6	97.9	98.4	**98.3**

The classification accuracies were slightly lower for the 2-fold than the 10-fold cross-validation for all three classifiers (Table 5.3), although the same patterns as described above were observed. This reduction in accuracy was expected for this method of cross-validation, since less data is used for classifier training.

Table 5.3 Classification accuracy (%) of 2-fold cross-validation for each classifier. KNN = K-nearest neighbour; RFS = random forest; SVM = support vector machine.

	Healthy	Early AMD	nAMD	Mean
KNN	96.7	93.8	91.4	**94.0**
RFS	88.3	81.7	90.2	**86.7**
SVM	97.7	96.7	97.6	**97.3**

For the leave-one-out cross-validation, the mean accuracy was substantially lower for all classifiers (Table 5.4). For this validation method, no b-scans from the eyes in the test set had been used for classifier training. In the 10-fold and 2-fold cross-validations however, all b-scans were randomly assigned to the training and test sets. Therefore, a number of b-scans from each eye (90% or 50% on average, respectively) were used to train the classifiers. The large differences in accuracy between cross-validation methods suggests that the classifiers were poor at generalising to the population, from the sample used for each class (n=25).

Table 5.4 Classification accuracy (%) of leave-one-out cross-validation for each classifier. KNN = K-nearest neighbour; RFS = random forest; SVM = support vector machine.

	Healthy	Early AMD	nAMD	Mean
KNN	40	48	48	**45.3**
RFS	56	44	80	**60.0**
SVM	40	60	72	**57.3**

The best-performing classifier in this analysis was the RFS (60.0% mean accuracy), whilst the poorest was KNN (45.3% mean accuracy). This is unsurprising, since KNN is the most basic of the classifiers used, and RFS is the least prone to over-fitting. Despite the ability of RFS to generalise to the population, classes with high within-class variability still result in limited classification accuracy. The poorest performance was for the early AMD group, suggesting that this group had high within-class variability. This is not surprising, since this disease group contained both early and intermediate AMD (as defined by AREDS 2001a), and had the highest standard deviation in several of the choroidal parameters evaluated in Section 4.4.

The nAMD class had the highest accuracy for all three classifiers. This indicated that the choroidal structure is most different in this group, compared to the early AMD and healthy groups. Choroidal structure may have been more similar

in eyes with no disease or early disease, with more overlap in textural appearance between groups, resulting in limited ability of the classifiers to distinguish between these two groups. This is consistent with the findings of the manual choroidal parameters, where no significant differences were found between early AMD and healthy eyes with any parameter evaluated (see Section 4.4).

The sensitivity and specificity of each classifier were evaluated for each cross-validation method (Figure 5.18). For this analysis, classes were combined to allow two different comparisons: AMD (combining early and nAMD) versus non-AMD (healthy); and neovascular (nAMD) versus non-neovascular (combining early AMD and healthy). Specificity of the leave-one out cross-validation was considerably higher for the latter of these comparisons, whilst sensitivity was similar. This suggests that the classifiers were more accurate at identifying the presence of nAMD than of any stage of AMD, supporting the hypothesis that the choroid has a more

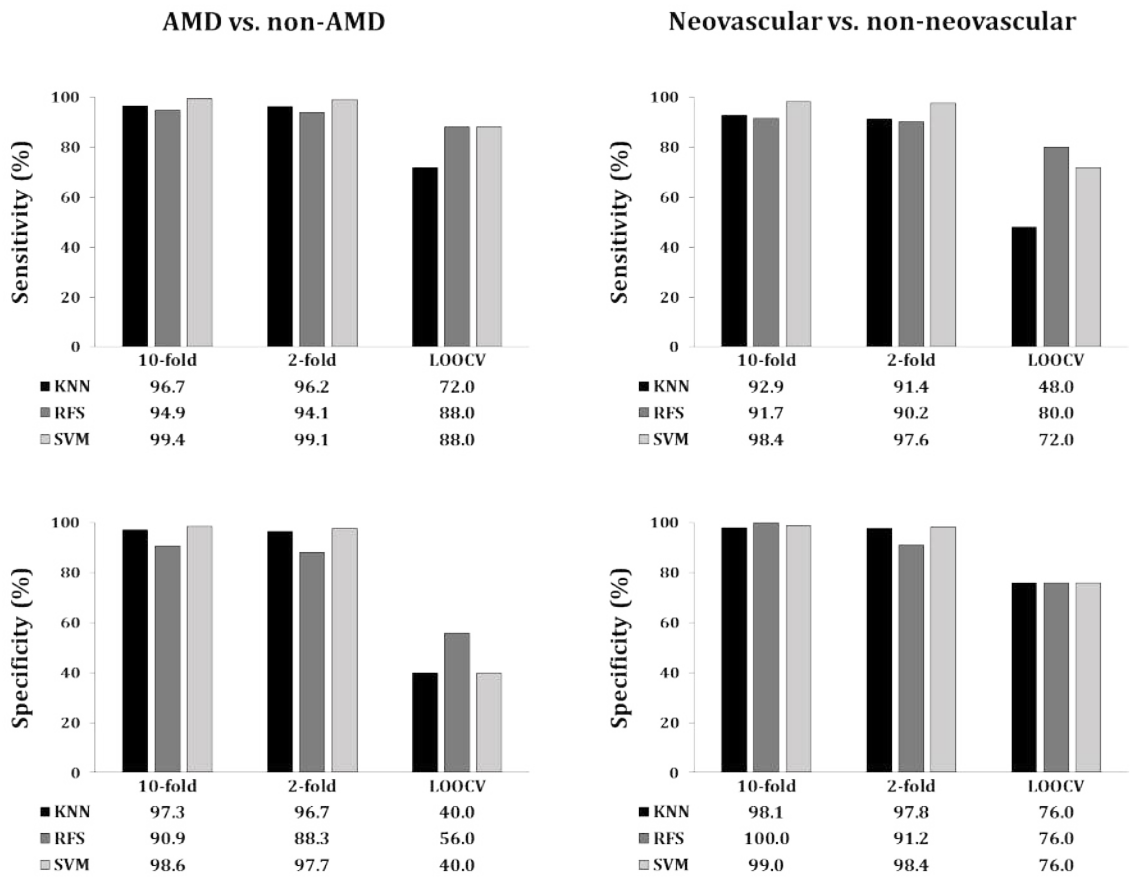

Figure 5.18 Sensitivity (%) and specificity (%) of each classifier, using the three methods of cross-validation. The diagnostic ability of the classifiers to identify any stage of AMD (left column) and nAMD (right column) were evaluated. For the purposes of this figure, AMD = early + nAMD groups; non-AMD = healthy group; neovascular = nAMD group; non-neovascular = healthy + early AMD groups. KNN = K-nearest neighbour; RFS = random forest; SVM = support vector machine; LOOCV = leave-one-out cross-validation.

distinct appearance in nAMD than in the other groups. This is in agreement with the results in Section 4.4, whereby little difference in choroidal structure was found between healthy eyes and early AMD, but was significantly different in nAMD. However, this was a predominantly treated-nAMD group, and the potential implications of anti-VEGF therapy on the choroidal structure must be considered (discussed further in Section 5.3). SVM consistently performed the best of all classifiers, with the exception of the leave-one-out cross-validation, where it was out-performed by RFS.

To improve classifier accuracy in the leave-on-out cross-validation, a substantially larger dataset would be required, to compensate for the large within-class variation, and improve generalisation of the choroidal features of each group to the population, hence minimising over-fitting (discussed in Section 5.3). Despite this, the accuracy of all classifiers evaluated was considerably higher than chance (33% for three classes), confirming the feasibility of applying machine learning techniques to classification of AMD by disease severity, based on the choroidal region in long-wavelength OCT images.

However, it was not possible to conclude from these findings whether the features used in the classification were true structural features, or 'artefactual' image features produced during image acquisition or processing. It was therefore necessary to evaluate the textural image features in the classifier used to discriminate between classes, and to associate these with previously demonstrated changes to choroidal physiology with advancing disease.

5.2.2 Associating textural image features to choroidal structure

To provide an indication of the choroidal features used to predict the disease stage, the relative importance of each image feature in the classifier (i.e. each of the Gabor filters used) was established. The size and orientation of these filters was associated with the structural features of the choroidal vasculature, predominantly from the histological literature. The possible influence of artefacts was also considered (e.g. those inherent to OCT imaging).

The classifier with the highest accuracy in the leave-one-out cross-validation (RFS) was used for this analysis. The 'permuted delta error' was used as a measure

of importance of each image feature to the classifier (Ishwaran 2007; Baas 2016). The increase in prediction error (i.e. misclassification rate) in the leave-one-out cross-validation was established for when the values from each Gabor filter (n=40) were permuted (i.e. removed from each decision tree). Delta error was calculated as the average of the errors for each tree in the decision forest, divided by the standard deviation of the errors. This was performed for each b-scan, and then averaged across all b-scans in the dataset. These values were normalised from 0 to 1, and the results are shown in Figure 5.19. The higher the delta error, the greater the increase in prediction error of the classifier, and therefore the more important that feature was in determining the classification of each previously unseen image.

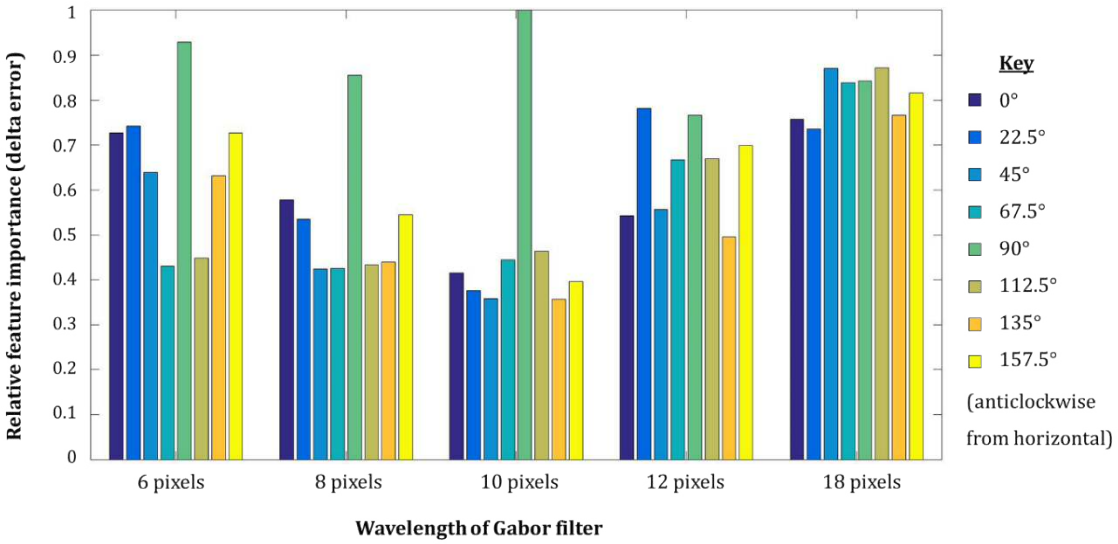

Figure 5.19 Relative feature importance (delta error; y-axis) for each Gabor filter (n=40; x-axis). Filter orientations are indicated by different colours (see key), whilst filters of the same grating size are grouped along the x-axis.

For the 3 smallest filters, the vertical gratings (90°) were of highest importance to the classifier. In OCT imaging, each a-scan is acquired sequentially, representing a reflectivity profile with increasing depth in the imaged structure. The reflectivity at a given depth in each a-scan is relative to the proportion of light reflected by overlying structures. For instance, more light is reflected from a CNV, resulting in an area of relatively reduced intensity in the underlying choroid, when compared to choroid without overlying retinal disruption. This can result in vertically-oriented, sharply demarcated intensity boundaries between neighbouring a-scans (Figure 5.20).

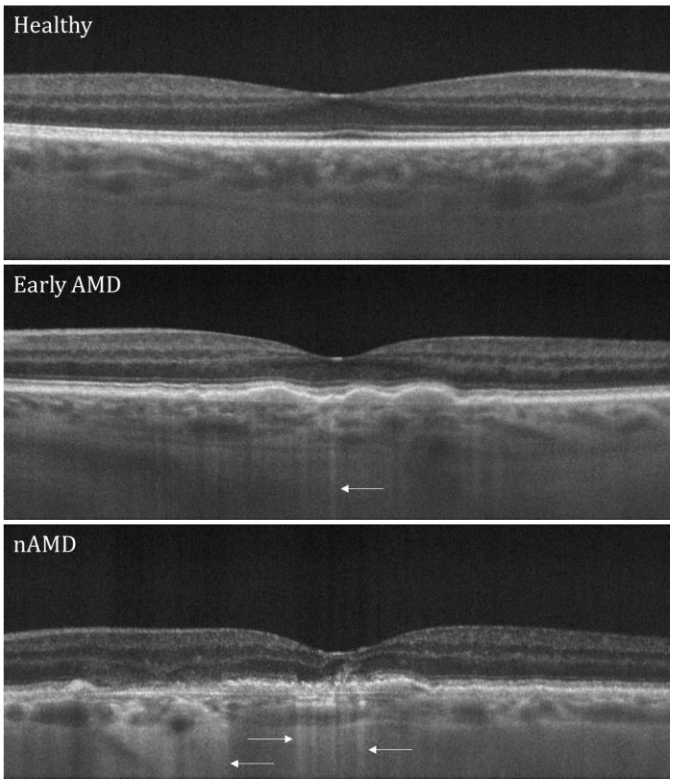

Figure 5.20 An increase in the number of shadow artefacts caused by overlying retinal features can typically be seen with advancing disease stage. These produce sharply demarcated vertical features in the deeper structures (choroid and sclera; examples indicated by arrows in the sclera, where they are most visible).

These vertical features are likely to be increasingly common in advancing disease, due to increased disruption of the retinal layers (particularly the hyper-reflective RPE). This orientation was likely to produce discriminative features for classification influenced by features of the overlying retina, rather than solely the choroidal structure. This argument is supported by an analysis of the 10 most important features in the classifier, which included all 5 gratings with vertical orientation (Figure 5.21). There was little difference in discriminative ability between the other filter orientations (Figure 5.22A).

The mean delta error for each filter size and orientation was calculated, and was used as an indicator of feature importance to disease classification. The largest grating size (lowest spatial frequency; wavelength 18 pixels) was generally of high importance to the classifier, with 5 of the 8 orientations appearing in the top 10 features (Figure 5.21 and Figure 5.22B). The size of this grating equated to a vessel diameter of ~102 μm for the vertical grating orientation; most similar in size to the large choroidal vessels of this cohort. This indicates that the size of the large choroidal vessels was discriminative between disease groups, and therefore that the large vessels may be most affected throughout the disease process. This is supported

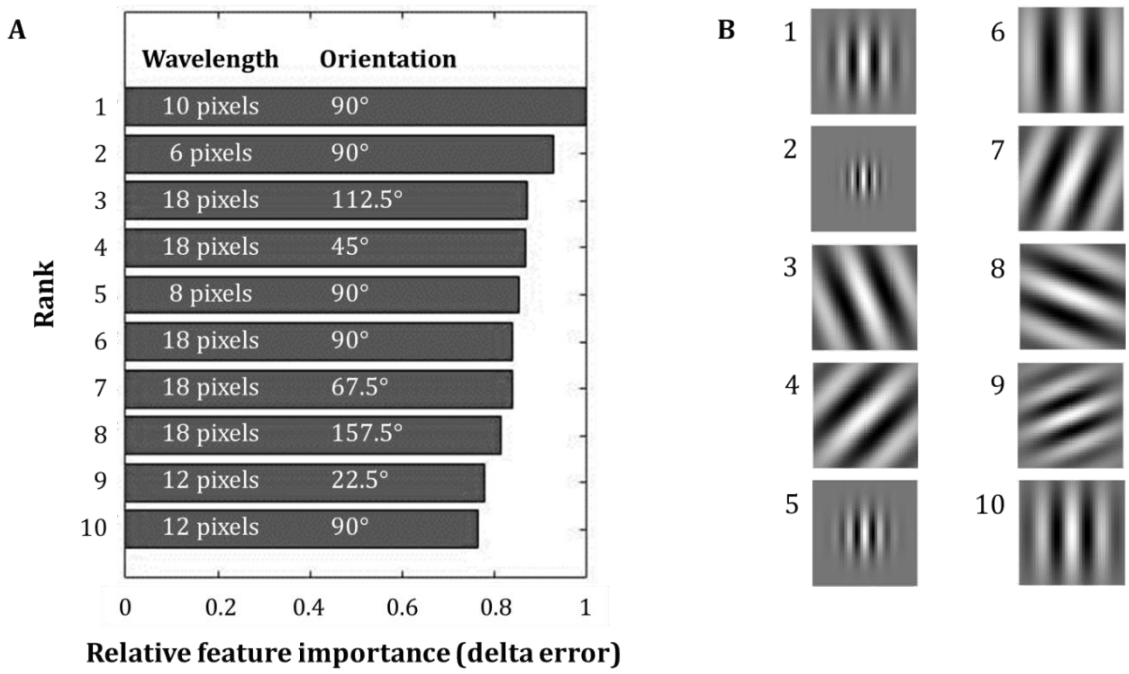

Figure 5.21 The top 10 features sorted by relative importance to the classifier (A). The corresponding Gabor filters are also shown (B).

by the results of the manual choroidal parameters evaluated in Section 4.4, in which the mean visible vessel diameter (VVD) was lower in nAMD than the other two groups. However, it is difficult to draw direct comparisons between these analyses, due to the difference in measurement orientations. VVD was consistently measured axially, whilst the largest grating was applied at various orientations, with marginally higher discriminative ability in the near-vertical orientations (Figure 5.19). Although there is little literature on histological changes to the large vessels in AMD, Spraul et al. (1999) reported a decrease in vascular density, which is consistent with the decrease in choroidal vascular index (CVI) identified using *in vivo* imaging (Sonoda et al. 2014; Wei et al. 2016).

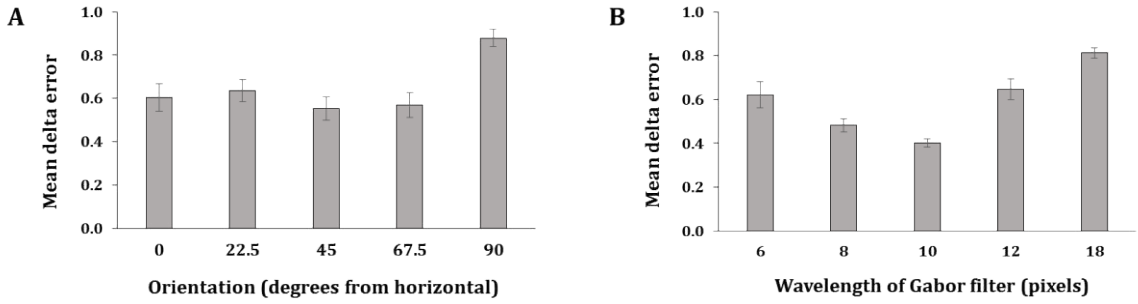

Figure 5.22 Mean (± SE) delta error for each Gabor filter orientation (A) and grating size (B). The vertical gratings were excluded from the grating size analysis (B), due to their likely non-choroidal origin.

The smaller grating sizes (particularly the filter with highest spatial frequency; wavelength 6 pixels) also contributed to disease classification (Figure 5.22B). This filter was more discriminative for the near-horizontal orientations (0°, 22.5°, and 157.5°) than the near-vertical orientations (67.5° and 112.5°; Figure 5.19). In fact, with increasing filter size, the features of higher importance transitioned from the near-horizontal orientations to the near-vertical orientations (when considering the 90° filters as non-choroidal). This trend is in line with the expected energy response for each filter, considering the difference in axial and lateral scaling, and the resulting axial and lateral components of each grating size (described in Section 5.1.2 and demonstrated in Figure 5.23). Due to the decoupling of axial and lateral scaling in OCT imaging, filters of different orientation were theoretically more sensitive to vessels of different diameter. Considering the image scaling factors (x1.9 axially and x11.3 laterally, assuming an AEL of 24 mm), the range of filter sizes used corresponds to vessel diameters of approximately 6 μm to 17 μm axially, and 34 μm to 102 μm laterally. In other words, the higher spatial frequency filters should generate a greater response to the small choroidal vessels, with highest sensitivity in the axial direction (near-horizontal filters). For the larger filters, the response should be greatest for the large choroidal vessels, particularly

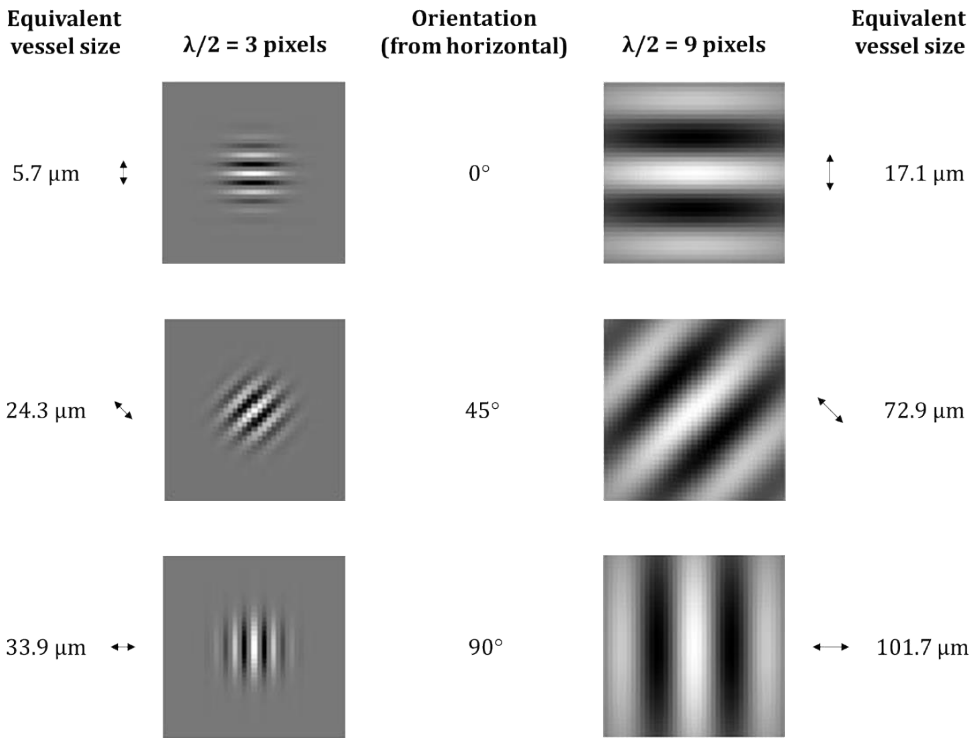

Figure 5.23 Equivalent feature size for the smallest and largest Gabor filters used, with varying orientation. The equivalent size describes the vessel diameter with the expected greatest energy response to a given filter, at a given orientation.

in the lateral direction (near-vertical filters). This is consistent with the trend seen in Figure 5.19.

5.2.3 Investigation of convolutional neural networks (CNN)

The evaluated classifiers required input of 'hand-crafted' features; responses from the Gabor filters were used in this case. However, defining the features on which to base the classification may introduce an element of bias. In an attempt to minimise the effect of this, the filters used were selected to correspond to a wide range of vessel sizes, in both the axial and lateral directions (discussed in the previous section). To eliminate this bias altogether, the use of an alternative classifier (CNN) was also explored, which produced a classification without the need for predefined hand-crafted features.

For this type of machine learning technique to be successful, very large datasets are typically required, to include the wide range of textural appearances, thereby allowing generalisation to the population (Krizhevsky et al. 2012). A total of 75 eyes were included in this analysis (n=25 per class), which is unlikely to include the sufficient range of choroidal appearances in eyes with and without AMD, for accurate results with this type of classifier. Therefore, the aim of this analysis was to explore the feasibility of applying CNN to a dataset of OCT images of various AMD disease stages. This would be confirmed by a high accuracy of the 2-fold cross-validation, although the size of this dataset was expected to result in over-fitting of the classifier, and therefore limited accuracy in the leave-one-out cross-validation. Due to the computational time required to train the CNN, the 10-fold cross-validation (the least stringent validation method due to the smallest number of samples in the testing set) was not performed as part of this analysis.

The CNN yielded near-perfect classification accuracy with 2-fold cross-validation (Table 5.5). The accuracy was improved when the individual patches in a b-scan were combined to determine the final classification, and was higher-still when all b-scans in the volume were considered in the final decision for that eye. Although the CNN showed near-perfect sensitivity and specificity with this method of cross-validation (Table 5.6), it performed poorly in the leave-one-out cross-validation (no better than chance; 33% for three classes; Table 5.5).

Table 5.5 Classification accuracy (%) of the convolutional neural network (CNN), with 2-fold cross-validation, and leave one out cross-validation (LOOCV). 2-fold cross-validation was evaluated by establishing the classification accuracy per patch, by combining all patches within a single b-scan (per b-scan), and by combining all b-scans within a single volume (per eye).

	Healthy	**Early AMD**	**nAMD**	**Mean**
2-fold (per patch)	92.5	91.1	92.0	**91.9**
2-fold (per b-scan)	100.0	99.6	99.3	**99.6**
2-fold (per eye)	100.0	100.0	100.0	**100.0**
LOOCV (per eye)	25	25	33	**27.7**

Table 5.6 Sensitivity (%) and specificity (%) of the convolutional neural network (CNN), using the 2-fold and leave-one-out cross-validation (LOOCV). The diagnostic ability of the classifiers to identify any stage of AMD (3rd column) and nAMD (4th column) were evaluated. For the purposes of this table, AMD = early + nAMD groups; non-AMD = healthy group; neovascular = nAMD group; non-neovascular = healthy + early AMD groups.

		AMD vs. non-AMD	**Neovascular vs. non-neovascular**
2-fold	Sensitivity	99.9	99.3
	Specificity	100.0	99.8
LOOCV	Sensitivity	64.6	33.0
	Specificity	25.0	64.6

As expected, this large difference in accuracy between validation methods indicates that the within-class variability of the data was large, and the classifier was over-fit to the training data. However, the classifier accuracy with 2-fold cross-validation was higher than that of the classifiers evaluated in Section 5.2.1. This suggests that CNN may be a promising technique for this application, given a sufficient sample size; its full potential for automated classification of AMD severity should therefore be evaluated on a substantially larger dataset (discussed further in Section 5.3). This could provide further knowledge of changes to the vasculature in AMD, without the bias of handcrafted features.

5.3 Discussion

The three classifiers evaluated in Section 5.2.1 produced high classification accuracy for the 10-fold and 2-fold cross-validation, confirming the feasibility of applying these machine learning techniques to automated classification of AMD

disease stage, based on choroidal appearance. The accuracy was substantially lower for the leave-one-out cross-validation, suggesting poor generalisation of the classifiers to the population. This was likely due to limited sample size and high within-group variability in choroidal structure. The best-performing classifier in the leave-one-out cross-validation was RFS, followed by SVM. KNN produced the lowest classification accuracy, which is unsurprising since this was the most basic of the methods evaluated.

The use of a CNN was also explored, as an alternative to these classifiers (Section 5.2.3). This is a deep learning technique, using the image data as input, rather than hand-crafted features. Salient image features are learnt through a series of feedback loops in the network, and are used as a basis for classification of previously unseen images. As expected, the classification accuracy of the leave-one-out cross-validation was substantially lower for this method, likely due to high within-class variability in choroidal appearance. Despite this, the CNN produced near-perfect classification accuracy with 2-fold cross-validation; this demonstrates excellent potential for this application given the relatively small sample sized used, and indicates likely success should it be applied to a substantially larger dataset (e.g. n≈1500 eyes; discussed later in this section).

From the literature, only one study has applied machine learning techniques to automated classification of OCT images based on choroidal structure. Koprowski et al. (2013) used RFS to classify macular lesions as neovascular, ischemic, or fibrovascular scarring. Using 20% of the images for testing, accuracies of 73%, 83%, and 69% were achieved for the three groups respectively. These values are comparable to the current study, with an accuracy of 80% for the nAMD group using the RFS classifier (Table 5.4). Since the groups were not the same (i.e. there were no healthy or early disease groups), potential comparisons are of limited value. However, this does support the hypothesis that structural choroidal differences are present within OCT images, and that these images can be used to detect and assess this pathology.

Other studies classifying AMD from OCT images have been published, in particular using SVM as a classifier (Srinivasan et al. 2014b; Albarrak et al. 2016; Section 1.7.3). The more recent of these studies classified images into two groups (healthy or AMD), and demonstrated performance ranging between 86% and 100%

with 10-fold cross-validation. The mean accuracy of the present study was 98.3% with SVM (Table 5.2), which was at the higher end of this range, despite the use of a smaller dataset (n=75 eyes, versus n=140 eyes).

Srinivasan et al. (2014b) achieved an average of 93.3% accuracy with leave-one-out cross-validation for normal versus dry AMD, using an SVM classifier. This is higher than the present study (57.3%), likely because the analysis was based on retinal (rather than choroidal) features. The difference in these textural features between groups would be expected to be well-defined, due to the distinct characteristic retinal appearance of the disease (e.g. disruptions to the RPE overlying drusen). Images were cropped to exclude the choroidal region, making comparison between these findings difficult. Furthermore, two eyes with AMD were selectively excluded from classifier training, as they were 'unrepresentative' of the dataset (although the nature of this was not defined by the authors). No eyes were excluded from classifier training in the present study, which may have limited the accuracy of the results, but is more likely to be representative of the population. In relatively small training samples (such as the dataset used in this thesis), the inclusion of atypical disease appearance may skew the importance of features in the classifier. However, this is of particular importance with regard to large-scale clinical application, where accurate classification of atypical disease would require the classifier to be exposed to atypical clinical appearance during the training process.

A further study evaluated the use of CNN to classify normal (n=1259) versus AMD (n=347) from OCT images (Lee et al. 2017). This study used one of the most extensive datasets to date for this type of analysis, and achieved a sensitivity of 88.6% and specificity of 87.8%, with one fifth of images used for testing only (no b-scans from test eyes were used in classifier training). The patients in the AMD group had nAMD in at least one eye, and VA poorer than 0.20 logMAR in the better-seeing eye. The mean VA of that group was 0.38 ± 0.50 logMAR, which is similar to that of the nAMD group in the present study (0.37 ± 0.37 logMAR; see Section 4.3), suggesting similar functional disease severity between studies. For this reason, the results are compared to the nAMD versus non-nAMD analysis in the present study. Although the results of the CNN classifier were poor due to over-fitting, the RFS classifier yielded a sensitivity of 80% and specificity of 76%. These values are lower

than those reported by Lee and colleagues, although this is be expected due to the inclusion of retinal features in the classification, and the substantial difference in sample size.

The nAMD group typically had the highest classification accuracy of the three classes. This suggests that this group had a distinct choroidal appearance, detectably different to that of the other two groups. This is consistent with the results of the manual choroidal parameters evaluated in Section 4.4, with significant differences in choroidal structure detectable only in the nAMD group. From this, one may conclude that the majority of detectable choroidal changes occur in the more advanced disease stages. This is also consistent with the literature, where significant thinning of the choroid has predominantly been identified in late-stage disease (Chung et al. 2011; Esmaeelpour 2014a; Lu et al. 2016; Wei et al. 2016). However, since the majority of individuals in the nAMD group were currently undergoing (or had previously undergone) anti-VEGF therapy, it was not possible to determine whether the vascular features used to classify this disease group were attributed to pathological degeneration or resulting from pharmacological intervention (see Sections 1.4.6 and 4.5).

Classification accuracy was considerably higher than chance (range 40-60%, versus 33%) for the differentiation of early AMD and healthy eyes. This suggests that there are changes in the textural appearance of the vasculature visible in OCT images, even at the early stages of the disease. To further explore these structural differences, the discriminative image features in the classification were compared to the physiological structure of the choroid, established with histological techniques (Ramrattan et al. 1994; Spraul et al. 1999). This analysis was performed on the classifier yielding the highest accuracy (RFS), as this would provide greatest confidence that the features used by the classifier reflect the choroidal structure. Although knowledge of the features learnt by the CNN would provide structural information unbiased by the use of hand-crafted features, the classification accuracy was not significantly better than chance for the sample size used here. It would not be possible to have confidence in the features learnt, and this analysis was therefore not undertaken.

The importance of the vertical features in the classifier was likely (at least in part) artefactual, resulting from pathological disruption to the overlying retina. An

area of relative retinal hyper- or hypo-reflectance caused differences in choroidal intensity between neighbouring a-scans, producing vertical intensity boundaries. Whilst present in all images, the prevalence of these shadow artefacts may be expected to increase with advancing disease stage, due to an increase in retinal disruption (Figure 5.20). Since it is likely that this artefact contributed to accurate classification of disease groups in this analysis, the classification was influenced by overlying retinal features, rather than being based solely on choroidal appearance. For this reason, the artefactual delta errors were removed prior to association of the discriminative filters to choroidal structure. Since this 'shadow' artefact is inherent to OCT imaging, this filter orientation should be removed from feature extraction of sub-retinal structures in future analysis, where possible.

Both the small and large Gabor filters were discriminative between disease groups, with the medium-sized filters providing a smaller contribution to the classification (Figure 5.19). For the small filters, the near-horizontally oriented filters were most discriminative, which equated to ~6-10 μm vessel diameter. This corresponds to the vessels of the choriocapillaris (mean diameter ~7-10 μm; Ramrattan et al. 1994; Spraul et al. 1999), suggesting that the choriocapillaris becomes increasingly abnormal throughout the AMD disease process. This is consistent with histologically identified changes primarily to diameter and density of the choriocapillaris in both early- and late-stage AMD, compared to healthy control eyes (Sarks 1976; Ramrattan et al. 1994; Spraul et al. 1999; McLeod et al. 2009). It should be noted that this filter size is nearing the axial resolution limit of the OCT device (~6 μm); structures smaller than this would therefore not be detectable with this imaging technique.

For the large filters, there was less difference between the filter orientations, although the near-horizontal orientations were generally of less importance to the classification. Considering the near-vertical orientations (excluding the 90° orientation), these filters correspond to vessel diameters of ~68-102 μm (i.e. the vessels of the Haller and Sattler layers). This suggests that changes to the larger vessels also occur with advancing disease. This is again consistent with Spraul et al. (1999), who reported a lower density of veins in eyes with AMD than healthy controls (by nearly 50%). To summarise, these findings support the reported

histological changes to the structure of all vessel layers (choriocapillaris and the medium/large choroidal vessels), throughout the AMD disease process.

There were a number of limitations to this work, which will be outlined and discussed here. Firstly, the sample size was relatively small for a study applying machine learning techniques. However, the aim of this research was to investigate the feasibility of this analysis for automated classification of AMD by disease severity, which has been achieved. To confirm these findings, and to fully investigate the potential of these techniques for large-scale clinical application, a large dataset would be required. The findings are consistent with reported histological changes to the choroidal structure in AMD, and suggest that these changes are detectable *in vivo*, using long-wavelength OCT imaging.

Based on previous studies which have applied machine learning to AMD disease classification from OCT images, the sample size required to achieve accurate classification would likely be ~1000-1600 images (Koprowski et al. 2013; Lee et al. 2017). The upper end of this range relates to the application of CNN to a binary classification problem (i.e. disease versus non-disease); for accurate classification into three groups, an even larger dataset may therefore be required. However, considering that these previous studies utilised conventional OCT, optimisation of imaging techniques to enhance visualisation of the choroidal features (e.g. long-wavelength OCT imaging, in conjunction with enhanced depth imaging and swept-source OCT) may result in a smaller dataset proving sufficient to identify the choroidal features which best discriminate between groups.

The selection of handcrafted features limited the range of feature sizes that could be detected and utilised by the classifiers. To minimise the effect of this, Gabor filter sizes were selected to reflect an appropriate range of vessel sizes in both the axial and lateral orientations (Figure 5.23; see Section 5.1.2). The smallest filter size used was equivalent to ~6 μm. The inclusion of smaller filters than this (i.e. higher spatial frequency) would exceed the axial resolution limit of the OCT; they would therefore not be capable of detecting smaller features in the image, and would become sensitive to high-frequency noise. However, the filters used did not encompass the largest choroidal vessels (>102 μm), as described by the VVD parameter in Section 4.4. Since the largest Gabor filter used was generally the most discriminative in the classifier, and the large choroidal vessels were found to be

smaller in this nAMD cohort, it would be interesting to explore the potential of larger filters (i.e. lower spatial frequency) for including these larger vessels in the classification.

Every b-scan from a volume scan was given the same ground truth classification. Each b-scan was then treated individually by the algorithm, and a majority voting system used to determine the final classification for each eye. This system is based on the assumption that any choroidal changes with advancing disease occur uniformly across the central 20° 20° of choroid. Although areas of vascular change have been shown to correlate with areas of retinal atrophy in GA (McLeod et al. 2002), it is unclear from the literature whether structural changes in the choroid in early AMD are diffuse, or localised to the regions of overlying retinal features. In nAMD, a decrease in percentage vascular area (similar to CVI) has been demonstrated to extend beyond the area of the CNV, by at least 1 mm (McLeod et al. 2009). In the present study, every b-scan was given equal weighting in the final classification, regardless of position in relation to the foveal pit, or the presence or absence of overlying retinal features indicative of disease (Figure 5.24). During the majority voting of an eye with nAMD, if the choroid had a healthy appearance in a high proportion of b-scans (over one third of the total), the eye would have been given an incorrect final classification of healthy. This may have limited the sensitivity of the classifiers, particularly for the detection of nAMD.

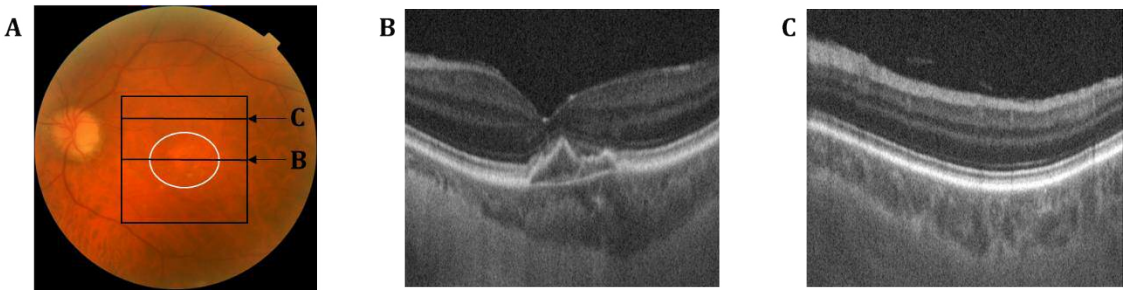

Figure 5.24 Retinal photograph of an eye with nAMD (A). The visible retinal features on OCT are confined to the foveal and parafoveal area (outlined in white). A b-scan through the fovea (B) shows visible disruption to the retinal layers, whilst a b-scan of a more peripheral location (C) contains no obvious retinal signs of any stage of AMD. Both b-scans are given equal weighting in the final disease classification of the eye.

The ground truth data was based on clinical grading, using an adapted version of the AREDS classification system (AREDS 2001a). This system is based upon the appearance of retinal features (described in Section 4.2), although how this relates to choroidal appearance throughout the disease process is unclear. The

correlation between AREDS disease severity and structural change to the choroid is not known (despite a gross relationship shown with histology), although the results of Section 4.3 suggest that these changes are detectable only at the nAMD stage (group 4; advanced). Additionally, the early AMD group included AREDS groups 2 and 3 (early and intermediate). This was partially for ease of classifier training, but also since the original statistical power was calculated assuming three groups. Dividing the dataset into four groups would reduce the amount of training data available for each group. However, since the early group was less easily differentiated from the healthy group, comparing between an early and intermediate group may help to pinpoint where in the disease process the observed vessel changes occur.

Furthermore, the disease status of the fellow eye was not considered in this analysis. In the early AMD group, the increased risk of progression to nAMD in those with a diagnosis of nAMD in the fellow eye may be related to choroidal structure (see Section 4.4.2). Given a dataset of sufficient size, inclusion of fellow eye diagnosis in the classifier may reveal potential for using machine learning techniques to predict the development of late-stage AMD. The present study was cross-sectional, and therefore no conclusions can be drawn regarding vessel changes over time. A longitudinal study could be conducted to investigate the timeline of vascular changes throughout the AMD disease process, as well as the effect of anti-VEGF therapy on choroidal structure, to differentiate structural changes relating to pathology and intervention.

To summarise, the novel use of machine learning techniques for automated classification of AMD by disease severity, based on choroidal appearance, was shown to be feasible. Reasonable classification accuracy was achieved using classifiers trained with hand-crafted features. Despite limitations in the size of the training dataset, the application of an additional classifier based on self-learnt features (CNN) produced promising results. These findings suggest that changes to the choroidal vasculature occur throughout the AMD disease process, and that these changes are detectable using *in vivo* long-wavelength OCT imaging.

6 Discussion, conclusions, and future work

6.1 General discussion

The overall aim of this research was to determine whether structural changes to the choroidal vasculature in AMD are detectable using *in vivo* OCT imaging. It was evident from the literature (Chapter 1) that such changes have been identified *ex vivo*, using histological techniques. However, *in vivo* quantification of the choroid using OCT imaging has mostly been limited to choroidal thickness measurement, which is highly variable between individuals, and is affected by many physiological factors. A literature review revealed a small number of other quantification techniques that had been applied to images of other choroidal pathologies, such as central serous chorioretinopathy. From this review, three supplementary aims were developed: to optimise image acquisition and processing protocols to allow enhanced visualisation of the choroidal vasculature; to develop and evaluate repeatable parameters for describing and quantifying the vasculature; and to explore the feasibility of applying machine learning techniques to automated classification of AMD by disease severity, based on choroidal appearance.

The studies in this thesis utilised a non-commercial long-wavelength (1040 nm) OCT, intended to maximise visualisation of the choroidal vasculature compared to the conventional OCT devices available at the outset of this work. Image acquisition and processing techniques were optimised for choroidal visualisation, including scan parameters, artefact correction, and noise reduction (Chapter 2). To ensure that these investigations would be clinically applicable, it was decided that the images used in further analysis should be of comparable size to those commonly collected on commercial devices. Isometric volume scans were used to provide a three-dimensional representation of the vasculature, whilst averaged, over-sampled line scans allowed for higher definition of the structural boundaries.

To ensure that images were scaled appropriately, a study investigating the effect of lateral scaling on image quantification was performed (Chapter 3). It was shown that inappropriate scaling resulted in errors which affected the consistency and reliability of image measurements, and therefore axial eye length (AEL)-dependent lateral scaling should be employed (Terry et al. 2016). For this reason,

the AEL of all participants included in this thesis was acquired to allow for accurate quantification of the OCT images.

The feasibility of eight parameters were then evaluated for quantifying the choroidal structure, and inter-session repeatability on healthy eyes (n=25) was established. All parameters demonstrated reasonable repeatability (CoR < 20% in all cases), and were therefore likely sufficient to detect structural differences between disease groups. The over-sampled line scans produced more reliable measurements, due to improved visibility of the deeper vessels and posterior choroidal boundary, particularly in eyes with thicker choroids. The volume scans allowed for enface analysis of vessels across the entire macula, at a given depth beneath the RPE. To ensure a consistent sampling depth across the scan, a MATLAB-based program was developed to flatten the scans to the RPE. Furthermore, an existing device-independent algorithm for automated choroidal segmentation was evaluated (Iowa Reference Algorithms), albeit at a beta stage of development. Its performance was not reliable enough to be applied to this work, although it showed potential for future work. Manual segmentation of the choroid was therefore used throughout this thesis.

A 3-D analysis approach was also attempted, however, this did not yield meaningful results due to the low SNR inherent to choroidal imaging. This should be revisited with the advent of long-wavelength SS-OCT, which demonstrates reduced signal roll-off, and allows acquisition of higher quality images than the non-commercial device used in this study.

A dataset of long-wavelength OCT images was acquired from eyes with early AMD (n=25), nAMD (n=25), and healthy controls (n=25). Due to the limitations of the established grading scales (associated with imaging modalities and the introduction of anti-VEGF therapy), a modified AREDS classification system was developed for clinical classification of eyes by disease severity (Chapter 4). A significant difference in the nAMD group was identified in four of the eight manual choroidal parameters evaluated (subfoveal choroidal thickness, vessel ratio, choroidal area, and luminal area). Visible vessel diameter was also found to produce a difference which neared statistical significance. Subfoveal choroidal thickness and vessel ratio demonstrated the greatest diagnostic potential for nAMD, although the sensitivity and specificity were relatively low for a potential clinical test.

Nevertheless, in conjunction with other structural and functional measures (e.g. retinal layer disruption, visual acuity, etc.), these parameters show potential for monitoring of AMD, particularly for those with late-stage disease. No significant difference was found between the healthy and early AMD groups, with any of the parameters used.

It should be noted that it was not possible to differentiate pathological structural changes from the changes caused by anti-VEGF therapy (Yamazaki et al. 2012; Koizumi et al. 2015; Ting et al. 2016) in the nAMD group. There was no access to participants' medical records in the present study, and treatment history (approximate number of injections) was self-reported. For this reason, no further analysis was performed to investigate the relationship between anti-VEGF therapy and choroidal structure.

The sample size used in the analysis in Chapter 4 was based on a power calculation, and was selected to detect a predefined minimum difference between groups of 8.5 μm. This difference was based on histological data, which may not have been a suitable approximation to differences in the parameters evaluated *in vivo*. The mean differences and within-group standard deviations found in this study (e.g. ~15 μm and ~30 μm respectively for vessel diameter) could be used in future power calculations investigating changes to the choroidal vasculature. Since the intra-group variation was higher than expected, a larger sample size would be required to detect a significant difference between disease groups (with the same power and significance level), particularly for the parameters with little inter-group difference.

Since these manual measurements were time-consuming and likely to be limited by inter-observer variability, the use of machine learning techniques for automated disease classification was investigated (Chapter 5). This technique had not been previously used to investigate pathological changes to choroidal structure in different stages of AMD. Since the dataset used was relatively small for a study of this nature, the aim was to determine the feasibility of these techniques, rather than to develop a classifier with near-perfect classification accuracy. Of the classifiers investigated, the random forest (RFS) classifier achieved the highest accuracy, particularly in the leave-one-out cross-validation (representing the clinical scenario of an eye previously unseen by the classifier). This demonstrated the feasibility of

applying machine learning techniques to automated classification of AMD by disease severity, based on choroidal appearance.

Classification accuracy was highest for the nAMD group, suggesting that vascular changes were most pronounced in this group, which was consistent with the manual choroidal parameters evaluated in Chapter 4, and both histological and *in vivo* evidence (McLeod et al. 2009; Lu et al. 2016; Wei et al. 2016). However, since this disease stage is more easily diagnosed from other pathological signs visible on OCT imaging (e.g. CNV development and/or intra- or sub-retinal fluid), identification of nAMD based solely on choroidal appearance alone has limited clinical applications. Optimisation of machine learning algorithms to include both choroidal and retinal features, similarly to that performed by Lee et al. (2017), allows for automated detection of nAMD with high accuracy. For this to be effective for automated clinical diagnosis of nAMD, training data should include untreated (newly diagnosed) eyes with nAMD, to minimise the effects of anti-VEGF therapy on the appearance of the structures. This may be of benefit in triaging patients in referral refinement schemes, prioritising those individuals requiring therapeutic intervention. There may also be potential for monitoring AMD in 'virtual' macular clinics within the hospital eye service, allowing for clinical follow-up without the need for extensive ophthalmological examination. To this end, an 'active' versus 'inactive' nAMD classification protocol would be required. These applications could provide potential benefits to the health service, including reduction of clinic oversubscription and costs. This is particularly pertinent, given the ageing population and the predicted increase in AMD prevalence (Owen et al. 2012; Wong et al. 2014).

The RFS classifier was successful at differentiating between the early AMD and healthy groups. However, the possibility of the discriminative image features being artefactual rather than structural must be considered, particularly the influence of shadow artefacts from overlying retinal features. Although these contributed in part to the classifier accuracy, other (non-vertical) structural features were also discriminative between disease groups, which were more likely of choroidal origin. This suggests that structural changes to the choroid may occur early in the disease process. These changes were not detected by applying the

manual choroidal parameters to the same image dataset, indicating that the machine learning techniques were potentially more sensitive to early structural change.

These findings are consistent with the hypothesis that the choroid is involved in the pathogenesis of AMD, although the extent of this involvement (i.e. a cause or effect relationship) would be speculative at this time. If these changes occur prior to retinal degeneration, identification of this could be significant for early detection of AMD (alongside other biomarkers, e.g. from dark adaptation; Owsley et al. 2016), prior to onset of symptoms including visual loss, and irreversible retinal damage. Furthermore, this could have a potential application in disease monitoring, through identification of patients at risk of progressing to the sight-threatening late-stages of the disease. However, longitudinal investigation is required to identify those participants who develop AMD, or progress to nAMD, and to explore choroidal changes associated with this progression.

It is important to note that the ground truth classification (i.e. the method by which images were labelled with a disease group), was based upon clinical appearance. This was undertaken using a modified AREDS system (AREDS 2001a), and was therefore based on retinal features, with no influence from the structure of the choroid. Results obtained from this dataset are therefore dependent on the assumption that changes to the choroidal vasculature throughout the disease process are congruous with the retinal changes upon which the classification system is based. The exact relationship between choroidal and retinal changes throughout the AMD process is unclear, although a gross relationship has been demonstrated with histology (McLeod et al. 2009; Whitmore et al. 2015). It is possible that there are choroidal changes which precede the development of clinically detectable early AMD or nAMD, but would be classified as healthy or early AMD respectively using this clinical classification. Whilst these features would be considered sub-clinical, they may affect the outcome measures of these groups. This limitation is inherent to cross-sectional study designs such as this one, which involve dividing data based on assumptions. A definitive method of identifying these individuals with sub-clinical disease is to conduct a longitudinal study, and to retrospectively subdivide these groups by stable versus advancing disease severity. However, this was not feasible in the timescale of this project.

Furthermore, the 'early AMD' group included AREDS severity groups 2 and 3 (early and intermediate AMD). The three groups used in the present study were expected to produce relatively large differences in choroidal appearance between groups, as indicated by previous histological and *in vivo* studies (Spraul et al. 1999; Sigler and Randolph 2013; Wei et al. 2016). These coarse groups were chosen to explore the feasibility of detecting structural differences *in vivo*. No significant difference was found between the healthy and early AMD groups using manual quantification, although the difference between the early and nAMD groups was significant. The within-group variability was highest in the early AMD group, suggesting a large range of choroidal appearances within this disease stage. Given that there is some evidence of a detectable difference in choroidal structure between intermediate AMD and nAMD (Esmaeelpour 2014a), this should be explored further by subdividing into early and intermediate disease groups. However, this sub-analysis was not performed in the present study, due to sample size restrictions.

6.2 Summary and conclusions

The main aim of this research was to determine whether structural changes to the choroidal vasculature in AMD are detectable using *in vivo* imaging. To achieve this, three supplementary aims were developed (outlined in Section 1.7), which have been addressed as follows:

1) To optimise protocols for image acquisition and processing for enhanced visualisation of the choroidal vasculature.

A series of preliminary investigations were carried out to determine the optimal protocols for visualising the vasculature. The importance of image over-sampling, and accurate lateral image scaling were demonstrated. A non-commercial long-wavelength (1040 nm) SD-OCT was successfully used to acquire volume scans, and over-sampled line scans from the participants included in this thesis, which underwent AEL-dependent lateral scaling. Using the acquisition and processing protocols developed, the choroidal vasculature could be visualised in all participants.

2) To evaluate parameters describing the choroidal vasculature, including assessment of inter-session repeatability.

Eight parameters were developed to quantify the choroidal structure, and assessed for inter-session repeatability. The over-sampled line scans produced more reliable measurements than the volume scans, and hence were used for these measurements (with the exception of the enface analysis). All parameters demonstrated high inter-session repeatability, and were therefore assessed for their ability to distinguish between disease severity groups. Four of these parameters identified a statistically significant difference in late-stage disease. The choroid was shown to be thinner in eyes with advanced disease, with a reduction in luminal area, although it is not possible to differentiate between changes caused by the disease and by anti-VEGF therapy. No changes to the choroidal structure were identified in early AMD. Although these parameters are easily applied to OCT images, their diagnostic ability is limited due to a relatively poor sensitivity and specificity for a clinical test. Despite their limitations as standalone biomarkers, they may be useful parameters to be used in conjunction with other clinical information, to inform clinical follow-up (i.e. monitoring of individuals likely to progress to late-stage disease).

3) To explore the feasibility of applying machine learning techniques to automated classification of AMD by disease severity, based on choroidal appearance.

Due to the relatively low contrast and SNR of the choroidal images, a texture analysis-based machine learning approach was utilised. Although the restricted size of this dataset did not allow for the development of highly accurate classifiers, it was of sufficient size to confirm that textural changes to the choroidal region with advancing disease are detectable in long-wavelength OCT images. The discriminative features in the classifier were consistent with previous histological findings; this supported the hypothesis that structural changes to the choroidal vasculature are detectable *in vivo*. Although these changes are most pronounced in the advanced disease stage, it is not known whether this is due to the pathology or pharmacological intervention. The classification results indicate that changes are present in early disease stage, supporting the theory that the choroid is involved in the pathogenesis of AMD. Although very large datasets are required to enable highly accurate classifiers to be trained, machine learning shows great potential for

automated screening and computer-aided diagnosis of AMD from OCT images (Apostolopoulos et al. 2016; Lee et al. 2017).

To conclude, these results show that structural changes to the choroidal vasculature in AMD are detectable *in vivo* with OCT imaging, using both manual and automated analysis techniques. Although these changes are prominent in late-stage disease, subtle structural changes in early AMD can be identified with texture analysis. This furthers our understanding of changes to the choroidal structure throughout the disease progression.

6.3 Future work

Following on from the work in this thesis, future research should be directed towards optimising machine learning algorithms for automated detection and classification of AMD by disease severity. This would be extended from solely the choroidal region (as in this thesis) to include pathological retinal signs visible on OCT images (e.g. disruption to the intra-retinal layers and RPE), allowing for highly accurate prediction of disease stage. Such a study would require a large dataset of clinically labelled OCT images (n≈1500 eyes; Koprowski et al. 2013; Lee et al. 2017) of various disease stages (healthy, early, intermediate, and advanced AMD) in order to train convolutional neural networks capable of generalisation to the population. The learned features could then be explored to further our understanding of choroidal involvement in the pathogenesis of AMD.

To maximise the clinical applicability of the classifiers, images from a commercial OCT device should be used for training (and testing). These devices are commonplace in primary and secondary care, facilitating data collection and subsequent integration of algorithms into these clinical settings. However, conventional-wavelength OCT devices do not provide sufficient visualisation of the choroidal vasculature to obtain reliable results. Long-wavelength swept-source OCT devices are now commercially available (Topcon DRI OCT Triton, and Zeiss PLEX Elite 9000), which are optimised for visualising the choroid. Images from these devices would produce the clearest view of the choroidal vasculature but, to the author's knowledge, no large AMD datasets have yet been acquired with these

devices. The potential of OCT imaging for automated screening and computer-aided diagnosis of AMD should be investigated using these devices.

The effects of nAMD and anti-VEGF therapy on choroidal structure were confounded in the research, since the majority of the nAMD group were undergoing (or had previously undergone) this treatment. To differentiate the treatment effects from those of the underlying pathology, it would be necessary to obtain long-wavelength OCT images from treatment-naïve eyes. The simplest and most ethically acceptable method of achieving this would be to acquire images at the time of diagnosis, i.e. prior to the initial intravitreal injection. If choroidal changes are part of the natural history of AMD, one would expect to observe these changes in choroidal structure at this point in time (prior to pharmacological intervention). To further explore the effects of treatment, subsequent OCT images could be obtained from the same cohort in a longitudinal study. For example, given that AMD progresses slowly, if significant changes to the choroidal vasculature were observed one month post-treatment follow-up, the most likely explanation would be that these observed effects are related to the treatment rather than the disease. Additional longitudinal data may be used to determine the characteristics of the dose-response relationship.

With the increasing need for large datasets, particularly for studies applying machine learning techniques (Krizhevsky et al. 2012), multi-centre studies will likely be used to meet this demand. Due to the imaging equipment available at each centre, these studies often include images from a number of different OCT devices. Due to the size of these datasets, device-independent algorithms for automated segmentation of the choroidal boundaries (such as the Iowa Reference Algorithms) should be optimised and validated on each device, to minimise analysis time and inter-observer variability associated with manual segmentation.

Finally, the time-course of structural changes to the choroid in the AMD disease process could be investigated. If these changes occur prior to severe retinal degeneration, and are detectable with *in vivo* imaging, this may provide novel biomarkers for identifying individuals at risk of progressing to nAMD, which could help inform clinical follow-up regimes. A large longitudinal study utilising long-wavelength SS-OCT imaging, with retrospective subgroup analysis of stable versus progressing disease, would strengthen our understanding of the underlying

pathophysiology of AMD. This may identify vascular features which predispose an individual to retinal degeneration, allowing early detection of disease prior to irreversible visual loss.

References

Abràmoff, M.D., Garvin, M.K. and Sonka, M. 2010. Retinal imaging and image analysis. IEEE Reviews in Biomedical Engineering 3, pp. 169–208.

Adhi, M., Brewer, E., Waheed, N.K. and Duker, J.S. 2013. Analysis of morphological features and vascular layers of choroid in diabetic retinopathy using spectral-domain optical coherence tomography. JAMA Ophthalmology 131(10), pp. 1267–74.

Adhi, M., Lau, M., Liang, M.C., Waheed, N.K. and Duker, J.S. 2014. Analysis of the thickness and vascular layers of the choroid in eyes with geographic atrophy using spectral-domain optical coherence tomography. Retina 34(2), pp. 306–12.

Adhi, M., Ferrara, D., Mullins, R.F., Baumal, C.R., Mohler, K.J., Kraus, M.F., Liu, J., Badaro, E., Alasil, T., Hornegger, J., Fujimoto, J.G., Duker, J.S., Waheed, N.K. and Ablonczy, Z. 2015. Characterization of choroidal layers in normal aging eyes using enface swept-source optical coherence tomography. PLoS ONE 10(7), pp. 1–13.

Agawa, T., Miura, M., Ikuno, Y., Makita, S., Fabritius, T., Iwasaki, T., Goto, H., Nishida, K. and Yasuno, Y. 2011. Choroidal thickness measurement in healthy Japanese subjects by three-dimensional high-penetration optical coherence tomography. Graefe's Archive for Clinical and Experimental Ophthalmology 249(10), pp. 1485–92.

Agrawal, R., Gupta, P., Tan, K.-A., Cheung, C.M.G., Wong, T.-Y. and Cheng, C.-Y. 2016a. Choroidal vascularity index as a measure of vascular status of the choroid: Measurements in healthy eyes from a population-based study. Scientific Reports 6, p. 21090.

Agrawal, R., Chhablani, J., Tan, K.-A., Shah, S., Sarvaiya, C. and Banker, A. 2016b. Choroidal vascularity index in central serous chorioretinopathy. Retina (Philadelphia, Pa.) 36, pp. 1646–51.

Agrawal, R., Li, L.K.H., Nakhate, V., Khandelwal, N. and Mahendradas, P. 2016c. Choroidal vascularity index in Vogt-Koyanagi-Harada disease: An EDI-OCT derived tool for monitoring disease progression. Translational Vision Science & Technology 5(4), p. 7.

Agrawal, R., Salman, M., Tan, K.A., Karampelas, M., Sim, D.A., Keane, P.A. and Pavesio, C. 2016d. Choroidal vascularity index (CVI) - A novel optical coherence tomography parameter for monitoring patients with panuveitis? PLoS ONE 11(1), pp. 1–14.

Ahmed, J., Braun, R.D., Dunn, R. and Linsenmeier, R.A. 1993. Oxygen distribution in the macaque retina. Investigative Ophthalmology & Visual Science 34(3), pp. 516–21.

Akay, F., Gundogan, F.C., Yolcu, U., Toyran, S. and Uzun, S. 2015. Choroidal thickness in systemic arterial hypertension. European Journal of Ophthalmology 26(2), pp. 152–7.

Albarrak, A., Coenen, F. and Zheng, Y. 2016. Volumetric image classification using homogeneous decomposition and dictionary learning: A study using retinal optical coherence tomography for detecting age-related macular degeneration. Computerized Medical Imaging and Graphics 55, pp. 113–23.

Alpaydin, E. 2014. Introduction to Machine Learning. 3rd ed. Cambridge, MA: MIT Press.

Altinkaynak, H., Ceylan, E., Kartal, B., Keleş, S., Ekinci, M. and Olcaysu, O.O. 2015. Measurement of choroidal thickness following caffeine intake in healthy subjects. Current Eye Research 41(5), pp. 708–14.

Altman, D.G. 1991. Practical statistics for medical research. London: Chapman & Hall/CRC.

Alwassia, A., Adhi, M., Zhang, J., Regatieri, C., Al-Quthami, A., Salem, D., Fujimoto, J. and Duker, J. 2013. Exercise-induced acute changes in systolic blood pressure do not alter choroidal thickness as measured by a portable spectral-domain optical coherence tomography. Retina (Philadelphia, Pa.) 33(1), pp. 160–5.

Ambati, J. and Fowler, B.J. 2012. Mechanisms of age-related macular degeneration. Neuron 75(1), pp. 26–39.

Anderson, D., Mullins, R., Hageman, G. and Johnson, L. 2002. A role for local inflammation in the formation of drusen in the aging eye. American Journal of Ophthalmology 134, pp. 411–31.

Anger, E.M., Unterhuber, A., Hermann, B., Sattmann, H., Schubert, C., Morgan, J.E., Cowey, A., Ahnelt, P.K. and Drexler, W. 2004. Ultrahigh resolution optical coherence tomography of the monkey fovea. Identification of retinal sublayers by correlation with semithin histology sections. Experimental Eye Research 78(6), pp. 1117–25.

ANSI 2000. Safe use of lasers & safe use of optical fiber communications. American National Standards Institute - Z136 Committee. Orlando: The Laser Institute of America, p. 168.

Antony, B., Abràmoff, M.D., Tang, L., Ramdas, W.D., Vingerling, J.R., Jansonius, N.M., Lee, K., Kwon, Y.H., Sonka, M. and Garvin, M.K. 2011. Automated 3-D method for the correction of axial artifacts in spectral-domain optical coherence tomography images. Biomedical Optics Express 2(8), pp. 1734–46.

Apostolopoulos, S., Ciller, C., De Zanet, S.I., Wolf, S. and Sznitman, R. 2016. RetiNet: Automatic AMD identification in OCT volumetric data. In: Computer Vision and Pattern Recognition (cs.CV). pp. 1–14.

AREDS 2001a. The Age-Related Eye Disease Study System for classifying age-related macular degeneration from stereoscopic color fundus photographs: The AREDS report no. 6. American Journal of Ophthalmology 132(5), pp. 668–81.

AREDS 2001b. A randomized, placebo-controlled, clinical trial of high-dose supplementation with vitamins C and E, beta carotene, and zinc for age-related macular degeneration and vision: AREDS report no. 8. Archives of Ophthalmology 119, pp. 1417–36.

Ashraf, H. and Nowroozzadeh, M.H. 2014. Diurnal variation of retinal thickness in healthy subjects. Optometry and Vision Science 91(6), pp. 615–23.

Baas, S.P.R. 2016. A machine learning approach to the automatic classification of female uroflowmetry measurements. University of Twente.

Barteselli, G., Lee, S.N., El-Emam, S., Hou, H., Ma, F., Chhablani, J., Conner, L., Cheng, L., Bartsch, D.U. and Freeman, W.R. 2014. Macular choroidal volume variations in highly myopic eyes with myopic traction maculopathy and choroidal neovascularization. Retina (Philadelphia, Pa.) 34(5), pp. 880–9.

Bayhan, H.A., Bayhan, S.A., Intepe, Y.S., Muhafız, E. and Gurdal, C. 2014a. Evaluation of the macular choroidal thickness using spectral optical coherence tomography in patients with obstructive sleep apnea syndrome. Clinical & Experimental Ophthalmology 43(2), pp. 139–44.

Bayhan, H.A., Bayhan, S.A., Tanık, N. and Gürdal, C. 2014b. Evaluation of the chorioretinal thickness changes in Alzheimer's disease using spectral-domain optical coherence tomography. Clinical & Experimental Ophthalmology 43(2), pp. 145–51.

Beatty, S., Koh, H., Phil, M., Henson, D. and Boulton, M. 2000. The role of oxidative stress in the pathogenesis of age-related macular degeneration. Survey of Ophthalmology 45(2), pp. 115–34.

Beatty, S., Murray, I.J., Henson, D.B., Carden, D., Koh, H. and Boulton, M.E. 2001. Macular pigment and risk for age-related macular degeneration in subjects from a Northern European population. Investigative Ophthalmology & Visual Science 42(2), pp. 439–46.

Bengtsson, B. and Krakau, C. 1992. Correction of optic disc measurements on fundus photographs. Graefe's Archive for Clinical and Experimental Ophthalmology 230, pp. 24–8.

Bennett, A., Rudnicka, A. and Edgar, D. 1994. Improvements on Littmann's method of determining the size of retinal features by fundus photography. Graefe's Archive for Clinical and Experimental Ophthalmology 232(6), pp. 361–7.

Bhutto, I.A., McLeod, D.S., Hasegawa, T., Kim, S.Y., Merges, C., Tong, P. and Lutty, G.A. 2005. Pigment epithelium-derived factor (PEDF) and vascular endothelial

growth factor (VEGF) in aged human choroid and eyes with age-related macular degeneration. Experimental Eye Research 82(1), pp. 99–110.

Bhuvaneswari, P. and Therese, a. B. 2015. Detection of cancer in lung with K-NN classification using genetic algorithm. In: Procedia Materials Science. Elsevier B.V., pp. 433–40.

Bird, A.C., Bressler, N.M., Bressler, S.B., Chisholm, I.H., Coscas, G., Davis, M.D., de Jong, P.T.V.M., Klaver, C.C.W., Klein, B.E.K., Klein, R., Mitchell, P., Sarks, J.P., Sarks, S.H., Soubrane, G., Taylor, H.R. and Vingerling, J.R. 1995. An international classification and grading system for age-related maculopathy and age-related macular degeneration. Survey of Ophthalmology 39(5), pp. 367–74.

Bittencourt, M.G., Kherani, S., Ferraz, D. a, Ansari, M., Nasir, H., Sepah, Y.J., Hanout, M., Do, D. V and Nguyen, Q. 2014. Variation of choroidal thickness and vessel diameter in patients with posterior non-infectious uveitis. Journal of Ophthalmic Inflammation and Infection 4, pp. 1–10.

Bogner, B., Tockner, B., Runge, C., Strohmaier, C., Trost, A., Branka, M., Radner, W., Kiel, J.W., Schroedl, F. and Reitsamer, H.A. 2011. The effect of vasopressin on choroidal blood flow, intraocular pressure, and orbital venous pressure in rabbits. Investigative Ophthalmology & Visual Science 52(10), pp. 7134–40.

Booij, J.C., Baas, D.C., Beisekeeva, J., Gorgels, T.G.M.F. and Bergen, A.A.B. 2010. The dynamic nature of Bruch's membrane. Progress in Retinal and Eye Research 29(1), pp. 1–18.

Bradley, A.P. 1997. The use of the area under the ROC curve in the evaluation of machine learning algorithms. Pattern Recognition 30(7), pp. 1145–59.

Branchini, L.A., Adhi, M., Regatieri, C. V, Nandakumar, N., Liu, J.J., Laver, N., Fujimoto, J.G. and Duker, J.S. 2013. Analysis of choroidal morphologic features and vasculature in healthy eyes using spectral-domain optical coherence tomography. Ophthalmology 120(9), pp. 1901–8.

Breiman, L. 2001. Random forests. Machine Learning 45(1), pp. 5–32.

British Medical Association 2017. British National Formulary [Online]. Available at: https://www.bnf.org/ [Accessed: 23 January 2017].

Brody, B., Gamst, A., Williams, R., Smith, A., Lau, P., Dolnak, D., Rapaport, M., Kaplan, R. and Brown, S. 2001. Depression, visual acuity, comorbidity, and disability associated with age-related macular degeneration. Ophthalmology 108(10), pp. 1893–900.

Brown, J.S., Flitcroft, D.I., Ying, G., Francis, E.L., Schmid, G.F., Quinn, G.E. and Stone, R.A. 2009. In vivo human choroidal thickness measurements: evidence for diurnal fluctuations. Investigative Ophthalmology & Visual Science 50(1), pp. 5–12.

De Bruijne, M. 2016. Machine learning approaches in medical image analysis: From detection to diagnosis. Medical Image Analysis 33, pp. 94–7.

Bunce, C., Xing, W. and Wormald, R. 2010. Causes of blind and partial sight certifications in England and Wales: April 2007-March 2008. Eye (London, England) 24(11), pp. 1692–9.

Campbell, F.W. and Robson, J.G. 1968. Application of Fourier analysis to the visibility of gratings. The Journal of Physiology 197(3), pp. 551–66.

Campbell, M. and Humphries, P. 2012. The blood-retina barrier: tight junctions and barrier modulation. Advances in Experimental Medicine and Biology 763, pp. 70–84.

De Carlo, T.E., Romano, A., Waheed, N.K. and Duker, J.S. 2015. A review of optical coherence tomography angiography (OCTA). International Journal of Retina and Vitreous 1, pp. 1–15.

Casten, R.J. and Rovner, B.W. 2013. Update on depression and age-related macular degeneration. Current Opinion in Ophthalmology 24(3), pp. 239–43.

Chakraborty, R., Read, S.A. and Collins, M.J. 2011. Diurnal variations in axial length, choroidal thickness, intraocular pressure, and ocular biometrics. Investigative Ophthalmology & Visual Science 52(8), pp. 5121–9.

Chakraborty, R., Read, S.A. and Collins, M.J. 2012. Monocular myopic defocus and daily changes in axial length and choroidal thickness of human eyes. Experimental Eye Research 103, pp. 47–54.

Chakraborty, R., Read, S.A. and Collins, M.J. 2013. Hyperopic defocus and diurnal changes. Optometry and Vision Science 90(11), pp. 1187–98.

Chakravarthy, U., Wong, T.Y., Fletcher, A., Piault, E., Evans, C., Zlateva, G., Buggage, R., Pleil, A. and Mitchell, P. 2010. Clinical risk factors for age-related macular degeneration: a systematic review and meta-analysis. BMC Ophthalmology 10(1), p. 31.

Chamie, J. 2005. World population prospects: The 2004 revision. New York: United Nations Department of Economic and Social Affairs.

Chew, E.Y., Clemons, T.E., Agrón, E., Sperduto, R.D., Sangiovanni, J.P., Davis, M.D. and Ferris 3rd, F.L. 2014. Ten-year follow-up of age-related macular degeneration in the Age-Related Eye Disease Study: AREDS Report No. 36. JAMA Ophthalmology 132(3), pp. 272–7.

Chirco, K.R., Sohn, E.H., Stone, E.M., Tucker, B.A. and Mullins, R.F. 2016. Structural and molecular changes in the aging choroid: implications for age-related macular degeneration. Eye (August), pp. 1–16.

Chiu, S.J., Li, X.T., Nicholas, P., Toth, C.A., Izatt, J.A. and Farsiu, S. 2010. Automatic segmentation of seven retinal layers in SDOCT images congruent with expert manual segmentation. Optics Express 18(18), pp. 19413–28.

Chiu, S.J., Izatt, J.A., O'Connell, R. V., Winter, K.P., Toth, C.A. and Farsiu, S. 2012. Validated automatic segmentation of AMD pathology including drusen and geographic atrophy in SD-OCT images. Investigative Ophthalmology & Visual Science 53(1), pp. 53–61.

Cho, G.E., Cho, H.Y. and Kim, Y.T. 2013a. Change in subfoveal choroidal thickness after argon laser panretinal photocoagulation. International Journal of Ophthalmology 6(4), pp. 505–9.

Cho, H., Shah, C.P., Weber, M. and Heier, J.S. 2013b. Aflibercept for exudative AMD with persistent fluid on ranibizumab and/or bevacizumab. The British Journal of Ophthalmology 97(8), pp. 1032–5.

Choma, M., Sarunic, M., Yang, C. and Izatt, J. 2003. Sensitivity advantage of swept source and Fourier domain optical coherence tomography. Optics Express 11(18), pp. 2183–9.

Chong, N.H.V., Keonin, J., Luthert, P.J., Frennesson, C.I., Weingeist, D.M., Wolf, R.L., Mullins, R.F. and Hageman, G.S. 2005. Decreased thickness and integrity of the macular elastic layer of Bruch's membrane correspond to the distribution of lesions associated with age-related macular degeneration. The American Journal of Pathology 166(1), pp. 241–51.

Chong, E.W., Wong, T.Y., Kreis, A.J., Simpson, J.A. and Guymer, R.H. 2007. Dietary antioxidants and primary prevention of age related macular degeneration: systematic review and meta-analysis. British Medical Journal 335(7623), pp. 755–9.

Chong, E.W., Robman, L.D., Simpson, J.A., Hodge, A.M., Aung, K.Z., Dolphin, T.K., English, D.R., Giles, G.G. and Guymer, R.H. 2009. Fat consumption and its association with age-related macular degeneration. Archives of Ophthalmology 127(5), pp. 674–80.

Chung, S.E., Kang, S.W., Lee, J.H. and Kim, Y.T. 2011. Choroidal thickness in polypoidal choroidal vasculopathy and exudative age-related macular degeneration. Ophthalmology 118(5), pp. 840–5.

Chylack, L., Wolfe, J., Singer, D., Leske, C., Bullimore, M., Bailey, I., Friend, J., McCarthy, D. and Wu, S. 1993. The lens opacities classification system III. Archives of Ophthalmology 111, pp. 831–6.

Cortes, C. and Vapnik, V. 1995. Support-Vector Networks. Machine Learning 20(3), pp. 273–97.

Coscas, G., Zhou, Q., Coscas, F., Zucchiatti, I., Rispoli, M., Uzzan, J., De Benedetto, U., Savastano, M.C., Soules, K., Goldenberg, D., Loewenstein, A. and Lumbroso, B. 2012. Choroid thickness measurement with RTVue optical coherence tomography in emmetropic eyes, mildly myopic eyes, and highly myopic eyes. European Journal of Ophthalmology 22(6), pp. 992–1000.

Cukras, C., Wang, Y.D. and Meyerle, C.B. 2009. Optical coherence tomography-based decision making in exudative age-related macular degeneration: comparison of time-vs spectral-domain devices. Eye (London, England) 24(5), pp. 775–83.

Cunha-Vaz, J., Bernardes, R. and Lobo, C. 2011. Blood-retinal barrier. European Journal of Ophthalmology 21 Suppl 6, pp. S3–9.

Curcio, C.A. 2001. Photoreceptor topography in ageing and age-related maculopathy. Eye (London, England) 15, pp. 376–83.

Curcio, C.A., Messinger, J.D., Sloan, K.R., Mitra, A., McGwin, G. and Spaide, R.F. 2011. Human chorioretinal layer thicknesses measured in macula-wide, high-resolution histologic sections. Investigative Ophthalmology & Visual Science 52(7), pp. 3943–54.

Dalal, N. and Triggs, B. 2005. Histograms of oriented gradients for human detection. In: IEEE Computer Society Conference on Computer Vision and Pattern Recognition (CVPR). pp. 886–93.

Dallinger, S., Bobr, B., Findl, O., Eichler, H.G. and Schmetterer, L. 1998. Effects of acetazolamide on choroidal blood flow. Stroke 29(5), pp. 997–1001.

Danis, R.P., Domalpally, A., Chew, E.Y., Clemons, T.E., Armstrong, J., SanGiovanni, J.P. and Ferris, F.L. 2013. Methods and reproducibility of grading optimized digital color fundus photographs in the Age-Related Eye Disease Study 2 (AREDS2 Report Number 2). Investigative Ophthalmology & Visual Science 54(7), pp. 4548–54.

Davis, M.D., Gangnon, R.E., Lee, L.-Y., Hubbard, L.D., Klein, B.E.K., Klein, R., Ferris, F.L., Bressler, S.B. and Milton, R.C. 2005. The Age-Related Eye Disease Study severity scale for age-related macular degeneration: AREDS Report No. 17. Archives of ophthalmology (Chicago, Ill. : 1960) 123(11), pp. 1484–98.

Dawson, S.R., Mallen, C.D., Gouldstone, M.B., Yarham, R. and Mansell, G. 2014. The prevalence of anxiety and depression in people with age-related macular degeneration: a systematic review of observational study data. BMC Ophthalmology 14(78).

Deng, J., Xie, X., Terry, L., Wood, A., White, N., Margrain, T.H. and North, R. V 2016. Age-related macular degeneration detection and stage classification using choroidal OCT images. In: International Conference on Image Analysis and Recognition (ICIAR). pp. 1–9.

Dervişoğulları, M.S., Totan, Y., Yüce, A. and Kulak, A.E. 2016. Acute effects of caffeine on choroidal thickness and ocular pulse amplitude. Cutaneous and Ocular Toxicology 35(4), pp. 281–6.

Ding, X., Li, J., Zeng, J., Ma, W., Liu, R., Li, T., Yu, S. and Tang, S. 2011. Choroidal thickness in healthy Chinese subjects. Investigative Ophthalmology & Visual Science 52(13), pp. 9555–60.

Donoso, L. a, Vrabec, T. and Kuivaniemi, H. 2010. The role of complement Factor H in age-related macular degeneration: a review. Survey of Ophthalmology 55(3), pp. 227–46.

Drexler, W. 2004. Ultrahigh-resolution optical coherence tomography. Journal of Biomedical Optics 9(1), pp. 47–74.

Drexler, W. and Fujimoto, J.G. 2008. State-of-the-art retinal optical coherence tomography. Progress in Retinal and Eye Research 27(1), pp. 45–88.

Duan, L., Hong, Y.-J. and Yasuno, Y. 2013. Automated segmentation and characterization of choroidal vessels in high-penetration optical coherence tomography. Optics Express 21(13), pp. 529–33.

Dubuc, B. 2014. Photoreceptors [Online]. Available at: http://thebrain.mcgill.ca.

Early Treatment Diabetic Retinopathy Study Research Group 1991. Grading diabetic retinopathy from stereoscopic color fundus photographs— An extension of the Modified Airlie House Classification. Ophthalmology 98(5), pp. 786–806.

Ellabban, A.A., Tsujikawa, A., Matsumoto, A., Ogino, K., Hangai, M., Ooto, S., Yamashiro, K., Akiba, M. and Yoshimura, N. 2012. Macular choroidal thickness and volume in eyes with angioid streaks measured by swept source optical coherence tomography. American Journal of Ophthalmology 153(6), pp. 1133–43.

Esmaeelpour, M., Považay, B., Hermann, B., Hofer, B., Kajic, V., Hale, S.L., North, R. V, Drexler, W. and Sheen, N.J.L. 2011. Mapping choroidal and retinal thickness variation in type 2 diabetes using three-dimensional 1060-nm optical coherence tomography. Investigative Ophthalmology & Visual Science 52(8), pp. 5311–6.

Esmaeelpour, M., Brunner, S., Shahrezaei, S., Nemetz, S., Povazay, B., Kajic, V., Drexler, W. and Binder, S. 2012. Choroidal thinning in diabetes type 1 detected by 3-dimensional 1060 nm optical coherence tomography. Investigative Ophthalmology & Visual Science 53(11), pp. 6803–9.

Esmaeelpour, M., Ansari-Shahrezaei, S., Glittenberg, C., Nemetz, S., Kraus, M.F., Hornegger, J., Fujimoto, J.G., Drexler, W. and Binder, S. 2014a. Choroid, Haller's, and Sattler's layer thickness in intermediate age-related macular degeneration with and without fellow neovascular eyes. Investigative Ophthalmology & Visual Science 55(8), pp. 5074–80.

Esmaeelpour, M., Kajic, V., Zabihian, B., Othara, R., Ansari-Shahrezaei, S., Kellner, L., Krebs, I., Nemetz, S., Kraus, M.F., Hornegger, J., Fujimoto, J.G., Drexler, W. and Binder, S. 2014b. Choroidal Haller's and Sattler's layer thickness measurement using 3-dimensional 1060-nm optical coherence tomography. PLoS ONE 9(6), p. e99690.

Evans, J.R. 2001. Risk factors for age-related macular degeneration. Progress in Retinal and Eye Research 20(2), pp. 227–53.

Evans, J. and Lawrenson, J. 2012. Antioxidant vitamin and mineral supplements for preventing age-related macular degeneration. Cochrane Database of Systematic Reviews 6, pp. 1–49.

Falavarjani, K.G. and Nguyen, Q.D. 2013. Adverse events and complications associated with intravitreal injection of anti-VEGF agents: a review of literature. Eye (London, England) 27(7), pp. 787–94.

Feigl, B. 2007. Age-related maculopathy in the light of ischaemia. Clinical & Experimental Optometry: Journal of the Australian Optometrical Association 90(4), pp. 263–71.

Feigl, B., Brown, B., Lovie-Kitchin, J. and Swann, P. 2007. Functional loss in early age-related maculopathy: the ischaemia postreceptoral hypothesis. Eye (London, England) 21(6), pp. 689–96.

Fercher, A.F., Mengedoht, K. and Werner, W. 1988. Eye-length measurement by interferometry with partially coherent light. Optics Letters 13(3), pp. 186–8.

Fercher, A.F., Hitzenberger, C., Drexler, W., Kamp, G. and Sattmann, H. 1993. In-vivo optical coherence tomography. American Journal of Ophthalmology 116(1), pp. 113–5.

Ferrara, D., Waheed, N.K. and Duker, J.S. 2016. Investigating the choriocapillaris and choroidal vasculature with new optical coherence tomography technologies. Progress in Retinal and Eye Research 52, pp. 130–55.

Ferrington, D.A., Sinha, D. and Kaarniranta, K. 2016. Defects in retinal pigment epithelial cell proteolysis and the pathology associated with age-related macular degeneration. Progress in Retinal and Eye Research 51, pp. 69–89.

Ferris, F.L., Kassoff, A., Bresnick, G.H. and Bailey, I. 1982. New visual acuity charts for clinical research. American Journal of Ophthalmology 94(1), pp. 91–6.

Ferris, F., Davis, M., Clemons, T., Lee, L., Chew, E., Lindblad, A., Milton, R., Bressler, S., Klein, R. and Group, A.R. 2005. A simplified severity scale for age-related macular degeneration: AREDS Report No. 18. Archives of Ophthalmology 123(11), pp. 1570–4.

Ferris, F.L., Wilkinson, C.P., Bird, A., Chakravarthy, U., Chew, E., Csaky, K. and Sadda, S.R. 2013. Clinical classification of age-related macular degeneration. Ophthalmology 120(4), pp. 844–51.

Fitt, E., Pell, D. and Cole, D. 2013. Assessing caffeine intake in the United Kingdom diet. Food Chemistry 140(3), pp. 421–26.

Forooghian, F., Cukras, C. and Meyerle, C.B. 2008. Evaluation of time domain and spectral domain optical coherence tomography in the measurement of diabetic macular edema. Investigative Ophthalmology & Visual Science 49(10), pp. 4290–6.

Foster, P.J., Broadway, D.C., Hayat, S., Luben, R., Dalzell, N., Bingham, S., Wareham, N.J. and Khaw, K. 2010. Refractive error, axial length and anterior chamber depth of the eye in British adults: the EPIC-Norfolk Eye Study. The British Journal of Ophthalmology 94(7), pp. 827–30.

Frank, R.N., Amin, R.H., Eliott, D., Puklin, J.E. and Abrams, G.W. 1996. Basic fibroblast growth factor and vascular endothelial growth factor are present in epiretinal and choroidal neovascular membranes. American Journal of Ophthalmology 122(3), pp. 393–403.

Fujimoto, J.G., De Silvestri, S., Ippen, E.P., Puliafito, C.A., Margolis, R. and Oseroff, A. 1986. Femtosecond optical ranging in biological systems. Optics Letters 11(3), pp. 150–2.

Fujiwara, T., Imamura, Y., Margolis, R., Slakter, J.S. and Spaide, R.F. 2009. Enhanced depth imaging optical coherence tomography of the choroid in highly myopic eyes. American Journal of Ophthalmology 148(3), pp. 445–50.

Garg, A., Oll, M., Yzer, S., Chang, S., Barile, G.R., Merriam, J.C., Tsang, S.H. and Bearelly, S. 2013. Reticular pseudodrusen in early age-related macular degeneration are associated with choroidal thinning. Investigative Ophthalmology & Visual Science 54(10), pp. 7075–81.

Garvin, M.K., Abràmoff, M.D., Wu, X., Russell, S.R., Burns, T.L. and Sonka, M. 2009. Automated 3-D intraretinal layer segmentation of macular spectral-domain optical coherence tomography images. IEEE Transactions on Medical Imaging 28(9), pp. 1436–47.

Giani, A., Cigada, M., Choudhry, N., Deiro, A.P., Oldani, M., Pellegrini, M., Invernizzi, A., Duca, P., Miller, J.W. and Staurenghi, G. 2010. Reproducibility of retinal thickness measurements on normal and pathologic eyes by different optical coherence tomography instruments. American Journal of Ophthalmology 150(6), pp. 815–24.

Gloesmann, M., Hermann, B., Schubert, C., Sattmann, H., Ahnelt, P.K. and Drexler, W. 2003. Histologic correlation of pig retina radial stratification with ultrahigh-

resolution optical coherence tomography. Investigative Ophthalmology & Visual Science 44(4), pp. 1696–703.

Gonzalez-Lopez, A., Remeseiro, B., Ortega, M., Panedo, M.G. and Charlon, P. 2015. A texture-based method for choroidal segmentation in retinal EDI-OCT images. In: Computer Aided Systems Theory — EUROCAST 2015: 15th International Conference. pp. 487–93.

Grunwald, J.E., Hariprasad, S.M., DuPont, J., Maguire, M.G., Fine, S.L., Brucker, A.J., Maguire, A.M. and Ho, A.C. 1998. Foveolar choroidal blood flow in age-related macular degeneration. Investigative Ophthalmology & Visual Science 39(2), pp. 385–90.

Gupta, V., Gupta, P., Singh, R., Dogra, M.R. and Gupta, A. 2008. Spectral-domain Cirrus high-definition optical coherence tomography is better than time-domain Stratus optical coherence tomography for evaluation of macular pathologic features in uveitis. American Journal of Ophthalmology 145(6), pp. 1018–22.

Gupta, P., Thakku, S.G., Sabanayagam, C., Tan, G., Cheung, C.M.G., Lamoureux, E.L., Wong, T.-Y. and Cheng, C.-Y. 2017. Characterisation of choroidal morphological and vascular features in diabetes and diabetic retinopathy. British Journal of Ophthalmology, p. 309366.

Guymer, R., Luthert, P. and Bird, A. 1998. Changes in Bruch's membrane and related structures with age. Progress in Retinal and Eye Research 9462(98), pp. 59–90.

Haas, P., Esmaeelpour, M., Ansari-Shahrezaei, S., Drexler, W. and Binder, S. 2014. Choroidal thickness in patients with reticular pseudodrusen using 3D 1060-nm OCT maps. Investigative Ophthalmology & Visual Science 55(4), pp. 2674–81.

Hageman, G., Luthert, P., Chong, V., Johnson, L., Anderson, D. and Mullins, R. 2001. An integrated hypothesis that considers drusen as biomarkers of immune-mediated processes at the RPE-Bruch's membrane interface in aging and age-related. Progress in Retinal and Eye Research 20(6), pp. 705–32.

Hammer, M., Roggan, A., Schweitzer, D., Müller, G. and Muller, G. 1995. Optical properties of ocular fundus tissues--an in vitro study using the double-integrating-sphere technique and inverse Monte Carlo simulation. Physics in Medicine and Biology 40(6), pp. 963–78.

Han, Y.S., Lim, H. Bin, Lee, S.H. and Kim, J.Y. 2015. Diurnal variation in choroidal and retinal thickness of the early treatment of diabetic retinopathy study macular subfields determined using swept-source optical coherence tomography. Ophthalmologica 233, pp. 192–7.

Hanumunthadu, D., Ilginis, T., Restori, M., Sagoo, M., Tufail, A., Balaggan, K.S. and Patel, P.J. 2017. Repeatability of swept-source optical coherence tomography

retinal and choroidal thickness measurements in neovascular age-related macular degeneration. British Journal of Ophthalmology 101, pp. 603–8.

Harper, C.L., Boulton, M.E., Bennett, D., Marcyniuk, B., Jarvis-Evans, J.H., Tullo, A.B. and Ridgway, A.E. 1996. Diurnal variations in human corneal thickness. British Journal of Ophthalmology 80(12), pp. 1068–72.

Hayashi, Y., Nakagawa, T., Hatanaka, Y., Aoyama, A., Kakogawa, M., Hara, T., Fujita, H. and Yamamoto, T. 2007. Detection of retinal nerve fiber layer defects in retinal fundus images using Gabor filtering. Proceedings of SPIE 6514, p. 65142Z.

Heier, J.S., Brown, D.M., Chong, V., Korobelnik, J.F., Kaiser, P.K., Nguyen, Q.D., Kirchhof, B., Ho, A., Ogura, Y., Yancopoulos, G.D., Stahl, N., Vitti, R., Berliner, A.J., Soo, Y., Anderesi, M., Groetzbach, G., Sommerauer, B., Sandbrink, R., Simader, C. and Schmidt-Erfurth, U. 2012. Intravitreal aflibercept (VEGF trap-eye) in wet age-related macular degeneration. Ophthalmology 119(12), pp. 2537–48.

Hendrickson, A. 2005. Organization of the Adult Primate Fovea. In: Penfold, P. L. and Provis, J. M. eds. Macular Degeneration. Heidelburg: Springer, pp. 1–20.

Van Herick, W., Shaffer, R.N. and Schwartz, A. 1969. Estimation of width of angle of anterior chamber. American Journal of Ophthalmology 68(4), pp. 626–9.

Hirata, M., Tsujikawa, A., Matsumoto, A., Hangai, M., Ooto, S., Yamashiro, K., Akiba, M. and Yoshimura, N. 2011. Macular choroidal thickness and volume in normal subjects measured by swept-source optical coherence tomography. Investigative Ophthalmology & Visual Science 52(8), pp. 4971–8.

Hitzenberger, C.K. 2003. Principles of optical coherence tomography. In: Fankhauser, F. and Kwasniewska, S. eds. Lasers in Ophthalmology: Basic, Diagnostic, and Surgical Aspects. The Hague, The Netherlands: Kugler Publications, pp. 61–72.

Hofman, A., Breteler, M.M.B., Van Duijn, C.M., Krestin, G.P., Pols, H. a., Stricker, B.H.C., Tiemeier, H., Uitterlinden, A.G., Vingerling, J.R. and Witteman, J.C.M. 2007. The Rotterdam Study: Objectives and design update. European Journal of Epidemiology 22(11), pp. 819–29.

Hogan, M.J., Alvarado, J.A. and Weddell, J.E. 1971. Histology of the human eye: an atlas and textbook. Philadelphia: Saunders.

Hogg, R.E. 2014. Reticular pseudodrusen in age-related macular degeneration. Optom Vis Sci 91(8), pp. 854–9.

Holz, F.G., Bellman, C., Staudt, S., Schütt, F. and Völcker, H.E. 2001. Fundus autofluorescence and development of geographic atrophy in age-related macular degeneration. Investigative Ophthalmology & Visual Science 42(5), pp. 1051–6.

Huang, D., Swanson, E.A., Lin, C.P., Schuman, J.S., Stinson, W.G., Chang, W., Hee, M.R., Flotire, T., Gregory, K., Puliafito, C.A. and Fujimoto, J.G. 1991. Optical Coherence Tomography. Science 254, pp. 1178–81.

ICNIRP 2013. ICNIRP guidelines on limits of exposure to incoherent visible and infrared radiation. Health Physics 71(5), pp. 271–95.

Ikram, M.K., Van Leeuwen, R., Vingerling, J.R., Hofman, A. and De Jong, P.T.V.M. 2003. Relationship between refraction and prevalent as well as incident age-related maculopathy: The Rotterdam study. Investigative Ophthalmology & Visual Science 44(9), pp. 3778–82.

Ikuno, Y., Kawaguchi, K., Nouchi, T. and Yasuno, Y. 2010. Choroidal thickness in healthy Japanese subjects. Investigative Ophthalmology & Visual Science 51(4), pp. 2173–6.

Imamura, Y., Fujiwara, T., Margolis, R. and Spaide, R.F. 2009. Enhanced depth imaging optical coherence tomography of the choroid in central serous chorioretinopathy. Retina (Philadelphia, Pa.) 29(10), pp. 1469–73.

Irving, E.L., Sivak, J.G. and Callender, M.G. 1992. Refractive plasticity of the developing chick eye. Ophthalmic & Physiological Optics 12(4), pp. 448–56.

Ishwaran, H. 2007. Variable importance in binary regression trees and forests. Electronic Journal of Statistics 1, pp. 519–37.

Jain, A.K. and Farrokhnia, F. 1990. Unsupervised texture segmentation using Gabor filters. In: Systems, Man and Cybernetics Conference Proceedings., IEEE International Conference on. pp. 14–9.

Jarrett, S.G. and Boulton, M.E. 2012. Consequences of oxidative stress in age-related macular degeneration. Molecular Aspects of Medicine 33(4), pp. 399–417.

Jia, Y., Bailey, S.T., Wilson, D.J., Tan, O., Klein, M.L., Flaxel, C.J., Potsaid, B., Liu, J.J., Lu, C.D., Kraus, M.F., Fujimoto, J.G. and Huang, D. 2014. Quantitative optical coherence tomography angiography of choroidal neovascularization in age-related macular degeneration. Ophthalmology 121(7), pp. 1435–44.

Jin, X. and Kim, J. 2017. A 3D skeletonization algorithm for 3D mesh models using a partial parallel 3D thinning algorithm and 3D skeleton correcting algorithm. Applied Sciences 7(2), p. 139.

Jirarattanasopa, P., Ooto, S., Tsujikawa, A., Yamashiro, K., Hangai, M., Hirata, M., Matsumoto, A. and Yoshimura, N. 2012. Assessment of macular choroidal thickness by optical coherence tomography and angiographic changes in central serous chorioretinopathy. Ophthalmology 119(8), pp. 1666–78.

Jo, Y.-J., Heo, D.-W., Shin, Y.-I. and Kim, J.-Y. 2011. Diurnal variation of retina thickness measured with time domain and spectral domain optical coherence

tomography in healthy subjects. Investigative Ophthalmology & Visual Science 52(9), pp. 6497–500.

Johnson, L., Ozaki, S., Staples, M.K., Erickson, P.A. and Anderson, D.H. 2000. A potential role for immune complex pathogenesis in drusen formation. Experimental Eye Research 70, pp. 441–9.

Johnson, L. V, Leitner, W.P., Staples, M.K. and Anderson, D.H. 2001. Complement activation and inflammatory processes in Drusen formation and age related macular degeneration. Experimental Eye Research 73(6), pp. 887–96.

Jonas, J.B., Forster, T.M., Steinmetz, P., Schlichtenbrede, F.C. and Harder, B.C. 2014. Choroidal thickness in age-related macular degeneration. Retina (Philadelphia, Pa.) 34(6), pp. 1149–55.

Kajić, V., Esmaeelpour, M., Glittenberg, C., Kraus, M.F., Honegger, J., Othara, R., Binder, S., Fujimoto, J.G. and Drexler, W. 2013. Automated three-dimensional choroidal vessel segmentation of 3D 1060 nm OCT retinal data. Biomedical Optics Express 4(1), pp. 134–50.

Kang, H.M., Woo, Y.J., Koh, H.J., Lee, C.S. and Lee, S.C. 2016. The effect of consumption of ethanol on subfoveal choroidal thickness in acute phase. British Journal of Ophthalmology 100, pp. 383–8.

Kankanahalli, S., Burlina, P.M., Wolfson, Y., Freund, D.E. and Bressler, N.M. 2013. Automated classification of severity of age-related macular degeneration from fundus photographs. Investigative Ophthalmology & Visual Science 54(3), pp. 1789–96.

Kantarci, F. a., Tatar, M.G., Colak, H.N., Uslu, H., Yildirim, A., Goker, H., Gurler, B. and Karaca, E.E. 2016. A pilot study of choroidal thickness in long-term smokers. Retina 36(5), pp. 986–91.

Kara, N., Sayin, N., Pirhan, D., Vural, A.D., Araz-Ersan, H.B., Tekirdag, A.I., Yildirim, G.Y., Gulac, B. and Yilmaz, G. 2014. Evaluation of subfoveal choroidal thickness in pregnant women using enhanced depth imaging optical coherence tomography. Current Eye Research 39(6), pp. 642–7.

Karwatowski, W.S.S., Jeffries, T.E., Duance, V.C., Albon, J., Bailey, A.J. and Easty, D.L. 1995. Preparation of Bruch's membrane and analysis of the age-related changes in the structural collagens. British Journal of Ophthalmology 79(10), pp. 944–52.

Katz, J., Tielsch, J.M. and Sommer, A. 1997. Prevalence and risk factors for refractive errors in an adult inner city population. Investigative Ophthalmology & Visual Science 38(2), pp. 334–40.

Kennedy, C.J., Rakoczy, P.E. and Constable, I.J. 1995. Lipofuscin of the retinal pigment epithelium: a review. Eye (London, England) 9(6), pp. 763–71.

Kim, R., Faktorovich, E., Kuo, C. and Olson, J. 1997. Retinal function abnormalities in membranoproliferative glomerulonephritis type II. American Journal of Ophthalmology 123(5), pp. 619–28.

Kim, K.I., Jung, K., Park, S.H. and Kim, H.J. 2002. Support vector machines for texture classification. IEEE Transactions on Pattern Analysis and Machine Intelligence 24(11), pp. 1542–50.

Kim, S., Oh, J., Kwon, S., Yoo, J. and Huh, K. 2011. Comparison of choroidal thickness among patients with healthy eyes, early age-related maculopathy, neovascular age-related macular degeneration, central serous chorioretinopathy, and polypoidal choroidal vasculopathy. Retina (Philadelphia, Pa.) 31, pp. 1904–11.

Kim, J.T., Lee, D.H., Joe, S.G., Kim, J.G. and Yoon, Y.H. 2013. Changes in choroidal thickness in relation to the severity of retinopathy and macular edema in type 2 diabetic patients. Investigative Ophthalmology & Visual Science 54(5), pp. 3378–84.

Kinoshita, T., Mitamura, Y., Shinomiya, K., Egawa, M., Iwata, A., Fujihara, A., Ogushi, Y., Semba, K., Akaiwa, K., Uchino, E., Sonoda, S. and Sakamoto, T. 2016. Diurnal variations in luminal and stromal areas of choroid in normal eyes. British Journal of Ophthalmology, p. 308594.

Klaassen, I., Van Noorden, C.J.F. and Schlingemann, R.O. 2013. Molecular basis of the inner blood-retinal barrier and its breakdown in diabetic macular edema and other pathological conditions. Progress in Retinal and Eye Research 34, pp. 19–48.

Klaver, C.C.W., van Leeuwen, R., Vingerling, J.R. and de Jong, P.T.V.M. 2004. Epidemiology of Age-Related Maculopathy: A review. In: Holz, F. G., Pauleikhoff, D., Spaide, R. F., and Bird, A. C. eds. Age-related Macular Degeneration. Heidelburg: Springer, pp. 1–17.

Klaver, C.C.W., Buitendijk, G.H., Verhoeven, V.J., Springelkamp, H., Jansonius, N.M. and Vingerling, J.R. 2012. Retinal and Choroidal Thickness measured by Swept-source Optical Coherence Tomography in the Population-based Rotterdam Study. In: ARVO Annual Meeting. p. 2123.

Klein, R., Davis, M.D., Magli, Y.L., Segal, P., Klein, B.E.K. and Hubbard, L. 1991. The Wisconsin Age-related Maculopathy Grading System. Ophthalmology 98(7), pp. 1128–34.

Klein, R., Klein, B. and Moss, S.E. 1998. Relation of smoking to the incidence of age-related maculopathy - The Beaver Dam Eye Study. American Journal of Epidemiology 147(2), pp. 103–10.

Klein, R., Peto, T., Bird, A. and Vannewkirk, M.R. 2004. The epidemiology of age-related macular degeneration. American Journal of Ophthalmology 137(3), pp. 486–95.

Klein, R., Klein, B.E.K., Knudtson, M.D., Meuer, S.M., Swift, M. and Gangnon, R.E. 2007. Fifteen-year cumulative incidence of age-related macular degeneration. The Beaver Dam Eye Study. Ophthalmology 114(2), pp. 253–62.

Ko, A., Cao, S., Pakzad-Vaezi, K., Brasher, P.M., Merkur, A.B., Albiani, D.A., Kirker, A.W., Cui, J., Matsubara, J. and Forooghian, F. 2013. Optical coherence tomography-based correlation between choroidal thickness and drusen load in dry age-related macular degeneration. Retina (Philadelphia, Pa.) 33(5), pp. 1005–10.

Koh, A.H.C., Chen, L.-J., Chen, S.-J., Chen, Y., Giridhar, A., Iida, T., Kim, H., Yuk Yau Lai, T., Lee, W.K., Li, X., Han Lim, T., Ruamviboonsuk, P., Sharma, T., Tang, S. and Yuzawa, M. 2013. Polypoidal choroidal vasculopathy: evidence-based guidelines for clinical diagnosis and treatment. Retina (Philadelphia, Pa.) 33(4), pp. 686–716.

Koh, L.H.L., Agrawal, R., Khandelwal, N., Sai Charan, L. and Chhablani, J. 2017. Choroidal vascular changes in age-related macular degeneration. Acta Ophthalmologica, pp. 1–5.

Kohjiya, S., Katoh, A., Suda, T., Shimanuki, J. and Ikeda, Y. 2006. Visualisation of carbon black networks in rubbery matrix by skeletonisation of 3D-TEM image. Polymer 47(10), pp. 3298–301.

Koizumi, H., Yamagishi, T., Yamazaki, T., Kawasaki, R. and Kinoshita, S. 2011. Subfoveal choroidal thickness in typical age-related macular degeneration and polypoidal choroidal vasculopathy. Graefe's Archive for Clinical and Experimental Ophthalmology 249(8), pp. 1123–8.

Koizumi, H., Kano, M., Yamamoto, A., Saito, M., Maruko, I., Kawasaki, R., Sekiryu, T., Okada, A. a. and Iida, T. 2015. Short-term changes in choroidal thickness after aflibercept therapy for neovascular age-related macular degeneration. American Journal of Ophthalmology 159(4), pp. 627–33.

Kolb, B. 2014. Simple anatomy of the retina [Online]. Available at: www.webvision.med.utah.edu.

Koprowski, R., Teper, S., Wróbel, Z. and Wylegala, E. 2013. Automatic analysis of selected choroidal diseases in OCT images of the eye fundus. Biomedical Engineering Online 12(117), pp. 1–17.

Kotsidis, S.T., Lake, S.S., Alexandridis, A.D., Ziakas, N.G. and Ekonomidis, P.K. 2012. 24-hour variation of optical coherence tomography-measured retinal thickness in diabetic macular edema. European Journal of Ophthalmology 22(5), pp. 785–91.

Koustenis, A., Harris, A., Gross, J., Januleviciene, I., Shah, A. and Siesky, B. 2016. Optical coherence tomography angiography: an overview of the technology and an assessment of applications for clinical research. British Journal of Ophthalmology, p. 309389.

Krizhevsky, A., Sutskever, I. and Hinton, G.E. 2012. ImageNet classification with deep convolutional neural networks. In: Advances In Neural Information Processing Systems. pp. 1106–14.

Kuroda, S., Ikuno, Y., Yasuno, Y., Nakai, K., Usui, S., Sawa, M., Tsujikawa, M., Gomi, F. and Nishida, K. 2013. Choroidal thickness in central serous chorioretinopathy. Retina 33(2), pp. 302–8.

Kuroda, Y., Ooto, S., Yamashiro, K., Oishi, A., Nakanishi, H., Tamura, H., Ueda-Arakawa, N. and Yoshimura, N. 2016. Increased choroidal vascularity in central serous chorioretinopathy quantified using swept-source optical coherence tomography. American Journal of Ophthalmology 169, pp. 199–207.

Lamb, T.D. and Pugh, E.N. 2004. Dark adaptation and the retinoid cycle of vision. Progress in Retinal and Eye Research 23(3), pp. 307–80.

Landis, J.R. and Koch, G.G. 1977. The measurement of observer agreement for categorical data. Biometrics 33(1), pp. 159–74.

Larsen, M., Wang, M. and Sander, B. 2005. Overnight thickness variation in diabetic macular edema. Investigative Ophthalmology & Visual Science 46(7), pp. 2313–6.

Lawrence, S., Giles, C.L., Ah Chung Tsoi and Back, A.D. 1997. Face recognition: a convolutional neural-network approach. IEEE Transactions on Neural Networks 8(1), pp. 98–113.

LeCun, Y., Bengio, Y. and Hinton, G. 2015. Deep learning. Nature 521(7553), pp. 436–44.

Lee, K., Garvin, M., Russell, S., Sonka, M. and Abràmoff, M. 2010. Automated intraretinal layer segmentation of 3-D macular OCT scans using a multiscale graph search. In: ARVO Annual Meeting. p. 1767.

Lee, J.Y., Chiu, S.J., Srinivasan, P.P., Izatt, J.A., Toth, C.A., Farsiu, S. and Jaffe, G.J. 2013a. Fully automatic software for retinal thickness in eyes with diabetic macular edema from images acquired by cirrus and spectralis systems. Investigative Ophthalmology & Visual Science 54(12), pp. 7595–602.

Lee, J.Y., Lee, D.H., Lee, J.Y. and Yoon, Y.H. 2013b. Correlation between subfoveal choroidal thickness and the severity or progression of nonexudative age-related macular degeneration. Investigative Ophthalmology & Visual Science 54(12), pp. 7812–8.

Lee, S.W., Yu, S.-Y., Seo, K.H., Kim, E.S. and Kwak, H.W. 2013c. Diurnal variation in choroidal thickness in relation to sex, axial length, and baseline choroidal thickness in healthy Korean subjects. Retina (Philadelphia, Pa.) 34(2), pp. 1–9.

Lee, S., Lebed, E., Sarunic, M. V and Beg, M.F. 2015. Exact surface registration of retinal surfaces from 3-D optical coherence tomography images. IEEE Transactions on Biomedical Engineering 62(2), pp. 609–17.

Lee, C.S., Baughman, D.M. and Lee, A.Y. 2017. Deep learning is effective for classifying normal versus age-related macular degeneration optical coherence tomography images. Ophthalmology Retina 1(4), pp. 322–7.

Leitgeb, R., Hitzenberger, C. and Fercher, A. 2003. Performance of fourier domain vs. time domain optical coherence tomography. Optics Express 11(8), pp. 889–94.

Li, K., Wu, X., Chen, D.Z. and Sonka, M. 2006. Optimal surface segmentation in volumetric images -a graph-theoretic approach. IEEE Transactions on Pattern Analysis and Machine Intelligence 28(1), pp. 119–34.

Li, X.Q., Larsen, M. and Munch, I.C. 2011. Subfoveal choroidal thickness in relation to sex and axial length in 93 Danish university students. Investigative Ophthalmology & Visual Science 52(11), pp. 8438–41.

Li XQ, Heegaard S, Kiilgaard JF, et al. (2016) Enhanced-depth imaging optical coherence tomography of the human choroid in vivo compared with histology after enucleation. Investigative Ophthalmology and Visual Science 57: 371–6.

Likert, R. 1932. A technique for the measturement of attittudes. Archives of Psychology 22(140), pp. 1–55.

Lindner, M., Bezatis, A., Czauderna, J., Becker, E., Brinkmann, C.K., Schmitz-Valckenberg, S., Fimmers, R., Holz, F.G. and Fleckenstein, M. 2015. Choroidal thickness in geographic atrophy secondary to age-related macular degeneration. Investigative Ophthalmology & Visual Science 56(2), pp. 875–82.

Lippmann, R.P. 1987. An introduction to computing with neural nets. ASSP Magazine, IEEE 4(2), pp. 4–22.

Littmann, H. 1982. [Determination of the real size of an object on the fundus of the living eye]. Klinische Monatsblätter für Augenheilkunde 180(4), pp. 286–9. (In German).

Liu, J.H.K. 1998. Circadian rhythm of intraocular pressure. Journal of Glaucoma 7(2), pp. 141–7.

Llorente, L., Barbero, S., Cano, D., Dorronsoro, C. and Marcos, S. 2004. Myopic versus hyperopic eyes: axial length, corneal shape and optical aberrations. Journal of Vision 4(2004), pp. 288–98.

Loffler, K. and Lee, W. 1986. Basal linear deposit in the human macula. Graefe's Archive for Clinical and Experimental Ophthalmology 224, pp. 493–501.

Lotfi, K. and Grunwald, J.E. 1991. The effect of caffeine on the human macular circulation. Investigative Ophthalmology & Visual Science 32(12), pp. 3028–32.

Lu, L., Xu, S., He, F., Liu, Y., Zhang, Y., Wang, J., Wang, Z. and Fan, X. 2016. Assessment of choroidal microstructure and subfoveal thickness change in eyes with different stages of age-related macular degeneration. Medicine (Baltimore) 95(10), p. e2967.

Ludewig, E., Richter, A. and Frame, M. 2010. Diagnostic imaging--evaluating image quality using visual grading characteristic (VGC) analysis. Veterinary Research Communications 34(5), pp. 473–9.

Major, J.C., Wykoff, C.C., Mariani, A.F., Chen, E., Croft, D.E. and Brown, D.M. 2014. Comparison of spectral-domain and time-domain optical coherence tomography in the detection of neovascular age-related macular degeneration activity. Retina (Philadelphia, Pa.) 34(1), pp. 48–54.

Mansouri, K., Medeiros, F.A., Marchase, N., Tatham, A.J., Auerbach, D. and Weinreb, R.N. 2013. Assessment of choroidal thickness and volume during the water drinking test by swept-source optical coherence tomography. Ophthalmology 120(12), pp. 2508–16.

Margolis, R. and Spaide, R.F. 2009. A pilot study of enhanced depth imaging optical coherence tomography of the choroid in normal eyes. American Journal of Ophthalmology 147(5), pp. 811–5.

Margrain, T.H., Boulton, M., Marshall, J. and Sliney, D.H. 2004. Do blue light filters confer protection against age-related macular degeneration? Progress in Retinal and Eye Research 23(5), pp. 523–31.

Markelj, P., Tomaževič, D., Likar, B. and Pernuš, F. 2012. A review of 3D/2D registration methods for image-guided interventions. Medical Image Analysis 16(3), pp. 642–61.

Martin, D.F., Maguire, M.G., Ying, G.S., Grunwald, J.E., Fine, S.L. and Jaffe, G.J. 2011. Ranibizumab and bevacizumab for neovascular age-related macular degeneration. The New England Journal of Medicine 364(20), pp. 1897–908.

Martin, D.F., Maguire, M.G., Fine, S.L., Ying, G., Jaffe, G.J., Grunwald, J.E., Toth, C., Redford, M. and Ferris, F.L. 2012. Ranibizumab and bevacizumab for treatment of neovascular age-related macular degeneration: two-year results. Ophthalmology 119(7), pp. 1388–98.

Maruko, I., Iida, T., Sugano, Y., Oyamada, H., Sekiryu, T., Fujiwara, T. and Spaide, R.F. 2011. Subfoveal choroidal thickness after treatment of Vogt-Koyanagi-Harada disease. Retina (Philadelphia, Pa.) 31(3), pp. 510–7.

Masis, M., Hernandez, E. and Wu, L. 2011. Choroidal thickness in patients with systemic hypertension. In: ARVO Annual Meeting. p. 5296.

Mayer, M.A., Hornegger, J., Mardin, C.Y. and Tornow, R.P. 2010. Retinal nerve fiber layer segmentation on FD-OCT scans of normal subjects and glaucoma patients. Biomedical Optics Express 1(5), pp. 1358–83.

McLeod, D.S. and Lutty, G.A. 1994. High-resolution histologic analysis of the human choroidal vasculature. Investigative Ophthalmology & Visual Science 35(11), pp. 3799–811.

McLeod, D.S., Taomoto, M., Otsuji, T., Green, W.R., Sunness, J.S. and Lutty, G. a 2002. Quantifying changes in RPE and choroidal vasculature in eyes with age-related macular degeneration. Investigative Ophthalmology & Visual Science 43(6), pp. 1986–93.

McLeod, D.S., Grebe, R., Bhutto, I., Merges, C., Baba, T. and Lutty, G. a 2009. Relationship between RPE and choriocapillaris in age-related macular degeneration. Investigative Ophthalmology & Visual Science 50(10), pp. 4982–91.

Mitchell, P., Wang, J.J., Smith, W. and Leeder, S.R. 2002. Smoking and the 5-year incidence of age-related maculopathy - The Blue Mountains Eye Study. Archives of Ophthalmology 120, pp. 1357–63.

Mitchell, D.C., Knight, C. a., Hockenberry, J., Teplansky, R. and Hartman, T.J. 2014. Beverage caffeine intakes in the U.S. Food and Chemical Toxicology 63, pp. 136–42.

Monadjemi, A. 2004. Towards efficient texture classification and abnormality detection. University of Bristol (PhD thesis).

Nagaoka, T., Kitaya, N., Sugawara, R., Yokota, H., Mori, F., Hikichi, T., Fujio, N. and Yoshida, A. 2004. Alteration of choroidal circulation in the foveal region in patients with type 2 diabetes. British Journal of Ophthalmology 88(8), pp. 1060–3.

Nakayama, M., Keino, H., Okada, A.A., Watanabe, T., Taki, W., Inoue, M. and Hirakata, A. 2012. Enhanced depth imaging optical coherence tomography of the choroid in Vogt-Koyanagi-Harada disease. Retina (Philadelphia, Pa.) 32(10), pp. 2061–9.

National Institute for Health and Care Excellence 2009. Glaucoma: diagnosis and management [Online]. Available at: https://www.nice.org.uk [Accessed: 2 February 2017].

Niblack, W. 1986. An Introduction to Digital Image Processing. Prentice Hall.

Nickla, D.L. and Wallman, J. 2010. The multifunctional choroid. Progress in Retinal and Eye Research 29(2), pp. 144–68.

Nishida, Y., Fujiwara, T., Imamura, Y., Lima, L.H., Kurosaka, D. and Spaide, R.F. 2012. Choroidal thickness and visual acuity in highly myopic eyes. Retina (Philadelphia, Pa.) 32(7), pp. 1229–36.

Nozaki, M., Raisler, B.J., Sakurai, E., Sarma, J.V., Barnum, S.R., Lambris, J.D., Chen, Y., Zhang, K., Ambati, B.K., Baffi, J.Z. and Ambati, J. 2006. Drusen complement components C3a and C5a promote choroidal neovascularization. Proceedings of the National Academy of Sciences of the United States of America 103(7), pp. 2328–33.

Oakley, J., Gabilondo, I., Songster, C., Russakoff, D., Caballero, I., Green, A. and Villoslada, P. 2014. Assessing manual versus automated segmentation of the macula using optical coherence tomography. ARVO Annual Meeting, p. 4790.

Odell, D., Dubis, A.M., Lever, J.F., Stepien, K.E. and Carroll, J. 2011. Assessing errors inherent in OCT-derived macular thickness maps. Journal of Ophthalmology 2011, pp. 1–9.

Ohno-Matsui, K., Akiba, M., Moriyama, M., Ishibashi, T., Hirakata, A. and Tokoro, T. 2012. Intrachoroidal cavitation in macular area of eyes with pathologic myopia. American Journal of Ophthalmology 154(2), pp. 382–93.

Okawa, H., Sampath, A.P., Laughlin, S.B. and Fain, G.L. 2008. ATP consumption by mammalian rod photoreceptors in darkness and in light. Current Biology 18(24), pp. 1917–21.

Okuno, T., Sugiyama, T., Tominaga, M., Kojima, S. and Ikeda, T. 2002. Effects of caffeine on microcirculation of the human ocular fundus. Japanese Journal of Ophthalmology 46(2), pp. 170–6.

Osmanbasoglu, O.A., Alkin, Z., Ozkaya, A., Ozpınar, Y., Yazici, A.T. and Demirok, A. 2013. Diurnal choroidal thickness changes in normal eyes of Turkish people measured by spectral domain optical coherence tomography. Journal of Ophthalmology 2013(2013), p. 687165.

Otsu, N. 1979. A threshold selection method from gray-level histograms. IEEE Transactions on Systems, Man, and Cybernetics 9(1), pp. 62–6.

Owen, C.G., Jarrar, Z., Wormald, R., Cook, D.G., Fletcher, A.E. and Rudnicka, A.R. 2012. The estimated prevalence and incidence of late stage age related macular degeneration in the UK. The British Journal of Ophthalmology 96(5), pp. 752–6.

Owsley, C., McGwin, G., Clark, M.E., Jackson, G.R., Callahan, M.A., Kline, L.B., Witherspoon, C.D. and Curcio, C.A. 2016. Delayed rod-mediated dark adaptation is a functional biomarker for incident early age-related macular degeneration. Ophthalmology 123(2), pp. 344–51.

Park, K.-A. and Oh, S.Y. 2014. An optical coherence tomography-based analysis of choroidal morphologic features and choroidal vascular diameter in children and adults. American Journal of Ophthalmology 158(4), pp. 716–23.

Parvathi, S.S. and Devi, N. 2007. Automatic drusen detection from colour retinal images. In: International Conference on Computational Intelligence and Multimedia Applications (ICCIMA). pp. 61–5.

Parver, L.M. 1991. Temperature modulating action of choroidal blood flow. Eye (London, England) 5 (Pt 2), pp. 181–5.

Penfold, P., Madigan, M., Gillies, M. and Provis, J. 2001. Immunological and aetiological aspects of macular degeneration. Progress in Retinal and Eye Research 20(3), pp. 385–414.

Philip, A.-M., Gerendas, B.S., Zhang, L., Faatz, H., Podkowinski, D., Bogunovic, H., Abramoff, M.D., Hagmann, M., Leitner, R., Simader, C., Sonka, M., Waldstein, S.M. and Schmidt-Erfurth, U. 2016. Choroidal thickness maps from spectral domain and swept source optical coherence tomography: algorithmic versus ground truth annotation. The British Journal of Ophthalmology 100, pp. 1372–6.

Ploner, S.B., Moult, E.M., Choi, W., Waheed, N.K., Lee, B., Novais, E. a, Cole, E.D., Potsaid, B., Husvogt, L., Schottenhamml, J., Maier, A., Rosenfeld, P.J., Duker, J.S., Hornegger, J. and Fujimoto, J.G. 2016. Toward quantitative optical coherence tomography angiography: Visualizing blood flow speeds in ocular pathology using variable interscan time analysis. Retina (Philadelphia, Pa.) 36, pp. S118–26.

Polito, A., Del Borrello, M., Polini, G., Furlan, F., Isola, M. and Bandello, F. 2006. Diurnal variation in clinically significant diabetic macular edema measured by the Stratus OCT. Retina (Philadelphia, Pa.) 26(1), pp. 14–20.

Povazay, B., Bizheva, K., Hermann, B., Unterhuber, A., Sattmann, H., Fercher, A., Drexler, W., Schubert, C., Ahnelt, P., Mei, M., Holzwarth, R., Wadsworth, W., Knight, J. and Russell, P.S.J. 2003. Enhanced visualization of choroidal vessels using ultrahigh resolution ophthalmic OCT at 1050 nm. Optics Express 11(17), pp. 1980–6.

Povazay, B., Hermann, B., Unterhuber, A., Hofer, B., Sattmann, H., Zeiler, F., Morgan, J.E., Falkner-Radler, C., Glittenberg, C., Blinder, S. and Drexler, W. 2007. Three-dimensional optical coherence tomography at 1050 nm versus 800 nm in retinal pathologies: enhanced performance and choroidal penetration in cataract patients. Journal of Biomedical Optics 12(4), p. 041211.

Priya, R. and Aruna, P. 2011. Automated diagnosis of age-related macular degeneration from color retinal fundus images. In: 3rd International Conference on Electronics Computer Technology (ICECT). pp. 227–30.

Provis, J.M., Penfold, P.L., Cornish, E.E., Sandercoe, T.M. and Madigan, M.C. 2005. Anatomy and development of the macula: specialisation and the vulnerability to macular degeneration. Clinical & Experimental Optometry: Journal of the Australian Optometrical Association 88(5), pp. 269–81.

Pryds, A. and Larsen, M. 2012. Choroidal thickness following extrafoveal photodynamic treatment with verteporfin in patients with central serous chorioretinopathy. Acta Ophthalmologica 90(8), pp. 738–43.

Rahman, W., Chen, F.K., Yeoh, J., Patel, P., Tufail, A. and Da Cruz, L. 2011. Repeatability of manual subfoveal choroidal thickness measurements in healthy subjects using the technique of enhanced depth imaging optical coherence tomography. Investigative Ophthalmology & Visual Science 52(5), pp. 2267–71.

Rahman, W., Chen, F.K., Yeoh, J. and da Cruz, L. 2013. Enhanced depth imaging of the choroid in patients with neovascular age-related macular degeneration treated with anti-VEGF therapy versus untreated patients. Graefe's Archive for Clinical and Experimental Ophthalmology 251(6), pp. 1483–8.

Ramrattan, R.S., Schaft, T.L. Van Der, Mooy, C.M., Bruijn, W.C. De, Mulder, P.G.H. and Paulus, T.V.M. 1994. Morphometric analysis of Bruch's membrane, the choriocapillaris, and the choroid in aging. Investigative Ophthalmology & Visual Science 35(6), pp. 2857–64.

Ravenscroft, D. 2016. Automated diagnosis of age-related macular degeneration using machine learning techniques. Swansea University (MSc thesis).

Read, S.A., Collins, M.J. and Alonso-Caneiro, D. 2012. Diurnal variation of retinal thickness with spectral domain OCT. Optometry & Vision Science 89(5), pp. 611–9.

Redmond, T., Yu, S., Lee, E., Bok, D., Hamasaki, D., Chen, N., Goletz, P. and Al., E. 1998. Rpe65 is necessary for production of 11-cis-vitamin A in the retinal visual cycle. Nature Genetics 20, pp. 344–51.

Rees, A., Zekite, A., Bunce, C. and Patel, P.J. 2014. How many people in England and Wales are registered partially sighted or blind because of age-related macular degeneration? Eye (London, England) 28(7), pp. 832–7.

Regatieri, C. V, Branchini, L.A., Carmody, J., Fujimoto, J.G. and Duker, J.S. 2012a. Choroidal thickness in patients with diabetic retinopathy analyzed by spectral-domain optical coherence tomography. Retina (Philadelphia, Pa.) 32(3), pp. 563–8.

Regatieri, C. V, Branchini, L.A., Fujimoto, J.G. and Duker, J.S. 2012b. Choroidal imaging using spectral-domain optical coherence tomography. Retina (Philadelphia, Pa.) 32(5), pp. 865–76.

Reif, R., Qin, J., An, L., Zhi, Z., Dziennis, S. and Wang, R. 2012. Quantifying optical microangiography images obtained from a spectral domain optical coherence tomography system. International Journal of Biomedical Imaging 2012, p. 509783.

Remington, L. 2005. Clinical Anatomy of the Visual System. 2nd ed. Elsevier.

Riva, C.E., Cranstoun, S.D., Grunwald, J.E. and Petrig, B.L. 1994. Choroidal blood flow in the foveal region of the human ocular fundus. Investigative Ophthalmology & Visual Science 35(13), pp. 4273–81.

Riva, C.E., Titze, P., Hero, M., Movaffaghy, A. and Petrig, B.L. 1997. Choroidal blood flow during isometric exercises. Investigative Ophthalmology & Visual Science 38(11), pp. 2338–43.

Rosenfeld, P.J., Brown, D.M., Heier, J.S., Boyer, D.S., Kaiser, P.K., Chung, C.Y. and Kim, R.Y. 2009. Ranibizumab for neovascular age-related macular degeneration. The New England Journal of Medicine 355(14), pp. 1419–31.

Roth, F., Bindewald, A. and Holz, F.G. 2004. Keypathophysiologic pathways in age-related macular disease. Graefe's Archive for Clinical and Experimental Ophthalmology 242(8), pp. 710–6.

Rudnicka, A.R., Jarrar, Z., Wormald, R., Cook, D.G., Fletcher, A. and Owen, C.G. 2012. Age and gender variations in age-related macular degeneration prevalence in populations of European ancestry: a meta-analysis. Ophthalmology 119(3), pp. 571–80.

Saidha, S., Syc, S.B., Ibrahim, M. a., Eckstein, C., Warner, C. V., Farrell, S.K., Oakley, J.D., Durbin, M.K., Meyer, S. a., Balcer, L.J., Frohman, E.M., Rosenzweig, J.M., Newsome, S.D., Ratchford, J.N., Nguyen, Q.D. and Calabresi, P. a. 2011. Primary retinal pathology in multiple sclerosis as detected by optical coherence tomography. Brain 134(2), pp. 518–33.

Sanabria, M.R., Montero, J. a, Losada, M.V., Fernández-Muñoz, M., Galindo, A., Fernández, I., Coco, R.M. and Sampedro, A. 2013. Ocular pain after intravitreal injection. Current Eye Research 38(2), pp. 278–82.

Sanchez-Cano, A., Orduna, E., Segura, F., Lopez, C., Cuenca, N., Abecia, E. and Pinilla, I. 2014. Choroidal thickness and volume in healthy young whites and their relationship with axial length, ammetropy and sex. American Journal of Ophthalmology 158(3), pp. 574–83.

Sarks, S.H. 1976. Ageing and degeneration in the macular region: a clinico-pathological study. British Journal of Ophthalmology 60(5), pp. 324–41.

Sayanagi, K., Sharma, S., Yamamoto, T. and Kaiser, P.K. 2009. Comparison of spectral-domain versus time-domain optical coherence tomography in management of age-related macular degeneration with ranibizumab. Ophthalmology 116(5), pp. 947–55.

Schindelin, J., Arganda-Carreras, I., Frise, E., Kaynig, V., Longair, M., Pietzsch, T., Preibisch, S., Rueden, C., Saalfeld, S., Schmid, B., Tinevez, J.-Y., White, D.J., Hartenstein, V., Eliceiri, K., Tomancak, P. and Cardona, A. 2012. Fiji: an open-source platform for biological-image analysis. Nature Methods 9(7), pp. 676–82.

Schlingemann, R. 2004. Role of growth factors and the wound healing response in age-related macular degeneration. Graefe's Archive for Clinical and Experimental Ophthalmology 242(1), pp. 91–101.

Schmitt, J.M. 1999. Optical coherence tomography (OCT): a review. IEEE Journal of Selected Topics in Quantum Electronics 5(4), pp. 1205–15.

Seddon, J.M., George, S. and Rosner, B. 2006. Cigarette smoking, fish consumption, omega-3 fatty acid intake, and associations with age-related macular degeneration. Archives of Ophthalmology 124(7), pp. 995–1001.

Seddon, J.M., Rosner, B., Sperduto, R.D., Yannuzzi, L., Haller, J.A., Blair, N.P. and Willett, W. 2001. Dietary fat and risk for advanced age-related macular degeneration. Archives of Ophthalmology 119(8), pp. 1191–9.

Seddon, J.M., McLeod, D.S., Bhutto, I.A., Villalonga, M.B., Silver, R.E., Wenick, A.S., Edwards, M.M. and Lutty, G.A. 2016. Histopathological insights into choroidal vascular loss in clinically documented cases of age-related macular degeneration. JAMA ophthalmology 134(11), pp. 1272–80.

Shimizu, N., Nomura, H., Ando, F., Niino, N., Miyake, Y. and Shimokata, H. 2003. Refractive errors and factors associated with myopia in an adult Japanese population. Japanese Journal of Ophthalmology 47(1), pp. 6–12.

Sidman, R.L. 1957. The structure and concentration of solids in photoreceptor cells studied by refractometry and interference microscopy. The Journal of Biophysical and Biochemical Cytology 3(1), pp. 15–30.

Sigler, E.J. and Randolph, J.C. 2013. Comparison of macular choroidal thickness among patients older than age 65 with early atrophic age-related macular degeneration and normals. Investigative Ophthalmology & Visual Science 54(9), pp. 6307–13.

Sigler, E.J., Randolph, J.C., Calzada, J.I. and Charles, S. 2014. Smoking and choroidal thickness in patients over 65 with early-atrophic age-related macular degeneration and normals. Eye (London, England) 28(7), pp. 838–46.

Sim, D.A., Keane, P.A., Mehta, H., Fung, S., Zarranz-Ventura, J., Fruttiger, M., Patel, P.J., Egan, C.A. and Tufail, A. 2013. Repeatability and reproducibility of choroidal vessel layer measurements in diabetic retinopathy using enhanced depth optical coherence tomography. Investigative Ophthalmology & Visual Science 54(4), pp. 2893–901.

Simó, R., Villarroel, M., Corraliza, L., Hernández, C. and Garcia-Ramírez, M. 2010. The retinal pigment epithelium: something more than a constituent of the blood-retinal barrier—implications for the pathogenesis of diabetic retinopathy. Journal of Biomedicine and Biotechnology 2010, p. 190724.

Sizmaz, S., Küçükerdönmez, C., Pinarci, E.Y., Karalezli, A., Canan, H. and Yilmaz, G. 2013. The effect of smoking on choroidal thickness measured by optical coherence tomography. British Journal of Ophthalmology 97(5), pp. 601–4.

Snell, R. and Lemp, M. 1998. Clinical anatomy of the eye. 2nd ed. London: Blackwell Science.

Snodderly, D.M., Brown, P.K., Delori, F.C. and Auran, J.D. 1984a. The macular pigment. I. Absorbance spectra, localization, and discrimination from other yellow pigments in primate retinas. Investigative Ophthalmology and Visual Science 25(6), pp. 660–73.

Snodderly, D., Auran, J. and Delori, F. 1984b. The macular pigment. II. Spatial distribution in primate retinas. Investigative Ophthalmology & Visual Science 25, pp. 674–85.

Snodderly, D.M. 1995. Evidence for protection against degeneration by carotenoids and antioxidant. Americal Journal of Clinical Nutrition 62 (suppl), pp. S1448–61.

Soares, J.V.B., Leandro, J.J.G., Cesar, R.M., Jelinek, H.F. and Cree, M.J. 2006. Retinal vessel segmentation using the 2-D Gabor wavelet and supervised classification. IEEE Transactions on Medical Imaging 25(9), pp. 1214–22.

Sohn, E.H., Chen, J.J., Lee, K., Niemeijer, M., Sonka, M. and Abràmoff, M.D. 2013. Reproducibility of diabetic macular edema estimates from SD-OCT is affected by the choice of image analysis algorithm. Investigative Ophthalmology & Visual Science 54(6), pp. 4184–8.

Sohrab, M.A., Smith, R.T., Salehi-Had, H., Sadda, S.R. and Fawzi, A.A. 2011. Image registration and multimodal imaging of reticular pseudodrusen. Investigative Ophthalmology & Visual Science 52(8), pp. 5743–8.

Sohrab, M., Wu, K. and Fawzi, A.A. 2012. A pilot study of morphometric analysis of choroidal vasculature in vivo, using en face optical coherence tomography. PLoS ONE 7(11), p. 48631.

Sonka, M. and Abràmoff, M.D. 2016. Quantitative analysis of retinal OCT. Medical Image Analysis 33, pp. 165–9.

Sonoda, S., Sakamoto, T., Yamashita, T., Shirasawa, M., Uchino, E., Terasaki, H. and Tomita, M. 2014. Choroidal structure in normal eyes and after photodynamic therapy determined by binarization of optical coherence tomographic images. Investigative Ophthalmology & Visual Science 55(6), pp. 3893–8.

Sonoda, S., Sakamoto, T., Yamashita, T., Uchino, E., Kawano, H., Yoshihara, N., Terasaki, H., Shirasawa, M., Tomita, M. and Ishibashi, T. 2015. Luminal and stromal areas of choroid determined by binarization method of optical coherence tomographic images. American Journal of Ophthalmology 159(6), pp. 1123–31.

Spaide, R.F., Koizumi, H. and Pozzoni, M.C. 2008. Enhanced depth imaging spectral-domain optical coherence tomography. American Journal of Ophthalmology 146(4), pp. 496–500.

Spaide, R.F., Fujimoto, J.G. and Waheed, N.K. 2015. Image artifacts in optical coherence tomography angiography. Retina 35(11), pp. 2163–80.

Sparrow, J.M., Dickinson, A.J. and Duke, A.M. 1997. The Wisconsin Age-related Macular Degeneration grading system: performance in an independent centre. Ophthalmic Epidemiology 4(1), pp. 49–55.

Specht, D.F. 1990. Probabilistic neural networks. Neural Networks 3(1), pp. 109–18.

Sperduto, R.D., Seigel, D., Roberts, J. and Rowland, M. 1983. Prevalence of myopia in the United States. Archives of Ophthalmology 101(3), pp. 405–7.

Spraul, C., Lang, G. and Grossniklaus, H. 1996. Morphometric analysis of the choroid, Bruch's membrane, and retinal pigment epithelium in eyes with age-related macular degeneration. Investigative Ophthalmology & Visual Science 37(13), pp. 2724–35.

Spraul, C.W., Lang, G.E., Grossniklaus, H.E. and Lang, G.K. 1999. Histologic and morphometric analysis of the choroid, Bruch's membrane, and retinal pigment epithelium in postmortem eyes with age-related macular degeneration and histologic examination of surgically excised choroidal neovascular membranes. Survey of Ophthalmology 44(Suppl 1), pp. S10–32.

Srinivasan, P.P., Heflin, S.J., Izatt, J.A., Arshavsky, V.Y. and Farsiu, S. 2014a. Automatic segmentation of up to ten layer boundaries in SD-OCT images of the mouse retina with and without missing layers due to pathology. Biomedical Optics Express 5(2), pp. 348–65.

Srinivasan, P.P., Kim, L. a, Mettu, P.S., Cousins, S.W., Comer, G.M., Izatt, J. a and Farsiu, S. 2014b. Fully automated detection of diabetic macular edema and dry age-related macular degeneration from optical coherence tomography images. Biomedical Optics Express 5(10), pp. 3568–77.

Stefánsson, E., Geirsdóttir, A. and Sigurdsson, H. 2011. Metabolic physiology in age related macular degeneration. Progress in Retinal and Eye Research 30(1), pp. 72–80.

Steffens, D., Fisher, G., Langa, K., Potter, G. and Plassman, B. 2009. Prevalence of depression among older Americans: the aging, demographics and memory study. International Psychogeriatrics 21(5), pp. 879–88.

Stone, R.A., Quinn, G.E., Francis, E.L., Ying, G., Flitcroft, D.I., Parekh, P., Brown, J., Orlow, J. and Schmid, G. 2004. Diurnal axial length fluctuations in human eyes. Investigative Ophthalmology & Visual Science 45(1), pp. 63–70.

Strauss, O. 2005. The retinal pigment epithelium in visual function. Physiological Reviews 85, pp. 845–81.

Sui, G., Liu, G.-C., Liu, G., Gao, Y., Deng, Y., Wang, W.-Y., Tong, S. and Wang, L. 2013. Is sunlight exposure a risk factor for age-related macular degeneration? A systematic review and meta-analysis. The British Journal of Ophthalmology 97(4), pp. 389–94.

Swanson, E.A., Izatt, J., Hee, M.R., Huang, D., Lin, C.P., Schuman, J.S., Puliafito, C.A. and Fujimoto, J.G. 1993. In vivo retinal imaging by optical coherence tomography. Optics Letters 18(21), pp. 1864–6.

Switzer, D.W., Mendonca, L.S., Saito, M., Zweifel, S.A. and Spaide, R.F. 2012. Segregation of ophthalmoscopic characteristics according to choroidal thickness in patients with early age-related macular degeneration. Retina (Philadelphia, Pa.) 32(7), pp. 1265–71.

Syc, S.B., Saidha, S., Newsome, S.D., Ratchford, J.N., Levy, M., Ford, E., Crainiceanu, C.M., Durbin, M.K., Oakley, J.D., Meyer, S. a., Frohman, E.M. and Calabresi, P. a. 2012. Optical coherence tomography segmentation reveals ganglion cell layer pathology after optic neuritis. Brain 135(2), pp. 521–33.

Takahashi, A., Nagaoka, T., Sato, E. and Yoshida, A. 2008. Effect of panretinal photocoagulation on choroidal circulation in the foveal region in patients with severe diabetic retinopathy. The British Journal of Ophthalmology 92(10), pp. 1369–73.

Takahashi, J., Kado, M., Mizumoto, K., Igarashi, S. and Kojo, T. 2013. Choroidal thickness in pregnant women measured by enhanced depth imaging optical coherence tomography. Japanese Journal of Ophthalmology 57(5), pp. 435–9.

Takahashi, H., Takase, H., Ishizuka, A., Miyanaga, M., Kawaguchi, T., Ohno-Matsui, K. and Mochizuki, M. 2014. Choroidal thickness in convalescent Vogt–Koyanagi–Harada disease. Retina (Philadelphia, Pa.) 34(4), pp. 775–80.

Tan, J.S.L., Mitchell, P., Kifley, A., Flood, V., Smith, W. and Wang, J.J. 2007. Smoking and the long-term incidence of age-related macular degeneration - The Blue Mountains Eye Study. Archives of Ophthalmology 125(8), pp. 1089–95.

Tan, C.S., Ouyang, Y., Ruiz, H. and Sadda, S.R. 2012. Diurnal variation of choroidal thickness in normal, healthy subjects measured by spectral domain optical coherence tomography. Investigative Ophthalmology & Visual Science 53(1), pp. 261–6.

Tan, C.S.H., Cheong, K.X., Lim, L.W. and Li, K.Z. 2014. Topographic variation of choroidal and retinal thicknesses at the macula in healthy adults. The British Journal of Ophthalmology 98(3), pp. 339–44.

Tan, K.-A., Laude, A., Yip, V., Loo, E., Wong, E.P. and Agrawal, R. 2016. Choroidal vascularity index - a novel optical coherence tomography parameter for disease monitoring in diabetes mellitus? Acta Ophthalmologica, pp. 1–5.

Terry, L., Cassels, N., Lu, K., Acton, J.H., Margrain, T.H., North, R. V., Fergusson, J., White, N. and Wood, A. 2016. Automated retinal layer segmentation using spectral domain optical coherence tomography: evaluation of inter-session repeatability and agreement between devices. PLoS ONE 11(9), p. 0162001.

Terry, L. 2017. OCT: past, present and future. Optometry Today 57(10), pp. 71-5.

Thévenaz, P., Ruttimann, U.E. and Unser, M. 1998. A pyramid approach to subpixel registration based on intensity. IEEE Transactions on Image Processing 7(1), pp. 27–41.

Ting, D.S.W., Ng, W.Y., Ng, S.R., Tan, S.P., Yeo, I.Y.S., Mathur, R., Chan, C.M., Tan, A.C.S., Tan, G.S.W., Wong, T.Y. and Cheung, C.M.G. 2016. Choroidal thickness changes in age-related macular degeneration and polypoidal choroidal vasculopathy: A 12-month prospective study. American Journal of Ophthalmology 164, pp. 128–36.

Toth, C., Narayan, D., Boppart, S., Hee, M., Fujimoto, J., Birngruber, R., Cain, C., DiCarlo, C. and Roach, W. 1997. A comparison of retinal morphology viewed by optical coherence tomography and by light microscopy. Archives of Ophthalmology 115(11), pp. 1425–8.

Toyokawa, N., Kimura, H., Fukomoto, A. and Kuroda, S. 2012. Difference in morning and evening choroidal thickness in Japanese subjects with no chorioretinal disease. Ophthalmic Surgery, Lasers & Imaging 43(2), pp. 109–14.

Ueda-Arakawa, N., Ooto, S., Ellabban, A. a., Takahashi, A., Oishi, A., Tamura, H., Yamashiro, K., Tsujikawa, A. and Yoshimura, N. 2014. Macular choroidal thickness and volume of eyes with reticular pseudodrusen using swept-source optical coherence tomography. American Journal of Ophthalmology 157(5), pp. 994–1004.

Ulaş, F., Çelik, F., Doğan, Ü. and Çelebi, S. 2014. Effect of smoking on choroidal thickness in healthy smokers. Current Eye Research 39(5), pp. 504–11.

Unsal, E., Eltutar, K., Zirtiloğlu, S., Dinçer, N., Ozdoğan Erkul, S. and Güngel, H. 2014. Choroidal thickness in patients with diabetic retinopathy. Clinical Ophthalmology (Auckland, N.Z.) 8, pp. 637–42.

Unterhuber, A., Povazay, B., Hermann, B., Sattmann, H., Chavez-Pirson, A. and Drexler, W. 2005. In vivo retinal optical coherence tomography at 1040 nm - enhanced penetration into the choroid. Optics Express 13(9), pp. 3252–8.

Usui, S., Ikuno, Y., Akiba, M., Maruko, I., Sekiryu, T., Nishida, K. and Iida, T. 2012. Circadian changes in subfoveal choroidal thickness and the relationship with

circulatory factors in healthy subjects. Investigative Ophthalmology & Visual Science 53(4), pp. 2300–7.

Vance, S.K., Imamura, Y. and Freund, K.B. 2011. The effects of sildenafil citrate on choroidal thickness as determined by enhanced depth imaging optical coherence tomography. Retina (Philadelphia, Pa.) 31(2), pp. 332–5.

Van Velthoven, M.E.J., Faber, D.J., Verbraak, F.D., van Leeuwen, T.G. and de Smet, M.D. 2007. Recent developments in optical coherence tomography for imaging the retina. Progress in Retinal and Eye Research 26(1), pp. 57–77.

Vuong, V.S., Moisseiev, E., Cunefare, D., Farsiu, S., Moshiri, A. and Yiu, G. 2016. Repeatability of choroidal thickness measurements on enhanced depth imaging OCT using different posterior boundaries. American Journal of Ophthalmology 169, pp. 104–12.

Vural, A.D., Kara, N., Sayin, N., Pirhan, D. and Ersan, H.B.A. 2014. Choroidal thickness changes after a single administration of coffee in healthy subjects. Retina (Philadelphia, Pa.) 34(6), pp. 1223–8.

Wang, Q., Klein, B.E., Klein, R. and Moss, S.E. 1994. Refractive status in the Beaver Dam Eye Study. Investigative Ophthalmology & Visual Science 35(13), pp. 4344–7.

Wang, S. and Linsenmeier, R.A. 2007. Hyperoxia improves oxygen consumption in the detached feline retina. Investigative Ophthalmology & Visual Science 48(3), pp. 1335–41.

Wang, N.-K., Lai, C.-C., Chou, C.L., Chen, Y.-P., Chuang, L.-H., Chao, A.-N., Tseng, H.-J., Chang, C.-J., Wu, W.-C., Chen, K.-J. and Tsang, S.H. 2013. Choroidal thickness and biometric markers for the screening of lacquer cracks in patients with high myopia. PLoS One 8(1), p. 53660.

Wei, W. Bin, Xu, L., Jonas, J.B., Shao, L., Du, K.F., Wang, S., Chen, C.X., Xu, J., Wang, Y.X., Zhou, J.Q. and You, Q.S. 2013. Subfoveal choroidal thickness: The Beijing Eye Study. Ophthalmology 120(1), pp. 175–80.

Wei, X., Ting, D.S.W., Ng, W.Y., Khandelwal, N., Agrawal, R. and Cheung, C.M.G. 2016. Choroidal vascularity index - A novel optical coherence tomography based parameter in patients with exudative age-related macular degeneration. Retina (Philadelphia, Pa.), pp. 1–6.

Weiner, D.E., Tighiouart, H., Reynolds, R. and Seddon, J.M. 2011. Kidney function, albuminuria and age-related macular degeneration in NHANES III. Nephrology, Dialysis, Transplantation: Official Publication of the European Dialysis and Transplant Association - European Renal Association 26(10), pp. 3159–65.

Wernick, M.N., Yang, Y., Brankov, J.G., Yourganov, G. and Strother, S.C. 2010. Machine Learning in Medical Imaging: Drawing conclusions from medical images. IEEE Signal Prossessing Magazine (July), pp. 25–38.

Whitmore, S.S., Sohn, E.H., Chirco, K.R., Drack, A. V., Stone, E.M., Tucker, B. a. and Mullins, R.F. 2015. Complement activation and choriocapillaris loss in early AMD: Implications for pathophysiology and therapy. Progress in Retinal and Eye Research 45, pp. 1–29.

Wilde, C., Patel, M., Lakshmanan, A., Morales, M.A., Dhar-Munshi, S. and Amoaku, W.M.K. 2016. Prevalence of reticular pseudodrusen in eyes with newly presenting neovascular age-related macular degeneration. European Journal of Ophthalmology 26(2), pp. 128–34.

Wildsoet, C. and Wallman, J. 1995. Choroidal and scleral mechanisms of compensation for spectacle lenses in chicks. Vision Research 35(9), pp. 1175–94.

Willoughby, A.S., Chiu, S.J., Silverman, R.K., Farsiu, S., Bailey, C., Wiley, H.E., Ferris, F.L. and Jaffe, G.J. 2017. Platform-independent Cirrus and Spectralis thickness measurements in eyes with diabetic macular edema using fully automated software. Translational Vision Science & Technology 6(1), p. 9.

Witmer, A.N., Vrensen, G.F.J.M., Van Noorden, C.J.F. and Schlingemann, R.O. 2003. Vascular endothelial growth factors and angiogenesis in eye disease. Progress in Retinal and Eye Research 22(1), pp. 1–29.

Wong, T.Y., Foster, P.J., Hee, J., Ng, T.P., Tielsch, J.M., Chew, S.J., Johnson, G.J. and Seah, S.K. 2000. Prevalence and risk factors for refractive errors in adult Chinese in Singapore. Investigative Ophthalmology & Visual Science 41(9), pp. 2486–94.

Wong, I.Y., Wong, R.L., Zhao, P. and Lai, W.W. 2013. Choroidal thickness in relation to hypercholesterolemia on enhanced depth imaging optical coherence tomography. Retina (Philadelphia, Pa.) 33(2), pp. 423–8.

Wong, W.L., Su, X., Li, X., Cheung, C.M.G., Klein, R., Cheng, C.-Y. and Wong, T.Y. 2014. Global prevalence of age-related macular degeneration and disease burden projection for 2020 and 2040: a systematic review and meta-analysis. The Lancet Global Health 2(2), pp. 106–16.

Wood, A., Binns, A., Margrain, T., Drexler, W., Považay, B., Esmaeelpour, M. and Sheen, N. 2011. Retinal and choroidal thickness in early age-related macular degeneration. American Journal of Ophthalmology 152(6), pp. 1030–8.

Wu, H.M., Seet, B., Yap, E.P., Saw, S.M., Lim, T.H. and Chia, K.S. 2001. Does education explain ethnic differences in myopia prevalence? A population-based study of young adult males in Singapore. Optometry and Vision Science 78(4), pp. 234–9.

Yabushita, H., Bouma, B., Houser, S., Aretz, T., Jang, I., Schlendorf, K., Kauffman, C., Shishkov, M., Kang, D., Halpern, E. and Tearney, G. 2002. Characterization of human atherosclerosis by optical coherence tomography. Circulation 106(13), pp. 1640–5.

Yamada, Y., Ishibashi, K., Ishibashi, K., Bhutto, I.A., Tian, J., Lutty, G.A. and Handa, J.T. 2006. The expression of advanced glycation endproduct receptors in rpe cells

associated with basal deposits in human maculas. Experimental Eye Research 82(5), pp. 840–8.

Yamazaki, T., Koizumi, H., Yamagishi, T. and Kinoshita, S. 2012. Subfoveal choroidal thickness after ranibizumab therapy for neovascular age-related macular degeneration: 12-month results. Ophthalmology 119(8), pp. 1621–7.

Yang, L., Jonas, J.B. and Wei, W. 2013. Choroidal vessel diameter in central serous chorioretinopathy. Acta Ophthalmologica 91(5), pp. 358–62.

Yiu, G., Chiu, S.J., Petrou, P.A., Stinnett, S., Sarin, N., Farsiu, S., Chew, E.Y., Wong, W.T. and Toth, C.A. 2015. Relationship of central choroidal thickness with age-related macular degeneration status. American Journal of Ophthalmology 159(4), pp. 617–26.

Yumusak, E., Ornek, K., Durmaz, S.A., Cifci, A., Guler, H.A. and Bacanli, Z. 2016. Choroidal thickness in obese women. BMC Ophthalmology 16(1), p. 48.

Zarbin, M.A. 2004. Current concepts in the pathogenesis of age-related macular degeneration. Archives of Ophthalmology 122(4), pp. 598–614.

Zengin, M.O., Cinar, E., Karahan, E., Tuncer, I. and Kucukerdonmez, C. 2015. The effect of caffeine on choroidal thickness in young healthy subjects. Cutaneous and Ocular Toxicology 34(2), pp. 112–6.

Zhang, L., Lee, K., Niemeijer, M., Mullins, R.F., Sonka, M. and Abràmoff, M.D. 2012. Automated segmentation of the choroid from clinical SD-OCT. Investigative Ophthalmology & Visual Science 53(12), pp. 7510–9.

Zhang, L., Buitendijk, G.H.S., Lee, K., Sonka, M., Springelkamp, H., Hofman, A., Vingerling, J.R., Mullins, R.F., Klaver, C.C.W. and Abràmoff, M.D. 2015. Validity of automated choroidal segmentation in SS-OCT and SD-OCT. Investigative Ophthalmology & Visual Science 56(5), pp. 3202–11.

Zhao, M., Yang, X.-F., Jiao, X., Lim, A., Ren, X.-T., Snellingen, T. and Liu, N.-P. 2016. The diurnal variation pattern of choroidal thickness in macular region of young healthy female individuals using spectral domain optical coherence tomography. International Journal of Ophthalmology 9(4), pp. 561–6.

Zheng, F., Gregori, G., Schaal, K.B., Legarreta, A.D., Miller, A.R., Roisman, L., Feuer, W.J. and Rosenfeld, P.J. 2016. Choroidal thickness and choroidal vessel density in nonexudative age-related macular degeneration using swept-source optical coherence tomography imaging. Investigative Opthalmology & Visual Science 57(14), pp. 6256–64.

Appendices

A) Specifications of a subset of commercially available OCT devices
B) MATLAB code to flatten OCT images to the RPE
C) Image quality grading instructions
D) Participant information sheet and consent form
E) MATLAB code to establish inter-observer agreement of manual choroidal segmentation
F) Supplementary machine learning results
G) Publication: Automated Retinal Layer Segmentation Using Spectral Domain Optical Coherence Tomography: Evaluation of Inter-Session Repeatability and Agreement between Devices

A – Specifications of a subset of commercially available OCT devices

Device*	**Heidelberg Spectralis**	**Zeiss Cirrus HD-OCT 5000**	**Topcon 3D-OCT 2000**
Centre wavelength	870 nm	840 nm	840 nm
Imaging type	Spectral-domain	Spectral-domain	Spectral-domain
Scanning speed	40,000 a-scans/sec	27,000-68,000 a-scans/sec	27,000-50,000 a-scans/sec
Axial resolution	3.5 µm (digital) 7 µm (optical)	5 µm	5-6 µm
Transverse resolution	14 µm	15 µm	20 µm
Minimum pupil diameter	unstated	2 mm	2.5 mm

*Information from product manuals.

#The Topcon 3D-OCT 1000 (as described in this thesis) is no longer manufactured.

B – MATLAB code to flatten OCT images to the RPE

```
%-------------------------------------------------------------------------
%NAME
%  main.m
%PURPOSE
%  Main program
%ACRONYM
%  MAIN
%DESCRIPTION
%  This program flattens choroidal OCT images by displacing columns of
%  pixels vertically. The input images are stacked TIFF files, with 8
%  bit greyscale (0 is black, 255 is white).
%AUTHORS
%  Louise Terry
%  Tom Bower
%-------------------------------------------------------------------------
%=========================================================================
%                INITIALISE
%=========================================================================
%               Clear MATLAB workspace and variables
clear; clc;
%               Get filename from user with "open" windows dialog
[ifile path fi] = uigetfile('*.tif','Select the MATLAB code file');
%               Concatenate strings for path and filename into ifile
ifile=strcat(path,ifile);
%               Add suffixes to generate temp and output filename
strings
ofile=strcat(ifile(1:end-4),'-temp.tif');
ofile2=strcat(ifile(1:end-4),'-flat.tif');
%               Print the input and output files to the command windows
disp(ifile);
disp(ofile2);
%               Open TIFF file for reading
tin = Tiff(ifile);
%               Store TIFF information (dimensions, compression...)
info = imfinfo(ifile);

%=========================================================================
%                GET USER INPUT DATA
%=========================================================================
%                Maximum possible number of slices assumed (nmax)
nmax = 1024;
%               First assume zero slices
nslice = 0;
last = 0;
%               Loop until last slice, or maximum slices
while (nslice <= nmax) && (last~=1)
%               Increment slice counter
  nslice=nslice+1;
%               Set the current slice to the new counted slice
  setDirectory(tin,nslice);
%               Binary query for last slice, last=0 unless current
%               slice is the final slice, loop exits when last==1
  last=lastDirectory(tin);
end
%               Print the total number of slices to the command window
disp(['Number of slices: ' num2str(nslice)]);
%               Get image dimensions
width=int64(tin.getTag('ImageWidth'));
height=int64(tin.getTag('ImageLength'));
%                Print image dimensions to command window
disp(['Image width: ' num2str(width)]);
disp(['Image height: ' num2str(height)]);
```

```
%               Call slicenos function, this asks the user which
%               slices to sample
[slices nsample] = slicenos(nslice);

%=========================================================================
%               PROCESS INPUT DATA AND APPLY TRANSFORMATIONS
%=========================================================================
%               Call sampleddisps function, asks the user for clicks
%               on each sampling image, then interpolates the parabola
%               using fourth order regression
sampled = sampleddisps(tin,slices,nslice,nsample,width,height);

%               Print current stage to command window
disp('Interpolating columns with polyfit');
%               Call alldisp funcion, this interpolates each parabola
%               between slices and outputs the displacement matrix for
%               the entire stacked image
alldisps = alldisp(width,nslice,slices,nsample,sampled);

%               Start timer
tic;
%               Print current stage to command window
disp('Applying interpolated displacements');
%               Call applydisps function, this takes the displacement
%               matrix and transforms the image, the output is a three
%               dimensional matrix containing the 0-255 greyscale
%               values for each pixel in the TIFF stack
newimg=applydisps(alldisps,width,height,nslice,tin);

%=========================================================================
%               SAVE NEW IMAGE
%=========================================================================
%               Print current stage to command window
disp('Saving image');
%               Create new image and store in t
t = Tiff(ofile,'w');
%               Set properties for new image
t.setTag('ImageLength',size(newimg,1));
t.setTag('ImageWidth',size(newimg,2));
t.setTag('Photometric',Tiff.Photometric.MinIsBlack);
t.setTag('BitsPerSample',8);
t.setTag('PlanarConfiguration', Tiff.PlanarConfiguration.Chunky);
t.setTag('Software', 'MATLAB');
%               Save the 3-D matrix in the new TIFF file
saveimg(newimg,nslice,tin,ofile);
%               Duplicate the written file (workaround for TIFF save
%               failure)
copyfile(ofile,ofile2,'f');
%               Close the file
close(t);
%               Delete the temporary file
delete(ofile);
%               Print completion notification to the command window
disp('----------------------------------------');
disp('Program complete');
%               Stop timer, this command also outputs the elapsed time
to
%               the command window
toc;
```

```
%-------------------------------------------------------------------------
%NAME
%  slicenos.m
%PURPOSE
%  Gets the sample slice numbers from the user
%ACRONYM
%  SLICE_NumberS
%DESCRIPTION
%  The user is first asked to enter the number of slices to be
%  sampled,this function then asks the user to type each slice number.
%  The total number of slices has already been displayed and an error
%  shows when the user input is out of range.
%AUTHORS
%  Louise Terry
%  Tom Bower
%-------------------------------------------------------------------------

function [slices nsample]=slicenos(nslice)
%               Ask user for input of slice numbers
nsample=input('Enter the number of slices to be sampled: ');
%               Initialise counter
i = 1;
%               Loop over entered number of samples
while i<=nsample
%               Output message to user
  disp(['Enter slice number ',num2str(i)]);
%               Request user input in command window
  slices(i)=input('-> ');
%               If out of range, re-enter
  if(slices(i)>nslice || slices(i)<=0)
    disp(['Please enter value between 1 and ',num2str(nslice)]);
    i=i-1;
  end
  i=i+1;
end
end
```

```
%-------------------------------------------------------------------------
%NAME
%  applydisps.m
%PURPOSE
%  Applies the displacements to each slice and stores in a 3-D matrix
%ACRONYM
%  APPLY_DISPlacementS
%DESCRIPTION
%  This function takes the transformation matrix (alldisps) and
%  applies it to the original image (tin) to create the new image
%  matrix (newimg). The   image is also cropped to remove black
%  regions generated by the transformation.
%AUTHORS
%  Louise Terry
%  Tom Bower
%-------------------------------------------------------------------------

function newimg=applydisps(alldisps,width,height,nslice,tin)
%               largest displacement below original
lgblw = min(alldisps(:));
%               largest displacement above original
lgabv = max(alldisps(:));
%               Set the size of image depending on smallest and
%               largest displacement
newheight = height + lgabv - lgblw;
%               loop over slices
for islice=1:nslice
  disp(['processing slice ' num2str(islice) ' of ' num2str(nslice)]);
%               Get the displacements for the current slice
  d=alldisps(islice,:);
%               Set next slice
  setDirectory(tin,islice);
%               Get the image matrix from the current slice
  img=tin.read;
%               Apply displacements to current slice
  newslice=imgproc(img,d,width,height,newheight,lgabv);
%               Store current slice in 3-D matrix which will form the
%               new image
  newimg(:,:,islice)=newslice;
end
end
```

```
%-------------------------------------------------------------------------
%NAME
%  imgproc.m
%PURPOSE
%  Applies displacements to a single slice
%ACRONYM
%  IMaGe_PROCess
%DESCRIPTION
%  This function takes the displacements for a single slice (d) and
%  applies them to a single slice. lim1 and lim2 are the new limits
%  for the top and bottom of each column, the original column is moved
%  to between these limits.
%AUTHORS
%  Louise Terry
%  Tom Bower
%-------------------------------------------------------------------------

function newimg=imgproc(im8,d,width,height,newheight,lgabv);
%               Set size of new matrix
newimg=zeros(newheight,width);
%               Apply the vertical displacement
%               Loop over each column, then apply the displacement to
%               the entire height
for iw=1:width
%               Set lower limit
  lim1 = lgabv-d(iw)+1;
%               Upper limit is the lower limit plus the image height
  lim2 = lim1+height-1;
%               Place the column from the original slice (im8) and
%               place between the limits in the new image
  newimg(lim1:lim2,iw)=im8(1:height,iw);
end
%               Scale colour values for greyscale
newimg=newimg-min(min(newimg,[],1));
newimg=newimg/max(max(newimg,[],1));
end
```

```
%-------------------------------------------------------------------------
%NAME
%  sampleddisps.m
%PURPOSE
%  Gets displacements for each sampled slice
%ACRONYM
%  SAMPLED_DISPlacementS
%DESCRIPTION
%  This function loops over each sample slice and uses the 'disp'
%  function to interpolate within each slice.
%AUTHORS
%  Louise Terry
%  Tom Bower
%-------------------------------------------------------------------------
function sampled =
sampleddisps(tin,slices,nslice,nsample,width,height)
%               Initialise displacements (ds) to zero
ds(1:nsample,1:width)=0;
%               Loop over each sample image
for isample=1:nsample
%               Store the slice number
  slice=slices(isample);
%               Set the next slice
  setDirectory(tin,slice);
%               Get the current slice
  im=tin.read;
%               Call disps fucntion to get displacements for current
%               slice
  d=disps(im,width,height);
%               Store in displacement matrix ds
  sampled(isample,1:width)=d(1:width);
end
end
```

```
%-------------------------------------------------------------------------
%NAME
%  disps.m
%PURPOSE
%  Gets displacements for one sampled slice
%ACRONYM
%  DISPlacementS
%DESCRIPTION
%  This takes user clicks for a given slice, and interpolates a
%  polynomial using a fourth order regression
%AUTHORS
%  Louise Terry
%  Tom Bower
%-------------------------------------------------------------------------
function d=disps(img,width,height)
%               Initialise displacement vector
d=zeros(width,1);
%               Get mouse clicks
[x,y]=clicks(img);
%               Get number of clicks
nclicks=size(x,1);
%               Order of curve fitting algorithm
order=4;
%               Curve fitting between points
p=polyfit(x,y,order);
%               Set up x linear spaced array for each column
x1=linspace(1,single(width),single(width));
%               Convert the polynomial into an array of ordinates
f1=polyval(p,x1);
%               Use the midpoint as a datum for all displacements
y0=height/int64(2);
%               Convert to vertical displacement
d=int64(f1)-y0;
end
```

```
%-------------------------------------------------------------------------
%NAME
%  clicks.m
%PURPOSE
%  Gets x-y coordinates of user clicks for one slice
%ACRONYM
%  CLICKS
%DESCRIPTION
%  This function displays a slice, then records user clicks on the
%  image.
%AUTHORS
%  Louise Terry
%  Tom Bower
%-------------------------------------------------------------------------
function [x,y]=clicks(img)
%               Display original image
imageHandle=imshow(img);
%               Get mouse clicks from user until Return key pressed
[x,y]=ginput;
%               Close the image
close;
end
```

```
%-------------------------------------------------------------------------
%NAME
%  alldisp.m
%PURPOSE
%  Interpolates the displacements between sampling slices
%ACRONYM
%  ALL_DISPlacementS
%DESCRIPTION
%  This function interpolates the displacements between each sampled
%  slice for every column in turn. A second order polynomial
%  regression is used here.
%AUTHORS
%  Louise Terry
%  Tom Bower
%-------------------------------------------------------------------------
function alldisps=alldisp(width,nslice,slices,nsample,sampled)
%               loop over each column 1-> 512
for icol=1:width
%               Convert to single precision (required for polyfit)
%               X values
    x=single(slices');
%               Displacements for column
    y=single(sampled(:,icol));
%               Order of polynomial interpolation algorithm
    order=2;
%               Interpolate displacements between slices
    p=polyfit(x,y,order);
%               Set up x array for displacement curve
    x1=linspace(1,single(nslice),single(nslice));
%               Get displacement for each x1 value
    f1=polyval(p,x1);
%               Store displacements in alldisps
    alldisps(:,icol)=int64(f1);
end
end
```

```
%-------------------------------------------------------------------------
%NAME
%  saveimg.m
%PURPOSE
%  Saves the final processed image to a file
%ACRONYM
%  SAVE_IMaGe
%DESCRIPTION
%  The input for this function is a three dimensional matrix
%  containing the greyscale pixel values (newimg). This function
%  writes the image to a stacked TIFF file. The first slice is saved
%  as a new image, hence use of the 'Overwrite' tag; all slices
%  thereafter simply 'Append' to the image to generate the new stack.
%AUTHORS
%  Louise Terry
%  Tom Bower
%-------------------------------------------------------------------------

function saveimg(newimg,nslice,tin,ofile)
%               Loop over each slice
for islice = 1:nslice
%               Provide some output to the user
  disp(['saving slice ' num2str(islice) ' of ' num2str(nslice)]);
%               Set the active slice to 'islice'
  setDirectory(tin,islice);
%               Store 2D slice into 'newslice'
  newslice(:,:) = newimg(:,:,islice);
  if islice==1
%               For the first slice only, allow overwriting of
%               previously flattened file
    imwrite(newslice,ofile,'tif','WriteMode','Overwrite',
'compression','none');
  else
%               For subsequent slices, add each slice to the stack
    imwrite(newslice,ofile,'tif','WriteMode','Append',
'compression','none');
  end
end
end
```

C – Image quality grading instructions

Task

You will be presented with 135 macular OCT en-face images of the choroid of several individuals. These images will be of the central 3° of choroid, centred on the fovea. Please assess each image on the two grading criteria explained below. Try to assess each image as a whole, rather than concentrating on individual vessels.

We will start with 5 test images; these are to allow you to familiarise yourself with the images, and your grades for these will not be used. These test images are a cover a range of good and poor quality images.

After every 10 images, you will be presented with a blank frame. This allows you time for a short break, and to check that you are in the correct place on your record sheet.

Grading Criteria

1. Overall contrast of the image

This is the difference in luminance between the vessels (dark) and the surrounding tissue (light). A bigger difference in luminance scores a good grade, whereas a small difference in luminance scores a poor grade (see below for grading scale).

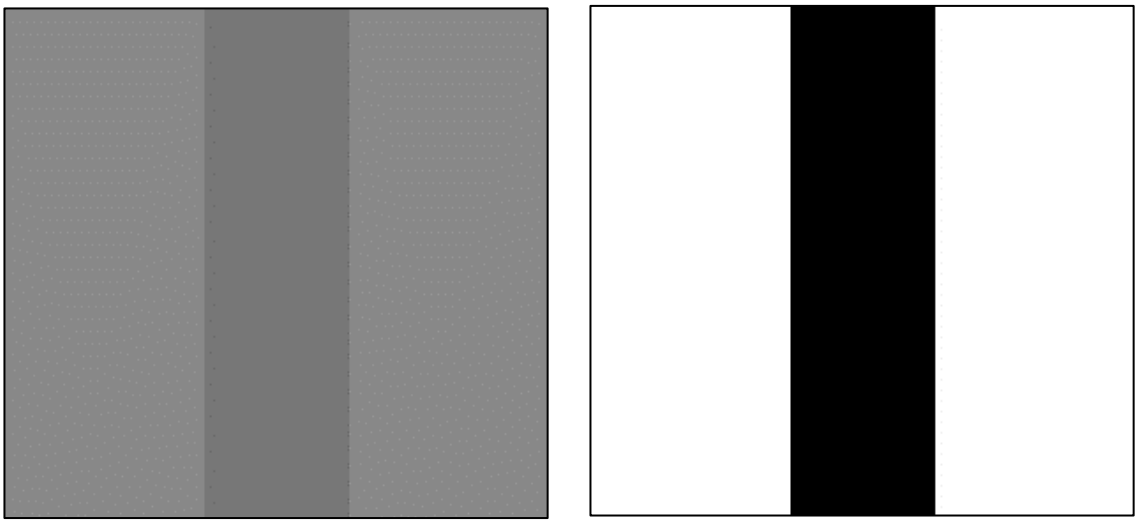

The example above shows poor contrast (left) and excellent contrast (right).

2. Overall edge definition of the vessels

This is how distinct the edges of the vessels appear in the image. A sharp, distinct edge scores a good grade, whereas a blurred, indistinct edge scores a poor grade.

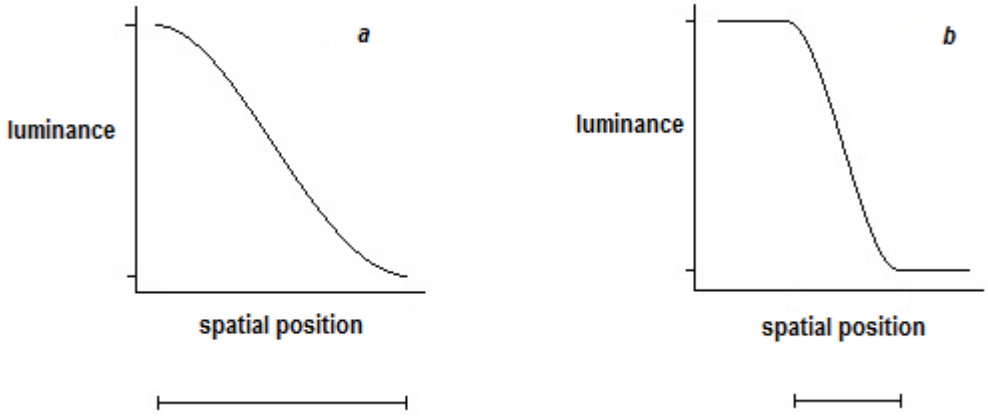

The diagram above shows luminance profiles for 2 different edges. Edge (*a)* has a more gradual change in luminance than Edge (*b)*. They both undergo the same change in luminance, therefore have the same contrast, but Edge (*b)* is more clearly defined than Edge (*a)*.

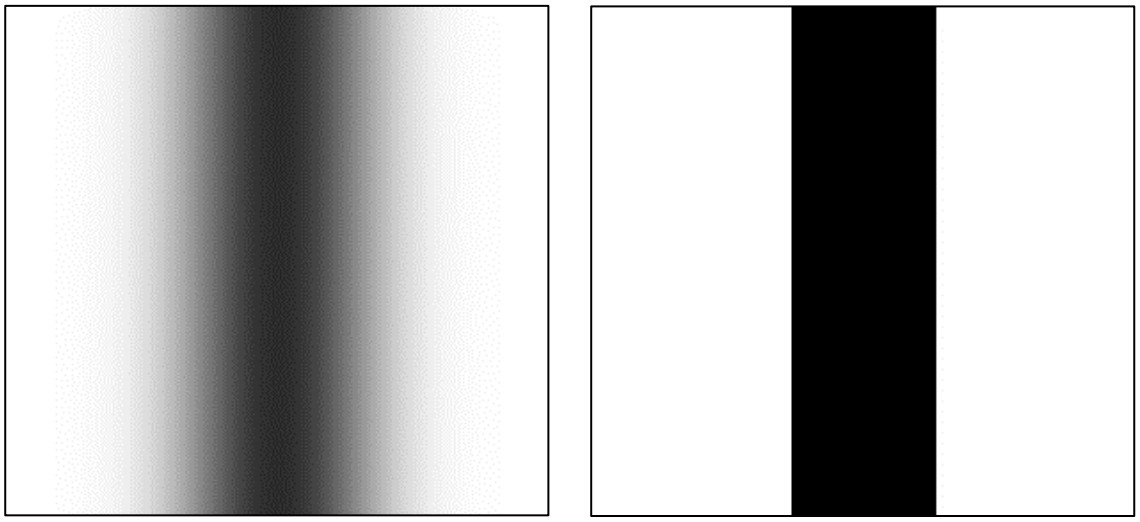

The example above shows poorly-defined edges (left) and well-defined edges (right).

Grading Scale

Each of the criteria listed above will be graded on a scale of 1 to 5, as follows:

1. Poor
2. Restricted
3. Sufficient
4. Good
5. Excellent

Please record a grade (1-5) for the each of the three criteria, for each image presented, on the grading sheet provided.

D – Participant information sheet and consent form

Participant Information Sheet

An In vivo investigation of choroidal vasculature in Age-related Macular Degeneration (Study A)

We would like to invite you to take part in our research study. Before you decide, we would like you to understand why the research is being done and what it would involve for you. Please take the time to read this information sheet, feel free to talk to others about the study if you wish. Prior to beginning the study we will go through the information sheet with you and answer any questions you may have. Ask us if there is anything that is not clear.

It is up to you to decide to join the study. If you agree to take part, we will then ask you to sign a consent form. You are free to withdraw at any time, without giving a reason. This would not affect the usual care that you receive.

The following information sheet has two parts as follows:

Part 1 *tells you the purpose of this study and what will happen if you take part.*

Part 2 *gives you more detailed information about the conduct of the study.*

PART 1

What is this study about?

Age-related Macular Degeneration (AMD) is a common eye condition that mostly affects those aged 55 and over. AMD affects the retina at the back of the eye responsible for detailed vision which can affect the ability to carry out activities such as reading, driving and recognising familiar faces.

Many affected individuals only develop early AMD with only some ageing changes visible at the back of the eye and often do not experience any change to their vision. However these individuals, particularly with increasing age, are at greater risk of developing more advanced types of AMD. In some individuals new blood vessels can grow beneath the retina, this is known as "Wet" or neovascular AMD, which can cause a loss of vision but may be treated if detected quickly. In other individuals both the blood vessels and overlying retina may slowly degenerate leading to a gradual loss of vision, often over many years.

We are carrying out research to improve our understanding of AMD and in particular how changes to the blood vessels beneath the retina contribute to the disease. We aim to use the results of this research to help us develop tests that can identify and monitor those at most risk of advanced AMD. To do this we are looking for people **with** (both early and advanced) AMD and **without** AMD to help us with this research.

How will we find these things out?

This study will also use a new clinical technique to take a detailed three-dimensional photograph of the back of the eye. These images will allow us to see and measure the individual layers of cells which make up the retina and the blood vessels beneath. We would like to see people **with** and **without** AMD to allow comparison.

What will happen to me if I take part?

If you decide to volunteer for this study, we will ask you to give up approximately **1 hour and a half** of your time. The study will take place in the School of Optometry and Vision Sciences on Maindy Road.

Firstly we will collect some background information about your eyes and give you an opportunity to ask any questions about the research. We will then assess different aspects of your vision and examine the front and back of your eyes, using tests and techniques found in everyday optometric practice. We will also perform a quick blood pressure check**,** and check the pressure in your eyes using a small puff of air (you may remember this from visits to the optician). We will then put some drops into your eyes (Tropicamide*) to enlarge the pupils before taking the 3-D photographs of the back of your eyes. If you are interested we will be happy to show the completed image(s) to you.

You will be asked not to drink tea or coffee on the day of the visit, prior to the session. This is to minimise the potential effect that caffeine has on the circulation of the eye.

*If you have a known allergy to Tropicamide or other dilating drops, please inform one of the investigators and you should not particpate in the study.

Are there any risks involved?

This study is very safe, however the drops that enlarge the pupil may make your vision temporarily a little blurred and more sensitive to bright lights, these effects can last for about 6 hours. During this time we advise you not to drive or to operate any dangerous machinery. You may find that the drops sting slightly when they go in, this is normal and the stinging wears off quickly. The drops have been known to, on the very rare occasion, cause closed-angle glaucoma, resulting in red and sore eyes a few hours after putting in the eye drops. In the extremely unlikely event that this should occur you should contact any of us on the numbers shown below (we are all registered optometrists). If however we are unavailable then you should attend eye casualty for assessment.

If you are taking part in any other research projects, please inform one of the investigators and you should not participate in this study.

Is this the same as having an 'eye test' with my own optometrist or optician?

No. This does not replace any examination by your regular optometrist (optician). Everybody should have regular check-ups with their optician at least every two years.

What are the possible disadvantages of taking part?

If the researchers discover anything that indicates you should see another eye specialist or your GP, they will explain why and write to your GP with your permission, but remember this is not a complete eye examination and does not replace regular appointments with your ophthalmologist and optometrist.

What are the possible benefits of taking part?

There are no intended benefits.

Do I have to take part?

No – it is up to you whether you decide to take part or not. Participation in this study is purely voluntary and you will receive £20 towards your expenses. If you do decide to take part, you will be given this information sheet to keep and be asked to sign a consent form. You can withdraw at any time without giving a reason. Please note that if you do not wish to take part in the study it will not affect your current or future care.

What if there is a problem?

If you do have a concern about any aspect of this study, you should ask to speak to the researchers (contact details below) who will do their best to answer your questions. If you remain unhappy and wish to complain formally, you can do this through the Cardiff University Complaints Procedure – details can be obtained from the researchers.

What if I have any questions?

Please ask. We are very happy to discuss any aspect of the study.

Miss Louise Terry	E-mail: TerryL1@cardiff.ac.uk	Tel: (029) 20870247
Dr Ashley Wood	E-mail: WoodA2@cardiff.ac.uk	Tel: (029) 20875063
Prof Rachel North	E-mail: North@cardiff.ac.uk	Tel: (029) 20875114
Dr Tom Margrain	E-mail: MargrainTH@cardiff.ac.uk	Tel: (029) 20876118

School of Optometry & Vision Sciences
College of Biomedical and Life Sciences
Cardiff University
Maindy Road
Cardiff
CF24 4HQ

PART 2

What will happen if I don't want to carry on with the study?

The study will usually require only a single visit to the School of Optometry and you are free to withdraw at any time without giving a reason; however we will retain non identifiable data collected up to your withdrawal. Please note that if you do not wish to take part in the study it will not affect your current or future care.

What if there is a problem?

In the unlikely event that harm should occur as a result of negligence, cover is provided by the Cardiff University insurance policy.

Will my taking part in this study be kept confidential?

All information collected during the study will be processed and stored securely by the researchers using password-protected systems. Your personal information will be coded and only the researchers will be able to identify you during the study. When the study is over, the data may be retained for use in future studies, but will be anonymous from this point. All procedures are compliant with the Data Protection Act 1998.

What will happen to the results of the research study?

The study results will be analysed and presented at national and international meetings, as well as comprising part of a PhD thesis. A copy of the thesis will eventually be held in Cardiff University's Bute Library. Identities of participating volunteers will not be revealed in any resulting published material. If you wish to be provided with a summary of the research findings at the end of the study please tick the appropriate box on the consent form.

Who is organising and funding the research?

This study is funded by Cardiff University.

Who has reviewed the study?

This study was reviewed and approved by the South East Wales Research Ethics Committee.

School of Optometry & Vision Sciences
College of Biomedical and Life Sciences
Cardiff University
Maindy Road
Cardiff
CF24 4HQ

Study Number:

Patient Identification Number for this trial:

CONSENT FORM

Title of Project: **An In vivo investigation of choroidal vasculature in Age-related Macular Degeneration (Study A)**

Name of Researcher: **Miss Louise Terry**

Please initial all boxes

1. I confirm that I have read and understand the information sheet dated Jun2015 (version A5) for the above study. I have had the opportunity to consider the information, ask questions and have had these answered satisfactorily. ☐

2. I understand that my participation is voluntary and that I am free to withdraw at any time without giving any reason, without my medical care or legal rights being affected. ☐

3. I understand that relevant sections of my medical notes and data collected during the study, may be looked at by individuals from Cardiff University, from regulatory authorities or from the NHS Trust, where it is relevant to my taking part in this research. I give permission for these individuals to have access to my records. ☐

4. I agree to my GP being informed of my participation in the study. ☐

5. I agree to take part in the above study. ☐

6. I would like to receive a summary of the research findings at the end of the study. ☐

Name of participant	Date	Signature
Name of person taking consent	Date	Signature

E – MATLAB code to establish inter-observer agreement of manual choroidal segmentation

```
%-------------------------------------------------------------------------
%NAME
%  imageoverlap.m
%PURPOSE
%  Establishes percentage overlap between two labelled regions of
%  interest
%DESCRIPTION
%  This function loads two sets of labelled regions of interest and
%  calculates the area of overlap as a percentage of the total area
%  contained within the two regions. The regions are also displayed
%  graphically.
%  Inputs 'labs1'and 'labs2' are the names of files containing the
%  choroidal labels. 'islice' is an integer which selects the slice
%  number within the volume to use.
%AUTHOR
%  Dafydd Ravenscroft
%-------------------------------------------------------------------------

function imageoverlap(labs1, labs2, islice)
%               Load two sets of labels defining the region of
%               interest
labels1=load(labs1);
labels2=load(labs2);
%               Select the slice number in the volume
slice1=islice;
slice2=slice1;
%               Ensure all values are of the same type
for i=1:length(labels1.labelAll)
    labels1.labelAll{i,1}=uint16(labels1.labelAll{i,1});
end
for i=1:length(labels2.labelAll)
    labels2.labelAll{i,1}=uint16(labels2.labelAll{i,1});
end
%               Create a mask from the labels
x1=labels1.labelAll{cell2mat(labels1.labelAll(:,1))==slice1,3}(:,1);
y1=labels1.labelAll{cell2mat(labels1.labelAll(:,1))==slice1,3}(:,2);
x2=labels2.labelAll{cell2mat(labels2.labelAll(:,1))==slice2,3}(:,1);
y2=labels2.labelAll{cell2mat(labels2.labelAll(:,1))==slice2,3}(:,2);
%               Convert cell array to ordinary array
x1=cell2mat(x1);
y1=cell2mat(y1);
x2=cell2mat(x2);
y2=cell2mat(y2);
%
x1(length(x1)+1)=x1(1);
y1(length(y1)+1)=y1(1);
x2(length(x2)+1)=x2(1);
y2(length(y2)+1)=y2(1);
%               Plot both regions of interest
plot(x1,y1);
hold on;
plot(x2,y2);
%               Convert region of interest polygon to region mask
Image1=poly2mask(x1,y1,1024,512);
Image2=poly2mask(x2,y2,1024,512);
%               Create overlap of the two regions
overlapImage = Image1 & Image2;
%               Count number of common pixels
numOverlapPixels = nnz(overlapImage);
%               Count number of pixels in each region
```

```
numPixels1=nnz(Image1);
numPixels2=nnz(Image2);
%               Calculate percentage overlap of the two regions
ImgOverlap=100*numOverlapPixels/numPixels1+numPixels2-
numOverlapPixels);
%               Display percentage image overlap
fprintf('Image overlap is %.1f%% \n',ImgOverlap);
end
```

F – Supplementary machine learning results

10-fold cross-validation

Table 1 Confusion matrix for 10-fold cross-validation of K-nearest neighbour (KNN).

KNN (%)		Clinical classification		
		Healthy	Early AMD	nAMD
Algorithmic prediction	Healthy	97.3	3.4	3.1
	Early AMD	0.9	94.6	4.0
	nAMD	1.8	1.9	92.9

Table 2 Confusion matrix for 10-fold cross-validation of random forest (RFS).

RFS (%)		Clinical classification		
		Healthy	Early AMD	nAMD
Algorithmic prediction	Healthy	90.9	5.6	4.5
	Early AMD	3.7	85.1	3.8
	nAMD	5.4	9.2	91.7

Table 3 Confusion matrix for 10-fold cross-validation of support vector machine (SVM).

SVM (%)		Clinical classification		
		Healthy	Early AMD	nAMD
Algorithmic prediction	Healthy	98.6	0.8	0.5
	Early AMD	0.6	97.9	1.1
	nAMD	0.8	1.3	98.4

2-fold cross-validation

Table 4 Confusion matrix for 2-fold cross-validation of K-nearest neighbour (KNN).

KNN (%)		Clinical classification		
		Healthy	Early AMD	nAMD
Algorithmic prediction	Healthy	96.7	3.9	3.8
	Early AMD	1.2	93.8	4.8
	nAMD	2.1	2.4	91.4

Table 5 Confusion matrix for 2-fold cross-validation of random forest (RFS).

RFS (%)		Clinical classification		
		Healthy	Early AMD	nAMD
Algorithmic prediction	Healthy	88.3	7.0	5.0
	Early AMD	5.4	81.7	4.9
	nAMD	6.3	11.3	90.2

Table 6 Confusion matrix for 2-fold cross-validation of support vector machine (SVM).

SVM (%)		Clinical classification		
		Healthy	Early AMD	nAMD
Algorithmic prediction	Healthy	97.7	1.2	0.7
	Early AMD	1.1	96.7	1.7
	nAMD	1.2	2.1	97.6

Table 7 Confusion matrix for 2-fold cross-validation per b-scan of convolutional neural network (CNN).

CNN (%)		Clinical classification		
		Healthy	Early AMD	nAMD
Algorithmic prediction	Healthy	100.0	0.0	0.1
	Early AMD	0.0	99.6	0.5
	nAMD	0.0	0.3	99.3

Leave-one-out cross-validation (LOOCV)

Table 8 Confusion matrix for LOOCV of K-nearest neighbour (KNN).

KNN (%)		Clinical classification		
		Healthy	Early AMD	nAMD
Algorithmic prediction	Healthy	40	32	24
	Early AMD	32	48	28
	nAMD	28	20	48

Table 9 Confusion matrix for LOOCV of random forest (RFS).

RFS (%)		Clinical classification		
		Healthy	Early AMD	nAMD
Algorithmic prediction	Healthy	56	24	0
	Early AMD	28	44	20
	nAMD	16	32	80

Table 10 Confusion matrix for LOOCV of support vector machine (SVM).

SVM (%)		Clinical classification		
		Healthy	Early AMD	nAMD
Algorithmic prediction	Healthy	40	16	8
	Early AMD	36	60	20
	nAMD	24	24	72

Table 11 Confusion matrix for LOOCV of convolutional neural network (CNN).

CNN (%)		Clinical classification		
		Healthy	Early AMD	nAMD
Algorithmic prediction	Healthy	25.0	37.5	33.3
	Early AMD	41.7	25.0	33.3
	nAMD	33.3	37.5	33.3

PLOS ONE

RESEARCH ARTICLE

Automated Retinal Layer Segmentation Using Spectral Domain Optical Coherence Tomography: Evaluation of Inter-Session Repeatability and Agreement between Devices

Louise Terry[1], Nicola Cassels[1], Kelly Lu[1], Jennifer H. Acton[1], Tom H. Margrain[1], Rachel V. North[1], James Fergusson[1,2], Nick White[1,2], Ashley Wood[1]*

1 School of Optometry and Vision Sciences, Cardiff University, Cardiff, United Kingdom, **2** Vision Science Bioimaging Labs, Cardiff University, Cardiff, United Kingdom

* wooda2@cardiff.ac.uk

Citation: Terry L, Cassels N, Lu K, Acton JH, Margrain TH, North RV, et al. (2016) Automated Retinal Layer Segmentation Using Spectral Domain Optical Coherence Tomography: Evaluation of Inter-Session Repeatability and Agreement between Devices. PLoS ONE 11(9): e0162001. doi:10.1371/journal.pone.0162001

Editor: Marinko Sarunic, Simon Fraser University, CANADA

Received: April 5, 2016

Accepted: August 16, 2016

Published: September 2, 2016

Data Availability Statement: All images, metadata and associated segmentation data files are available from the Figshare (https://figshare.com/) database (DOI: https://dx.doi.org/10.6084/m9.figshare.c.3286643.v1).

Funding: This work was funded by Cardiff University. VSBL acknowledges the Medical Research Council and School of Optometry and Vision Sciences for support.

Abstract

Retinal and intra-retinal layer thicknesses are routinely generated from optical coherence tomography (OCT) images, but on-board software capabilities and image scaling assumptions are not consistent across devices. This study evaluates the device-independent Iowa Reference Algorithms (Iowa Institute for Biomedical Imaging) for automated intra-retinal layer segmentation and image scaling for three OCT systems. Healthy participants (n = 25) underwent macular volume scans using a Cirrus HD-OCT (Zeiss), 3D-OCT 1000 (Topcon), and a non-commercial long-wavelength (1040nm) OCT on two occasions. Mean thickness of 10 intra-retinal layers was measured in three ETDRS subfields (fovea, inner ring and outer ring) using the Iowa Reference Algorithms. Where available, total retinal thicknesses were measured using on-board software. Measured axial eye length (AEL)-dependent scaling was used throughout, with a comparison made to the system-specific fixed-AEL scaling. Inter-session repeatability and agreement between OCT systems and segmentation methods was assessed. Inter-session coefficient of repeatability (CoR) for the foveal subfield total retinal thickness was 3.43μm, 4.76μm, and 5.98μm for the Zeiss, Topcon, and long-wavelength images respectively. For the commercial software, CoR was 4.63μm (Zeiss) and 7.63μm (Topcon). The Iowa Reference Algorithms demonstrated higher repeatability than the on-board software and, in addition, reliably segmented all 10 intra-retinal layers. With fixed-AEL scaling, the algorithm produced significantly different thickness values for the three OCT devices ($P<0.05$), with these discrepancies generally characterized by an overall offset (bias) and correlations with axial eye length for the foveal subfield and outer ring ($P<0.05$). This correlation was reduced to an insignificant level in all cases when AEL-dependent scaling was used. Overall, the Iowa Reference Algorithms are viable for clinical and research use in healthy eyes imaged

Competing Interests: The authors have declared that no competing interests exist.

with these devices, however ocular biometry is required for accurate quantification of OCT images.

Introduction

Optical coherence tomography (SD-OCT) is an essential imaging tool for the diagnosis and monitoring of retinal diseases such as age-related macular degeneration (AMD) [1,2] and diabetic macular oedema [3,4]. This non-invasive technique allows clinicians to produce three-dimensional (3-D) images of intraocular structures *in vivo*. In addition to subjective qualitative assessment, images can be analyzed objectively, providing quantitative measurements including retinal thickness. Such metrics are commonly used clinically and as outcome measures in research, for example in clinical trials [5,6]. Quantitative analysis of OCT images has become increasingly sophisticated [7,8] as image quality and software capabilities improve.

Whilst manual caliper tools and hand segmentation (hand tracing of intra-retinal layer boundaries) can be simple to perform, it is time consuming (particularly when implemented in 3-D scans) and subject to significant inter-observer variation [9]. These methods are therefore not feasible for use clinically or in large, multi-center clinical trials.

Commercial OCT devices are generally supplied with on-board segmentation software, designed to generate fast, reliable values for interpretation by clinicians. This software has historically been limited to total retinal thickness. Additionally, the definition of the retinal boundaries varies between manufacturers, with different reflective bands, as seen in OCT images, being chosen to represent the posterior retinal margin. This makes quantitative retinal thickness comparisons between commercial devices difficult [10]. Some instruments, such as the Topcon DRI OCT-1 Atlantis (Topcon Corp, Tokyo, Japan) and the latest Spectralis OCT (Heidelberg Engineering, Heidelberg, Germany), are now supplied with software that is capable of segmenting a number of intra-retinal layers. Furthermore, the commercial software is almost always limited to use with images captured by the parent device, and cannot be applied to images from other OCT devices. The diversity of segmentation methods and normative values confound comparisons between commercial systems [11–13].

OCTSeg is a module of OCT Explorer, itself part of the Iowa Reference Algorithms (Retinal Image Analysis Lab, Iowa Institute for Biomedical Imaging, Iowa City, IA). It is a publicly available, device-independent, graph theory-based tool for segmentation of 10 retinal layers in volumetric OCT images [7,14,15]. It produces retinal thickness values comparable to manual measurements of OCT images by retinal specialists [14,16], and to analysis by the Heyex software (Heidelberg Engineering) of images from participants with diabetic macular oedema [17]. Unlike the majority of commercial software, it can be applied to images from all widely-available clinical OCT devices, allowing direct comparison of images from multiple devices.

Since the segmentation software may be used with images from several different OCT instruments, it is important to establish agreement between devices. The majority of current devices utilize broad-band light sources with centre wavelengths (λ_c) of ~850nm, but longer wavelength OCT (λ_c ~1040nm) has recently become commercially available. The algorithm may perform differently on these images, due to differences in reflectivity of retinal layer boundaries at these wavelengths. We used a non-commercial long-wavelength OCT (λ_c ~1040nm) in our evaluation of the algorithm.

Based on the work of Littmann and others [18,19], the transverse size of any retinal feature can be calculated using the appropriate ocular biometry and instrument meta-data. A reasonably

accurate lateral scaling (converting feature sizes from pixels to microns) of any OCT image can be determined using (i) an estimate of the principal plane to retina distance of the eye (axial eye length (AEL) - 1.8mm), (ii) the angle of the OCT scan in air and (iii) an estimate of the bulk ocular refractive index. The on-board software of the two commercial instruments used in this study provide only a single lateral scaling value for all patients regardless of AEL, resulting in an error in the reported size of the image which scales with AEL. This error manifests as a discrepancy between the fixed size ETDRS grid and the AEL-dependent image size. Therefore, the position of retinal layer measurements and hence the regional thickness values become AEL-dependent; an important consideration when comparing different OCT instruments. By converting all our image files to a compatible TIFF format we were able to use the ability of OCTExplorer to accept an independently calculated, AEL-dependent lateral scaling for images from all devices used.

To the authors' knowledge, inter-session repeatability of the Iowa Reference Algorithms has not been assessed to date. Given the potential clinical and research utility of quantitative intra-retinal layer analysis [20–22], investigation of this feature of the algorithm is a key step in validating the sensitivity of this tool to detect retinal changes. Furthermore, to our knowledge, there has been no formal comparison between retinal thickness measurements produced by the Iowa algorithm and the on-board segmentation algorithms of many commonly available commercial devices.

The aims of the present study are to evaluate the use of Iowa Reference Algorithms as a means of generating repeatable intra-retinal layer thickness values from images of healthy eyes, captured using two commercial SD-OCT devices (λ_c ~850nm) and one non-commercial long-wavelength (λ_c ~1040nm) device. Secondary objectives are to assess agreement between the algorithm and commercial, device-dependent software, as well as inter-device agreement.

Materials and Methods

Participants

Healthy participants (n = 25) were recruited from staff, students and volunteers at the School of Optometry and Vision Sciences, Cardiff University. All participants had a corrected visual acuity of 0.0 logMAR (20/20) or better using a high contrast Early Treatment of Diabetic Retinopathy Study (ETDRS) chart and a mean refractive error of $\leq \pm 6.00$ diopters in the test eye. Approval for this study was obtained from the South East Wales NHS Research Ethics Committee. All experimental procedures adhered to the tenets of the Declaration of Helsinki, and written informed consent was obtained before data collection commenced.

Participants with disease affecting retinal function were excluded, including diabetes, glaucoma, and significant media opacities (Lens Opacities Classification System III grade 3 or more for any criteria [23]). These were identified using a medical history questionnaire, slit lamp examination and fundus photography. Those with narrow iridocorneal angles (grade 1 or less assessed by Van Herick) or intraocular pressure over 21mmHg were also excluded, as were those taking medication known to affect retinal function.

One eye was selected as the test eye for each participant; this was the eye with the better visual acuity (or lower refractive error if one eye was outside the ±6.00D range). One drop of Tropicamide 0.5% was instilled into the test eye of each participant prior to imaging. Following sufficient pupil dilation, fundus photographs were obtained to ensure participants did not have retinal disease. AEL (cornea to retinal pigment epithelium (RPE)) was measured using optical biometry (IOL Master, Carl Zeiss, Jena, Germany) to enable accurate lateral scaling calculations for all OCT images.

OCT Imaging

OCT images were obtained from all participants using a 3D-OCT 1000 (Topcon Corp, Tokyo, Japan), Cirrus HD-OCT (Carl Zeiss Meditec, Inc., Dublin, CA), and a non-commercial long-wavelength (λ_c 1040nm) SD-OCT [24–26]. Images from the latter were obtained using less than the maximum permissible corneal exposure for unlimited duration at this wavelength (less than 5mW/cm^2 averaged over a 7mm pupil) [27].

Volume scans centered on the fovea were acquired using each device. For comparison, all images had a scan angle of 20° x 20°, comprising 512 x 128 A-scans. Following dilation, all images were obtained by a single trained operator (LT). A second session was conducted within 1 month, using the same protocol and scheduled for the same time of day as the previous session (± 30 minutes).

Data Analysis

Long-wavelength OCT images were exported to Fiji (Rasband; National Institute of Health, USA) [28] and underwent stack registration, using the Fiji plugin StackReg [29], to remove eye movement artefacts. Images were then exported to OCTExplorer 3.5. Images from the two commercial instruments were directly imported into the Iowa software, with no alteration when using the instrument-supplied scaling, or via conversion to a standard TIFF format (via Fiji) in order to apply an AEL-dependent lateral scaling.

Automated retinal layer segmentation using the Iowa Reference Algorithms was performed on all images. Mean retinal thickness values of 10 retinal layers were obtained on all images for the foveal subfield and the inner and outer rings of a standard ETDRS grid (shown in Fig 1). Total retinal thickness was also calculated, as the distance from the most anterior hyper-reflective line (corresponding to the inner limiting membrane; ILM) to the posterior of the outermost hyper-reflective line (corresponding to the outer boundary of RPE).

For all comparisons with the commercial software, the posterior retinal boundary used by the commercial segmentation was adopted in the Iowa Reference Algorithm segmentation (inner boundary of outer segment photoreceptor/RPE complex, and inner boundary of RPE for Topcon and Zeiss respectively; see Fig 1). These parameters will be referred to in this paper as 'equivalent retinal thicknesses'.

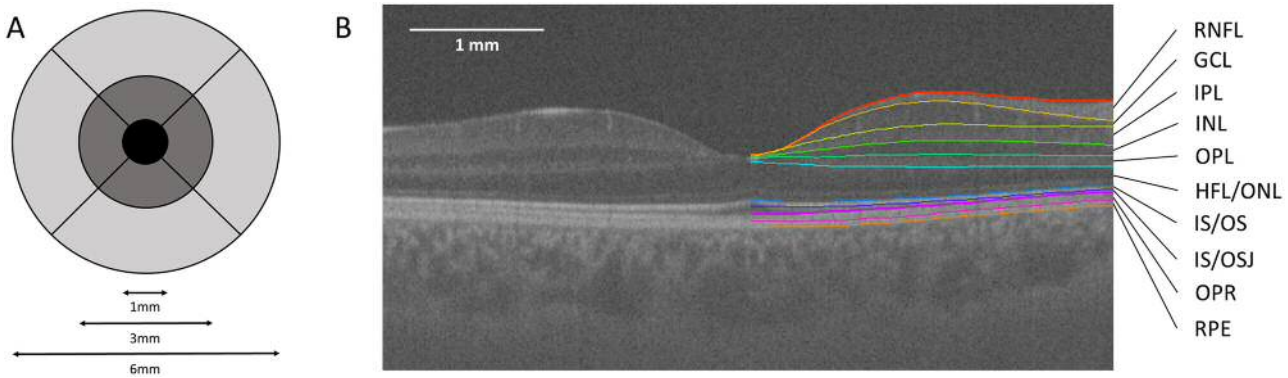

Fig 1. ETDRS grid and example 10 intra-retinal layer segmentation. (A) Standard ETDRS grid showing the foveal subfield (black). The inner ring is an average of the four parafoveal subfields (dark grey) and the outer ring of the four perifoveal subfields (light grey). (B) Screenshot of 10 layer (11 boundary) segmentation of a long-wavelength OCT image, produced by the Iowa Reference Algorithms. The left half of the image shows the image prior to segmentation. Layers 1–10 (top to bottom; as defined by the software): retinal nerve fiber layer (RNFL); ganglion cell layer (GCL); inner plexiform layer (IPL); inner nuclear layer (INL); outer plexiform layer (OPL); outer plexiform layer-Henle fiber layer to boundary of myoid and ellipsoid of inner segments (OPL-HFL ~ BMEIS); photoreceptor inner/outer segments (IS/OS); inner/outer segment junction to inner boundary of outer segment photoreceptor/retinal pigment epithelium complex (IS/OSJ ~ IB_RPE); outer segment photoreceptor/retinal pigment epithelium complex (OPR); retinal pigment epithelium (RPE).

doi:10.1371/journal.pone.0162001.g001

For images from the two commercial instruments, meta-data supplied by the manufacturer were used in determining lateral pixel size for analyses using the on-board software to show the importance of correct scaling. In all other cases, lateral scaling was obtained from the scan angle, measured AEL and an assumed bulk ocular refractive index of 1.336. Axial scaling of all images was obtained from the supplied instrument meta-data. This included a group refractive index for retinal tissue of 1.4, 1.38 and 1.36 for the long-wavelength, Topcon and Zeiss instruments respectively.

Coefficients of repeatability (CoR), a measure of repeatability familiar to clinicians [30], were used to assess the inter-session variations in retinal thickness values produced by both the Iowa Reference Algorithms and on-board software of each device (versions 3.51.003.04 and 7.0.1.290 for the Topcon and Zeiss instruments respectively). CoR was calculated as 1.96 times the standard deviation (SD) of the differences between sessions [31], and is also expressed as a percentage of the mean retinal layer thickness. Bland-Altman plots [31] were used to assess agreement between these segmentation methods, and for inter-device comparisons. The bias (mean difference) and 95% limits of agreement (LoA) were calculated for each comparison, and Friedman's two way ANOVA was used to identify statistically significance differences. In these comparisons, data points outside ±3 SD of the difference were defined as significant outliers (by Grubbs' test [32] for n = 25) and were excluded from the analysis. These were classified as failings of the segmentation algorithm.

The relationship between retinal thickness discrepancies using the commercial instrument scaling and the AEL-correct scaling for our long wavelength images vs measured AEL was evaluated using Spearman's rank correlation.

Results

Twenty-five eyes from 25 healthy participants were included in the study. The age range of the participants was 20 to 62 years (mean ± SD, 34.9 ± 13.5 years). Sixteen participants were female (64%). The mean AEL and refractive error (mean sphere) were 23.7 ± 1.3 mm (range 21.6 to 26.6) and -0.58 ± 1.93 diopters (range -4.50 to +3.00) respectively. The maximum cylindrical power was 3.00 diopters.

Lateral scaling for AEL

OCTSeg reported automated segmentation of 10 intra-retinal layers for all images. Mean values across all eyes for each retinal layer are shown in Table 1. These values underwent AEL-corrected lateral scaling as described above. The percentage difference of these corrected values from the fixed scaling values (by OCTSeg) ranged from -15% to +26% (corresponding to Topcon and Zeiss GCL layer respectively, both in the foveal subfield). Mean total retinal thickness measurements produced by both segmentation methods for the three devices can be seen in Table 2. These values underwent fixed-AEL scaling to allow comparison to the commercial software. In this case, correcting for AEL yielded mean differences of less than 2% in all cases when compared to the fixed-AEL scaling (by OCTSeg).

An inter-device comparison of AEL-corrected scaled retinal thickness measurements produced by the Iowa Reference Algorithms is shown in Table 3. One significant outlier was removed from the 1040nm-Topcon comparison (foveal subfield only). Images from the Topcon instrument yielded significantly higher values for retinal thickness than the long-wavelength system (Friedman test, $P<0.05$), but significantly lower values than the Zeiss OCT (with the exception of the foveal subfield). This bias between the Zeiss and long-wavelength OCT images was similar across the three ETDRS subfields. However, the bias between the Topcon

Table 1. Mean thickness of 10 intra-retinal layers. Thickness values (mean ± SD; μm) produced by segmentation of images at session 1 using the Iowa Reference Algorithms.

Layer	Fovea			Inner ring			Outer ring		
	Topcon	Zeiss	1040nm	Topcon	Zeiss	1040nm	Topcon	Zeiss	1040nm
1. RNFL	7.0 ± 2.3	5.9 ± 2.9	5.2 ± 2.2	25.5 ± 2.3	25.2 ± 2.3	24.2 ± 2.4	39.3 ± 7.0	40.9 ± 5.9	39.3 ± 5.0
2. GCL	17.0 ± 6.3	13.4 ± 5.4	17.2 ± 5.1	48.5 ± 5.9	52.4 ± 5.7	50.5 ± 6.2	24.7 ± 3.0	27.2 ± 3.1	29.3 ± 3.8
3. IPL	29.3 ± 2.9	27.5 ± 4.1	24.4 ± 4.2	42.5 ± 4.2	40.7 ± 3.5	39.9 ± 4.2	35.3 ± 2.8	37.3 ± 2.8	36.0 ± 3.8
4. INL	17.7 ± 4.6	22.5 ± 5.3	18.9 ± 4.2	37.8 ± 3.5	43.2 ± 3.8	37.5 ± 3.6	28.1 ± 3.3	32.9 ± 3.0	29.6 ± 3.3
5. OPL	23.0 ± 3.4	20.7 ± 4.9	20.3 ± 5.3	29.6 ± 3.8	28.0 ± 5.0	30.0 ± 5.1	26.2 ± 2.6	24.1 ± 3.0	28.4 ± 4.2
6. OPL-HFL ~BMEIS	120.8 ± 10.2	122.3 ± 9.2	116.5 ± 10.7	95.5 ± 8.8	96.9 ± 9.2	90.3 ± 8.8	79.7 ± 10.1	79.4 ± 6.4	71.6 ± 6.8
7. IS/OS	13.9 ± 0.9	11.7 ± 0.6	14.8 ± 2.4	12.6 ± 0.6	10.3 ± 0.4	13.7 ± 1.7	12.5 ± 1.2	10.2 ± 0.8	13.0 ± 1.7
8. IS/OSJ ~IB_OPR	17.0 ± 1.8	19.7 ± 2.2	17.3 ± 3.0	11.7 ± 1.4	14.0 ± 2.9	12.6 ± 2.4	10.3 ± 2.1	15.5 ± 4.3	15.8 ± 4.4
9. OPR	20.1 ± 2.6	20.7 ± 3.0	20.6 ± 3.8	19.8 ± 2.2	21.3 ± 3.3	20.7 ± 3.4	18.5 ± 2.3	17.8 ± 4.8	15.2 ± 3.8
10. RPE	18.6 ± 2.1	15.5 ± 0.5	15.6 ± 0.2	18.6 ± 1.7	15.5 ± 0.4	15.5 ± 0.2	18.6 ± 1.6	15.3 ± 0.5	15.5 ± 0.4

doi:10.1371/journal.pone.0162001.t001

Table 2. Total retinal thickness measurements from different segmentation methods. Thickness values (mean ± SD; μm) for the three ETDRS regions of images acquired at session 1.

		Fovea	Inner ring	Outer ring
Iowa Reference Algorithms	1040nm	270.9 ± *16.8*	335.2 ± *17.4*	294.0 ± *20.6*
	Topcon	281.5 ± *16.9*	342.8 ± *18.0*	295.2 ± *21.8*
	Zeiss	280.8 ± *17.5*	347.0 ± *18.0*	302.0 ± *21.4*
On-board segmentation	Topcon	244.6 ± *17.4*	306.0 ± *17.6*	260.9 ± *21.4*
	Zeiss	263.1 ± *17.4*	325.4 ± *18.1*	281.2 ± *21.4*
Iowa equivalent retinal thickness*	Topcon	242.8 ± *22.9*	304.4 ± *19.3*	258.0 ± *21.6*
	Zeiss	265.4 ± *18.6*	331.6 ± *18.7*	286.8 ± *21.6*

*Equivalent values from the Iowa Reference Algorithms (Topcon, ILM to inner boundary of OPR; Zeiss, ILM to inner boundary of RPE) are quoted for comparison to the commercial on-board software segmentation.

doi:10.1371/journal.pone.0162001.t002

and long-wavelength images decreases in magnitude with eccentricity (largest in the foveal subfield and smallest in the outer ring).

Discrepancies in fixed-AEL scaled retinal thickness measurements between the commercial and long-wavelength devices showed a strong correlation with AEL, for the commercial

Table 3. Agreement of total retinal thickness between OCT devices. Mean difference (bias; μm) and 95% limits of agreement (μm) for mean retinal thickness at session 1 produced by the Iowa Reference Algorithms, using AEL-dependent scaling, for each pairing of OCT instruments.

		Fovea	Inner ring	Outer ring
1040nm-Topcon	Mean difference	-14.18	-7.05	0.80
	Limits of agreement	*-20.05 to -8.30*	*-14.65 to 0.55*	*-6.95 to 8.55*
	Friedman test P	0.000*	0.000*	0.317
1040nm-Zeiss	Mean difference	-13.89	-12.46	-6.62
	Limits of agreement	*-21.62 to -6.16*	*-18.91 to -6.00*	*-13.53 to 0.30*
	Friedman test P	0.000*	0.000*	0.000*
Topcon-Zeiss	Mean difference	-0.21	-5.41	-7.42
	Limits of agreement	*-4.18 to 3.75*	*-8.67 to -2.15*	*-10.66 to -4.17*
	Friedman test P	0.841	0.000*	0.000*

*significant at 0.05 level.

doi:10.1371/journal.pone.0162001.t003

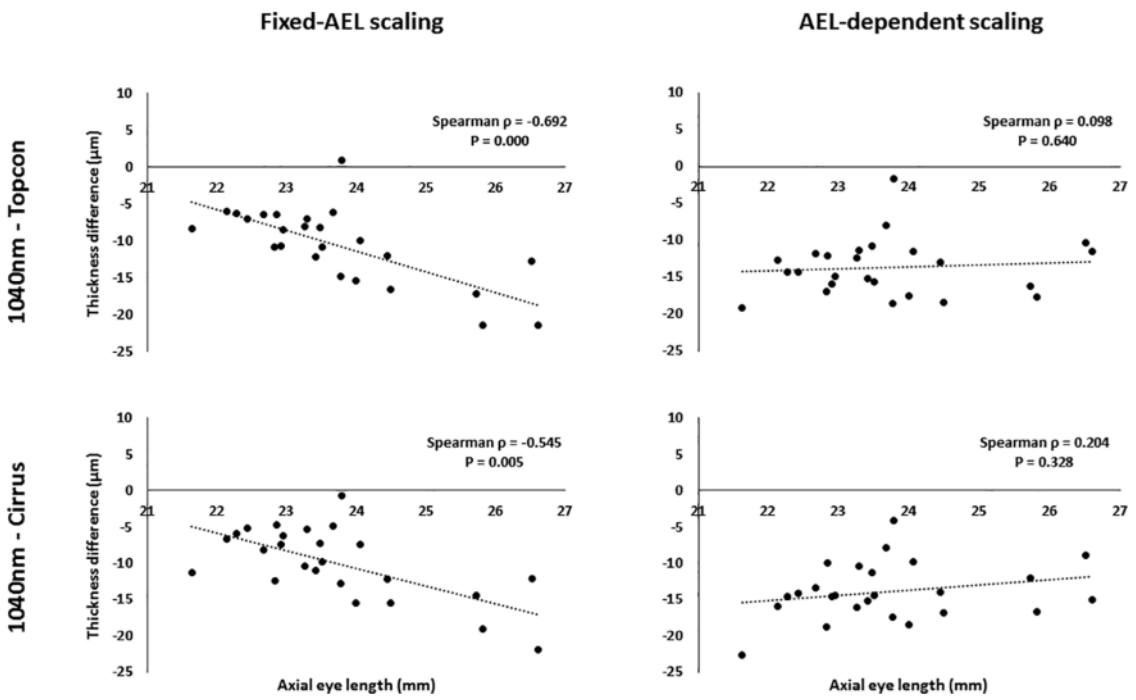

Fig 2. Correlation of retinal thickness differences against AEL. Difference in retinal thickness measurements (µm) versus axial eye length (mm) for the foveal subfield, as produced by the Iowa Reference Algorithms using two different transverse scaling methods.

doi:10.1371/journal.pone.0162001.g002

instrument data, in both the foveal subfield and the outer ring (Spearman rank $\rho>0.50$, $P<0.05$ in all cases), although only moderate to weak for the inner ring (Spearman $\rho<0.50$). A weak correlation was also seen across all subfields when comparing Topcon with Zeiss data. In all cases, the correlation was reduced and/or became not significant when the AEL-dependent scaling was used in the comparisons between data from any of the three sources (Fig 2).

Inter-Session Repeatability

Intra-retinal layer thickness values produced by the Iowa software were compared between session 1 and session 2. For these comparisons, AEL-corrected scaled data was used. Differences outside 3 SD of the mean difference (Grubbs' test) were considered failings in segmentation and were removed from further analysis (n = 26 of 2250 comparisons). Of these, 46%, 42% and 12% were attributed to images from the long-wavelength, Topcon and Zeiss instruments respectively. In general, CoR was similar across images from all devices, and across the three ETDRS subfields (Fig 3).

For layer thickness averaged across the entire ETDRS grid, the layers with best repeatability (as a percentage of the mean) were layer 10 (RPE; 1.2%), layer 4 (INL; 6.2%), and layer 10 (RPE; 4.1%) for the Zeiss, Topcon and long-wavelength devices respectively. The layers with poorest repeatability were layer 8 (IS/OSJ ~ IB_RPE; 22.5%), layer 1 (RNFL; 19.1%), and layer 8 (IS/OSJ ~ IB_RPE; 36.9%) respectively.

Total retinal thickness values were also compared between session 1 and session 2. In all cases, the mean bias was between ±1 µm, and there was no significant difference between session 1 and session 2 for any device or ETDRS subfield ($P>0.05$ in all cases). Fixed-AEL scaling was used to allow comparison to the commercial segmentation. One significant outlier was

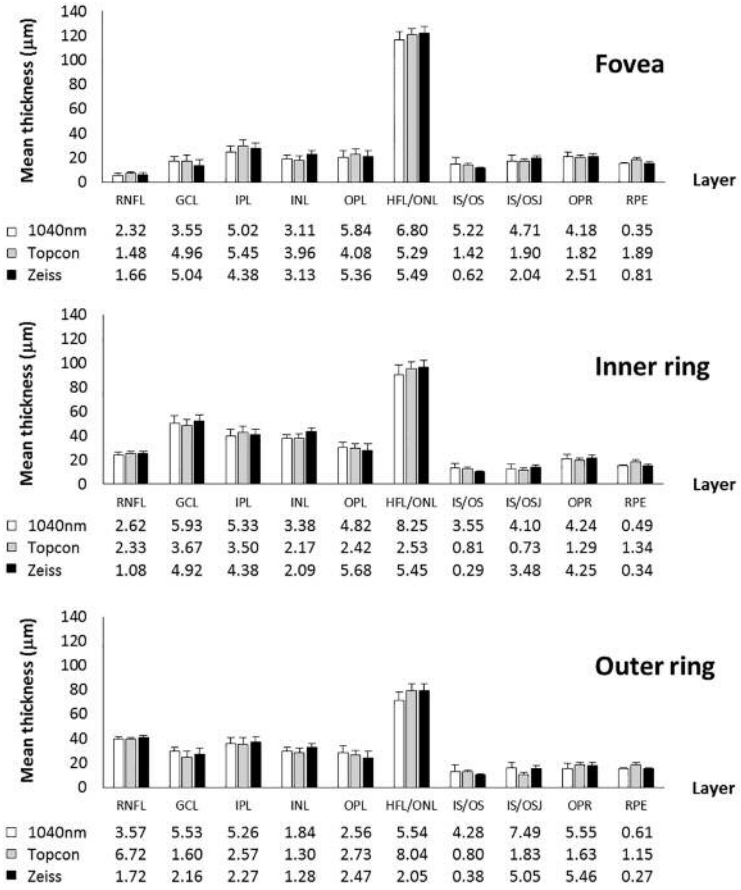

Fig 3. Intra-retinal layer thickness and CoR. Mean thickness of 10 intra-retinal layers segmented by the Iowa Reference Algorithms at session 1, on images from all three OCT devices. Error bars and table values represent inter-session CoR (μm) for each layer.

doi:10.1371/journal.pone.0162001.g003

removed from the long-wavelength data (all subfields), as identified by Grubbs' test. For the Iowa Reference Algorithms, the CoR for the foveal subfields was 4.76μm and 3.43μm for Topcon and Zeiss OCT images respectively. The CoR of both instruments was lower than that of the long-wavelength OCT, which had a CoR of 5.98μm. In all cases the CoR was higher for the foveal subfield than the inner and outer rings (Table 4).

Table 4. Inter-session repeatability of the Iowa Reference Algorithms. Coefficients of repeatability (μm; and percentage) of mean retinal thickness produced by the Iowa Reference Algorithms at session 1 and session 2.

		Fovea	Inner ring	Outer ring
1040nm	Full thickness	5.98 (*2.2%*)	5.86 (*1.7%*)	5.48 (*1.9%*)
Topcon	Full thickness	4.76 (*1.7%*)	3.99 (*1.2%*)	4.10 (*1.4%*)
	Equivalent thickness*	3.90 (*1.6%*)	3.48 (*1.1%*)	3.78 (*1.5%*)
Zeiss	Full thickness	3.43 (*1.2%*)	2.92 (*0.8%*)	3.19 (*1.1%*)
	Equivalent thickness*	3.37 (*1.3%*)	2.95 (*0.9%*)	3.14 (*1.1%*)

*Equivalent values from the Iowa Reference Algorithms (Topcon, ILM to inner boundary of OPR; Zeiss, ILM to inner boundary of RPE) are quoted for comparison to the commercial on-board software segmentation.

doi:10.1371/journal.pone.0162001.t004

Table 5. Inter-session repeatability of the on-board software. Coefficients of repeatability (μm; and percentage) of mean retinal thickness produced by the on-board analysis software of the commercial instruments at session 1 and session 2.

	Fovea	Inner ring	Outer ring
Topcon	7.63 (*3.1%*)	4.68 (*1.5%*)	5.68 (*2.2%*)
Zeiss	4.63 (*1.8%*)	5.06 (*1.6%*)	5.04 (*1.8%*)

doi:10.1371/journal.pone.0162001.t005

For the commercial segmentation, no AEL-correction was made in the scaling. Two significant outliers were removed from the Topcon segmentation data (foveal and inner ring subfields only). The CoR of the foveal subfield was 7.63μm and 4.63μm for the Topcon and Zeiss OCT respectively. Again, the CoR was higher for the foveal subfield than the inner and outer rings for the Topcon OCT images, but was similar across all subfields for the Zeiss OCT images (Table 5).

To allow for comparison between segmentation methods, the Iowa Reference Algorithm 'equivalent retinal thicknesses' were used (Table 4; Fig 4). The on-board software of both commercial instruments was less repeatable than the Iowa Reference Algorithms, for all three subfields (Fig 5).

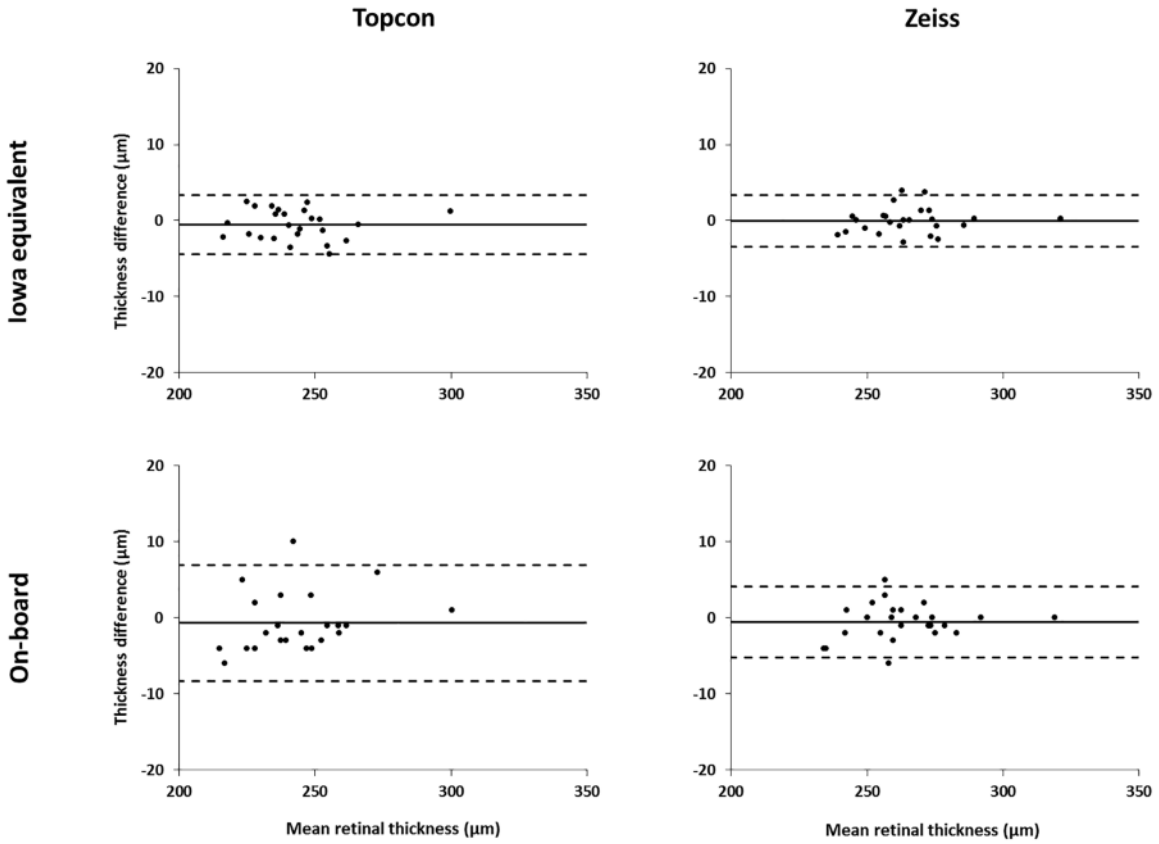

Fig 4. Bland-Altman plots showing inter-session repeatability. Total retinal thickness difference (μm) against mean (μm) for inter-session repeatability of the foveal subfield for both segmentation methods. 95% limits of agreement shown by dashed lines. Note that two significant outliers were removed from the Topcon on-board segmentation data.

doi:10.1371/journal.pone.0162001.g004

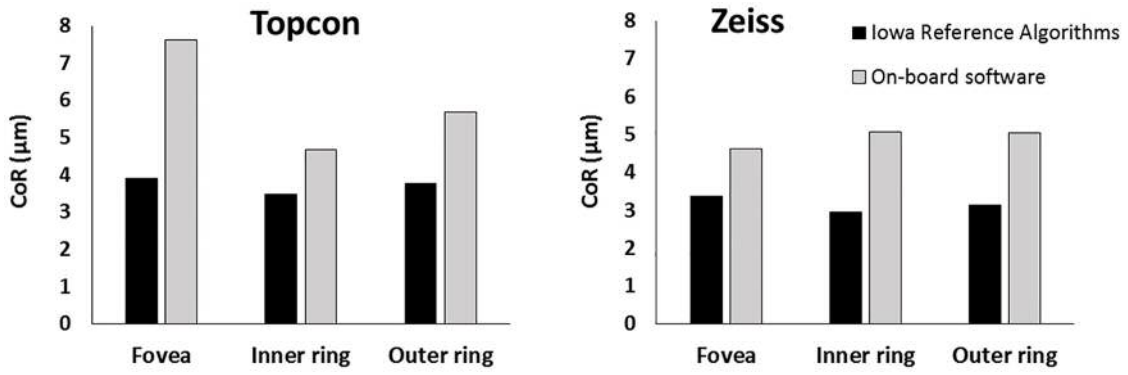

Fig 5. Comparison of inter-session repeatability for the two segmentation methods. Coefficients of repeatability for segmentation by the Iowa Reference Algorithms and on-board software are shown for the Topcon (left) and Zeiss (right) systems. The 'equivalent retinal thickness' values from the Iowa Reference Algorithms were used in this analysis.

doi:10.1371/journal.pone.0162001.g005

Segmentation Software Agreement

A comparison of retinal thickness measurements produced by the Iowa Reference Algorithms and the commercial segmentation software for the two commercial instruments is shown in Table 6. Again, the thickness values were fixed-AEL scaled to allow comparison between algorithms. One significant outlier was removed from the analysis of the Topcon data (foveal subfield only). The commercial segmentation software yielded similar to or marginally higher retinal thickness values than the Iowa Reference Algorithms for the Topcon OCT images. These differences were significant only in the outer ring (Friedman test, $P<0.05$). The commercial software yielded significantly lower values than the Iowa Reference Algorithms for the Zeiss OCT images in all three subfields (Friedman test, $P<0.05$).

Discussion

The Iowa Reference Algorithms produced automated segmentation of 10 intra-retinal layers on all images from all three devices. We have demonstrated a substantial impact of AEL-corrected lateral scaling on mean intra-retinal layer thickness values. If an AEL-dependent lateral scaling is not used, the ETDRS grid (defined in mm units at the retinal surface) will overlay a smaller or larger area of retina, depending on the AEL. The ETDRS subfield sizes could vary by up to 30% assuming a normal AEL range of 20-28mm, which is a little larger than for the cohort of this present study. Appropriate scaling to account for AEL is therefore an important

Table 6. Agreement of total retinal thickness between segmentation methods. Mean difference (bias; µm) and 95% limits of agreement (µm) for mean retinal thickness at session 1 produced by the Iowa Reference Algorithms and the commercial on-board equivalent.

		Fovea	Inner ring	Outer ring
Topcon	Mean difference	0.11	-1.65	-2.91
	Limits of agreement	*-13.05 to 13.28*	*-10.96 to 7.66*	*-12.97 to 7.15*
	Friedman test P	0.414	0.549	0.009*
Zeiss	Mean difference	2.00	6.07	5.73
	Limits of agreement	*-5.76 to 9.75*	*-5.95 to 17.82*	*-6.03 to 16.42*
	Friedman test P	0.028*	0.003*	0.009*

*significant at 0.05 level

doi:10.1371/journal.pone.0162001.t006

consideration for any quantitative retinal thickness analysis, particularly in cross-sectional applications.

The Iowa Reference Algorithms demonstrated good agreement between the Topcon and Zeiss instruments (as shown previously; [33]), and with the long-wavelength device. However, the Iowa Reference Algorithms produced significantly higher retinal thickness values on images from both commercial systems than the long-wavelength system, across all subfields, even when the AEL-dependent scaling was used. Refractive index assumptions for retinal tissues used by each instrument could result in a small difference in axial scaling. Knowing the assumptions made for each device, we expect a difference in absolute thickness values between instruments of between 1.4% and 2.9%, with largest thickness values from the Zeiss images (n = 1.36), then Topcon images (n = 1.38) and finally the long-wavelength OCT (n = 1.4). In general, this is consistent with our findings (Table 2).

Discrepancies in retinal thickness measurement between images from the long-wavelength and commercial systems were significantly correlated with AEL for the foveal and outer ring subfields, when using the fixed-AEL scaling. When the AEL-dependent scaling was used throughout this analysis, all these correlations were reduced and were no longer significant (Fig 2). This effect is consistent with the expected transverse magnification error that arises when fixed-AEL scaling is used for images from either of the commercial instruments. This confirms that the on-board software of the Zeiss and Topcon instruments used in this study do not make a scaling correction for AEL. The Iowa Reference Algorithms allow for direct input of transverse scaling factors prior to image segmentation which should be used, where possible, to reduce these demonstrated magnification errors.

Inter-session repeatability of the Iowa Reference Algorithms was assessed for each of the 10 intra-retinal layers on images from each device. Although the CoR was similar across the three devices and three ETDRS subfields, there were far fewer significant outliers excluded from the Zeiss data by Grubbs' test. Had these outliers been included, inter-session repeatability would have been poorer for the other two devices. Overall, RPE thickness was the most repeatable measure, particularly for the Zeiss and long-wavelength OCT (CoR 0.5μm for both). As a change in thickness of this layer greater than this value would indicate change outside the normal variation, these measures represent a useful clinical biomarker for diseases that affect the RPE, such as AMD [34].

The least repeatable measures were the inner retinal layers (1–5) in the foveal subfield (Fig 3). This is expected, since these layers are thin in this region. Additionally, some layers are more difficult to distinguish due to near iso-reflectivity, for example GCL from IPL, and HFL from OPL. The HFL commonly fluctuates in appearance between acquisitions, dependent on angle of incidence, which would also likely limit the repeatability of segmentation of this layer [35]. The inner retinal layers were generally more repeatable in the outer ring across all devices. However, the outer ring has the lowest RNFL repeatability across all devices, possibly attributed to the thickness variability due to nasal/temporal asymmetry at this eccentricity. However, if analyzed in an appropriate manner (by quadrant, for instance), this may have applications in a number of conditions [36–39].

Total retinal thickness in the foveal subfield was less repeatable than the inner and outer rings, which is also likely attributable to retinal anatomy (greater thickness variability in the foveal subfield). All repeated measures using the Iowa Reference Algorithms on the Topcon and Zeiss OCT images were within 1.7% and 1.3% of mean retinal thickness respectively for all subfields (Table 4). The long-wavelength OCT images had a marginally higher CoR (within 2.2% for all subfields, with one outlier removed). This non-commercial device was designed for optimal imaging of the deeper structures, including the choroid, due to reduced scatter at this wavelength [25]. However, differences in reflective properties of the layer boundaries are likely

to occur at this longer wavelength, which the Iowa Reference Algorithms may not be optimized to detect. Since the main function of the long-wavelength OCT is to image the deeper retinal structures, the acquisition protocol used to collect these images was similar to enhanced depth imaging [40], with the choroid intentionally positioned closer to the zero delay line. This may have resulted in reduced signal from the more superficial retinal layers, and may explain the reduced repeatability compared to the commercial devices.

The Iowa Reference Algorithms measurements were more repeatable than the equivalent commercial segmentation software assessed. The inter-session repeatability analysis of the Topcon commercial segmentation software revealed two clear outliers. Both images were of poorer quality than the rest of the sample (image quality <25 in the Topcon-generated report) which led to marked errors in ILM boundary position in the foveal subfield during segmentation. Removing these outliers from this subfield, the CoR was reduced from 21.56μm to 7.63μm, which is more comparable to the other subfields and to the Zeiss commercial software. It should be noted that segmentation of these same two images using the Iowa Reference Algorithms produced no marked errors in boundary placement in any subfield.

Since the majority of these CoR values are nearing the resolution limit of all three instruments (~5μm axially), this small inter-session thickness variation is unlikely to be clinically meaningful. However, since many thickness values are averaged over each region and/or over the entire cohort in this study, significant results of boundary positions can be obtained to a higher precision than the optical resolution of the instrument. The axial sampling resolution (3.5μm for the Topcon, and ~2μm for the Zeiss and long-wavelength systems) is another potential limiting factor but averaging over many thickness measurements can again, in theory, provide even higher resolution results limited ultimately by the signal-to-noise ratio of the devices and the repeatability of the scanning geometry.

Our inter-session findings for the Zeiss instrument are comparable to, if not slightly more repeatable than, previous findings [11,41]. Kotera and colleagues [42] reported slightly higher repeatability than our findings for the Topcon segmentation software (total retinal thickness CoR of 3.10μm and 2.01μm for the inner ring and outer ring respectively, in comparison to our values of 5.99μm and 5.68μm). However, their assessment was an intra- rather than inter-session repeatability, and did not include the ETDRS foveal subfield since their main outcome measure was retinal nerve fiber layer (RNFL) thickness in glaucoma. It is worth noting that we would expect the inter-session repeatability to be poorer in eyes with macular disease due to the nature of the pathological retinal features [43,44]. In some cases, the segmented boundaries may require manual repositioning to ensure accurate quantification. Measures in healthy participants were the focus of the present study, to evaluate the repeatability of the algorithm under ideal conditions.

Good agreement was shown between the Iowa Reference Algorithms and the commercial software, when equivalent segmentation boundaries were used (as shown in Table 6). There was slight bias in both cases, with the Topcon segmentation producing slightly higher values (Friedman test, $P<0.05$ in the outer ring only), and the Zeiss segmentation producing lower values than the Iowa Reference Algorithms (Friedman test, $P<0.05$ in all subfields). However, these discrepancies accounted for less than 2% of total retinal thickness in all subfields, and are unlikely to be significant in clinical applications. This is consistent with previous comparative studies using the Iowa Reference Algorithms and Cirrus and Spectralis OCT commercial software [17,45]. To our knowledge, no previous comparison has been made using the Topcon 3D-OCT.

This study had a relatively small sample size (n = 25) for an inter-session repeatability study and a relatively narrow distribution of AEL. Only participants without retinal disease were included in this study, therefore conclusions can only be applied to this group. Further study is necessary to assess the repeatability of the segmentation software in ocular disease. Lastly, the high

repeatability of the intra-retinal layer segmentation by the Iowa Reference Algorithms is promising, although further analysis is required to compare this with the available on-board software.

In conclusion, we have confirmed that lateral magnification errors affect the consistency and reliability of generated thickness values, and are therefore an important consideration in quantitative OCT retinal layer analysis. Nevertheless, the Iowa Reference Algorithms provide repeatable automated retinal thickness measurements, which outperform the commercial segmentation software, and allow a convenient mechanism to apply an accurate AEL-dependent lateral scaling to images from any OCT device. In these respects, this algorithm is viable for clinical and research applications, for eyes without ocular disease imaged using the three OCT devices in this study.

Author Contributions

Conceptualization: LT THM RVN NW AW.

Data curation: LT JF.

Formal analysis: LT KL JF AW.

Investigation: LT.

Methodology: LT NC KL JHA THM RVN JF NW AW.

Project administration: AW.

Resources: JHA THM RVN NW AW.

Software: LT NC KL JF NW.

Supervision: AW THM RVN.

Validation: LT JF NW AW.

Visualization: LT.

Writing – original draft: LT.

Writing – review & editing: LT THM RVN JF NW AW.

References

1. Hee MR, Baumal CR, Puliafito CA, Duker JS, Reichel E, Wilkins JR, et al. Optical coherence tomography of age-related macular degeneration and choroidal neovascularization. Ophthalmology. 1996; 103: 1260–1270. PMID: 8764797
2. Drexler W, Fujimoto JG. State-of-the-art retinal optical coherence tomography. Prog Retin Eye Res. 2008; 27: 45–88. PMID: 18036865
3. Browning DJ, Glassman AR, Aiello LP, Beck RW, Brown DM, Fong DS, et al. Relationship between optical coherence tomography-measured central retinal thickness and visual acuity in diabetic macular edema. Ophthalmology. 2007; 114: 525–36. PMID: 17123615
4. Puliafito CA, Hee MR, Lin CP, Reichel E, Schuman JS, Duker JS, et al. Imaging of macular diseases with optical coherence tomography. Ophthalmology. 1995; 102: 217–229. PMID: 7862410
5. Martin DF, Maguire MG, Fine SL, Ying G, Jaffe GJ, Grunwald JE, et al. Ranibizumab and bevacizumab for treatment of neovascular age-related macular degeneration: two-year results. Ophthalmology. 2012; 119: 1388–98. doi: 10.1016/j.ophtha.2012.03.053 PMID: 22555112
6. Avery RL, Pieramici DJ, Rabena MD, Castellarin AA, Nasir MA, Giust MJ. Intravitreal bevacizumab (Avastin) for neovascular age-related macular degeneration. Ophthalmology. 2006; 113: 363–372.e5. PMID: 16458968
7. Abràmoff MD, Garvin MK, Sonka M. Retinal imaging and image analysis. IEEE Rev Biomed Eng. 2010; 3: 169–208. doi: 10.1109/RBME.2010.2084567 PMID: 22275207

8. Jia Y, Bailey ST, Wilson DJ, Tan O, Klein ML, Flaxel CJ, et al. Quantitative optical coherence tomography angiography of choroidal neovascularization in age-related macular degeneration. Ophthalmology. 2014; 121: 1435–1444. doi: 10.1016/j.ophtha.2014.01.034 PMID: 24679442
9. Chiu SJ, Li XT, Nicholas P, Toth CA, Izatt JA, Farsiu S. Automatic segmentation of seven retinal layers in SDOCT images congruent with expert manual segmentation. Opt Express. 2010; 18: 19413–28. doi: 10.1364/OE.18.019413 PMID: 20940837
10. Giani A, Cigada M, Choudhry N, Deiro AP, Oldani M, Pellegrini M, et al. Reproducibility of retinal thickness measurements on normal and pathologic eyes by different optical coherence tomography instruments. Am J Ophthalmol. 2010; 150: 815–24. doi: 10.1016/j.ajo.2010.06.025 PMID: 20965494
11. Wolf-Schnurrbusch UEK, Ceklic L, Brinkmann CK, Iliev ME, Frey M, Rothenbuehler SP, et al. Macular thickness measurements in healthy eyes using six different optical coherence tomography instruments. Invest Ophthalmol Vis Sci. 2009; 50: 3432–7. doi: 10.1167/iovs.08-2970 PMID: 19234346
12. Buchser NM, Wollstein G, Ishikawa H, Bilonick RA, Ling Y, Folio LS, et al. Comparison of retinal nerve fiber layer thickness measurement bias and imprecision across three spectral-domain optical coherence tomography devices. Invest Ophthalmol Vis Sci. 2012; 53: 3742–3747. doi: 10.1167/iovs.11-8432 PMID: 22538423
13. Chopovska Y, Jaeger M, Rambow R, Lorenz B. Comparison of central retinal thickness in healthy children and adults measured with the Heidelberg Spectralis OCT and the Zeiss Stratus OCT 3. Ophthalmologica. 2011; 225: 27–36. doi: 10.1159/000316693 PMID: 20693819
14. Garvin MK, Abràmoff MD, Wu X, Russell SR, Burns TL, Sonka M. Automated 3-D intraretinal layer segmentation of macular spectral-domain optical coherence tomography images. IEEE Trans Med Imaging. 2009; 28: 1436–47. doi: 10.1109/TMI.2009.2016958 PMID: 19278927
15. Antony B, Abràmoff MD, Tang L, Ramdas WD, Vingerling JR, Jansonius NM, et al. Automated 3-D method for the correction of axial artifacts in spectral-domain optical coherence tomography images. Biomed Opt Express. 2011; 2: 1734–1746.
16. Lee K, Garvin M, Russell S, Sonka M, Abràmoff M. Automated intraretinal layer segmentation of 3-D macular OCT scans using a multiscale graph search. ARVO. 2010. p. E–abstract 1767.
17. Sohn EH, Chen JJ, Lee K, Niemeijer M, Sonka M, Abràmoff MD. Reproducibility of diabetic macular edema estimates from SD-OCT is affected by the choice of image analysis algorithm. Invest Ophthalmol Vis Sci. 2013; 54: 4184–8. doi: 10.1167/iovs.12-10420 PMID: 23696607
18. Littmann H. [Determination of the real size of an object on the fundus of the living eye]. Klin Monbl Augenheilkd. 1982; 180: 286–9. (In German). PMID: 7087358
19. Bennett A, Rudnicka A, Edgar D. Improvements on Littmann's method of determining the size of retinal features by fundus photography. Graefe's Arch Clin Exp Ophthalmol. 1994; 232: 361–7.
20. Bussel II, Wollstein G, Schuman JS. OCT for glaucoma diagnosis, screening and detection of glaucoma progression. Br J Ophthalmol. 2014; 98: ii15–ii19. doi: 10.1136/bjophthalmol-2013-304326 PMID: 24357497
21. Boey PY, Mansberger SL. Ocular hypertension: an approach to assessment and management. Can J Ophthalmol / J Can d'Ophtalmologie. 2014; 49: 489–496.
22. Kanagasingam Y, Bhuiyan A, Abràmoff MD, Smith RT, Goldschmidt L, Wong TY. Progress on retinal image analysis for age related macular degeneration. Prog Retin Eye Res. 2014; 38: 20–42. doi: 10.1016/j.preteyeres.2013.10.002 PMID: 24211245
23. Chylack L, Wolfe J, Singer D, Leske C, Bullimore M, Bailey I, et al. The lens opacities classification system III. Arch Ophthalmol. 1993; 111: 831–6. PMID: 8512486
24. Povazay B, Hermann B, Unterhuber A, Hofer B, Sattmann H, Zeiler F, et al. Three-dimensional optical coherence tomography at 1050 nm versus 800 nm in retinal pathologies: enhanced performance and choroidal penetration in cataract patients. J Biomed Opt. 2007; 12: 041211. PMID: 17867800
25. Povazay B, Bizheva K, Hermann B, Unterhuber A, Sattmann H, Fercher A, et al. Enhanced visualization of choroidal vessels using ultrahigh resolution ophthalmic OCT at 1050 nm. Opt Express. 2003; 11: 1980–6. PMID: 19466083
26. Wood A, Binns A, Margrain T, Drexler W, Považay B, Esmaeelpour M, et al. Retinal and choroidal thickness in early age-related macular degeneration. Am J Ophthalmol. 2011; 152: 1030–1038.e2. doi: 10.1016/j.ajo.2011.05.021 PMID: 21851922
27. ANSI. Safe use of lasers & safe use of optical fiber communications. American National Standards Institute—Z136 Committee. Orlando Laser Inst Am. 2000; 168.
28. Schindelin J, Arganda-Carreras I, Frise E, Kaynig V, Longair M, Pietzsch T, et al. Fiji: an open-source platform for biological-image analysis. Nat Methods. 2012; 9: 676–82. doi: 10.1038/nmeth.2019 PMID: 22743772

29. Thévenaz P, Ruttimann UE, Unser M. A pyramid approach to subpixel registration based on intensity. IEEE Trans Image Process. 1998; 7: 27–41. doi: 10.1109/83.650848 PMID: 18267377

30. Vaz S, Falkmer T, Passmore AE, Parsons R, Andreou P. The case for using the repeatability coefficient when calculating test-retest reliability. PLoS One. 2013; 8: 1–7.

31. Bland JM, Altman D. Statistical methods for assessing agreement between two methods of clinical measurement. Lancet. 1986; 327: 307–310.

32. Grubbs FE. Sample criteria for testing outlying observations. Ann Math Stat. 1950; 21: 27–58.

33. Rashid A, Schmidt-Erfurth U, Gerendas B, Waldstein SM, Wahle A, Simader C, et al. Reporoducibility of total retinal thickness in 5 SD-OCT scanners using Iowa Reference Algorithm. ARVO. 2014. p. E–abstract 4786.

34. Farsiu S, Chiu SJ, O'Connell R V., Folgar FA, Yuan E, Izatt JA, et al. Quantitative classification of eyes with and without intermediate age-related macular degeneration using optical coherence tomography. Ophthalmology. 2014; 121: 162–172. doi: 10.1016/j.ophtha.2013.07.013 PMID: 23993787

35. Lujan BJ, Roorda A, Knighton RW, Carroll J. Revealing Henle's fiber layer using spectral domain optical coherence tomography. Invest Ophthalmol Vis Sci. 2011; 52: 1486–92. doi: 10.1167/iovs.10-5946 PMID: 21071737

36. Thomson KL, Yeo JM, Waddell B, Cameron JR, Pal S. A systematic review and meta-analysis of retinal nerve fiber layer change in dementia, using optical coherence tomography. Alzheimer's Dement Diagnosis, Assess Dis Monit. 2015; 1: 136–143.

37. Rao HL, Zangwill LM, Weinreb RN, Sample PA, Alencar LM, Medeiros FA. Comparison of different spectral domain optical coherence tomography scanning areas for glaucoma diagnosis. Ophthalmology. 2010; 117: 1692–1699.e1. doi: 10.1016/j.ophtha.2010.01.031 PMID: 20493529

38. Martinez-de-la-Casa JM, Ruiz-Calvo A, Saenz-Frances F, Reche-Frutos J, Calvo-Gonzalez C, Donate-Lopez J, et al. Retinal nerve fiber layer thickness changes in patients with age-related macular degeneration treated with intravitreal ranibizumab. Invest Ophthalmol Vis Sci. 2012; 53: 6214–6218. doi: 10.1167/iovs.12-9875 PMID: 22915037

39. Garcia-Martin E, Pinilla I, Sancho E, Almarcegui C, Dolz I, Rodriguez-Mena D, et al. Optical coherence tomography in retinitis pigmentosa: reproducibility and capacity to detect macular and retinal nerve fiber layer thickness alterations. Retina. 2012; 32: 1581–91. PMID: 22922847

40. Spaide RF, Koizumi H, Pozzoni MC. Enhanced depth imaging spectral-domain optical coherence tomography. Am J Ophthalmol. 2008; 146: 496–500. doi: 10.1016/j.ajo.2008.05.032 PMID: 18639219

41. Garcia-Martin E, Pinilla I, Idoipe M, Fuertes I, Pueyo V. Intra and interoperator reproducibility of retinal nerve fibre and macular thickness measurements using Cirrus Fourier-domain OCT. Acta Ophthalmol. 2011; 89: e23–9. doi: 10.1111/j.1755-3768.2010.02045.x PMID: 21106044

42. Kotera Y, Hangai M, Hirose F, Mori S, Yoshimura N. Three-dimensional imaging of macular inner structures in glaucoma by using spectral-domain optical coherence tomography. Invest Ophthalmol Vis Sci. 2011; 52: 1412–21. doi: 10.1167/iovs.10-5572 PMID: 21087959

43. Parravano M, Oddone F, Boccassini B, Menchini F, Chiaravalloti A, Schiavone M, et al. Reproducibility of macular thickness measurements using Cirrus SD-OCT in neovascular age-related macular degeneration. Invest Ophthalmol Vis Sci. 2010; 51: 4788–91. doi: 10.1167/iovs.09-4976 PMID: 20435585

44. Forooghian F, Cukras C, Meyerle CB. Evaluation of time domain and spectral domain optical coherence tomography in the measurement of diabetic macular edema. Invest Ophthalmol Vis Sci. 2008; 49: 4290–4296. doi: 10.1167/iovs.08-2113 PMID: 18515567

45. Garvin MK, Lee K, Burns TL, Abràmoff MD, Sonka M, Kwon YH. Reproducibility of SD-OCT-based ganglion cell-layer thickness in glaucoma using two different segmentation algorithms. Invest Ophthalmol Vis Sci. 2013; 54: 6998–7004. doi: 10.1167/iovs.13-12131 PMID: 24045993